Printed Implantable Devices for Gastrooesophageal Reflux Disease (GORD) Diagnosis

This thesis is submitted for the degree of Doctor of Philosophy.

Ahmed Salem

Supervisor: Professor Manish K. Tiwari Clinical Collaborator: Professor Laurence Lovat

University College London

Department of Medical Physics and Biomedical Engineering

Declaration

I, Ahmed Salem, confirm that the work presented in this thesis is my own. Wherever information has been derived from other sources, has been indicated in the thesis.

Abstract

Ambulatory pH monitoring is crucial for diagnosing gastro-oesophageal reflux disease (GORD), but current devices are often large, uncomfortable, poorly tolerated, and inaccurate. This work introduces novel pH-sensing devices that address these issues through soft, miniaturised, flexible, and biocompatible mucosa-interfacing electronics. Designed to adhere seamlessly to the oesophageal mucosa, these enable less invasive and more accurate GORD diagnostics.

A comprehensive investigation into electrochemical pH sensors details the promise of polymer/carbon-based electrode materials due to their exceptional flexibility, biocompatibility, and high reactivity. Customised inks for nanosensor fabrication were developed, facilitating the creation of robust and highly sensitive sensors. Through refinement of both materials and fabrication methods, these sensors were optimised to deliver stable and reliable performance over a large pH range.

Further advancements involved integrating covalent organic frameworks (COFs) as electrochemical composites, enhancing the sensitivity and stability of the sensors. COFs were also tested for their biocompatibility, ensuring the sensors would be safe for long-term use in vivo.

Wireless communication was then incorporated into the device, employing near-field communication (NFC) to enable real-time data transmission. Simulations and experiments demonstrated the feasibility of transmitting data readings wirelessly and without a battery, offering an avenue for minimally invasive and efficient in vivo monitoring.

Finally, to ensure secure attachment to the oesophageal lining, bioadhesives were explored and built upon a gelatine-poly(acrylic acid) hydrogel matrix. This bioadhesive was characterised for its mechanical and oesophageal mucoadhesive properties, with successful ex-vivo testing showing its ability to withstand conditions mimicking the oesophagus during fluid intake.

This work demonstrates the feasibility of a novel mucosa-interfacing sensor for GORD diagnosis, combining advanced sensing materials, wireless communication, and secure bioadhesion into a fully integrated, minimally invasive device. Despite some

current limitations, particularly the need for in vivo validation, this approach offers a promising path toward more comfortable, accurate, and efficient GORD monitoring.

Impact Statement

Gastro-oesophageal reflux disease (GORD) is a common digestive disorder with increasing prevalence due to changing lifestyles and ageing populations. Current diagnostic methods rely on bulky, uncomfortable, and often unreliable sensors, limiting patient comfort and diagnostic accuracy. This research addresses these challenges by developing a novel, pH-sensing, mucosa-interfacing device for GORD diagnosis. The miniaturised, flexible, and biocompatible sensors provide a more comfortable and accurate means of diagnosis, improving patient experience. By seamlessly adhering to the mucosa, the sensors enable imperceptible, continuous, and highly sensitive monitoring, significantly enhancing symptom management.

This research also holds promise for improving the quality of life (QoL) for GORD patients, who often experience impaired eating, sleep disturbances, and decreased vitality. The development of these sensors facilitates a more data-driven approach to symptom management, enabling patients to track how lifestyle factors such as diet and stress correlate with their symptoms. This personalised approach could improve treatment effectiveness, reduce reliance on proton pump inhibitors (PPIs) linked to long-term side effects, and potentially prevent relapse in the 80% of patients who experience recurrence after discontinuing acid-suppressive treatment.

The implications of this technology extend beyond GORD diagnosis. The sensors' biocompatible and flexible design makes them highly adaptable for various biomedical applications, including continuous monitoring of other gastrointestinal conditions and chronic diseases. Additionally, by offering a less invasive alternative to current diagnostic methods, these sensors could reduce healthcare costs associated with inaccurate diagnoses and ineffective treatments, leading to better resource allocation within healthcare systems globally.

This work also contributes to material science and bioengineering. By leveraging the unique properties of graphene derivatives and covalent-organic frameworks, the research demonstrates how cutting-edge materials can be used to create high-performing, scalable, and cost-effective devices. These advances may drive innovation in other industries, such as environmental monitoring, where similar sensing technologies could track pH changes in water systems or detect pollutants.

Furthermore, introducing a minimally invasive, patient-friendly diagnostic device could improve adherence to medical procedures. A device that aligns with patients' comfort and lifestyle preferences may lead to earlier diagnoses, enabling timely interventions and reducing the burden of untreated chronic diseases. This work also addresses the need for healthcare systems to reduce costs while improving patient outcomes, helping to alleviate the financial strain caused by widespread conditions like GORD.

The development of this novel sensor may help change GORD diagnosis, empower patients with actionable insights, and inspire new directions in medical technology. By transforming discomfort and imprecision into opportunity and innovation, this research marks a significant step towards a more patient-centred, efficient, and sustainable diagnostic tool.

UCL Research Paper Declaration Form

Referencing the Doctoral Candidate's Own Published Work(s)

Please use this form to declare if parts of your thesis are already available in another format, e.g. if data, text, or figures:

- · have been uploaded to a preprint server
- are in submission to a peer-reviewed publication
- have been published in a peer-reviewed publication, e.g. journal, textbook.

This form should be completed as many times as necessary. For instance, if you have seven thesis chapters, two of which containing material that has already been published, you will complete this form twice.

1. For a research manuscript that has already been published

(if not yet published, skip to section 2):

a) Title of the manuscript:

Robust pH Sensing Using a Graphene Oxide and Covalent Organic Frameworks Composite for Gastro-esophageal Reflux Disease Diagnosis

b) Provide the DOI or direct link to the published the work:

https://doi.org/10.1002/adhm.202502106

c) Publication name (e.g. journal or textbook):

Advanced Healthcare Materials

d) Publisher name (e.g. Elsevier, Oxford University Press):

Wiley

e) Date of publication:

05/08/2025

f) List all authors as they appear in the publication:

Ahmed H. M. Salem, Jianhui Zhang, Ashley Lam, Haowei Wang, Umber Cheema, Laurence B. Lovat, Manish K. Tiwari

g) Was the work peer reviewed?

Yes

h) Do you retain copyright for the work?

Yes

i) Was an earlier version uploaded to a preprint server (e.g., medRxiv, arXiv)?

If 'Yes', provide the DOI or direct link. If not applicable, leave blank.

Click or tap here to enter text.

If 'No', please seek publisher permission and check the box below:



I acknowledge permission of the publisher named in item **1d** to include in this thesis portions of the publication cited in item **1c**.

For multi-authored work, please provide a contribution statement detailing each author's role (if single-authored, skip to section 4):

Ahmed Salem was involved in the conception and design, testing, synthesis, drafting the article and writing the final paper. Jianhui Zhang was involved in the testing, synthesis, conception and review and editing of the paper. Ashley Lam was involved in the cytotoxicity testing and was supervised by Umber Cheema. Haowei Wang helped with materials characterisation (XRD). Laurence B. Lovat and Manish K. Tiwari supervised the study, and were involved in the conception, review and editing of the final paper.

2. In which chapter(s) of your thesis can this material be found?

3

3. e-Signatures confirming accuracy of the above information

(This form should be co-signed by the supervisor/senior author unless the work is single-authored)

Candidate signature:



Ahmed Salem

Date:

22/08/2025

Supervisor/ Senior Author (where appropriate)

Prof. Manish K. Tiwari

Date:

22/08/2025

Acknowledgements

I am deeply grateful to my primary supervisor, Prof. Manish K. Tiwari, whose unwavering support, expert guidance, and encouragement have been a cornerstone of my academic journey, starting from my undergraduate degree through the application process that led to this PhD. His mentorship has been invaluable, and I cannot thank him enough for his dedication and belief in my abilities.

My sincere thanks also go to my second supervisor, Prof. Laurence B. Lovat, whose insightful guidance, encouragement, and expertise have inspired me to aim higher and achieve more. His academic and life advice have been instrumental in shaping my journey, and I am incredibly thankful for the opportunity to learn from him and for his steadfast support throughout my PhD. I look forward to continuing to work with both of my supervisors as we strive to translate this research into real-world impact that can benefit patients.

I would also like to express my heartfelt gratitude to the incredible team at the Nanoengineered Systems Lab. Jianhui Zhang, thank you for being an excellent collaborator, a supportive colleague, and a wonderful friend. Carmen Salvadores, my journey into this PhD would not have been possible without you. From our first year at UCL, your friendship and support have been a constant source of strength. To Matas Petreikis, Wei Huang, Mohammed Alabdullatif, and Nick Salaris, thank you for creating such a positive and uplifting environment at Charles Bell House. Your camaraderie and support not only provided good vibes, but also made it productive and truly enjoyable.

I am also grateful to Lulu Xu, Ashley Lam, Noora Al Marri, and Jiaxing Zhang for their invaluable contributions to different parts of my research. Your support and collaboration have been instrumental to the progress of this work, and I deeply appreciate all you have done.

This research would not have been possible without the funding and facilities provided by the UCL Wellcome/EPSRC Centre for Interventional Surgical Sciences. I am especially thankful for the support from the EPSRC Centre for Doctoral Training in Intelligent, Integrated Imaging in Healthcare (i4health), which enabled this work.

To my family—Hamdy, Naglaa, Omar, Khaled, and Mamalola—thank you for your endless love, understanding, and encouragement. Your unwavering belief in me has been my rock and a constant source of motivation throughout this journey.

Finally, I would like to extend special thanks to all the individuals who assisted me throughout my PhD. Your kindness, insights, and support, whether big or small, have been greatly appreciated and will never be forgotten.

Table of Contents

Chapter 1	Introduction	21
1.1	Motivation	22
1.2	Clinical Need	23
1.3	Current GORD Diagnostic Technology	25
1.3.1	Catheter-based Devices	26
1.3.2	Capsule-based Devices	29
1.4	Thesis Aim and Objectives	31
1.5	Thesis Outline and Chapters	32
1.5.1	Printed Robust pH Sensors	33
1.5.2	Covalent Organic Frameworks for Electrochemical Sensing	34
1.5.3	Wireless Signalling and Sensing	34
1.5.4	Biocompatible Mucoadhesives	35
1.5.5	Summary	35
Chapter 2	Printed, Robust pH Sensors	37
2.1	Background and Literature Review	38
2.1.1	Types of pH Sensors	38
2.1.2	Working Principle of pH Sensors	42
2.1.3	Sensing Materials of pH Sensors	48
2.1.4	Graphene-Based pH Sensors	50
2.1.5	pH Sensitive Mechanism of Graphene	56
2.1.6	Nanosensor Fabrication Techniques	59
2.1.7	Nanosensor Printing Techniques	60
2.1.8	Substrate Wettability and Adhesion	67
2.1.9	Summary of pH Sensor Literature and Gaps	69
2.2	Printed Graphene Oxide Sensors with Robust Sensing in Low Acidity Environments	70
2.2.1	Introduction	70
2.2.2	Materials and Methods	73
2.2.3	Results and Discussion	77
2.2.4	Conclusion	89
Chapter 3	Covalent Organic Frameworks for Electrochemical Sensing	92
3.1	Background and Literature Review	93
3.1.1	History of Covalent Organic Frameworks	93

3.1.2	COF Synthesis	94
3.1.3	Advantages of COFs for Chemical Detection	99
3.1.4	3.1.4 Disadvantages of COFs	
3.1.5	COF Electrochemical Sensors	103
3.2 p	H Sensitive Electrochemical GO+COF Composite	107
3.2.1	Introduction	107
3.2.2	Materials and Methods	110
3.2.3	Results and Discussion	115
3.2.4	Conclusion	132
Chapter 4 : V	/ireless Signalling and Sensing	133
4.1 B	ackground and Literature Review	134
4.1.1	Passive NFC Sensing Working Principle	135
4.1.2	Chipped vs Chipless NFC Tags	138
4.1.3	Potentiometric pH Sensing Using NFC	141
4.1.4	Batteryless, implantable pH sensors using NFC	142
4.2 T	urning the sensors into a standalone biomedical device	144
4.2.1	Introduction	144
4.2.2	Design and Fabrication	145
4.2.3	Results	153
4.2.4	Conclusion	158
Chapter 5 : B	iocompatible Mucoadhesives	160
5.1 B	ackground and Literature Review	161
5.1.1	Adhesive Types	162
5.1.2	Adhesion Mechanisms	163
5.1.3	Hydrogel Adhesion	164
5.1.4	Natural Bioadhesives	166
5.1.5	Synthetic and Semi-synthetic Bioadhesives	171
5.1.6	Summary of Bioadhesives Literature and Gaps	174
5.2 N	Aucoadhesive, biocompatible patches for oesophageal attachment	175
5.2.1	Introduction	175
5.2.2	Materials and Methods	178
5.2.3	Results and Discussion	181
5.2.4	Conclusion	191
Chapter 6: 0	Conclusion and Future Work	193

6.1 Conclusions		194	
6.2	Contributions	195	
6.3	Limitations and Future Work	199	
6.4	Concluding Remarks	202	
6.4	.1 Summation of Key Points	202	
6.4	.2 Broader Implications and Contributions of the Research	202	
6.4	.3 Final Thoughts and Future Directions	202	
Referenc	ees	203	
Appendia	x I	225	
High-F	Resolution Inkjet Printing	225	
Electro	ohydrodynamic Printing	226	
Self-As	ssembled Layers	228	
Appendix	x II	229	
Cyclic	Voltammetry Scans – COF/GO Composite	229	
Imped	lance Analyser Scans	232	
Appendix	x III	233	
Cell Vi	iability Analysis Procedure	233	
Appendix	x IV	237	
Blu	etooth-Based Communication Device	237	
Author C	Contribution Statement	245	

Table of Figures

Figure 1: (A) Prevalence of GORD cases by region (B) Age-standardised prevalence per 100,000 cases. Figure	re
created using source data from [6].	24
Figure 2: A diagram and image of the suction-based mechanical attachment mechanism used in one of the	e
current implantable pH monitoring systems, the Bravo™ capsule. Sourced from [31]	
Figure 3: Graphical abstract of the thesis	
Figure 4: (a) Diagram of a MOSFET including all 4 terminals, Body, Source, Drain, and Gate. (b) Diagram of	
ISFET highlighting the differences where the gate is replaced by a reference electrode and an	
electrolyte solution, and the gate dielectric is exposed and used as a sensing film. Both images are	
sourced from [63].	42
Figure 5: Diagram showing the different layers that contribute to the electric potential observed in the site	•
binding model. A complexation is also shown which shows that it is possible to have complex	•
compounds forming on the surface contributing to the electrical potential observed. Schematic	
sourced and adapted from [63]	47
Figure 6: The beakers have an equal concentration of graphene oxide (GO) yet react very differently when	-
the pH of the electrolytic solution is varied. (a)In an alkaline setting, the GO behaves as a salt where	
at an acidic pH level (b) sandwich-like structures are formed due to hydrogen bonding. Figure adopt	
from [84] under creative commons license.	53
Figure 7: GO concentration is plotted against surface tension in alkaline and acidic water-based electrolyti	•
solutions. Figure sourced from [83].	54
Figure 8: Chemical structure diagram of carbon atoms and graphene to detail the presence of π electrons	.54
which causes the electrical conductivity.	57
Figure 9: Chemi-resistive response of single-layer graphene. Adopted from [97] under creative commons	.37
license.	FO
	.58
Figure 10: Schematic detailing the defect-induced pH response. Adopted from [99] under creative commo	
license.	_59
Figure 11: (a) 2-D and (b) 3-D diagrams of the screen printer apparatus. The squeegee is dragged across the	
stencil which is used to deposit the ink in the specified orientation. Images adapted from [103,110]	.62
Figure 12: Schematic of an example direct-write printing setup supplemented with a collocated long-	
distance camera and microscope.	65
Figure 13: Schematic depicting the impact of pressure and nozzle-substrate distance on printing. When the	
pressure is too high leaking occurs. When the pressure is too low, no contact can be established, and	1
the desired pressure creates a stable meniscus to enable contact printing. Similarly for gap height, o	-
the desired gap height creates favourable printing conditions. Image adapted from [114]	_
Figure 14: Diagram describing the contact angle ($ heta$) for a liquid drop on an ideal solid substrate to show he	w
wettability is classified. Figure sourced from [124]	68

Figure 15: Schematics of the flexible three electrode sensor design detailing all the layers and materials used
for fabrication72
Figure 16: Chemical structures of working electrodes tested (A) pristine GO, (B) oxygen plasma treated GO
(C) components of the polyurethane, GO, and Pluronic® F-127 composite74
Figure 17: Optical images of the bare fabricated sensor (A) with no coating, (B) with GO on working
electrode prior to encapsulation with PDMS (C) and with GO+PU mixture on the working electrode. 7
Figure 18: Image of the direct-write printing setup used to encapsulate the conductive tracks of the sensor.
7!
Figure 19: Comparison 3-D renderings of the direct-write printing setup, highlighting the importance of
perpendicular alignment between the nozzle and the substrate. Even small (≤1°) misalignments cause
the nozzle-substrate distance to vary causing inconsistent ink volume ejection and poor prints70
Figure 20: Schematic of the experimental apparatus used to measure response of the produced sensors77
Figure 21: FT-IR spectra of pristine GO, oxygen plasma treated GO and GO, polyurethane (PU) and Pluronic ®
F-127 composite
Figure 22: Side-by-side SEM images of GO (A, C, E) and oxygen plasma-treated GO (B, D, F) at different
magnifications
Figure 23: SEM images of the GO, polyurethane (PU), and Pluronic® F-127 composite at increasing
magnifications: (A) 4 μm scale bar, (B) 1 μm scale bar, (C) 400 nm scale bar, and (D) 200 nm scale bar.
The red circle in (C) highlights pore formation in the composite80
Figure 24: Pristine GO CV results and analysis: (A) CV scans at 5 mV/s in different gastric acid pH solutions,
(B) CV at different scan rates in pH 1.5 solution. (C) Mean peak potential vs Ag/AgCl dependence on pH
solution. (D) Mean peak current dependence on pH. (E) Peak oxidative current dependence on square
root of scan rate82
Figure 25: Plasma treated GO CV results and analysis: (A) CV scans at 5 mV/s in different gastric acid pH
solutions, (B) CV at different scan rates in pH 1.5 solution. (C) Mean peak potential vs Ag/AgCl
dependence on pH solution. (D) Mean peak current dependence on pH. (E) Peak oxidative current
dependence on square root of scan rate8
Figure 26: GO and Polyurethane composite (CV) results and analysis: (A) CV scans at 50 mV/s in different
gastric acid pH solutions, (B) CV at different scan rates in pH 10 solution. (C) Mean peak potential vs
Ag/AgCl dependence on pH solution. (D) Mean peak current dependence on pH. (E) Peak oxidative
current dependence on square root of scan rate84
Figure 27: OCP vs pH measurements of representative examples of the three sensor types: (A) pristine GO,
(B) plasma-treated GO, and (C) GO+PU composite. (D) Variability among three samples of the
produced sensors comparing the OCP sensitivity and the R ² value80
Figure 28: Impedance analyser measurements performed on the working electrodes. (A) impedance and (B)
series resistance measurements on the pure/pristine GO WE. (C) Impedance and (D) series resistance
measurements on the GO and PU composite WE.

Figure 29: (A) Representative example of GO covered working electrode prior to pH sensitivity testing. (B)	
Representative example of GO following pH testing with yellow boxes showing loss of material from	1
silver substrate	_88
Figure 30: Comparison of open circuit potential stability of the pristine GO and the GO+Polyurethane	
composite in pH 1.5 solution.	_88
Figure 31: COF activation with ultralow surface tension solvents removes impurities from the COF and	
results in higher accessible surface area. Adopted with permission of the rights holder from [145]. $_$	_96
Figure 32: Reticular design strategies used for synthesis of COFs and corresponding most common dynami	С
bond types used to make COFs. Adopted from with permission of the rights holder [143].	_99
Figure 33: Schematic of the irreversible enol to keto tautomerization that occurs when TFP and PDA comb	ine
to form the keto form TpPa-1 or TpPa-2, and PXRD scans showing the stability of the COF in 9 N HCl	
after 1 week of submersion. Reproduced from [43].	101
Figure 34: Low processability of COFs leads to macroscopically-controlled engineering strategies for COF	
synthesis that can facilitate improved electrochemical performance. Sourced from [162]1	103
Figure 35: Common electrochemical COF sensors applications. Adopted reproduced with permission of the	9
rights holder, [164]1	104
Figure 36: Results of pH sensitive COF-HQ (A) solid state fluorescence spectra of pure 8-hydroxyquinoline	
(HQ) and formulated COF-HQ. (B) Fluorescnece spectra in various acidic solutions. (C) Images of the	
fluorescence spectra. (D) protonation and deprotonation response of HQ within the COF-HQ	
framework. (E) pH and fluorescence intensity plot exhibiting linear relationship. (F) Plot showing	
repeatability of fluorescence for 5 cycles. Sourced from [167].	105
Figure 37: (A) Voltammetric diagram showing pH response of COF _{DHTA-TTA} . (B) Peak voltage extracted from	
voltammetric response vs pH showing 64.2 mV/pH sensitivity. Sourced from [168]1	106
Figure 38: (A) Schematic of protonation and acidic instability of pure GO leading to poor stability. (B)	
Schematic showing the formation of COF nanopores on the GO adding increased surface area,	
functional sites, and stability. (C) Schematic showing sulfonic-COF formation of proton-selective nar	no-
channels that cause a pH-selective response. Chemical structure of linkers used to make (D) Pristine	
TpPa-1 COF, (E) Carboxyl COOH-COF and (F) Sulfonic (NUS-10-COF) showing the difference in functio	nal
groups present1	110
Figure 39: Schematic of method used for synthesising different types of COFs shown in this section1	L12
Figure 40: FTIR spectra of GO, GO+2,4,6-triformylphloroglucinol (TFP), and the different GO+COF mixtures	:
pristine, carboxyl, and sulfonic1	117
Figure 41: (A) Photograph of peeled GO+Sulfonic COF film showing a metallic-like lustre. (B) SEM image of	f
the stacked structure of the GO+Sulfonic COF film prior to exfoliation. (C) Cross-sectional SEM image	<u> </u>
following liquid exfoliation showing the layers of the flakes. (D) Cross-sectional SEM image of larger	
flakes present in the sample following liquid exfoliation. (E) SEM image of layers within flakes	
following liquid exfoliation. (F) AFM image of the sample following liquid exfoliation. White dashed	

line indicates cross-sectional line with height profile shown in (G). (H) Advancing contact angle	(ປ _{adv}) of
GO-COF sprayed on glass showing hydrophilic properties.	118
Figure 42: Energy dispersive X-ray spectroscopy (EDS) mapping of elemental composition on sulfonic	COF to
confirm COF formation. (A) SEM image and (B) Major elements detected and their locations: ca	arbon
(C), oxygen (O), nitrogen (N) and sulphur (S)	119
Figure 43: (A) AFM images on single GO sheet and (B) Surface roughness of GO/COF and GO, quantification (C) and GO, quantificatio	ed
through AFM scanning.	120
Figure 44: XRD patterns of GO and GO/COF composites, confirming successful synthesis and crystalling	nity of
the materials	120
Figure 45: (A) DPV response of Pristine COF in gastric acid simulant solution at different pHs. (B) Calib	ration
curve between oxidative peak and pH. (C) DPV Response of Carboxyl COF and corresponding pl	4
calibration curve (D). (E) DPV Response of Sulfonic COF and corresponding pH calibration curve	e (F).122
Figure 46: (A) CV Response of Sulfonic COF composite in different pHs. (B) Calibration curve peak oxid	dative
peak against pH derived from CV scans of the different COFs. (C) OCP sensitivity and linearity of	f
Sulfonic COF composite, in different COF:GO mass ratios (n=3). (D) OCP measurements against	varying
commonly ingested interfering ions to check for sensor selectivity.	124
Figure 47: Effect of pre-treatment on Sulfonic-COF. (A) OCP response to pH with acid pre-treatment of	only. (B)
with acid+base pretreatment. (C) Response time (90% of mean final value) of acid pretreatmen	t only
and (D) acid+base preteatment. (E) OCP with time in different pH gastric acid simulant solution	s with
acid pretreatment and (F) acid+base pre-treatment.	126
Figure 48: (A) OCP plotted against pH to create a calibration curve. (B) OCP of the sensor submerged	in pH
1.5 for several hours demonstrating remarkable stability.	127
Figure 49: Open-circuit potential (OCP) stability of the GO/Sulfonic COF sensor over 12 hours at vario	us pH
conditions (pH 1.5, 3, 4.5, 7, and 10)	128
Figure 50: Capacitance response of the Sulfonic COF and GO composite in pH solutions, demonstration	ig that
protons are the primary factor influencing the electrical double layer capacitance. (B) Calibration	on curve
of capacitance to pH at indicated dashed line shown in (A)	129
Figure 51: (A-C) Live-dead cytotoxicity results for untreated, GO, and GO with COF composite (GO+CO)F) at
passages 4-6, shown as the percentage of live cells (calcium green-stained) relative to total cell	s,
including ethidium homodimer-stained dead cells. Representative fluorescent images of passag	ge 4
cells at 100K seeding density are shown for (D) untreated sample, (E) GO only, and (F) GO+COF	
composite	131
Figure 52: Mean fluorescence of HEsEpiC cells stained with Prestoblue dye of not-treated control same	ıples,
GO and GO+COF composite samples for seeding densities of (A) 50K cells/well and (B) 100K cell	is/well.
	132
Figure 53: Equivalent circuit diagram of the transmitter and receiver coils demonstrating NFC operati	on.
Recreated from [181,183,189].	136
Figure 54: Coaxial coils depicting parameters used to calculate mutual inductance.	138

Figure 55: Block diagram of a wireless, chipless, NFC-based pH sensor, demonstrating frequency variatio	n
with pH. Figure sourced from [196]	_142
Figure 56: Relaxation oscillator circuitry for the BEST sensors: (a) impedance sensor and (b) pH sensor, as	;
developed by Cao et al. (Sourced from [198]).	_143
Figure 57: Operating principle of the flexible, batteryless device.	_146
Figure 58: (A) Schematic of the single-sided printed NFC coil (B) Schematic of the double-sided printed N	FC
coils with via Thru holes connecting both sides to form one larger NFC coil.	_147
Figure 59: Different coil fabrication strategies using 1-ink, 2-ink (thin silver nanoparticle design) and 2-in	k
(thick nanoparticle design)	_149
Figure 60: (A) Simulated impedance analyser data showing resonance frequency for a 3.1 μ H inductor with the contraction of t	ith
varying sensor coil resistances ($R2$) at a reference capacitance corresponding to pH 3. Higher $R2$	
values lead to indistinct resonance peaks, highlighting the importance of minimising resistance. (B)
Simulated frequency shifts based on empirical capacitance values measured for pH levels 3 and 7,	
demonstrating the clear relationship between capacitance changes and resonant frequency as	
predicted by Equation (37)	_151
Figure 61: Schematic (A) and image (B) of apparatus to measure the magnetic field with an impedance	
analyser with a built-in voltage supply.	_152
Figure 62: (A) DC Resistance results of each coil design (by case) detailed in Table 6. (B) Optical microsco	pe
images showing the 1-sided coil design vs the 2-sided coil design (C).	_153
Figure 63: (A) Inductance and resistance values measured from an exemplar Case 8 sample across the	
frequency range. (B) Impedance and Q-factor values measured from the same Case 8 sample,	
highlighting the frequency-dependent behaviour of the design.	_156
Figure 64: Capacitive pH Sensor with NFC coils.	_157
Figure 65: (A) Raw impedance analyser data showing the frequency response of the coil-capacitor system	n for
Capacitor 1 (530 pF) and Capacitor 2 (500 pF). (B) Processed data after moving mean subtraction,	
highlighting the resonant frequencies of 3.793 MHz and 3.918 MHz for Capacitor 1 and Capacitor 2	,
respectively.	_158
Figure 66: Bond types in tissue adhesives. Figure sourced from [206].	_164
Figure 67: Interactions between PVA-DOPA films with buccal mucosal layers. Figure sourced from [228].	170
Figure 68: (A) Schematic of the tensile mechanical tests performed on the bioadhesive. (B) Schematic of	the
lap shear adhesion tests performed on the bioadhesive with the oesophageal tissue	_180
Figure 69: Schematic of the ex vivo flow testing apparatus	_181
Figure 70: (A-B) Optical images of the 10% AA (w%/w) bioadhesive from the front and side. (C) Microsco	pe
image of the 10% AA (w%/w) bioadhesive showing high transparency. (D) Optical image of the	
bioadhesive formulations prior to UV polymerisation. (E) Optical images of the bioadhesive	
formulations following photopolymerization in 10mm x 20mm x 6mm moulds	_183
Figure 71: FTIR spectra of as-purchased gelatine, methacrylated gelatine (gelMA) and the synthesised	
higadhariya natch	10/

Figure 72: (A-D) Nominal stress vs engineering strain of the bioadhesive patches based on AA (w%/w)	
concentrations (Black cross indicates point of material failure). (E-H) Stress rate vs engineering strain	
used to compute the Young's modulus. (I) Young's modulus of the various bioadhesive patches (n=3).	
(J) Toughness of the bioadhesive patches (n=3). (K) Representative examples of the patches plotted	
together (L) Image of the patch undergoing tensile stress18	87
Figure 73: (A-D) Force vs displacement plots of the bioadhesive with varying AA (w%/w) concentrations	
undergoing lap shear stress testing on oesophageal tissue for adhesion measurements. (E) Maximum	1
shear stress of the bioadhesive patches (n=3) (F) Optical image of the setup used for testing18	88
Figure 74: (A) Schematic of patient with acid reflux, and where the sensor would be mounted [partially	
created using biorender.com] (B) Optical image of life-sized 3D printed oesophagus and stomach	
model showing the sensor's mounting and location. (C) Image of the model from the top of the	
oesophageal model showing its conformity to the oesophageal wall. (D) Image of the setup flow test	
model. (E) Image of the incision created to implant the sensor for the flow test19	90
Figure 75: Laparoscope and camera images extracted from a video following the flow testing. (A)	
laparoscope location in oesophagus prior to lower oesophageal sphincter. (B) Laparoscope at lower	
oesophageal sphincter showing adhered sensor19	91
Figure 76: Block diagram of a system which uses a power amplifier, and frequency generator to enhance the	ıe
RF powering. Adopted from [198]20	00
Figure 77: Proposed bioresorbable version of the full sensor design20	01
Figure 78: Schematic of EHD printing using the three most common modes, e-jet, EHD direct-writing, and	
electrospray. Figure sourced from [102]22	27
Figure 79: Cyclic Voltammetry results of pristine COF and GO composite22	29
Figure 80 Cyclic Voltammetry results of Carboxyl COF and GO composite23	30
Figure 81: Cyclic Voltammetry results of Sulfonic COF and GO composite23	31
Figure 82: Impedance analyser results showing changes in impedance, phase, and capacitance in different	
pHs23	32
Figure 83: (A) Channel 1 of the microscope file showing the Dead Cells (B) Channel 2 showing the live cells in	n
grayscale image (C) Overlay of the channels showing their original colours. (D) Histogram of Channel 2	2
image used for thresholding the Binary image shown in (E). (F) Applying filters to remove noisy data	
less than 10 pixels in size. (G) Applying a distance transform performed by Matlab image processing	
toolkit. (H) Applying the watershed technique to identify the boundaries of the cells. (I) Using the	
identified boundaries to segment the original image. (J) Removing oversegmentation by identifying	
minimum segmented distance (K) Image following full segmentation (L) Highlighted boundaries of live	e
	33
cells identified by function (shown in green)23	
cells identified by function (shown in green)23 Figure 84: Representative example of post-processed imaging to differentiate live and dead cells. (A)	
Figure 84: Representative example of post-processed imaging to differentiate live and dead cells. (A)	

Figure 85: Exploded (a) and assembled (b) views of the proposed battery-powered sensor. (Dimensions in	n
mm)	239
Figure 86: Mobile GIII design created on MIT Ann Inventor® for fabricating the proof-of-concept device	2/12

Chapter 1: Introduction

1.1 Motivation

Gastro-oesophageal reflux disease (GORD) is a prevalent digestive health condition in which stomach acid rises into the oesophagus, causing symptoms like heartburn, indigestion, and acid reflux. Patients often experience burning sensations in the chest and an unpleasant taste in the mouth. While GORD can be triggered by factors such as exercise or diet, chronic GORD is a persistent global issue [1].

GORD is associated with an excessive reflux of all contents of the stomach, including, ingested food and drink, acid, stomach enzymes such as pepsin, and bile, which cause primarily laryngeal damage to sufferers [2]. The acid itself causes damage to the oesophageal mucosa but studies have shown that this damage can be much more dramatic and beyond the upper oesophagus into the pharynx, airways, and middle ear [2,3]. Pepsin, an enzyme used in the first stage of the digestion process, has been largely associated as the culprit to the effects of GORD [2]. Normally, the stomach is protected from pepsin due to the mucus-producing stomach lining while the intestine is protected due to the alkaline environment causing its deactivation [3]. However, when found in the oesophagus or higher, where there is no protective layer, damage can be accumulated [2].

GORD is typically described as a sensorimotor disorder in which normal anti-reflux mechanisms, such as the function of the lower oesophageal sphincter and the phrenicoesophageal ligament, are impaired [4]. This can be coupled with the occurrence of changes in normal physiology such as impaired oesophageal peristalsis, increased intragastric pressure or excess gastric acid secretion [4]. Most treatments are focused on the use of acid-suppressive drugs such as antiacids, proton-pump inhibitors, anti-histaminic agents, etc. [4].

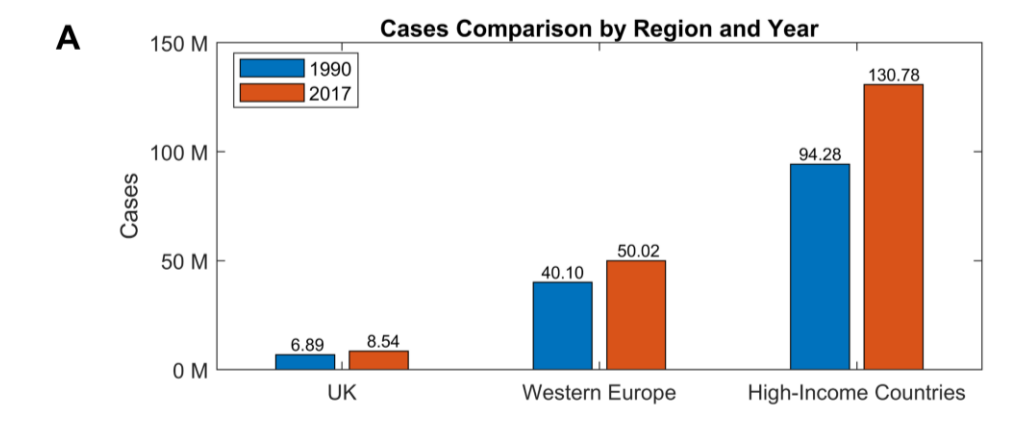
Proton pump inhibitors (PPIs) are prescribed for relief as they increase the pH of the stomach and decrease pepsin's activity via denaturing at pHs above 3 [2]. The denaturing of the enzyme is only permanent at pH>8 and it has been shown to remain active (albeit less) at a pH of 6 [2]. However, heartburn quickly can reoccur after PPI withdrawal leading to many patients becoming PPI-dependent [1]. Many side-effects have been reported with PPI's long-term use with strategies for discontinuing use conducted by many clinicians [1]. Further, 20-30% of patients display inadequate or

absent response to this treatment [4]. Controlling and reducing the symptoms of GORD remain highly influenced by diet and lifestyle [4].

1.2 Clinical Need

GORD is the most widespread digestive disorder and affects between 8-26% of adults depending on geographical region [5–7]. It is thought by experts that this prevalence is only increasing worldwide and that the number of affected adults may be higher than stated in [5–7]. According to one source, 250,000-270,000 cases annually require medical attention by a General Practitioner (GP) in the UK as over-the-counter medicines do not provide sufficient relief for the patients [8]. In 2004 alone, GORD diagnosis in the UK cost an estimated £750m on diagnostic, treatment, and sickness absence [9]. Symptoms of GORD are described as affecting 44% of the population monthly, 14% at least once weekly, and 7% daily in the US [10]. Figure 1A shows a comparison of the number of cases in the UK, western Europe and high-income countries between 1990 and 2017, from a systematic analysis study derived from 112 studies [6]. The number of cases is increasing more (~24%) than the population growth rate (14.2%). This is then confirmed by an age-standardised prevalence score by 1990 which accounts for an aging population, where it can be found that the prevalence is still increasing.

Studies have shown that patients with GORD experience a severe impairment in their quality of life (QOL) relative to the general population [11]. This decrease in QoL is thought to surpass chronic conditions such as diabetes or hypertension [11]. Poor QoL is experienced due to impaired ability to eat and drink normally, disturbed sleep, impaired vitality, emotional well-being, bodily pain, etc. [12]. Approximately 40-65% of patients with reflux disease have endoscopically evident oesophagitis (inflammation in the oesophagus) [12,13]. Heartburn symptoms have shown to affect people's enjoyment of food, eating out, getting a good night's sleep, concentration at work, spending time with the family, exercising, socialising and travel for pleasure [12]. Decrease in work productivity in studies conducted in the US was calculated to cost over \$5,000 per employee annually [12].



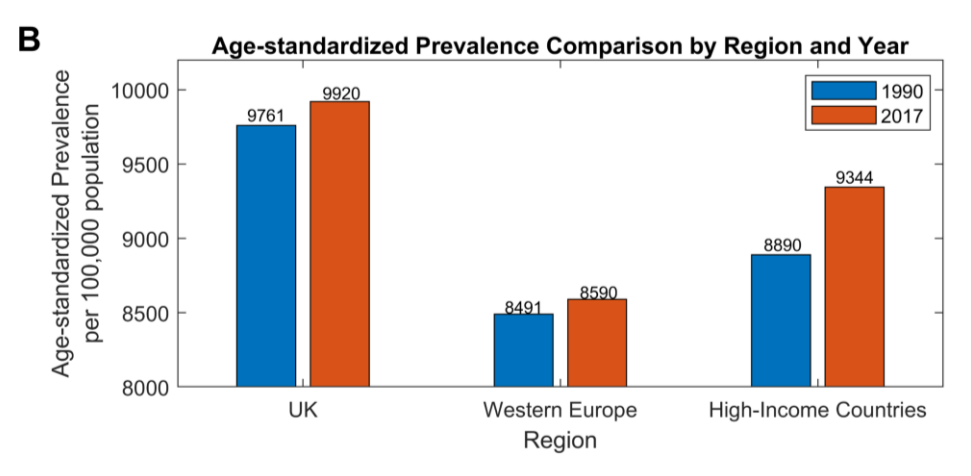


Figure 1: (A) Prevalence of GORD cases by region (B) Age-standardised prevalence per 100,000 cases. Figure created using source data from [6].

Improvements in QoL can be achieved through symptom relief such as PPIs, histamine-2 receptor antagonists and prokinetics, however, many patients using PPI therapy report incomplete symptom relief and as mentioned earlier has correlated to long term effects with continuous use [12]. Further, in 80% of patients using acid suppression treatment experience relapse after treatment is discontinued over the following 1-year treatment [13]. Lifestyle modifications such as dietary changes, weight loss, stress management, etc. that are guided by quality ambulatory reflux monitoring and identification has the potential to improve QoL significantly and improve patient satisfaction [12,13]. Such a tool would enable a data-driven approach to identify how patients' daily decisions correlate with their symptoms. In severe cases, however, surgical intervention may be required to restore QoL to levels comparable to the general population [13]. However, unfortunately, in more than half of patients that underwent surgical intervention such as laparoscopic fundoplication surgery, had to continue to use anti-reflux medications regularly [13].

1.3 Current GORD Diagnostic Technology

Despite its widespread prevalence, there is no gold standard for diagnosing GORD. Direct reflux monitoring is the most common diagnostic approach, with ambulatory pH or impedance-pH monitoring used to assess acid exposure time and frequency [1]. Ambulatory pH or pH-impedance monitoring is used in patients of GORD as they present typical or atypical reflux responses to stimuli [14]. However, even current diagnostic technologies, such as pH-impedance devices, are not without their respective limitations which are detailed below.

Diagnostic sensing can also be performed in an effort to understand which lifestyle changes can be incorporated to lessen or eliminate reflux episodes and can halt PPI-dependence in patients [1,15]. Current diagnostic equipment performs either pH monitoring or impedance-pH monitoring to account for non-acidic reflux episodes. However, pH-impedance devices are known to overestimate reflux episodes [16,17].

Clinically, one of two types of devices are used to assess oesophageal acid exposure via in situ monitoring: a nasoesophageal pH or pH-impedance catheter, or a wireless, telemetric, pH-sensing device known as the Bravo pH capsule (Medtronic, Minneapolis, Minn., USA). The utility of the monitoring is dependent on three main factors: patient tolerance, positioning of the device, and the duration of the test [15]. Since 1969, catheter-based 24-hour ambulatory pH measurements have been performed to correlate between symptoms reported by patients and reflux events [15,18].

Catheter-based monitoring requires trans-nasal placement with manometric guidance by a practitioner and can be left for up to 24 hours following taping to the patient's nose [18]. Studies report discomfort caused via dysphagia (swallowing difficulty), chest-pain or foreign body sensation [18,19]. It can induce social embarrassment, interference with work attendance and lifestyle changes such as decreased activity and reduced number of meals [15,18]. All of these are recognised GORD triggers that can enable a longer diagnosis time or cause misdiagnosis to occur. Further, with daily activity such as talking, body positional changes and eating, the position of the catheter can change from the initially defined position [15,18]. The limitation of 24 hours also leads to less reproducible results as oesophageal acid exposure typically varies from day to day [15,18].

The Bravo capsule was developed in 2003 in an attempt to overcome many of the inconveniences of the catheter system [14]. The Bravo capsule monitors physiological changes in the tract over a span of several days or longer as recommended by the practitioner [14,15,18]. It contains a catheter-like delivery system that is designed to place the capsule in the oesophagus via the nose or mouth [14]. The position of placement is determined via a previously performed gastroduodenoscopy and a vacuum pump is used to perform suction of the oesophageal wall to mount the capsule to the mucosa of the distal oesophagus using a spring-loaded stainless steel pin [14,18]. It is designed to record pH every 6 s with data sent to a belt-mounted receiver every 12 s and to be expulsed naturally by the body within 4-7 days [14,15,20]. It thus has improved monitoring duration and no positional movement [15]. The Bravo capsule is not without its drawbacks, however. Clinicians report early and late dislodgment, transmission issues, intolerable chest or throat pain, foreign-body sensation and other technical issues [19,21]. Often, this requires clinical intervention to remove the device, and cases have been reported where oesophageal perforation occurred during delivery of the device requiring emergency medical attention [10,21].

A significant challenge with current GORD diagnostic devices is the discomfort and tolerability experienced by patients during the monitoring period. Studies have reported discomfort due to dysphagia, chest pain, or a sensation of a foreign body in the throat or oesophageal area [18]. Tolerability varies among patients, but common issues include social discomfort, disruptions to work attendance, and lifestyle changes such as reduced activity and fewer meals [16]. These factors are known triggers for GORD, potentially prolonging the diagnostic process or leading to false positives. Additionally, problems with the lodging and dislodging of these devices have sometimes resulted in near-catastrophic outcomes. The following section details the GORD diagnostic devices currently used by clinicians, highlighting their advantages and outlining their limitations.

1.3.1 Catheter-based Devices

The first instance of prolonged pH oesophageal monitoring was reported in 1969, utilising a glass-electrode pH monitoring system on 26 inpatients. In this early setup, a pen recorder documented the pH levels on graph paper for 18 hours [16]. By the 1980s, battery-powered portable catheter pH monitoring devices were developed, and since then, these devices have been regarded by some clinicians as the gold standard

for GORD diagnosis [16,18]. The sensitivity of these systems is reported to range between 79-96%, with specificity between 85-100% [22]. Initially, this technique was reserved for patients being considered for surgical anti-reflux procedures or those with persistent symptoms following surgery. It is now also used for patients experiencing refractory symptoms despite proton pump inhibitor (PPI) therapy [22].

The monitoring approach has evolved significantly since the early stationary systems, which severely restricted patients' activities within hospital settings. Initially, patients were advised to avoid acidic foods that could affect the results. However, clinicians have recognised that immobility and deviations from normal daily behaviour could compromise diagnostic accuracy. Today, restrictions on patients are minimised with the catheter-based approach to better assess reflux during typical daily activities, thus improving diagnostic accuracy. For example, catheter-based systems like Medtronic's Digitrapper™ pH-Z allow for fully mobile, 24-hour pH and impedance monitoring for GORD diagnosis [23].

To quantify reflux burden and distinguish between pathologic and physiologic reflux patterns, specific metrics have been established [16]. These include acid exposure time (AET), the DeMeester score, the number of reflux episodes, symptom index, symptom association probability (SAP), mean nocturnal baseline impedance, and the post-reflux swallow-induced peristaltic wave (PSPW) index. AET is the primary metric for diagnosing pathological reflux, defined as being greater than 6% of the total monitoring time. Table 1 from [16] provides more details on the metrics used.

Despite advances in catheter-based systems, the test remains invasive and uncomfortable, inevitably leading to changes in lifestyle [22]. Studies show that patients spend significantly fewer hours being active during the day, engaging in activities such as shopping, working, visiting, and exercising. Patients also showed decreased appetite, skipping breakfast, having shorter meal times, and consuming fewer cups of coffee [22]. Finally, patients reported difficulty swallowing, throat discomfort, and runny noses. To summarise, lifestyle changes are inevitable with this diagnostic technique, and it can induce social embarrassment, decreased activity, and reduced meal frequency, despite 51% of patients describing it as a mild annoyance [18,22].

Table 1: Metrics used for ambulatory reflux monitoring and GORD diagnosis. Sourced from [16].

	Ambulatory monitoring technique	Upper limit of physiologic values	Comments
Acid exposure time	Catheter based pH- and pH-impedance monitoring; wireless pH monitoring	4%	>6%: pathologic reflux; 4-6%: inconclusive for pathologic reflux
DeMeester score	Catheter based pH- and pH-impedance monitoring; wireless pH monitoring	14	Most reliable for testing off PPI therapy
Number of reflux episodes	Catheter based pH- impedance monitoring	40 episodes	>80: suggestive of pathologic reflux; 40-80: inconclusive
Symptom index (SI)	Catheter based pH- and pH-impedance monitoring; wireless pH monitoring	50%	Number of symptoms reported need to be >3
Symptom association probability (SAP)	Catheter based pH- and pH-impedance monitoring; wireless pH monitoring	95%	SAP may be more robust than SI
Mean nocturnal baseline impedance	Catheter based pH- impedance monitoring	>2292 Ω	Other data suggests <1500 Ω indicates abnormal mucosal integrity; oesophageal dilation and esophagitis can lower baseline impedance; values increase following PPI therapy and healing of esophagitis
Post reflux swallow induced peristaltic wave (PSPW) index	Catheter based pH- impedance monitoring	50%-61%	Values can vary even in healthy volunteers; low values are reported in PPI refractory reflux

In addition to discomfort, catheter-based monitoring presents other challenges, including misdiagnosis due to the short monitoring period and difficulties in diagnosing specific types of GORD [18]. One study found that 27% of patients received inconsistent results from tests conducted on two separate days [18,24]. Furthermore, 23% of patients with erosive reflux disease had false negative results [18]. Another issue is the incorrect positioning of the catheter device, which can be affected by gravity, body position, talking, and swallowing, even after the device is initially placed correctly [15,25]. This problem is sometimes attributed to swallow-induced peristalsis or oesophageal spasms [15].

The monitoring catheter is traditionally positioned 5 cm above the proximal border of the lower oesophageal sphincter (LES), with techniques such as oesophageal manometry, endoscopy, radiology, and pH step-up used to locate the LES [25,26]. The catheter is typically placed after the application of topical anaesthesia and secured to the patient's nostril using tape or a similar adhesive [18,25]. Multiple electrode catheter-based devices are also available, with electrodes positioned at 3, 5, 7, 9, 15, and 17 cm above the LES to assess the extent to which bile from reflux events reaches above the LES [16]. This provides different data compared to other diagnostic devices, contributing to the continued use of the catheter-based technique despite its reported poor tolerability [16]. Additionally, this technique captures the significant 7-fold increase in acid exposure that occurs over the distal 5 cm above the LES, which is critical for accurate diagnosis [27]. Finally, the cost of catheter-based devices is significantly lower than that of the Bravo capsule [28].

1.3.2 Capsule-based Devices

In 2003, Medtronic developed the Bravo capsule, a wireless telemetric device for pH monitoring [18,27,29]. This device was designed to address many of the limitations of catheter-based systems, as it is implanted directly in the gastrointestinal tract and can perform extended monitoring for periods exceeding 48 hours, with modern versions reaching up to 96 hours [15,16,18]. The extended monitoring time significantly improves diagnostic sensitivity and enhances the correlation of symptoms, which is crucial for evaluating both typical and atypical GORD symptoms [28]. The Bravo capsule is reportedly better tolerated than catheter-based systems, with throat discomfort occurring in 4-14% of subjects compared to 77.8% for catheter-based systems [15,22].

The pre-packaged kit includes the capsule, capsule delivery system, calibration stands, buffer solution, infrared receiver device, and software [30]. The capsule itself contains an internal battery, a transmitter, an antimony pH electrode, and a reference electrode at the distal end [30]. It measures 6 mm x 5.5 mm x 25 mm. The delivery system is equipped with a vacuum pump and suction tubes, which are used to mechanically secure the capsule to the mucosal layer of the gastrointestinal tract [15,30]. The Bravo capsule is better tolerated than catheter probes, with higher patient satisfaction and less lifestyle disruption - in one study, no Bravo patients (0%) reported daily routine changes, compared with 36% of catheter probe patients [28].

The device is typically placed using transnasal insertion, although oral insertion is an option for patients with tightly angled nasopharynxes, provided a correction factor is applied [15]. Proper placement of the device requires previously defined manometric landmarks [15,28]. After correct placement, a vacuum pump applies suction to the capsule wall at 510-700 mmHg for 15-30 seconds. An activation button is then pressed, releasing a spring-loaded stainless steel pin that attaches the capsule to the mucosa [30]. The device takes measurements every 6 seconds and transmits data every 12 seconds [28]. Figure 2 shows a diagram of the device attached to the GI tract. This attachment mechanism causes the device to not have displacement issues (assuming no detachment) which is an advantage over catheter-based systems.

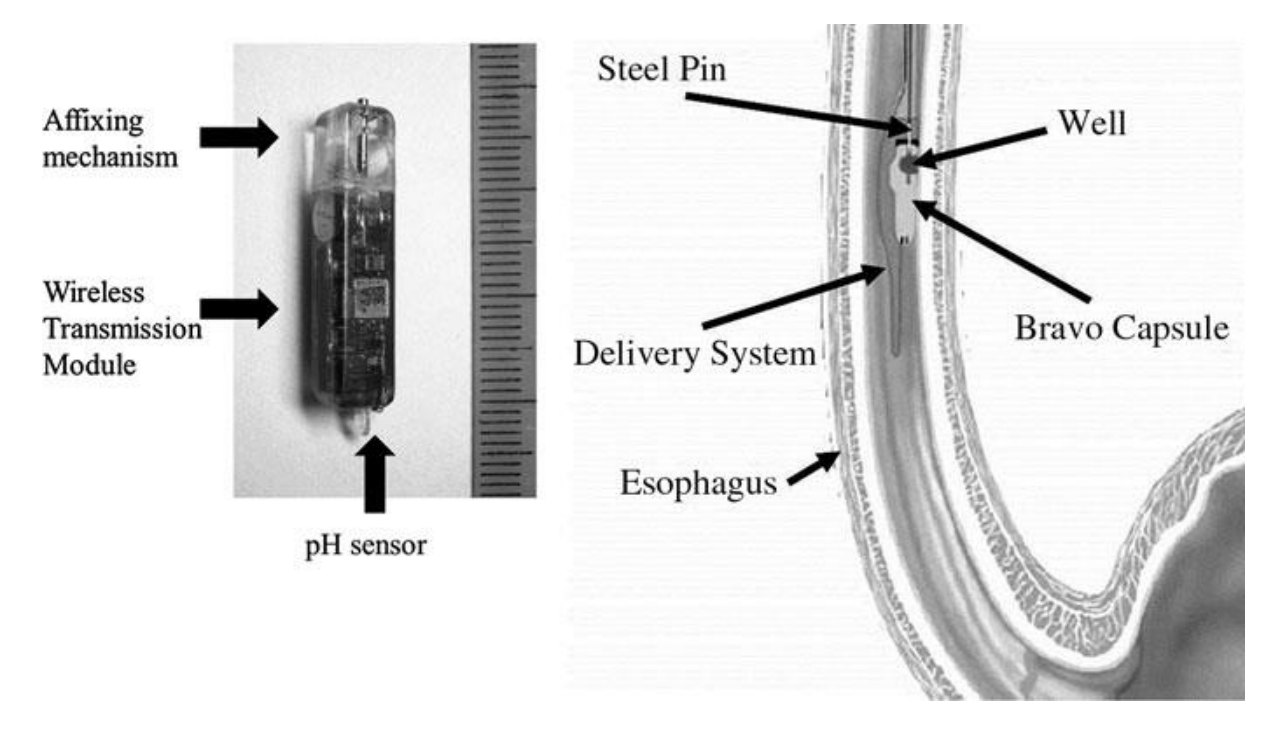


Figure 2: A diagram and image of the suction-based mechanical attachment mechanism used in one of the current implantable pH monitoring systems, the Bravo™ capsule. Sourced from [31].

The Bravo capsule is not without its drawbacks. Approximately 33-34% of subjects report oesophageal discomfort, and 5-9% experience severe odynophagia and chest pain, with some cases requiring endoscopic intervention for immediate removal [15]. Up to 65% of patients report chest pain, ranging from a foreign body sensation to severe discomfort necessitating the removal of the device either immediately after placement or after the monitoring period [14]. Mild, transient nosebleeds, attributed to the large size of the capsule, were reported in 86% of subjects in one study [32].

Issues with capsule detachment and retention have also been reported. In one study, 10% of examinations were compromised due to early capsule detachment (within 36

hours) and progression into the gastrointestinal tract [29]. Conversely, a case study by Aulakh et al. described a situation where the pH capsule remained lodged in the distal oesophagus 45 days after initial placement, with another 26 reports to the US Food and Drug Administration documenting capsule retention times ranging from 9 days to 6 weeks [20]. Tharavej et al. found that the Bravo capsule can induce hypertensive oesophageal contractions, which may account for some instances of chest pain [33]. Additionally, a case study reported oesophageal perforation caused by the suction during placement, underscoring the importance of clinicians being able to identify such complications [10]. Other serious incidents have included trauma, severe bleeding, and aspiration into the bronchus [21].

The capsule's lower sampling rate can result in up to twice as many missed reflux episodes compared to catheter-based systems [34]. Discrepancies between Bravo and catheter-based diagnostic methods are observed not only in the number of reflux events but also in recorded pH values [34]. This discrepancy impacts the DeMeester score, as outlined in Table 1, and likely contributes to the Bravo capsule's lack of validation with this score [28]. Additionally, the Bravo capsule is more expensive than catheter-based techniques, with costs influenced by the method used for accurate placement (e.g., endoscopy is more costly than manometry) [28].

The cost can further increase due to early dislodgment or primary attachment failure, requiring the use of a new capsule to complete the diagnostic procedure [28]. The device is also susceptible to technical and transmission failures, occurring at rates of 15.15% and 4.5%, respectively, in one study with 66 patients [21].

In summary, while the Bravo capsule offers improved tolerance and longer recording times, it faces challenges related to attachment complications, increased cost, and reduced sampling frequency. The choice of diagnostic test often depends on patient characteristics and symptoms, the availability of diagnostic techniques, healthcare coverage, cost, and clinical preference [16].

1.4 Thesis Aim and Objectives

The overarching aim of this thesis is to develop a novel biomedical diagnostic device that integrates seamlessly with the human body. This involves employing advanced materials, nanofabrication techniques, and mucoadhesive retention strategies to create flexible, biocompatible sensors capable of reliable performance in challenging environments, such as the gastrointestinal tract. This device aims to address critical diagnostic challenges, such as real-time, non-invasive monitoring, while providing a foundation for future innovations in personalised healthcare technologies.

- 1. **Develop High-Performance pH Sensors:** Fabricate pH sensors with enhanced sensitivity, robustness, and repeatability using traditional and advanced nanomaterials fabricated by modern nanofabrication techniques.
- 2. **Explore Nanofabrication Techniques:** Apply and refine nanofabrication methods to design and produce flexible, miniaturised sensors and associated electronics.
- Characterise Sensor Performance: Evaluate the fabricated sensors' sensitivity, stability, and robustness in controlled models to assess their suitability for GORD diagnosis.
- 4. **Investigate Wireless Communication Solutions:** Identify and develop ultralow-power wireless communication techniques suitable for implanted biomedical devices, focusing on signal stability and efficiency.
- Develop Biocompatible Mucoadhesives: Fabricate and optimise a nonimmunogenic, non-inflammatory, and biocompatible mucoadhesive capable of securely anchoring the sensor within the gastrointestinal tract for extended periods without causing discomfort.
- 6. **Integrate System Components:** Combine the pH sensor, wireless communication system, and bioadhesive to create a fully functional, integrated diagnostic device tailored for GORD monitoring.

1.5 Thesis Outline and Chapters

This research focuses on the development of a novel biomedical diagnostic device designed to integrate seamlessly with the human body. Building on the foundation of skin-interfacing electronics—widely adopted in commercial applications such as smartwatches, fitness trackers, and wound monitoring systems — this study extends the concept to mucosa-interfacing electronics [35]. Coined by Nan et al., this term describes technologies engineered for imperceptible in vivo sensing via integration with mucosal surfaces [35]. While promising, such technologies face unique challenges, including limited access to mucosal layers, stringent biocompatibility requirements, environmental resilience, and the need for extreme miniaturisation to meet implantation constraints. Overcoming these obstacles demands advanced

fabrication techniques alongside robust, accurate, and reliable diagnostic capabilities, particularly for GORD.

To achieve this, the research employed a multifaceted approach, combining investigations into diverse yet interconnected topics, culminating in the development of an innovative diagnostic platform. A graphical abstract illustrating the research process is shown in Figure 3.

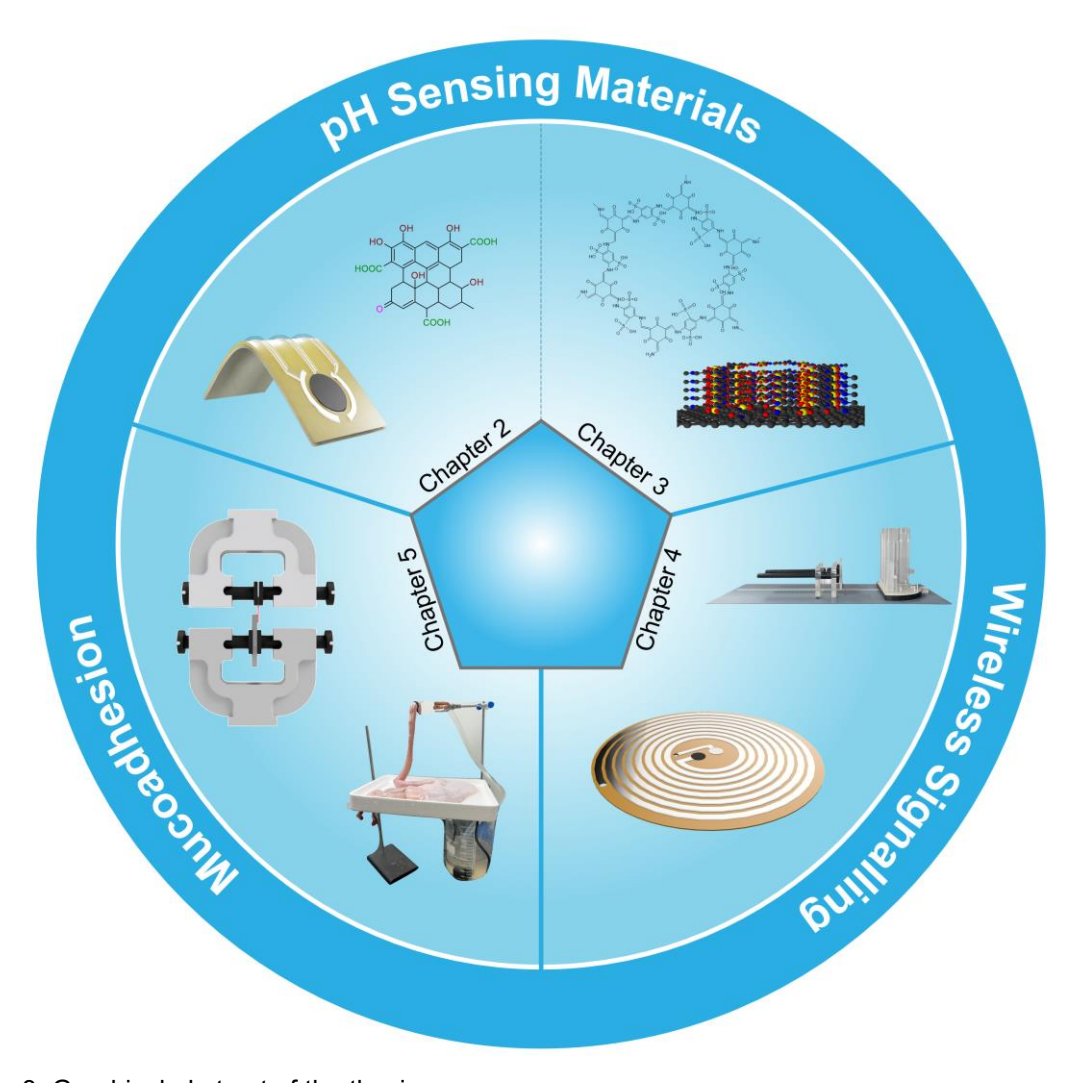


Figure 3: Graphical abstract of the thesis

1.5.1 Printed Robust pH Sensors

The initial phase focused on fabricating flexible pH sensors using thin-film printing techniques, ideal for interfacing with delicate mucosal surfaces. Graphene oxide (GO), known for its pH sensitivity and unique electrical properties, was selected for its potential in these sensors [36,37]. Printing offered precise control over sensor properties, enabling high-resolution patterns (<10 µm) with excellent repeatability and

scalability at low cost [36,38–42]. Literature reveals that variability in GO preparation methods causes batch-to-batch inconsistencies, impacting functional group content and further material deposition inconsistencies resulted in large performance variations.

To tackle these issues, a direct-write ink formulation was developed to reduce degradation and was deposited using direct-write printing ensuring more reliable and consistent sensor performance. Despite these advances, sensors still exhibited drift and material reduction over time, particularly in acidic conditions, limiting long-term stability. These persistent challenges highlighted the need for further innovation, shifting the focus to exploring more robust materials capable of improving sensor stability and pH sensitivity.

1.5.2 Covalent Organic Frameworks for Electrochemical Sensing

While incorporating polyurethane improved robustness, GO's reduction in low pH environments caused hydrophobicity and reduced sensitivity, both of which are key contributors to bio-fouling. To address these limitations of GO-based pH sensors, this study explored covalent organic frameworks (COFs), a class of advanced nanomaterials for sensing.

COFs, known for their high surface area, chemical stability, and tuneable functional groups, have demonstrated exceptional resilience under extreme conditions (e.g., 9 N HCI) [43]. This phase of the study investigated the integration of GO with COFs to combine their complementary properties, aiming to enhance sensitivity, consistency, and durability. Biocompatibility was also evaluated using epithelial oesophageal cells, confirming its suitability for biomedical applications. The results demonstrated significant progress toward developing robust, high-performance sensors capable of reliable operation in the challenging environment of the gastrointestinal tract.

1.5.3 Wireless Signalling and Sensing

The next challenge was developing a printed wireless, batteryless communication system to transmit sensor data. Traditional biomedical devices often depend on batteries or direct wiring, which limit their miniaturisation and biocompatibility. This study utilised inductive coupling between a transmitter and receiver coil, where capacitance changes induced by pH shifts caused detectable resonant frequency shifts.

A sensor design incorporating a GO-COF sheet directly as the tuning capacitor, rather than incorporating additional voltage to frequency signals, was evaluated alongside conventional capacitive elements. The system achieved proof-of-concept functionality, demonstrating the potential of miniaturised wireless pH sensing. Despite challenges such as coil alignment and dynamic capacitance stability, the results provided a foundation for future work efforts.

1.5.4 Biocompatible Mucoadhesives

With sensor robustness established, the focus shifted to retention within the oesophagus. Current technologies often rely on mechanical suction, which can be uncomfortable or lead to complications [10,15,44]. Mucosa-interfacing electronics must bond securely to mucosal surfaces in a biocompatible, imperceptible manner [35]. The current mechanical suction technique for current long-term implantable GORD diagnostic technology does not fit these requirements, but an adhesive model which is biocompatible, flexible, and safe to use within the body would likely solve these issues.

This study reviewed natural and synthetic mucoadhesives, materials designed to adhere to mucosal layers despite their lubricated nature [45,46]. While existing bioadhesives have been commercialised for applications such as surgical sealing, their limitations—particularly short-term retention and poor adaptability to dynamic environments—made them unsuitable for this application. An adhesive patch which built on existing works in literature was tested for retention under flow conditions in the oesophagus. By addressing the challenges of biocompatibility, mechanical flexibility, and adhesion under harsh physiological and dynamic conditions, this work established a foundation for reliable mucosal integration [45,47].

1.5.5 Summary

This research integrates multiple advancements into a cohesive system aimed at addressing the limitations of current GORD diagnostic technology. Beginning with the development of printed sensors using conventional materials, the study progressed to adopt advanced nanomaterials for enhanced performance. A wireless, batteryless communication system was implemented to enable data transmission without compromising miniaturisation or biocompatibility. Finally, a biocompatible adhesive

was developed to ensure secure retention within the oesophagus, overcoming the discomfort and risks of current methods.

These innovations collectively represent a significant step toward a reliable, minimally invasive diagnostic device for real-time pH monitoring in the gastrointestinal tract. This work lays the groundwork for future advancements in mucosa-interfacing electronics and their applications in biomedical diagnostics.

Chapter 2: Printed, Robust pH Sensors

2.1 Background and Literature Review

2.1.1 Types of pH Sensors

Sensors designed to measure ionic concentrations vary widely in terms of material composition, sensitivity mechanisms, and overall performance characteristics. Ideally, an electrochemical pH sensor should provide stable, reproducible readings across the full pH range of 0–14, irrespective of temperature fluctuations, ionic strength, or measurement duration, while maintaining high precision and minimal drift over time [48]. pH sensors are a form of ion-sensitive electrodes (ISE), where the ion of choice is hydrogen, a very common species encountered in most chemical reactions [49]. It is used to describe the acidic and basic nature of solutions, and can be described by equation (1). Equilibrium occurs between alkali (OH⁻) and acidic (H⁺).

$$H_2O = OH^- + H^+ \tag{1}$$

Among the most extensively used pH sensors are those utilising glass electrodes. These sensors detect hydrogen ion activity through the ion-exchange properties of their glass membrane and are classified as potentiometric sensors, as they generate an electrochemical potential proportional to the logarithm of the hydrogen ion concentration. The voltage response is governed by the Nernst equation, typically yielding a theoretical sensitivity of approximately 59.16 mV per pH unit at 25°C [49]. Although glass electrodes offer high accuracy and long-term stability, they are fragile, require frequent calibration, and may be unsuitable for miniaturised or implantable applications [50].

Other pH sensing technologies include chemi-resistive and conductimetric sensors, which alter their electrical resistance in response to changes in ionic concentration [49]. Similarly, capacitive, conductimetric, and inductive sensors operate by detecting variations in capacitance or impedance resulting from electrochemical interactions at the sensor's surface [49]. Conductimetric/inductive sensors were not considered in this study due to their significant degradation over time [51]. Similarly, chemi-resistive/conductimetric sensors were deemed unsuitable for implantation because they typically require high power and are too bulky for such applications [51]. While these techniques have been explored for pH measurement, they often suffer from

issues such as sensor drift, power consumption constraints, and susceptibility to biofouling, particularly in biological environments.

Ion-Sensitive Field-Effect Transistors (ISFETs) operate as potentiometric sensors but differ from traditional glass electrodes as they are based on the working principles of Metal Oxide Semiconductor Field-Effect Transistors (MOSFETs) [51]. These sensors offer rapid response times and miniaturisation potential but also suffer from long term stability and drift issues [51].

Alternative optical and imaging-based techniques, such as magnetic resonance imaging (MRI) and fluorescence imaging, have also been explored for pH measurement. However, these methods are not viable for continuous long-term, stable, and robust in vivo monitoring which this thesis aims to address [52].

Hydrogel-based pH sensors have also been explored for biomedical applications, leveraging pH-sensitive polymer networks that undergo swelling or contraction in response to proton concentration. These materials have been proposed for in vivo sensing, but their performance is limited to a pH range of 5–8, and their response time is relatively slow (approximately one hour), rendering them unsuitable for real-time monitoring of gastroesophageal reflux disease (GORD) [53].

Given these considerations, this literature review focuses on potentiometric sensors and ISFETs, given their potential applicability for GORD monitoring.

2.1.1.1 Potentiometric Sensors

Potentiometric sensors, which rely on ion-sensitive materials to characterise ionic concentrations, have been extensively researched for decades [50]. These sensors are relatively easy to prepare and fabricate, robust in operation, and offer sufficient electrochemical sensitivity [50]. The choice of sensing material can vary significantly depending on the specific application. For instance, traditional pH sensors that use glass electrodes for potentiometric readings offer several advantages, including excellent pH response, high accuracy and stability, and low cross-sensitivity to other dissolved ions [51].

For more miniaturised applications, metals, metal oxides, and polymers are often preferred as electrode materials because they are less prone to breakage, more durable, and compatible with various miniaturisation techniques [50,51,54]. These materials offer advantages over glass, which has high resistance, is vulnerable to

erosion by hydrofluoric acid, and can be influenced by certain ionic compounds, leading to incorrect readings [50].

Advancements in potentiometric sensor technology have focused on leveraging material properties such as biocompatibility, flexibility, and stability to produce accurate readings tailored to specific applications. For example, organic compounds have demonstrated hydrogen-ion carriers where protonation and deprotonation occur, resulting in a pH-sensitive response [37,40,50,54]. This pH sensitivity refers to the material's Nernstian response, where the electric potential is measured according to the Nernst equation, as detailed in Section 2.1.2 [50,55,56].

Typically, potentiometric sensors use an ion-sensitive electrode in a two-electrode system [51]. This configuration involves using a working electrode (WE) made of the pH-sensitive material and a reference electrode (RE) that is chemically stable, which is typically Ag/AgCl [54]. The sensor's sensitivity is based on the potential difference between the RE and the WE when immersed in an ionic solution [51]. Often these sensors can be fabricated by printing methods, which allows for mass manufacturing, consistent and reliable operation as a well as miniaturisation potential [51].

Electrochemical sensors have been applied in biomedical contexts, such as using iridium oxide to measure pH in rat brains and carbon nanotube-modified microneedles for in vivo transdermal pH monitoring [52,57,58].

Other electrochemical techniques, such as ion-sensitive field-effect transistors (ISFETs), also utilise principles of potentiometric sensing, which will be discussed in more detail in the next section.

2.1.1.2 ISFETs

Ion-Sensitive Field-Effect Transistors (ISFETs) are a type of potentiometric sensor that integrate electrochemical sensing with microelectronic technology. They are derived from Metal-Oxide-Semiconductor Field-Effect Transistors (MOSFETs), which are among the most widely used electronic components globally [59]. ISFETs are cost-effective, can be produced at a micro-scale, and are suitable for large-scale manufacturing [59].

These sensors operate by combining the principles of a MOSFET with an ion-sensitive electrode to generate a low-output impedance signal that can accurately measure pH

levels [60]. When in use, ISFETs display a near-ideal, rapid Nernstian response across a broad pH range [60].

ISFETs offer several advantages over traditional pH sensors. For instance, they can be stored in a dry state and do not require hydration with an electrolyte solution for extended use [54,61]. Additionally, they have the potential to integrate signal conditioning circuits, which enhance stability and signal amplification, and they require minimal maintenance and calibration [60–62]. Moreover, ISFETs are sterilisable, capable of operating over a wide temperature range, and provide reduced errors, even at the extremes of the pH scale [61]. These characteristics make ISFETs a versatile and reliable option for various applications.

ISFETs are widely used for pH measurement, but they do have significant drawbacks, particularly in terms of temporal and thermal drift over medium to long periods, which can severely impact their performance [59]. Thermal drift occurs because the solid-state nature of the device makes the mobility of electron carriers susceptible to temperature variations [59]. Temporal drift, on the other hand, results from hopping diffusion, where molecules from the electrolyte solution can penetrate and diffuse into the sensing film, degrading sensor accuracy over time [59].

Additional challenges with ISFETs include the complexity of their fabrication due to the need for intricate layered structures and the difficulty of mounting them on mechanically flexible substrates [60]. Furthermore, they are not ideal for measuring small sample volumes [60].

The basic working principles of an ISFET are similar to those of a MOSFET, so it is useful to describe a MOSFET to understand the primary differences. A typical MOSFET, which acts as a charge sensor, has four terminals: source, drain, gate, and body, as depicted in Figure 4A [59,63]. The channel, located between the source and drain, consists of a gate and a dielectric (insulating) material that separates the gate from the channel [63].

In its default state, the channel has poor electrical conductivity compared to the source and drain terminals, effectively disconnecting them [63]. However, when a positive voltage is applied to the gate, the resulting positive charges attract electrons to form a conductive channel between the source and drain, allowing current to flow. The modulation of this current is controlled by the gate voltage.

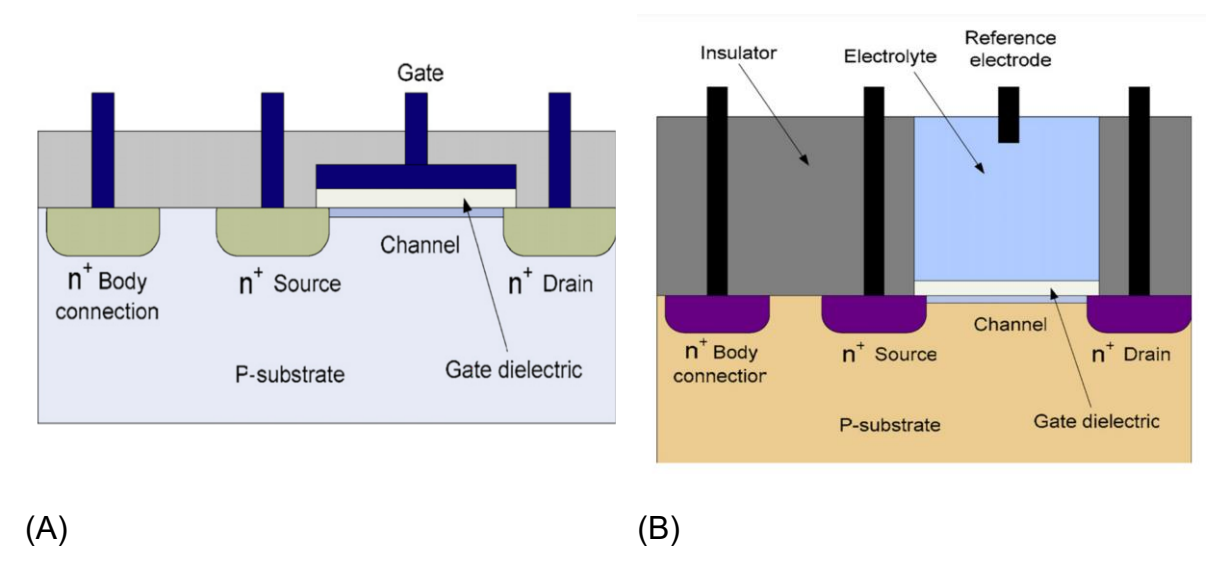


Figure 4: (a) Diagram of a MOSFET including all 4 terminals, Body, Source, Drain, and Gate. (b) Diagram of an ISFET highlighting the differences where the gate is replaced by a reference electrode and an electrolyte solution, and the gate dielectric is exposed and used as a sensing film. Both images are sourced from [63].

The key difference between a MOSFET and an ISFET lies in the exposure of the sensing material or film to the electrolyte solution in an ISFET, whereas in a MOSFET, the gate region is encapsulated [59]. Specifically, in an ISFET, the traditional gate terminal is replaced by an electrolyte solution and a reference electrode, as illustrated in Figure 4B. The reference electrode supplies a voltage to the electrolyte, which in turn modulates the channel current [59,63].

In this configuration, the gate dielectric layer in a MOSFET is substituted with a sensing layer or film in an ISFET. This sensing layer allows surface charges to accumulate, enabling the detection of changes in ion concentration within the solution. The relationship between the surface charge density and the ion concentration is described by the Gouy-Chapman-Stern-Graham model and the Nernst equation, which will be elaborated on in the subsequent sections.

2.1.2 Working Principle of pH Sensors

For completeness, the mechanisms which cause a sensing material in a potentiometric sensor to be sensitive to ion-concentration is described in the following subsections. The sensitivity is highly dependent on the micro and nano structures of the materials regardless of the material type, be it polymers, carbon, glass or metal/metal oxides [51]. The pH dependence of a potentiometric sensor arises from the potential difference measured between the RE and the WE across a selective

membrane. This relationship is quantitatively described by the Nernst equation and further explained by site-binding models, which account for ion adsorption and surface charge regulation.

2.1.2.1 Nernst Equation

As previously mentioned, Nernstian relations can be used to determine the pH by measuring the potential difference between the RE and the WE of potentiometric sensors. The Nernst equation describes the adsorption of potential-determining ions onto the solid-phase lattice and provides an accurate approximation of the electrochemical potential by considering equilibrium constants. In practical terms, the Nernst relations explain how the difference in ion concentrations between the RE and WE—across a perfectly selective membrane—leads to the development of a voltage potential difference. This principle extends beyond pH-dependent ions such as H⁺ and OH⁻, as the Nernst equation can be adapted to describe other ion-exchange processes. However, in this context, it is specifically applied to relate ion activity to pH [55]. The following theory describes the reactions by which a site can become negatively or positively charged at surface to cause a build-up of charges.

Equations (2)-(3) show positive, neutral and negative surface sites denoted as AH_2^+ , AH, A^- respectively [55]. In the context of pH, A^- can be regarded as equivalent to an adsorbed OH- ion.

$$AH = A^{-} + H^{+} \tag{2}$$

$$AH_2^+ \leftrightharpoons AH + H^+ \tag{3}$$

The respective electrochemical potentials ($\bar{\mu}$) for equations (2)-(3) are written as shown in equations (4)-(5).

$$\bar{\mu}_{AH} = \bar{\mu}_{A^-} + \bar{\mu}_{H^+} \tag{4}$$

$$\bar{\mu}_{AH} + \bar{\mu}_{H^+} = \bar{\mu}_{AH_2^+} \tag{5}$$

The equilibrium of H⁺ and OH⁻ ions that are adsorbed is explained by the site-binding model which is a function of dissociation constants due to protonation and deprotonation reactions, and ion activity at the sites near the interface between the sensing material and the aqueous solution [59]. The derivation of the dissociation

constants are specified below and is adapted from [55]. This was adapted to relate pH to an electrochemical potential.

As aforementioned, the Nernst equation is derived from the principle that the change in free energy, specified as F, is 0 at equilibrium conditions as detailed by equation (6) where $v_{\rm AH}$, $v_{\rm A^-}$ and $v_{\rm AH_2^+}$ are the number of the ions per unit area of the electrolytesolution and sensing interface [55].

$$0 = \left(\frac{\partial F}{\partial v_{AH}}\right)_{v_{AH} + v_{A^{-}}} = \left(\frac{\partial F}{\partial v_{AH}}\right)_{v_{AH} + v_{AH}^{+}_{2}} \tag{6}$$

$$F = -kT \ln h \tag{7}$$

F is an entropic term that can be described by equation (7), where k is Boltzmann's constant, T is the absolute temperature and k is the number of possible surface site arrangements described by equation (8) [55].

$$h = \frac{(v_{\text{AH}} + v_{\text{A}^-} + v_{\text{AH}_2^+})!}{v_{\text{AH}}! \, v_{\text{A}^-}! \, v_{\text{AH}_2^+}!} \tag{8}$$

Stirling's formula is used here to simplify the factorials in equation (8) and is applied to the relations described in equations (4)-(6) to yield equations (9)-(10), where e_0 is the proton charge, the superscript ° applied to μ is the chemical potential as a function of temperature and pressure, $a_{\rm H^+}$ refers to the activity of the H⁺ ion, ψ_0 is the mean electrostatic potential at the surface plane of the charged sites, and ϕ_0^-/ϕ_0^+ are discreteness-of-charge potentials for H⁺ and OH⁻ ions [55].

$$kT\ln\left(\frac{v_{\text{AH}}}{v_{\text{A}^{-}}}\right) + \mu_{\text{AH}}^{\circ} = \mu_{\text{A}^{-}}^{\circ} - e_{0}(\psi_{0} + \phi_{0}^{-}) + \mu_{\text{H}^{+}}^{\circ} + kT\ln(a_{\text{H}^{+}})$$
(9)

$$kT\ln\left(\frac{v_{\text{AH}}}{v_{\text{AH}_{2}^{+}}}\right) + \mu_{\text{AH}}^{\circ} + \mu_{\text{H}^{+}}^{\circ} + kT\ln(a_{\text{H}^{+}}) = \mu_{\text{AH}_{2}^{+}}^{\circ} + e_{0}(\psi_{0} + \phi_{0}^{+})$$
(10)

The dissociation-association processes for the aqueous solutions at the interface are detailed in equations (11)-(12), where NaCl is used as the ion in an electrolytic solution as a typical 1:1 supporting electrolyte [56]. Subsequently the electrochemical potentials can be written as shown in equations (13)-(14) as in equations (4)-(5).

$$AH_2^+ + Cl^- \leftrightarrows AH_2Cl \tag{11}$$

$$A^- + Na^+ \leq ANa \tag{12}$$

$$\bar{\mu}_{AH_2^+} + \bar{\mu}_{Cl^-} = \bar{\mu}_{AH_2Cl} \tag{13}$$

$$\bar{\mu}_{A^{-}} + \bar{\mu}_{Na^{+}} = \bar{\mu}_{ANa} \tag{14}$$

 AH_2Cl and ANa represent interfacial ion pairs which form as a result of NaCl [56]. Similarly as in equations (9)-(10), the equilibrium conditions for the dissociation-association processes of equations (11)-(12) may be written as shown in equations (15)-(16). Equations (11)- (12) are reversible and are therefore governed by equilibrium constants [63].

$$kT\ln\left(\frac{v_{\text{AH}_{2}^{+}}}{v_{\text{AH}}}\right) + \mu_{\text{AH}_{2}^{+}}^{\circ} + e_{0}\psi_{0} + \mu_{\text{Cl}^{-}}^{\circ} + kT\ln M = \mu_{\text{AH}_{2}\text{Cl}}^{\circ} - pE$$
 (15)

$$T\ln\left(\frac{v_{A^{-}}}{v_{ANa}}\right) + \mu_{A}^{\circ} + e_{0}\psi_{0} + \mu_{Na^{+}}^{\circ} + kT\ln M = \mu_{ANa}^{\circ} + pE$$
 (16)

pE refers to the electrostatic energy of an interfacial ion pair in the local electric field of strength E. Equations (9)-(10) and (15)-(16) can be simplified to obtain the dimensionless dissociation constants shown in equations (17)-(20) [56].

$$K_{+} = \exp\left[\frac{\mu_{\text{AH}_{2}^{+}}^{\circ} - \mu_{\text{AH}}^{\circ} - \mu_{\text{H}^{+}}^{\circ}}{kT}\right]$$
 (17)

$$K_{-} = \exp\left[\frac{\mu_{\text{AH}}^{\circ} - \mu_{\text{H}}^{\circ} - \mu_{\text{H}}^{\circ}}{kT}\right]$$
 (18)

$$K' = \exp\left[\frac{\mu_{AH_2Cl}^{\circ} - \mu_{AH_2^{+}}^{\circ} - \mu_{Cl^{-}}^{\circ}}{kT}\right]$$
 (19)

$$K'' = \exp\left[\frac{\mu_{ANa}^{\circ} - \mu_{A^{-}}^{\circ} - \mu_{Na^{+}}^{\circ}}{kT}\right]$$
 (20)

In order to express the dissociation constants in terms of pH, the relations used to calculate equations (17)-(20), can be used to obtain equations (21)-(22)

$$K_{+}K_{-} = \frac{v_{A^{-}}}{v_{AH_{+}^{+}}} a_{H^{+}}^{2} \exp\left(-\frac{2e\psi_{0}}{kT}\right)$$
 (21)

$$\frac{K_{-}}{K_{+}} = \frac{v_{\text{A}} - v_{\text{AH}_{2}^{+}}}{v_{\text{AH}}^{2}} \tag{22}$$

Finally, the terms u and v are introduced to represent the quantity of H⁺ and OH⁻ ions such that the dissociation constants can be related to the pH. The detailed steps to reaching equation (23), which shows the relationship between the K_+, K_-, K', K'' and ψ_0 to pH, can be found in [56].

$$2.303\Delta pH = -\frac{e\psi_0}{kT} - \frac{1}{2} \ln \left[\frac{(v+u)\alpha_-}{(v-u)\alpha_+} \right]$$
 (23)

 ΔpH is $pH - pH_{Point\ of\ Zero\ Charge}$ where $pH_{Point\ of\ Zero\ Charge} = -\log_{10}(K_+K_-)^{1/2}$. α_- and α_+ represent the fractions of the total positive and negative sites in the unbound A^- and AH_2^+ conditions, respectively. This equation is a modified form of the Nernst equation, specifically adapted to establish a direct relationship with pH. The Gouy-Chapman-Stern-Graham model, commonly referred to as the electric double layer or site-binding model, provides a framework for visualising ionic distributions and the factors contributing to the electrochemical potential described by the Nernst equation. A detailed explanation of this model is provided in the following section

2.1.2.2 Surface Electrochemistry (Gouy-Chapman-Stern-Graham Model)

At the sensing-layer/solution interface of pH potentiometric sensors, charge accumulation occurs, as described by the site-binding model and the Nernst equation. This surface charge density depends on pH, the density of amphoteric surface sites, and their dissociation constants [63]. pH-sensitive materials typically contain polar functional groups, such as carboxyl (-COOH), silanol (-SiOH), and primary amine (-NH₂) groups, which can accept or donate protons in response to changes in pH.

For consistency with convention, the site-binding model is described here in the context of an ISFET. When an external bias is applied to the ISFET gate, charge carriers rearrange along the sensor surface [63]. However, as Gouy and Chapman demonstrated, a single compact layer of charge is insufficient to produce the

necessary electrostatic potential drop and adequately screen the electric field from the electrode [63]. To account for this, they proposed the formation of a diffuse layer, which collectively forms what is now known as the Gouy-Chapman layer or the electric double layer (EDL). The potential distribution within this diffuse layer is described by the Poisson-Boltzmann equation [63].

However, the Gouy-Chapman model was later found to overestimate the potential drop because it did not account for the finite size of ions in solution, leading to an overestimation of capacitance in highly concentrated electrolytes [63]. To address this, Stern introduced a revised model in which the first layer of ions is considered compact, constrained by the finite ionic radii. This layer, known as the outer Helmholtz plane (OHP), was assumed to be free of mobile ionic charges and contributes a constant capacitance of approximately 20 µF/cm² [63].

Further refinement came from Graham, who discovered that specific ion adsorption at the interface causes some ions to be even closer to the surface than predicted by Stern. This led to the identification of an additional inner Helmholtz plane (IHP), which contributes further to the overall electric potential, as illustrated in Figure 5 [63].

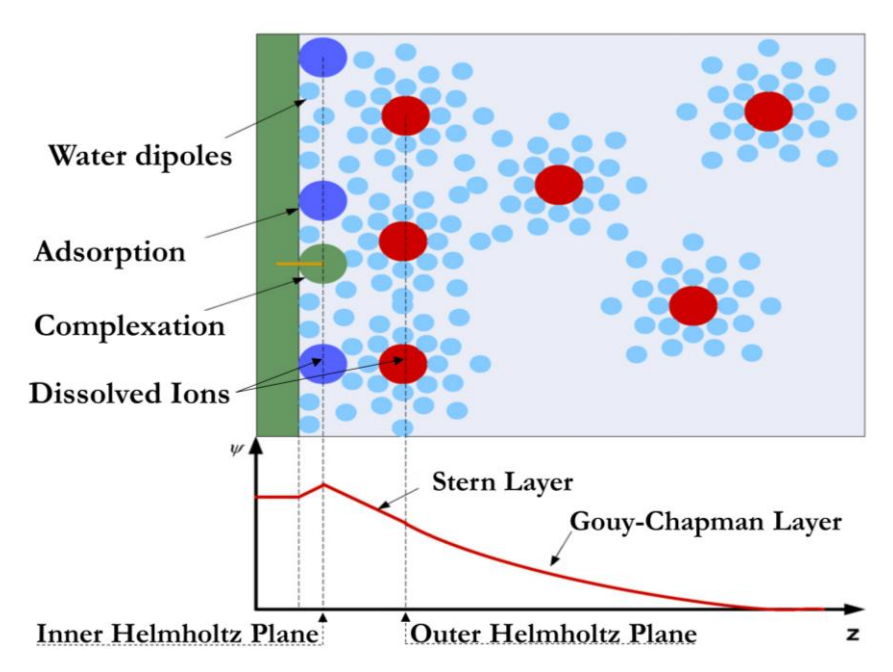


Figure 5: Diagram showing the different layers that contribute to the electric potential observed in the site binding model. A complexation is also shown which shows that it is possible to have complex compounds forming on the surface contributing to the electrical potential observed. Schematic sourced and adapted from [63].

In the context of a pH-sensitive ISFET, equation (23) can be rewritten as shown in equation (24), where it is in terms of gate voltage (V_g) as the ISFET measures pH when the source to drain channel current is varied due to the Gouy-Chapman-Stern model [64,65].

$$\frac{d\psi_0}{dpH} = 2.303\alpha \frac{kT}{q} \tag{24}$$

 α is a dimensionless sensitivity parameter following from equation (23) that varies between 0 and 1. As α approaches unity, the Nernstian limit is reached which is 59.5 mV/pH at room temperature (300°K). This is the theorical maximum sensitivity of an ISFET without signal conditioning. Sub-Nernstian sensitivity and super-Nernstian sensitivity have been widely reported in literature based on various material types and are detailed further in the following section.

2.1.3 Sensing Materials of pH Sensors

To choose a sensing material that is effective for GORD diagnosis, it is important to detail the requirements of the sensor clearly. pH sensing technology has focused on high sensitivity, operational stability (mechanically and chemically), response time, biocompatibility, flexibility, ease of manufacture, potential for miniaturisation and accuracy/repeatability. The different sensing material types are detailed in Table 2 where it must be noted that the difference between metal/metal oxide and metal oxide is the conductivity. Metal oxide is assumed to be non-conductive whereas metal/metal oxide is conductive.

Table 2: Criteria required for the sensor and material type. Scoring: Excellent, Very Good, Good, Fair,

Poor. Table information sourced from [51].

Criterion	Material Type				
	Glass	Metal oxide	Polymer/Carbon	Metal/Metal Oxide	
Sensitivity	Very Good	Excellent	Very Good	Good	
Accuracy	Very Good	Very Good	Good	Fair	
Stability	Very Good	Very Good	Fair	Excellent	
Biocompatibility	Poor	Fair	Excellent	Fair	
Mechanical robustness	Poor	Very Good	Fair	Excellent	
Response time	Very Good	Good	Very Good	Good	
Flexibility	Poor	Very Good	Excellent	Fair	
Potential for miniaturisation	Poor	Excellent	Excellent	Excellent	

Manjakkal *et al.* detailed effectively the various advantages and disadvantages of different material families when used as potentiometric pH sensors and this is summarised in Table 2 [51]. Manjakkal *et al.* also stated that the performance of a general pH sensor is determined primarily by the response time, selectivity, stability, and compensation of non-ideal effects such as drift and hysteresis [51]. Selectivity refers to the sensor's ability to respond specifically to hydrogen ions while minimising interference from other ions in the solution. One of the key assumptions of the Nernst equation is perfectly selective ion permeability, meaning that the sensor should ideally only be sensitive to H⁺. However, in real-world applications, other ions present in the solution (e.g., Na⁺, K⁺, Cl⁻) can also contribute to the measured potential, leading to deviations from ideal Nernstian behaviour and affecting accuracy.

Hysteresis, in the context of pH sensors, refers to variations in the sensor's output when subjected to repeated pH changes, particularly when it is submerged multiple times in different solutions. This effect can cause inconsistencies in measurements due to factors such as slow electrode response, incomplete charge equilibration, or surface adsorption/desorption of ions. For reference, Table 3 shows the sensitivity based on material types found in literature.

Table 3: pH sensitive material types and reported pH sensitivity in literature.

Material Type	Sensitivity (-mV/pH)	pH Range	Sensing Mode	Citation
Al ₂ O ₃	54-56	2-12	ISFET	[61]
Si ₃ N ₄	53-55	2-12	ISFET	[61]
Ta ₂ O ₅	56-58	2-12	ISFET	[61]
Epitaxial Graphene	98-99	2-12	ISFET	[66]
Graphene Oxide	31.8	4-10	Potentiometric	[67]
IrO ₂	47-69	-	Potentiometric	[51,68]
Thick Film Graphite Composite	47	6-9	Potentiometric	[51]
RuO ₂	55-58	2-6	Potentiometric	[69]
Polyaniline (PANI)	52-58	2-12	Potentiometric	[70–72]
WO ₃	~56	5-9	Potentiometric	[73]

After identifying the key parameters critical to sensor performance for diagnosing GORD, a pairwise comparison was conducted to select an initial material for testing.

The criteria were then ranked in the following order of importance: biocompatibility, potential for miniaturisation, cost, accuracy/repeatability, stability, sensitivity, response time, flexibility, and ease of manufacture.

Given the strong emphasis on miniaturisation and biocompatibility, as highlighted in Table 2, glass was immediately ruled out as a viable option. Instead, polymer and carbon-based materials were chosen, owing to their promising performance in terms of sensitivity, accuracy, and repeatability as reported in the literature. These materials are also more biocompatible and cost-effective, making them practical choices.

Among carbon-based materials, graphene has garnered significant attention in recent years due to its unique properties, especially for biomedical applications. This makes graphene a promising candidate for use as a sensing material, which is discussed in detail in the following section.

2.1.4 Graphene-Based pH Sensors

A growing field in potentiometric pH sensing involves the use of graphene as a sensing material as it enables the possibility of achieving a lightweight design, low cost and wearable sensor. Graphene, since its discovery by Novoselov *et al.*, has received significant attention due to its unique properties [74]. Graphene is the thinnest 2-D nanomaterial with a graphitised structure and possesses properties such as extremely sharp edges, ballistic electron transport, high carrier mobility (15000 cm² V-¹ s-¹), chemical robustness in an aqueous environment and strong mechanical stiffness (Young's modulus of 1 TPa) [38,40,54,66,74,75]. It is comprised of a one-atom layer plane of sp²-bonded carbon atoms arranged in a honeycomb lattice [76]. This in part allows it to act as an ideal material for high performance, durable transistors [37]. The symmetric band structure of graphene enables it to be modified chemically or physically such that it works as an ultra-sensitive biosensor that not only outperforms but is far cheaper than more expensive similar technologies [38,40,74,75].

Graphene is typically produced by mechanical exfoliation of pure graphite but can also be produced/synthesised by chemical vapour deposition (CVD) [37]. The main drawback is the difficulty of material handling and device fabrication as they are most widely used in ISFETs [37,75]. ISFETs require complex microfabrication techniques that involve lithography, etching, masking and aligning at micrometre precision [75]. Simplified graphene devices, used as planar chemiresitors have been shown in

literature on various substrate types [75,77]. Gate-free screen-printed electrodes can function as a three-electrode system or as a two-electrode system, where the counter electrode is either connected to the reference electrode or omitted entirely. This setup is useful for measuring pH through open circuit potential measurements or other electrochemical techniques [37].

Various studies have reported a wide range of potentiometric sensitivities for graphene in pH measurement, with values ranging from 12 to 99 mV/pH. This significant variation was investigated by Fu et al., who determined that the presence of defects in graphene, such as dangling bonds, could explain the sensitivities exceeding the Nernstian limit observed in the literature [78].

High-quality graphene, which is characterized by a near-absence of dangling bonds like hydroxyl and carbonyl groups, is inherently less sensitive to ionic [37,78]. Ristein et al. supported these findings, demonstrating that super-Nernstian sensitivity was only achieved when gate voltages were applied that damaged the graphene layer [79]. This damage likely resulted in the formation of larger defects or sites where protonation and deprotonation could occur, thereby increasing sensitivity beyond the typical Nernstian response [79].

To summarise, defects in graphite and graphene enhance their pH sensing capabilities due to the presence of oxygen-containing functional groups [80]. When immersed in an acidic solution, H^+ ions interact with the π -orbital of graphite or graphene, accepting electrons. This interaction increases the material's conductivity by reducing the abundance of electrons and increasing the majority carrier concentration [60,80]. Conversely, in a basic solution, OH^- ions donate electrons to the π -orbital, increasing the material's resistance, which contributes to the Gouy-Chapman-Stern effect discussed earlier.

Based on these studies, it can be concluded that the two primary adsorption mechanisms for H⁺ and OH⁻ ions are influenced by the modification of pure graphene. Chemical modifications introduce polar groups along the graphene surface, creating positive or negative sites that facilitate the adsorption of H⁺ and OH⁻ ions [56]. The polarity of the graphene surface is dependent on the pH of the surrounding liquid and adheres to the basic principles of the Nernst equation [37].

This underscores the importance of controlling defects to ensure that results are consistent and reproducible—a challenging task due to the high chemical reactivity of the edges of pure graphene [37]. These challenges have led to the exploration of graphene oxide, a less reactive variant of graphene, as a more stable sensing material, which will be discussed in the following section.

2.1.4.1 Graphene Oxide (GO) Sensors

When pure graphite is oxidised, graphite oxide is produced, which exhibits significantly different properties compared to pure graphite [81]. When graphite oxide is reduced to a single layer, it is known as graphene oxide (GO), which is highly oxygenated [81]. A typical GO sheet is rich in polar functional groups, including epoxy, hydroxyl, carbonyl, and carboxyl groups on its surface and edges. This high level of oxygenation makes GO very hydrophilic and effective for pH measurement in aqueous solutions [37,39,81,82]. GO can form stable aqueous dispersions of 1-nm thick sheets, a property discussed later in this section [81]. It is produced through mechanical or chemical exfoliation of graphite oxide, resulting in a quasi-two-dimensional carbon sheet [81]. GO acts as an electrical insulator with a randomly distributed sp² and sp³ carbon atom structure [37,81,82]. Its electrical conductivity can be improved by chemical reduction, which restores a graphitic network of sp² bonds but can cause irreversible coagulation in water [37,81,82]. Reduced GO (rGO), produced from GO reduction, is discussed in section 2.1.4.2.

The high hydrophilicity of GO makes it an excellent candidate for pH sensing, though its sensing mechanism differs from that of pure graphene. GO's pH sensitivity arises from the pH-dependent changes in its hydrophilicity. Hydrophilicity, or wettability, refers to a material's affinity for water, which is elaborated in section 0. GO exhibits a unique behaviour when immersed in an electrolytic solution: as the pH of the solution increases, so does its hydrophilicity [37]. Wu et al. investigated this phenomenon and found that GO primarily contains hydroxyl and epoxy groups, with carboxyl groups mainly present at the edges of the GO sheets, as described by Lerf and Klinowski's model [83]. However, it is the carboxyl groups that are crucial in determining GO's hydrophilicity [83].

The change in wettability is attributed to the protonation and deprotonation of the carboxyl groups in response to the pH of the electrolytic solution [84]. At low pH, the

carboxyl groups are protonated, leading to the formation of suspended GO aggregates with a sandwich-like structure of GO-water molecules-GO. At higher pH, the carboxyl groups are deprotonated, and GO behaves like a regular salt dissolved in water [84]. This behaviour is illustrated in Figure 6, which shows a clear distinction in GO's response.

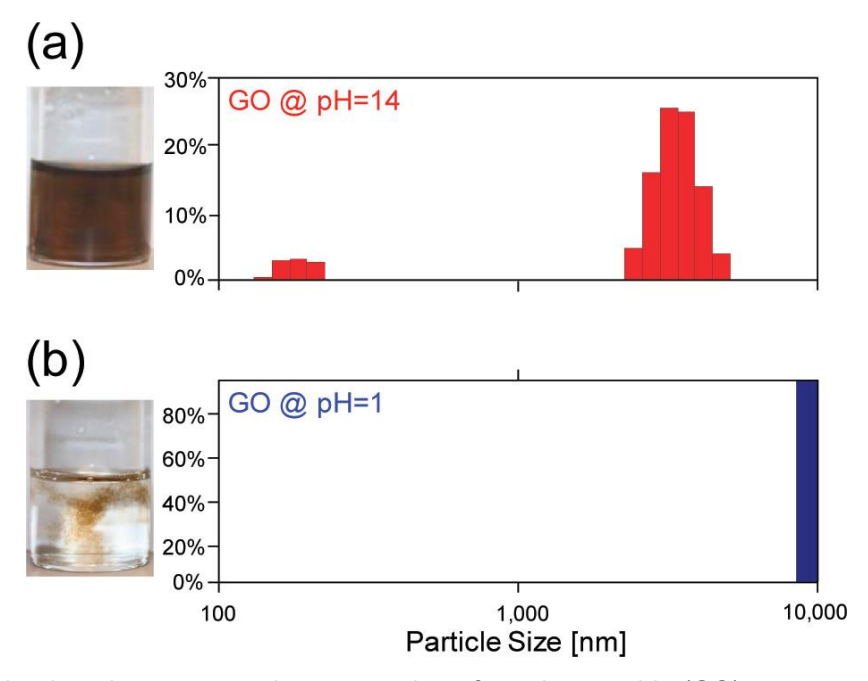


Figure 6: The beakers have an equal concentration of graphene oxide (GO) yet react very differently when the pH of the electrolytic solution is varied. (a)In an alkaline setting, the GO behaves as a salt whereas at an acidic pH level (b) sandwich-like structures are formed due to hydrogen bonding. Figure adopted from [84] under creative commons license.

As a sensing material, used in either an ISFET or a gate-free potentiometric sensor, the variability of the surface/edges of the material plays a vital role in its effectiveness as a pH sensor. GO at low pHs does behave somewhat as a surfactant although not entirely conventionally [83]. Figure 7 shows that it is surface active at pH 1 and causes decreases in surface tension steadily as concentration increases without reaching a plateau. It is less affected at pH 14 likely due to the deprotonated carboxyl groups pulling the GO sheets into the bulk water phase despite being more hydrophobic. This is also because of the presence of electrostatic repulsions between carboxyl groups which hinders the ability of the formation of the sandwich like structures shown in Figure 6.

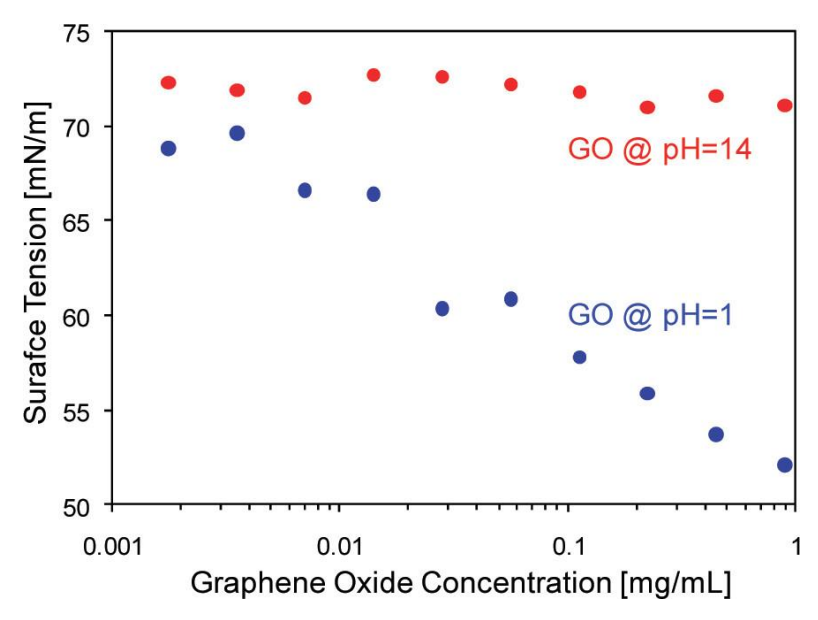


Figure 7: GO concentration is plotted against surface tension in alkaline and acidic water-based electrolytic solutions. Figure sourced from [83].

In a sensing context, pure GO can be employed as an optical pH sensor. However, this may not be ideal for the current research objectives. Instead, electrochemical GO-based pH sensors have been explored, such as those investigated by Melai et al. [67]. In their study, a layered approach was used, where a gold base served as the working electrode, onto which a drop-casted GO layer was applied to create a potentiometric pH sensor. This configuration achieved a sensitivity of 31.8 mV/pH, highlighting its potential for clinical applications due to the inert and biocompatible nature of the materials used.

Given that the sensing material was to be tested in water-based buffer solutions, and considering GO's hydrophilic properties, an investigation was conducted to assess its stability and adhesion to the chosen substrate. Nafion 115 and 117 have been used as protective and hydrogen selective layers for reference and working electrodes al. [37,40,82,85,86]. Ansari et demonstrated that graphite oxide-Nafion nanocomposite suspensions could be prepared within a highly oriented polyelectrolyte matrix, forming a stable material with similar properties to pure GO, such as low conductivity [87]. The conductivity of GO could be significantly improved through reduction using a hydrazine treatment, resulting in graphene sheets [87]. Ameri et al. found that pure graphene transistors could measure pH changes through a Nafion membrane, explaining that Nafion's permeability to protons makes it suitable for sensing HCl, which is relevant for gastrointestinal diagnostics [88]. Wu et al. used a 5% Nafion solution as a binding agent to ensure stable adherence of GO to the electrode surface [83].

2.1.4.2 Reduced Graphene Oxide (rGO) Sensors

Reduced graphene oxide (rGO) is obtained by chemically or mechanically reducing graphene oxide (GO), typically involving the removal of some oxygen-containing groups and restoring partial conductivity. This reduction process can be achieved through various methods, including hydrazine treatment or the use of L-ascorbic acid as a reducing agent [40]. Although rGO retains some functional groups within its microstructure, which contribute to its properties, it differs from pure GO in that it is more conductive [37]. Despite the restoration of some electrical conductivity, rGO still contains residual oxygen groups and defects, distinguishing it from graphene [37,87]. The reduction of GO can also be accomplished through thermal deoxygenation at temperatures as low as 120°C, with complete removal of oxygen groups typically occurring at around 750°C [89].

Similar to GO, rGO can be employed as a sensing material in potentiometric ISFETs, with reported sensitivities ranging from 29 to 57 mV/pH across a pH range of 1 to 13 [37,54]. rGO-based chemiresistor sensors have also been developed, with temperature and pH influencing the resistivity of rGO [37,40,54,90]. The functional groups in rGO facilitate the binding of polymer chains to the rGO sheets [90]. Its honeycomb-like structure generally offers improved performance over GO due to its reduced chemical instability in acidic and basic environments [90]. rGO is often paired with a conductive material in a layered configuration, as demonstrated by Semwal et al. [90].

Efforts to enhance the sensitivity of rGO sensors have focused on surface modifications, such as plasma treatment, to increase the density of active sensing sites, yielding promising results [91]. However, optimising plasma coating parameters is crucial to avoid damaging the rGO structure, as noted in subsequent research [92]. One approach to improving rGO-based sensor performance was demonstrated by Vivaldi et al., who utilised L-ascorbic acid as a reducing agent and further functionalised the material with a mixture of 3-(4-aminophenyl) propionic acid and sodium nitrite solution [40].

The improved sensitivity of rGO-based sensors is closely linked to the intrinsic pH-sensitive mechanism of graphene itself. The following section explores how graphene's unique electronic structure and surface chemistry enable efficient proton detection, making it a promising material for potentiometric pH sensing.

2.1.5 pH Sensitive Mechanism of Graphene

As discussed in section 2.1.4, the presence of defects in graphene is widely recognised as a key factor influencing pH sensitivity. For clarity, it is essential to detail the difference between graphene, GO and rGO. Graphene layers can be produced using methods such as the modified Hummers method, mechanical exfoliation (e.g., the "Scotch tape" method), or chemical vapour deposition. These techniques yield single-atom-thick sheets of GO or oxidised graphene, depending on the method employed [93,94]. According to Wang et al., the modified Hummers method involves the oxidation of graphite in the presence of acids, which disrupts the sp² network by introducing hydroxyl and epoxide groups along the surface and carboxylic and carbonyl groups along the edges [93]. As discussed in Section 2.1.4.1, this process results in GO that is readily dispersible in both aqueous and non-aqueous solvents [93,95].

These points are reiterated here to emphasise that GO is electrically insulating due to these disruptions, and only upon reduction to rGO are its electrical characteristics partially restored [93]. However, various studies have attempted to fully restore the electrical conductivity of pure graphene in rGO, but this has not yet been fully achieved because rGO remains partially oxidised [93,96]. The residual oxygen in rGO forms sp³ bonds with carbon atoms, resulting in only around 80% of the sp² bonding found in graphene being restored [96]. This sp³ bonding disrupts the mobility and conductivity of the rGO [96].

However, the literature has not clearly explained how or why pH response varies with defect density on graphene and its variants [97]. GO, which typically has the highest defect density, is often associated with the strongest pH response, and therefore, is discussed here. This lack of clarity is partly due to the changing water dispersibility of GO in response to pH, its overall low surface conductivity, and its semi-conductive nature [97]. To elaborate, a semiconductor is a material that only conducts electricity

under certain conditions (e.g., when exposed to specific voltages or temperatures), which makes it highly useful in modern electronics.

Common semiconductor materials include silicon, germanium, and gallium arsenide [98]. Angizi et al. sought to understand how defect density affects pH response by examining -COOH, -OH, and -NH2 groups (carboxyl, hydroxyl, and amine groups) [97,99]. This approach is part of defect engineering, a process where defects are deliberately introduced to study their effects. When applied to semiconductors like graphene, this process is known as doping.

Doping is the introduction of impurities and is classified into two types, n-doping and p-doping. n-doping refers to the introduction of a dopant that has an extra valence electron compared to the carbon atoms in the graphene network. This dopant donates an electron, which causes the material to become negatively charged and conductive. This effect can be described by equation (25), where σ is conductivity, n is the number of free electrons, μ is electron mobility, and e is the amount of charge each mobile particle possesses (single electron in this case).

$$\sigma = n\mu e$$
 (25)

Pure graphene naturally forms into a hexagonal structure where each carbon atom bonds to 3 other carbon atoms covalently. Carbon has 4 valence electrons, which means that in graphene, one free electron from each carbon atom is left which causes the electrical conductivity to occur. As a result, there is a large number of high-mobility electrons (μ) which are known as π electrons.

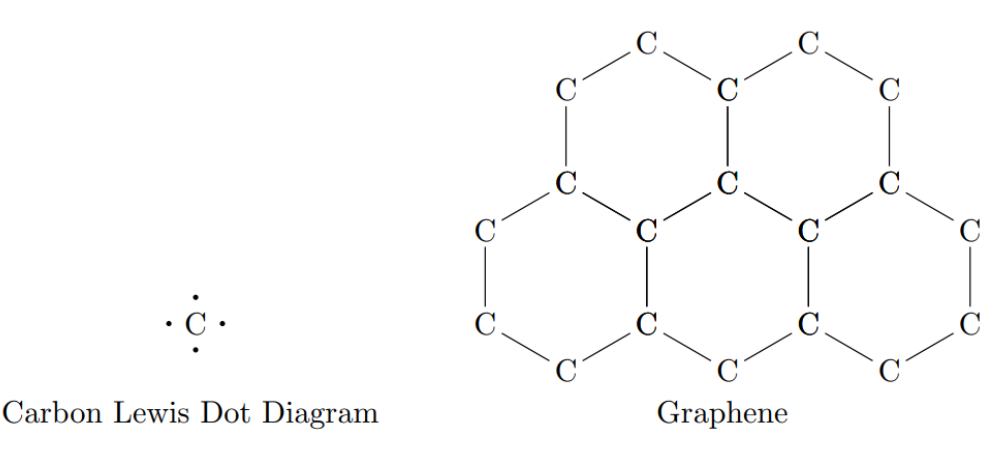


Figure 8: Chemical structure diagram of carbon atoms and graphene to detail the presence of π electrons which causes the electrical conductivity.

In p-doping, the opposite effect is exhibited where a 3-valent atom is introduced. This dopant acts as an acceptor and causes the formation of a hole which is represented by a proton atom where it should be covalently linked. This hole can swap places with neighbouring covalently bonded atoms to make the dopant negatively charged. p-doping and n-doping have a large effect on the conductivity of a material.

Angizi et al. employed chemical vapour deposition to produce graphene with minimal defects, constrained to 1-2% as detailed by Hong et al. [100]. They discovered that the chemi-resistivity of graphene arises from the electrostatic gating effect, which n-dopes the surface in the presence of H₃O⁺ and p-dopes it in the presence of OH⁻ [97]. Due to the inevitable presence of electron-withdrawing oxygen atoms in the graphene structure, its conductivity is predominantly influenced by p-doping [97]. Consequently, this results in the formation of positively charged holes that move counter to the flow of electrons through the semiconductor [97].

In a real-world sensing context, n-doping of the graphene surface (e.g., under low-pH, H_3O^+ -rich conditions) leads to a reduction in the effective number of mobile charge carriers, which increases resistivity [97]. Conversely, under high-pH conditions, hydroxide ions p-dope the surface, increasing the density of charge carriers (holes) and thereby enhancing conductivity [97]. Figure 9, adopted from [97], shows this phenomenon.

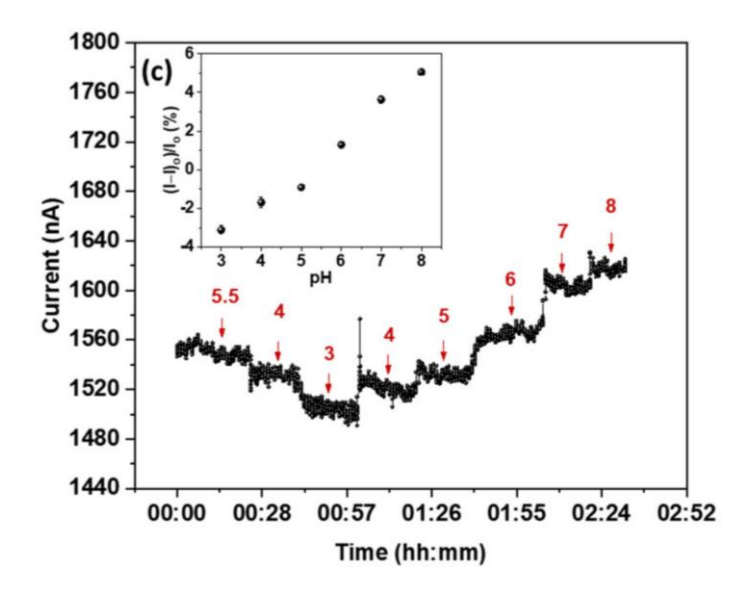


Figure 9: Chemi-resistive response of single-layer graphene. Adopted from [97] under creative commons license.

As the concentration of oxygen-containing functional groups in graphene increases, the mechanism underlying its pH sensitivity changes, leading to an opposite chemiresistive response. For clarity, high-defect graphene is often referred to as GO. GO exhibits increased conductivity at lower pH levels and higher resistivity at elevated pH levels. This behaviour can be attributed to the protonation and deprotonation of the functional groups on the GO surface [99]. At low pH, this is primarily due to the protonation and deprotonation of carboxyl and amine groups, while at high pH, hydroxyl groups dominate this process, as illustrated in Figure 10.

When the pH decreases to 3, carboxyl groups (-COO⁻) become protonated to form -COOH, resulting in p-doping of the GO surface [97]. Amine groups undergo protonation at a pH of 3.7, while hydroxyl groups are protonated at a pH of 8.2 [97]. Deprotonation leads to n-doping, whereas protonation results in p-doping on the GO surface. This response is the reverse of what is observed with single-layer graphene sensors.

Raman spectrometers are used to characterise the defect level of graphene, while X-ray photoelectron spectroscopy (XPS) is also employed to analyse defects and surface chemistry [97]. These techniques are crucial for understanding the impact of defects on the pH sensitivity and overall performance of the material.

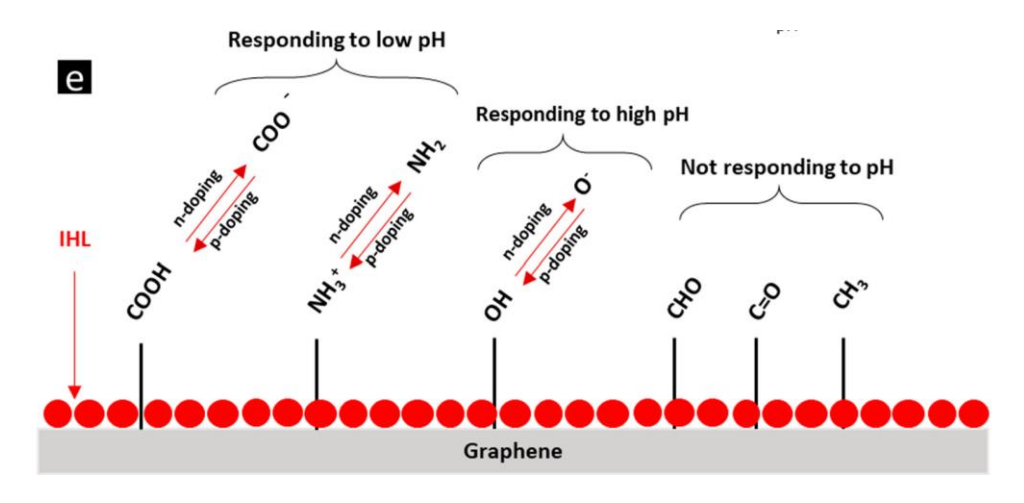


Figure 10: Schematic detailing the defect-induced pH response. Adopted from [99] under creative commons license.

2.1.6 Nanosensor Fabrication Techniques

There are numerous fabrication techniques for nanosensors which typically combine processes developed for integrated circuits (IC) with specialised nanotechnology

processes [101]. The main process flow for the majority of the techniques involves one or a combination of three types that are cycled dependent on the complexity and number of materials used [101]. These types are: deposition of material on a substrate, pattern transfer, and removal of material. The methods of depositing material are numerous, such as printing, sputtering, electrodeposition, spin/dip/spray coatings, etc [51]. Pattern transfer refers to the application of a pattern on the surface of a substrate or material and is often performed via photolithography or other lithography techniques [51,101]. For removal of material, methods such as plasma and chemical etching, chemical evaporation, etc. are also commonly used [51,101].

The technique chosen is highly dependent on the application required and the materials used for fabrication [101]. Huff reports that in nanosensor fabrication, there is little standardisation of processes and only through acquisition of detailed technical knowledge can one make good decisions [101]. This implies also that most of the process steps are completely customised. Huang et al. report that interest in standardisation of the processes has begun in recent times to account for complex geometries and increasingly strict design objectives and constraints [102]. As flexibility, bendability and stretchability are some of the important design constraints required for the GORD diagnosis device being developed, printing was explored. Graphene-based sensors, the material of choice for the sensing electrode, have also been reported to be printed using screen-printing or drop-casting using stencils [40,54]. This led to the literature review of printing techniques with miniaturisation ability for sensors explored in the next sections.

2.1.7 Nanosensor Printing Techniques

Printed electronics enable large-scale manufacturing at a low-cost and low environmental impact [103]. They have applications in photovoltaics, transistors, antennas, soft robotics, smart implants, medical devices and various other sensors [102,104]. Flexible printed electronics have increasingly gained attention over the past few decades for wearable electronic applications which is applicable to the present research [105]. A wide variety of materials have been used to print low-resistance electrodes at very high resolutions using conventional approaches such as screen printing, inkjet printing, direct-write printing and electrohydrodynamic printing [105]. The following sub-sections present an overview of these printing types highlighting their advantages and disadvantages respectively. Details of inkjet printing and

electrohydrodynamic printing is included in the appendix for completeness but is not utilised in the present work.

2.1.7.1 Screen Printing

Screen printing, discussed in this section, on various substrates has been investigated due to the increasing demand of flexible electronic circuits [106]. Screen-printing is a sensor and printed circuit board (PCB) fabrication technique that is simple, can be applied to flexible substrates and is economical [107]. Studies have reported printing on the micro scale at higher resolutions than inkjet printing, offset printing and gravure or flexographic printing [108]. From a high-level, the main steps in the screen-printing technique are: (1) Application of a tangential stress on the ink (2) passing of the ink through a screen mesh or stencil aligned with the desired substrate (3) recovery of the ink after the deposition on a substrate [107]. The quality, electrical performance, and electrochemical performance of the printed sensors is strongly dependent on the substrate choice, screen mesh parameters, and ink rheology [109].

Plastics, papers, and hybrid materials are typical substrates that offer lightweight and flexible characteristics [106]. A selection of these characteristics have been taken from [106] and consolidated into Table 3 for comparison.

Table 4: Consolidated table of substrate characteristics for screen printing. Adapted from [106].

Characteristics	Paper	Plastics (PET)	Glass	
Flexible	Yes	Yes	No	
Roughness (µm)	0.0175	0.015	0.005	
Transparency	No	Yes	Yes	
Porosity	High	Low	Low	
Surface Energy (dynes/cm)	53.9	43.8	58.21	
Thickness (μm)	177 ± 12	127 ± 1	629 ± 1	

The screen mesh parameters are influential in the overall quality of the ink and can be easily manipulated. The chosen parameters are largely dependent on the ink used, the substrate type and the overall size of the sensor. For plastic substrates, attaching a copper surface (to be etched) is a method that can be used to create a PCB.

Following printing of the required design using dark toners on glossy photo paper, the design should be aligned onto the substrate in the desired orientation. Applying heat causes the effusing of the toner layout onto the substrate. Drenching the substrate in an etching solution dissolves the copper surface in all areas where the toner is not applied.

Another method of screen printing, is known as stencil printing, and is typically performed by laser cutting the required design onto a low thickness sheet usually made from non-shiny aluminium to produce a stencil [103]. The maximum resolution of the print is largely dependent on the resolution of the printer and the sheet's ability to withstand the heat generated by the laser and remain solid. Polyimide and PET sheets are both also used as materials for stencils but are less robust than metallic stencils.

Finally, the most common screen-printing method is using an emulsion screen to deposit inks and pastes [103]. This is largely due to the low-capital cost and simple operation of the technique. It has been demonstrated to achieve resolutions as high as 30-50 µm [103]. This process involves the selection of a mesh with high thread count (for high resolution applications) and manipulating an emulsion screen to print the desired design stencil/screen mesh [103]. Once the stencil is prepared, it is secured to the frame of the screen printer as shown in Figure 11. The substrate is again aligned to the stencil and ink is deposited using a transient motion of the squeegee over the mesh/stencil [103].

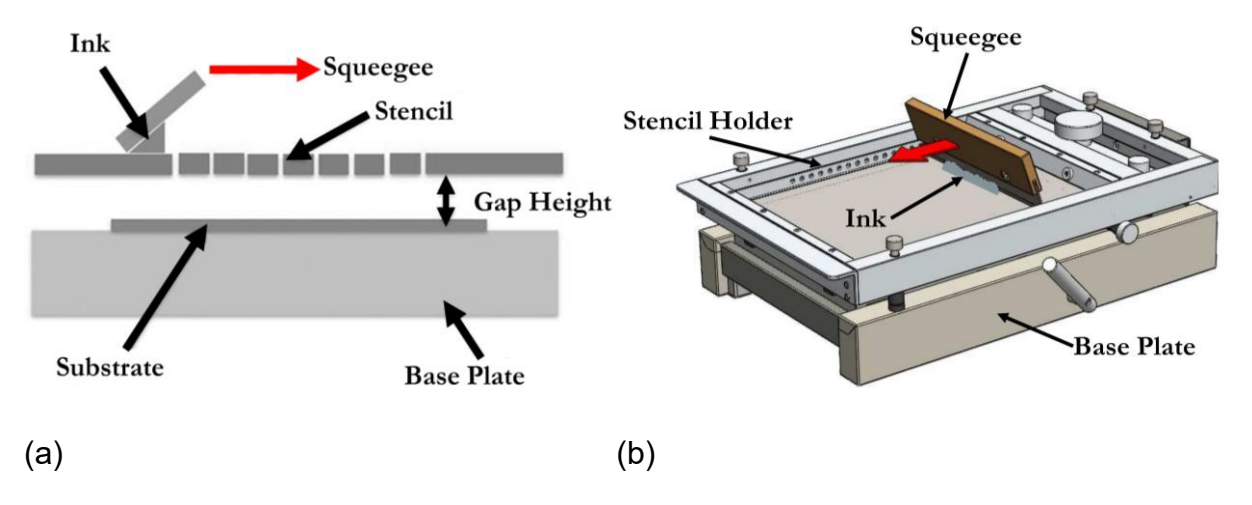


Figure 11: (a) 2-D and (b) 3-D diagrams of the screen printer apparatus. The squeegee is dragged across the stencil which is used to deposit the ink in the specified orientation. Images adapted from [103,110].

2.1.7.2 Screen Printing Ink Rheology

Screen printing inks' rheology is the study of how the viscosity or shear stress varies with shear rate. It has been widely studied for different applications and the properties which most influence the quality of printing are: ink viscosity, thixotropy and viscoelasticity [109]. Viscoelasticity is the property of a substance being both elastic and viscous and is a function of applied stress. Viscoelasticity is dependent on the elastic and viscous moduli which provide information on the solid-like and liquid-like properties of the ink respectively [109].

Thixotropy refers to the time-dependent decrease in viscosity when an ink at rest is subjected to flow conditions, followed by a recovery once the flow is halted [111]. It is a property of non-Newtonian fluids and is typically associated with viscoelastic effects due to stress-relaxation and normal stress differences [111]. It must be noted however that thixotropic materials may not be viscoelastic as thixotropy is described as an instantaneous step-down in shear rate whereas a viscoelastic fluid gradually decreases in stress up to a plateau value [111]. The desired levelling of screen-printed films is typically defined by the thixotropic properties of the ink due to the shorter drying times required for screen-printing compared to other techniques [112].

A given ink is comprised of a solid, dispersant, organic solvent and a binder [109]. The ingredients control the viscoelasticity and other properties of the ink which directly influence the quality of the prints. Somalu et al. concluded that the ideal binder content for screen printing was 1-3% by weight as this caused an increase in thixotropic properties [113]. Further, the binder content by percentage was found to dictate the presence of desirable particle networks within the inks more than the solvent type [109]. A higher particle network strength indicates increased particle connectivity, mechanical strength [109,113].

2.1.7.3 Direct-write Printing

Direct-write (DW) printing conventionally has a viscoelastic ink that is extruded from a nozzle, and either the nozzle or the stage (if the nozzle is fixed) moves in a preprogrammed path to deposit ink in the desired location [114]. High-resolution positioning stages, also known as nano-positioners, are used to facilitate the relative motion between the syringe and the substrate such that printed designs can be made for high-resolution applications [115]. The main difference between inkjet and DW

printing is that inkjet requires both the generation of droplets and optimising the nozzle-to-substrate space for control of many parameters. Instead, DW printing is known as a contact-printing method and it fills the nozzle-to-substrate space with continuous streams of ink which overcomes some of the shortcomings highlighted with inkjet printing [114]. The setup can be supplemented to include a collocated long-distance microscope and camera for monitoring and setup purposes as shown in Figure 12.

As with the other printing techniques mentioned, the ink used is very important and once again is dependent on the application and the substrate type. Many inks have been shown to work with DW printing, such as colloidal suspensions, organic inks, hydro-gels, sol-gels, polymers, polyelectrodes and nanoparticle filled inks [115]. The ink rheology, again, influences the print quality, as the inks have various degrees of capillary spreading, stability issues, etc. [115,116]. Direct-write has the ability to print higher viscosity inks and the ink's extrusion can be facilitated pneumatically using a control system which provides a backpressure, or using capillary action [115]. Direct-write printing performed layer-by-layer is the most common technique used for 3-D printing and is sometimes used interchangeably [114].

The print resolution for DW printing is primarily influenced by several factors, including nozzle size, ink adhesion to the substrate, nano-positioner resolution, ink rheology, and ink evaporation rate [115]. The nozzle size, which can be reduced to sub-micrometre dimensions, plays a key role in determining both the resolution and thickness of the printed lines. However, the substrate often causes some ink spreading, which increases the thickness of the deposited ink. Additionally, the evaporation rate and ink rheology can further impact the extent of ink spreading.

Interestingly, Yuk and Zhao demonstrated that certain properties of inks used in direct-write 3D printing, such as instability, deformation, and fracturing, can be leveraged to create ink fibres with diameters significantly smaller than the nozzle size. They achieved this by employing an ink-stretching process [117].

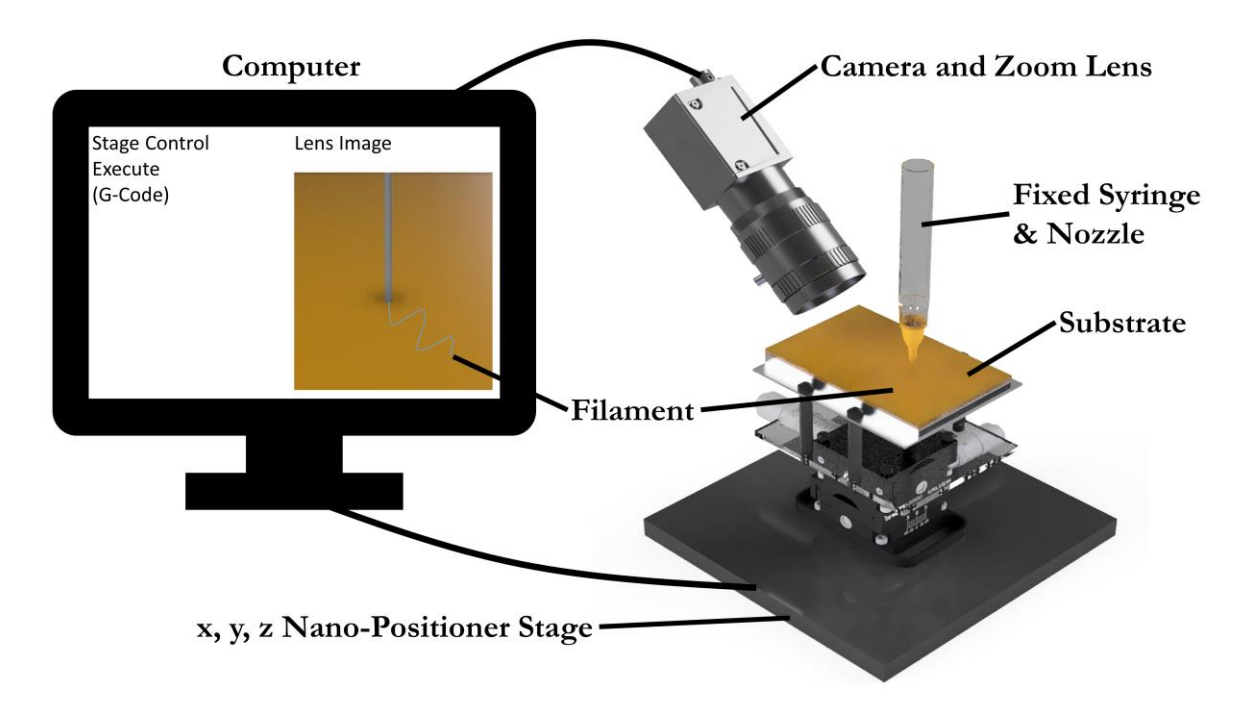


Figure 12: Schematic of an example direct-write printing setup supplemented with a collocated long-distance camera and microscope.

Upon extrusion of the ink, two parameters must be well-accounted for, the meniscus of the ink and its location on the nozzle, and the nozzle-substrate distance [114]. To maintain contact between the ink and the substrate, the pressure and the hydrostatic head of the ink must be balanced with the Laplace pressure of the ink [114]. The Laplace pressure gradient is described as the difference between the inside and outside pressure of a curved surface between two fluid regions. In the case of spherical droplets, this is commonly expressed as shown in equation (26) [114].

$$\Delta \text{Pressure} = \gamma \frac{2}{R} \tag{26}$$

 γ is the surface tension, R is the radius of curvature (which in this case is the nozzle diameter). This forms the balanced relationship described in equation (27) to prevent the ink from flowing excessively but still form a meniscus. P is the pneumatic pressure used to extrude the ink, ρ is the density, g is the gravitational constant and h is the height.

$$P + \rho g h \le \gamma \frac{2}{R} \tag{27}$$

Following balance of the left-side of equation (27), the gap height must also be well controlled and adjusted for the surface topology of the substrate to ensure uniform printing. This is illustrated in Figure 13.

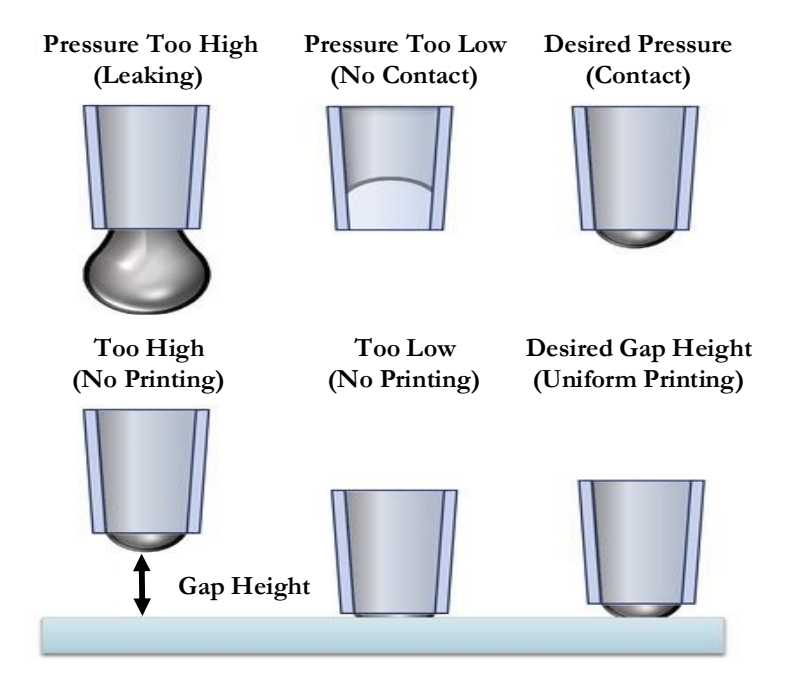


Figure 13: Schematic depicting the impact of pressure and nozzle-substrate distance on printing. When the pressure is too high leaking occurs. When the pressure is too low, no contact can be established, and the desired pressure creates a stable meniscus to enable contact printing. Similarly for gap height, only the desired gap height creates favourable printing conditions. Image adapted from [114].

Drawbacks of DW printing include slow printing time (similar to inkjet) and many inks' requirement for post-treatment processes such as thermal annealing and UV curing for stability [115,118]. The stability of the ink in general is dependent on the evaporation rate where higher-evaporation rates are required to improve mechanical properties of the ink [115]. This high evaporation rate comes at the cost of evaporation-led nozzle clogging which leads to the desirability of inks with shear-thinning properties [115]. Evaporation-led nozzle clogging occurs when the solvent evaporates prior to the ink being deposited causing it to solidify inside the nozzle. This also highlights the importance of the nozzle itself where wettability and size are the most important nozzle properties which must be accounted for [115].

2.1.7.4 Direct-Write Printing Ink Rheology

Prior to using direct-write printing, the parameters of the ink and the substrate must be considered as they contribute directly to the printability and quality of the electronic devices. Hou et al. report that the most influential parameters for printing are ink exiting

speed, nozzle size, dispenser moving speed, ambient temperature, and direct writing medium/substrate [119]. Hou et al. also report that the most important ink parameters are high shear-thinning behaviour, viscoelasticity and a high solid-content of the ink as they allow inks to be extruded from the nozzle as a continuous stream and rapidly cure while largely maintaining the volume of the extrusions [119]. Control of these parameters allows for stable dispersions that are suitable for printing as the transition from fluid to gel is promoted [119].

Fillers in the form of nanoparticles have been demonstrated to manipulate the ink rheology and improve mechanical, electrochemical and conductive properties [119]. Liu et al. demonstrated that by combining silver nanowires, GO and LTO (Li₄Ti₅O₁₂), a porous, highly conductive, thick ink, using a relatively simple fabrication process, can be used for printing 3D electrodes [120]. In addition, binders, adhesion promoters, and dispersants are commonly used in direct-write printing to optimise flow behaviour and improve adhesion [114]. Optimising ink-rheology can allow for the desired printing properties shown in Figure 13.

However, achieving the right balance of ink properties alone is not sufficient; the interaction between the ink and the substrate plays a crucial role in print quality. Substrate wettability and adhesion are key factors that influence the final print resolution and performance. These factors are explored further in the following section, which discusses the importance of substrate wettability and adhesion in direct-write printing.

2.1.8 Substrate Wettability and Adhesion

An issue that is commonly encountered when printing on various substrates is the adhesion of the ink to the substrate, particularly with surfaces of low or very high roughness [114,121]. Other issues with substrates that are especially relevant in medical applications are lack of biocompatibility, and desired wettability [122]. For an ideal solid substrate characterised by high smoothness, insolubility and chemical uniformity, degree of wettability (hydrophilic, hygrophilic or hydrophobic) is defined by the contact angle that a given liquid makes with it [123,124]. Although a single contact angle may not be unique for a given solid and liquid as stated by [124], from a high-level perspective, contact angle is defined as the observed angle between the solid

surface and that tangent to the liquid surface as shown in Figure 14. Hydrophilic is <90°, hydrophobic if >90° [123].

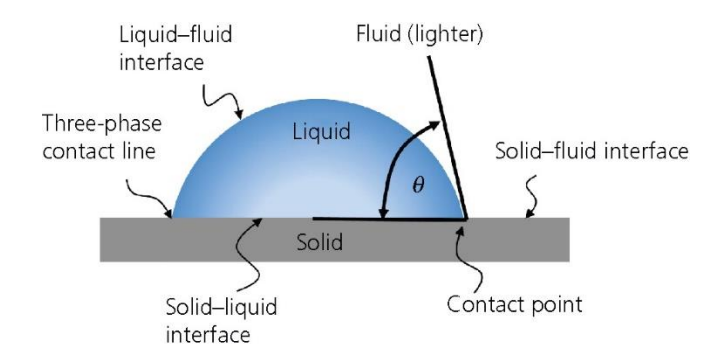


Figure 14: Diagram describing the contact angle (θ) for a liquid drop on an ideal solid substrate to show how wettability is classified. Figure sourced from [124].

Caulfield *et al.* have also explained that due to the non-unique contact angle possibility, it is common to measure contact angle using advancing and receding angles denoted by θ_A and θ_R , respectively [115]. This is performed via incremental increases and decreases in the volume of the droplet and measuring the contact angles dynamically. Surface treatment techniques such as surface roughening, plasma treatment, functionalisation, etc. can all improve the contact angle and ultimately improve wettability and adhesion of the inks to the substrate [115].

Plasma treatment, in particular, has the capacity to achieve desired wettability, biocompatibility, and adhesion properties while preserving the surface characteristics [122]. The gas composition, applied power, and duration of the treatment can have significant effects on the substrates, leading to activation, cross-linking, or an increased presence of free radicals and functional groups [122,125]. The duration of the treatment is particularly influential in achieving the desired properties, as excessively long treatments can cause degradation of polymer substrates due to rapid interaction with radicals [122].

Hegemann et al. demonstrated that applying oxygen-containing gas mixtures as plasmas onto polymer surfaces reduces the contact angle, rendering them hydrophilic, especially when SiOx gases are used [122]. This desired wettability property remained stable after ageing for one year, attributed to the formation of highly polar silanol groups at the expense of methyl groups [121,122]. However, an N₂ plasma pretreatment was necessary due to the formation of hydrolytically unstable siloxane bonds, which caused accelerated ageing on the polymer surface [122]. Hettlich et al.

showed that the application of pure O₂ and CO₂ plasma layers improved surface adhesion on silicone lenses [126]. Power levels of 200W, 400W, and 600W were tested, showing that increased power resulted in a greater number of functional groups on the material's surface [126]. Moreover, CO₂ was found to produce the desired wettability properties and could be applied for 300 seconds without causing damage or changes to the substrate composition in deeper layers [126].

In theory, this plasma technique would be highly effective with a GO ink, due to its hydrophilic nature and the abundance of functional groups on its surface, which would allow it to form weak Van der Waals interactions, enabling effective binding to the substrate. However, in practice, many research groups have found that these interactions are weak and reversible, leading to poor adhesion on various substrate types [121]. Sarycheva et al. showed that oxygen plasma treatment on the substrate also improved adhesion by removing residual contamination and oxygenating the substrate, resulting in an irreversible bond [125].

However, Kirikova et al. explain that while oxygen plasma treatments promote functional groups and significantly enhance hydrophilicity, their effects tend to be relatively short-lived [127]. They suggest using oxygen plasma as a surface preconditioning treatment, particularly on substrates with chemically inert surfaces, followed by the application of a self-assembled layer (SAL) [127]. This method is further detailed in the appendix, as it was not employed in the present work.

2.1.9 Summary of pH Sensor Literature and Gaps

This background and literature review section has looked at the current types of pH sensors and compared their working mechanisms. After selection of potentiometric sensors as the sensor of choice, the working mechanism of what causes the sensing material to be pH sensitive was detailed. Both the Nernstian relations and the surface electrochemistry model which explains the presence of the voltage potential between a RE and WE were explained. The various types of pH sensitive materials were then explored and compared. Following a pairwise comparison analysis to determine the most important parameters for successful performance for GORD diagnosis, polymer/carbon-based materials were selected for the WE. Graphene and its variants, GO and rGO, having unique properties suitable for this application, were then explained in detail, and compared following their selection as initial materials for the

WE. Fabrication methods for miniaturised sensors were then explored particularly for graphenic materials, with screen, and direct-write printing compared. Surface/substrate wettability was then highlighted to show its importance for adhesion of inks used, overall resolution, print quality and robustness.

The following section describes work that was done following the identification that graphene-based pH sensors possess low robustness in highly acidic environments such as the ones present in a GORD diagnostic implantable device environment – rendering them unsuitable.

2.2 Printed Graphene Oxide Sensors with Robust Sensing in Low Acidity Environments

2.2.1 Introduction

As discussed in the literature review, oxygen-rich materials are attractive for pH sensing materials as the functional groups, particularly carboxyl, amine, and hydroxyl groups are pH sensitive. These functional groups undergo protonation and deprotonation reactions changing the materials properties in a predictable fashion allowing for sensing using chemi-resistive, potentiometric, ISFET, and other electrochemical techniques [97]. GO is one such material that has been widely reported for pH sensing in either potentiometric thin-film or ISFET forms [39,67,91,92]. Typically, GO is functionalised to increase the abundance of surface functional groups using various methods such as chemical or electrochemical oxidation techniques to form oxygen functional groups.

rGO has also been investigated as a pH sensing material using electrochemical and hydrothermal reductions techniques. Briefly, following the oxidation of graphite using the modified Hummers method to create GO, the GO is then reduced to restore electrical conductivity of the material. While this does remove functional groups, XPS and elemental analysis reveal that functional groups remain present (oxygen/carbon atomic (O/C) ratio 8.5-10.3%) relative to GO's ~69.2% O/C ratio [128]. Despite this, 55 mV/pH sensitivity was obtained in hydrothermally-reduced GO samples on gold [129]. The loss in functional groups however drastically changes the robustness of the sensor as there is a lack of functional groups present for bonding of the material with the substrate. This makes rGO unsuitable for flexible sensing required in GORD diagnostic applications as the sensor's robustness is vastly affected.

Oxygen plasma surface treatment is widely used for the modification of polymer and carbon nanomaterials and can effectively be used for surface functionalisation [130,131]. XPS analysis found that initially, plasma treatment causes a reduction of GO and thus a decrease of oxygen-containing groups such as epoxides, carbonates, and carboxyl groups [131]. However, after a processing time of 5-7 mins, there was a large introduction of oxygen groups that could be beneficial for pH sensing [131]. The plasma process is also used for surface etching causing the introduction of new holes within the graphene lattice, exposing new sites for oxygen functional groups formation. Further, the increased hydrophilicity of GO because of the treatment could cause the improved robustness necessary for GORD diagnostics.

The sensor design as specified for GORD diagnosis which entails small radii, followed by flexibility, biocompatibility and mechanical softness. Although flexible, miniaturised ISFETs have been reported [132], ISFETs have complicated fabrication procedures due to the use of multiple layers and materials and suffer from high temporal and thermal drift [67]. Printed, facile potentiometric pH sensors like ones produced by Vivaldi *et al.* and Salvo *et al.* have simple and effective fabrication processes, while being lightweight, low-cost, flexible, robust, wearable and scalable in size and manufacturing volume [40,54]. A schematic of this sensor design is shown in Figure 15.

In previous work, for coating the working electrode area, graphene oxide (GO) was drop casted onto the conductive tracks which led to reported sensing inconsistencies between samples [40]. For this reason, fully printed sensors were selected in this work to decrease variability of performance amongst the sensors. This entailed the integration of measures to ensure sensor-to-sensor fabrication similarity by modification of the printing setup. Firstly, direct-write printing places high importance on the nozzle-substrate distance. Small misalignments of ≤1° can cause significant variation in the amount of ink deposited on the surface changing surface morphology and overall robustness due to inconsistent mechanical properties along the sample.

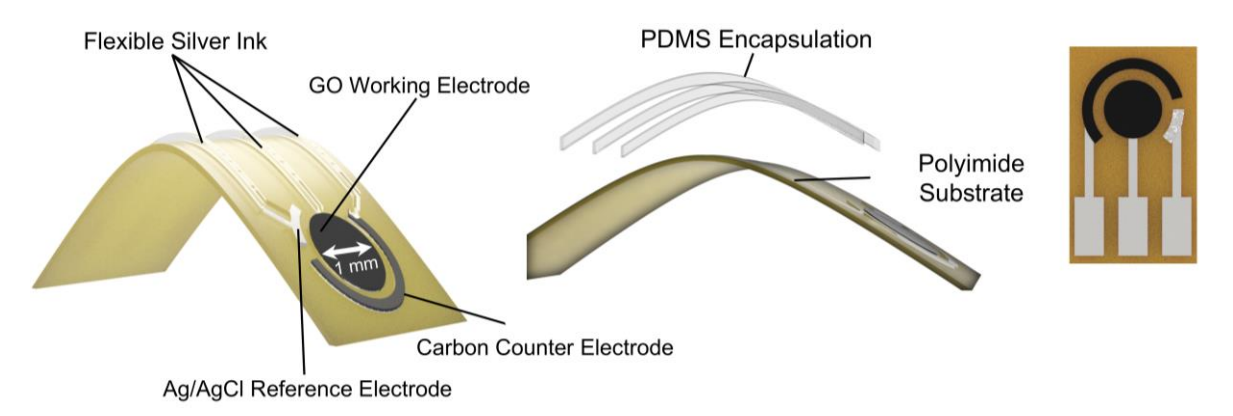


Figure 15: Schematics of the flexible three electrode sensor design detailing all the layers and materials used for fabrication.

Upon replication of Vivaldi *et al.* and Salvo *et al.*'s works, the fabricated pH sensors suffered from lack of robustness as the GO sheets would peel off the bare electrodes upon application of light bending and with acidity exposure.

Polyurethanes are commonly used as adhesives and sealants since their emergence in 1937 and have been used as additives for stabilising adhesion promotion, and rheological modification [133]. They can be found in one-component, two component, dispersion and solvent based form and have been found to have good adhesion to woods, metals and plastics used in applications such as construction, packaging, automotive, aerospace, pharmaceutical and healthcare applications [133,134]. These are due to their excellent qualities of durability, flexibility, resistance, biocompatibility and tuneable mechanical properties [133,134]. It is hypothesised that by incorporating a small amount of polyurethane, the mechanical and sensing robustness could be significantly improved without impacting the sensing performance due to the lack of electrical conductivity of the polymer.

This work aims to address the main issues of GO-based pH sensing, poor robustness in acidic or harsh environments, batch-to-batch performance inconsistency, and low pH sensitivity. This is particularly relevant as gastro-oesophageal pH sensing requires robustness in very harsh environments (pH<1) with enzymes and other biological species. Firstly, mechanical robustness and sample to sample consistency improvements were explored via modifications of the fabrication techniques used previously in literature, and modification of the ink for adhesion promotion. Surface functionalisation via oxygen plasma treatment was also explored for improving pH sensitivity.

2.2.2 Materials and Methods

2.2.2.1 Materials

The following materials were ordered from Sigma Aldrich: Silver/silver chloride (Ag/AgCl) paste (60:40 composition), Nafion 117 (5%), Pluronic® F-127, SYLGARD™ 184 Silicone (PDMS), and graphene oxide solution (GO, 4 mg/mL). Silver electronic screen printable ink (DM-SIP-2005) and carbon screen-printable carbon paste (DM-CAP-4311S) were ordered from Dycotec materials. Ethanol and Bahydrol® UH240 were purchased from Fischer Scientific. Polyimide sheets (50 microns thick) were procured from Goodfellow Cambridge. For calibration purposes, pH 1, 4, 7 and 10 buffered solutions were purchased from Fischer Scientific.

2.2.2.2 Working Electrode Ink Preparation

To fabricate the WE ink and make it suitable for direct-write printing, the approach of [135] was followed to increase the concentration of the GO mixture via centrifugation to 10 mg/mL, causing an increase in viscosity and surface tension. The GO was printed using a 100 micron nozzle onto the working electrode area. To prepare the plasma treated GO, following printing of the standard GO ink onto the working electrode, the counter and reference electrodes were temporarily encapsulated in PDMS. The coated working electrode was then placed in a plasma chamber (Diener Femto) at 0.1 mbar under a power of 30 W for 4 mins. The encapsulant was then carefully removed with a scalpel. For the GO polyurethane mixture, 3.2 mL of 10 mg/mL GO was added to 1 mL of 5 mmol of Pluronic® F-127 and 1 mL of 40% Bahydrol® UH240. Bahydrol® UH240 is a water-based adhesion-promoting polyurethane. Pluronic® F-127 was added as a stabilising surfactant to avoid precipitation of GO when mixed with other solutes following the approach of [136]. The ink was then mixed using the FlackTek SpeedMixer DAC 330-100 SE for 15 mins at 3500 RPM. This generated a highly viscous homogenous GO ink that was printed using a 100 micron nozzle onto the working electrode area. The chemical structures of the three tested working electrode materials are shown in Figure 16.

Figure 16: Chemical structures of working electrodes tested (A) pristine GO, (B) oxygen plasma treated GO (C) components of the polyurethane, GO, and Pluronic® F-127 composite.

2.2.2.3 Flexible, 3-electrode Sensor Fabrication

The 3-electrode design, shown in Figure 17A, was fabricated initially via screen-printing. Between each screen-printed ink used, the ink was dried and cured per manufacturer recommendations. Firstly, DM-SIP-2005 was screen printed to form the silver conductive tracks. Following this, DM-CAP-4311S, was screen printed onto the working and counter electrode areas to form the three-electrode system.

The sensor was then transferred to a bespoke direct-write printer setup comprised of a fixed syringe and an XYZ Aerotech Nanopositioner (ANT130L+ANT130XY) system as shown in Figure 18A. This was to print both the PDMS dielectric encapsulation layer, due to the flexibility and biocompatibility properties of PDMS, and coat the working electrodes with the sensing material. Due to the thermal curing nature of commercial PDMS, a heated stage was built and added to the 3-D stage for in-situ curing as shown in Figure 18B. This stage was comprised of a 220V PTC heating element, Red Lion PXU PID temperature controller, type k thermocouple, and a solid-state relay procured from RS components. Two goniometers were used to correct for nozzle-to-substrate distance variations, which could otherwise cause uneven layer thickness, as illustrated in Figure 19. After correction, a uniform GO coating was achieved (Figure 17B). However, the GO+PU mixture exhibited reduced smoothness

and uniformity, which is attributed to the surfactant Pluronic® F-127, inducing a foaming-like behaviour during deposition (Figure 17C.)

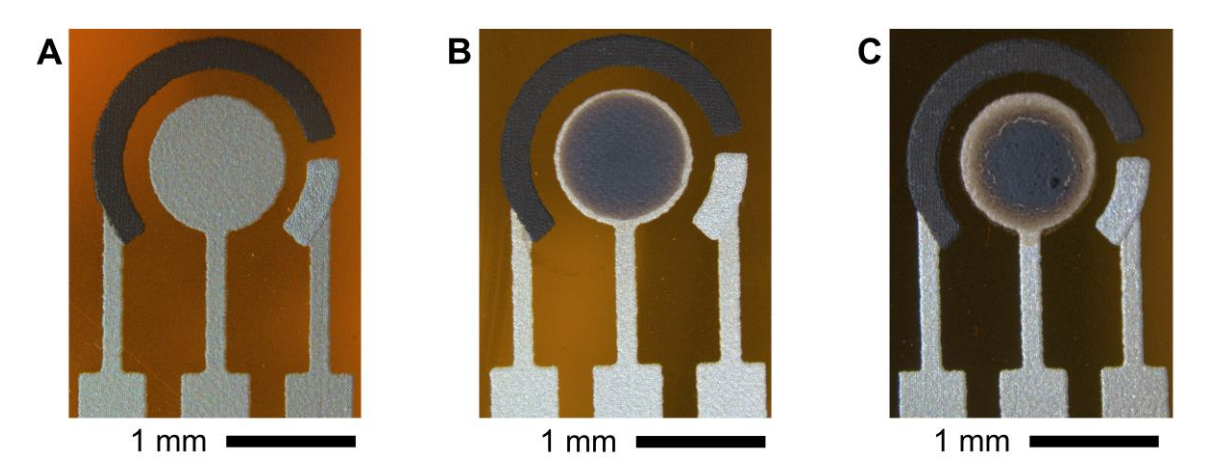


Figure 17: Optical images of the bare fabricated sensor **(A)** with no coating, **(B)** with GO on working electrode prior to encapsulation with PDMS **(C)** and with GO+PU mixture on the working electrode.

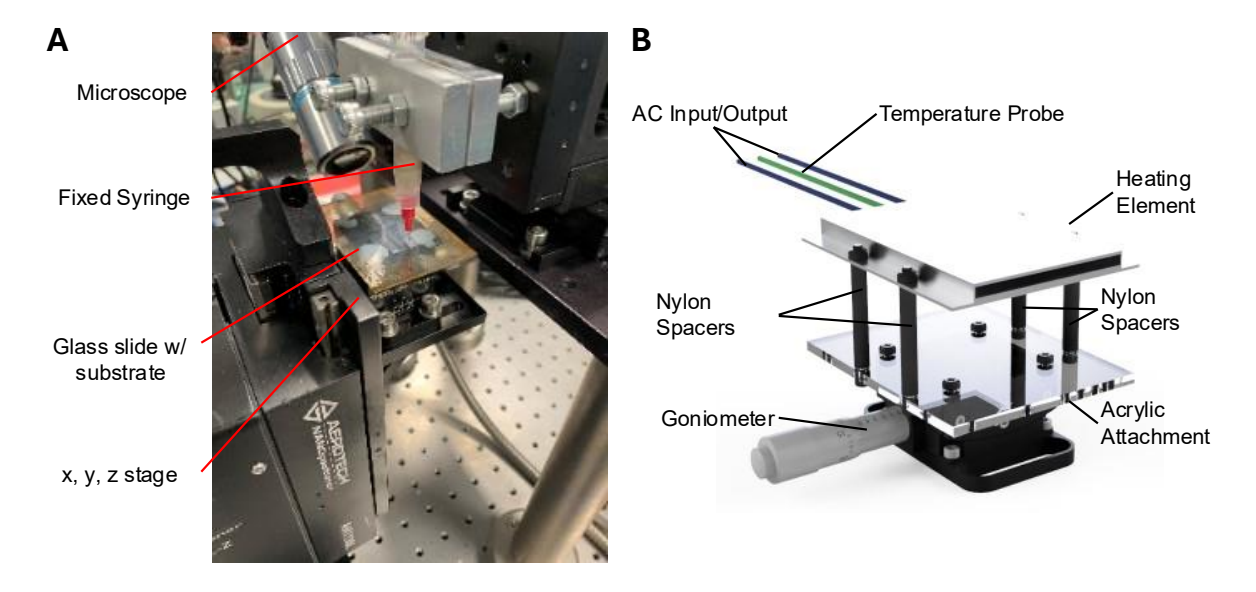


Figure 18: Image of the direct-write printing setup used to encapsulate the conductive tracks of the sensor.

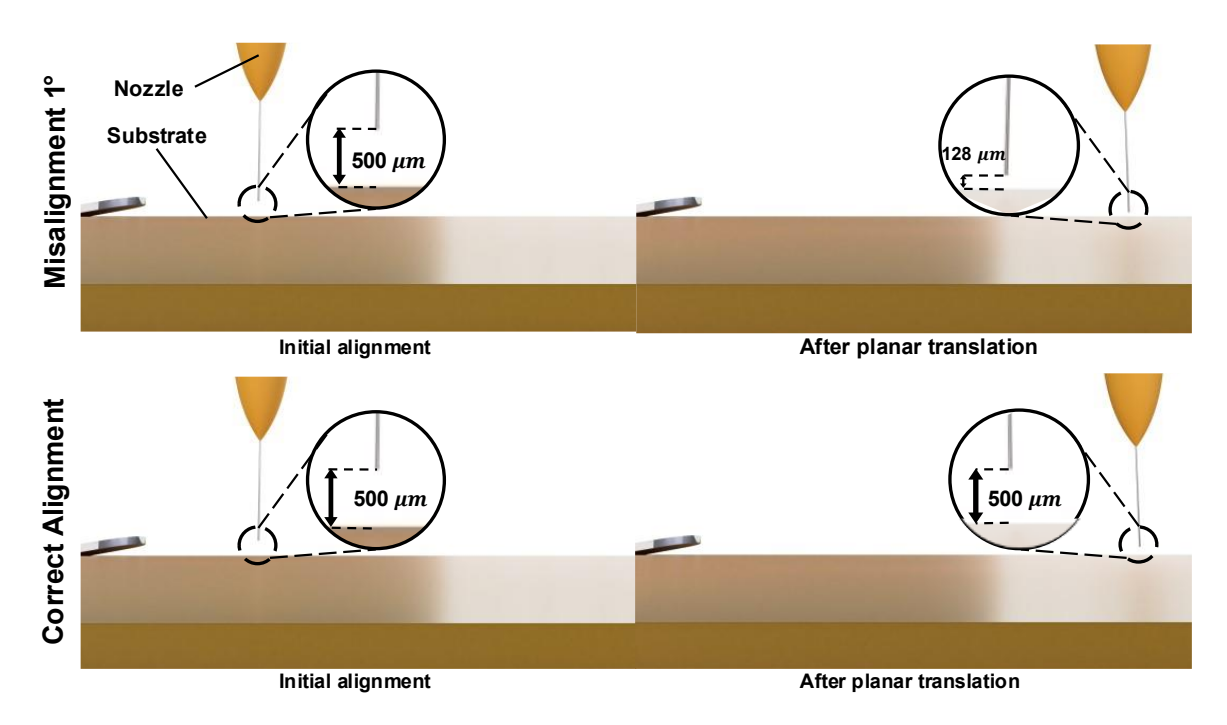


Figure 19: Comparison 3-D renderings of the direct-write printing setup, highlighting the importance of perpendicular alignment between the nozzle and the substrate. Even small (≤1°) misalignments cause the nozzle-substrate distance to vary causing inconsistent ink volume ejection and poor prints.

2.2.2.4 Electrochemical measurements

To assess the pH performance of the produced sensors, a potentiostat with an integrated impedance analyser (Ivium-n-stat d-module) was used to measure the open circuit potential (OCP) and perform cyclic voltammetry (CV) in 2 and 3-electrode configurations respectively. All measurements were performed with the sensor submerged in gastric acid simulant (Riddet Model) without pepsin following Ferrua and Singh's method [137]. The pH of the solutions tested were adjusted using low concentration HCl and NaOH gastric acid solutions. Five different solutions were prepared (pH 1.5, 3, 4.5, 7, 10) representing the acceptable range of pHs that would be experienced in the lower oesophagus via consumed food or drinks and gastric reflux events. A schematic of the experimental apparatus can be seen in Figure 20. Stability measurements were performed by leaving the sensor submerged in a pH 1.5 gastric acid solution for 12 hours and measuring the OCP at 1 second intervals.

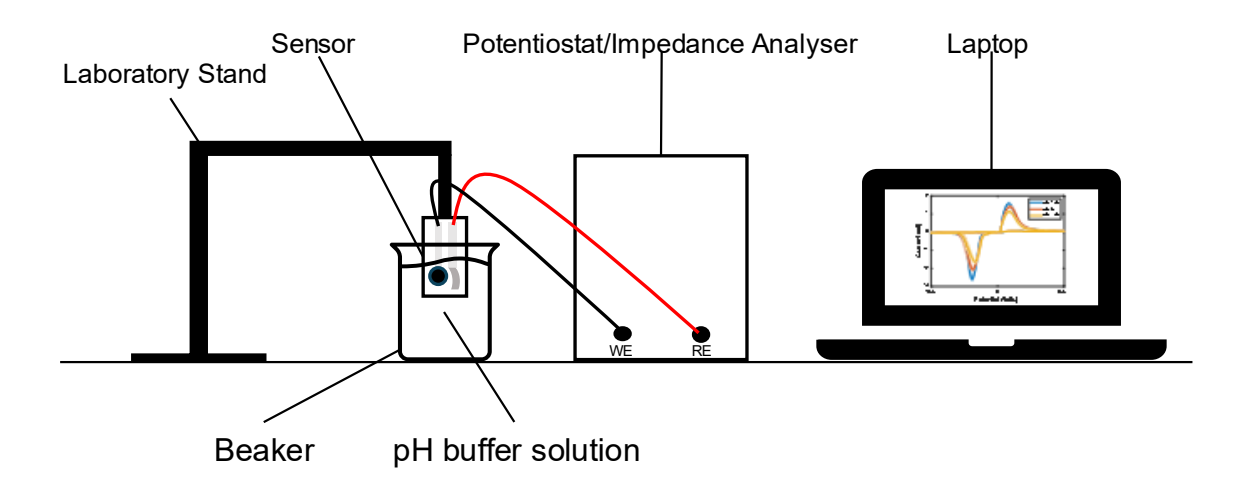


Figure 20: Schematic of the experimental apparatus used to measure response of the produced sensors.

2.2.2.5 Characterisation Techniques

To characterise the sensors, the Fourier-Transform Infrared (FTIR) spectra of the different working electrode materials were recorded using a (Spectrum Two™, Perkin Elmer) spectrophotometer in the region of 400 to 4000 cm⁻¹. The surface morphologies were imaged using scanning electron microscopy (SEM) (Carl Zeiss EVO25). Prior to SEM, the working electrode materials were applied on an aluminium thin sheet ~1mm using a nozzle used for printing. The sheet was then applied onto a metal stub with double-sided adhesive carbon tape and sputter coated with a thin gold film and was then observed at 3 kV voltage. Electrical measurements (impedance and series resistance) were performed before and after CV scans for comparison using an impedance analyser (Hioki IM3570). Microprobes were placed approximately 50 micrometres apart on the surface of the working electrode material and measurements were performed using a frequency sweep from 10⁴ to 5 x 10⁶ Hz.

2.2.3 Results and Discussion

2.2.3.1 FTIR Characterisation

The synthesised materials used for coating the working electrode were characterised by FT-IR spectroscopy shown in Figure 21. The FT-IR spectrum of GO shows peaks at 3189 cm⁻¹, 1719 cm⁻¹, 1582 cm⁻¹, 1048 cm⁻¹ and 580 cm⁻¹ indicating the presence of -OH, C=O, C=C, C-O, and O-H bonding respectively agreeing with literature [129]. The plasma treated GO shows the same peaks at similar locations indicating the continued presence of the bonds in pristine GO. The FT-IR spectrum of the GO, PU and Pluronic ® F-127 composite, shows the presence of bonds at 3322 cm⁻¹, 2933

cm⁻¹ and 2864 cm⁻¹, 1541 cm⁻¹, 1193 cm⁻¹ and 1139 cm⁻¹, indicating N-H, C-H, N-O, C-N bonds present in polyurethane respectively. C=O, O-H, C-O, and C=C bonds are still shown at 1693 cm⁻¹, 1048 cm⁻¹, 1256 cm⁻¹, and 929 cm⁻¹ respectively.

2.2.3.2 SEM Characterisation

SEM images of the pristine GO (Figure 22A, Figure 22C, Figure 22E) and oxygen plasma treated-GO (Figure 22B, Figure 22D, Figure 22F) show wrinkle formation and crumpled graphene sheets. No clear differences in structure can be spotted between the treated and untreated GO. SEM images of the GO composite (Figure 23) show increased texture present relative to the previous samples. Wrinkle and crumpled graphene structures are present along with smaller PU flakes scattered between and on top of the sheets. The surfactant and polymer combination lead to the formation of nanopores shown in Figure 23C.

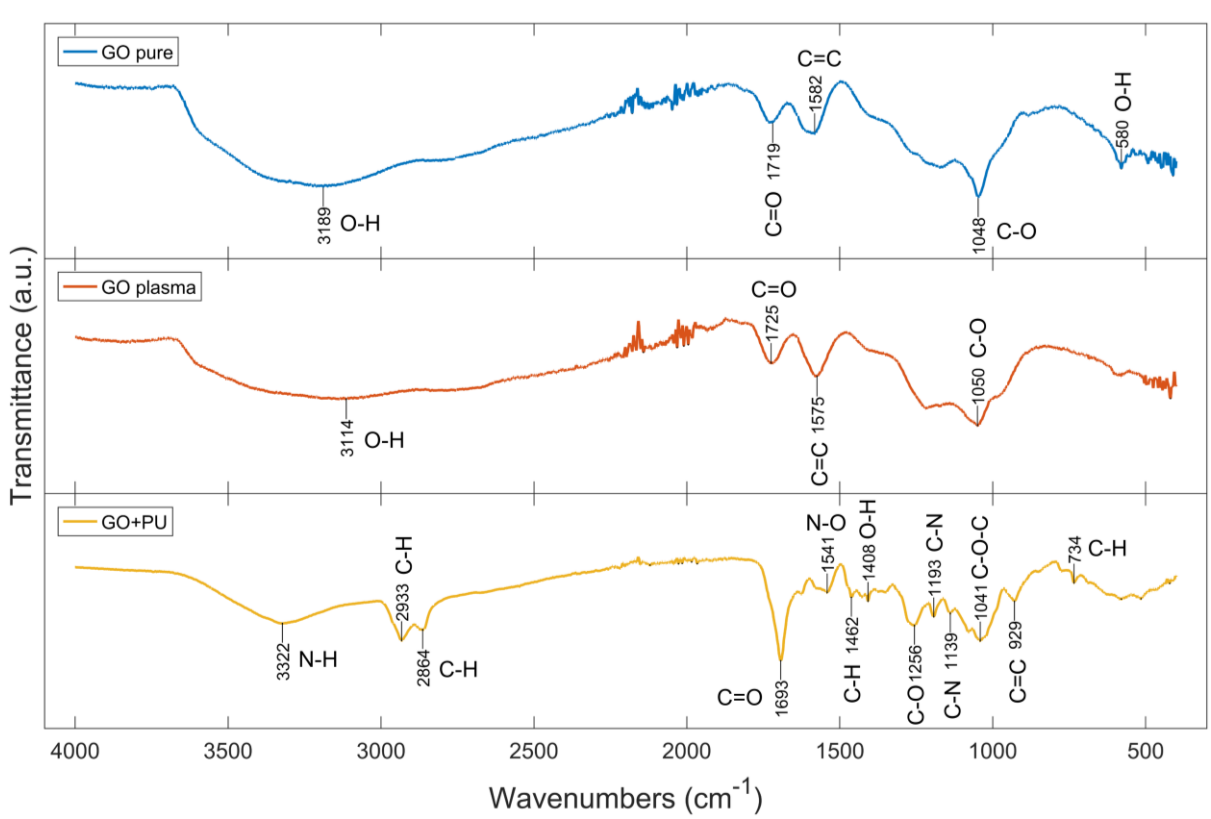
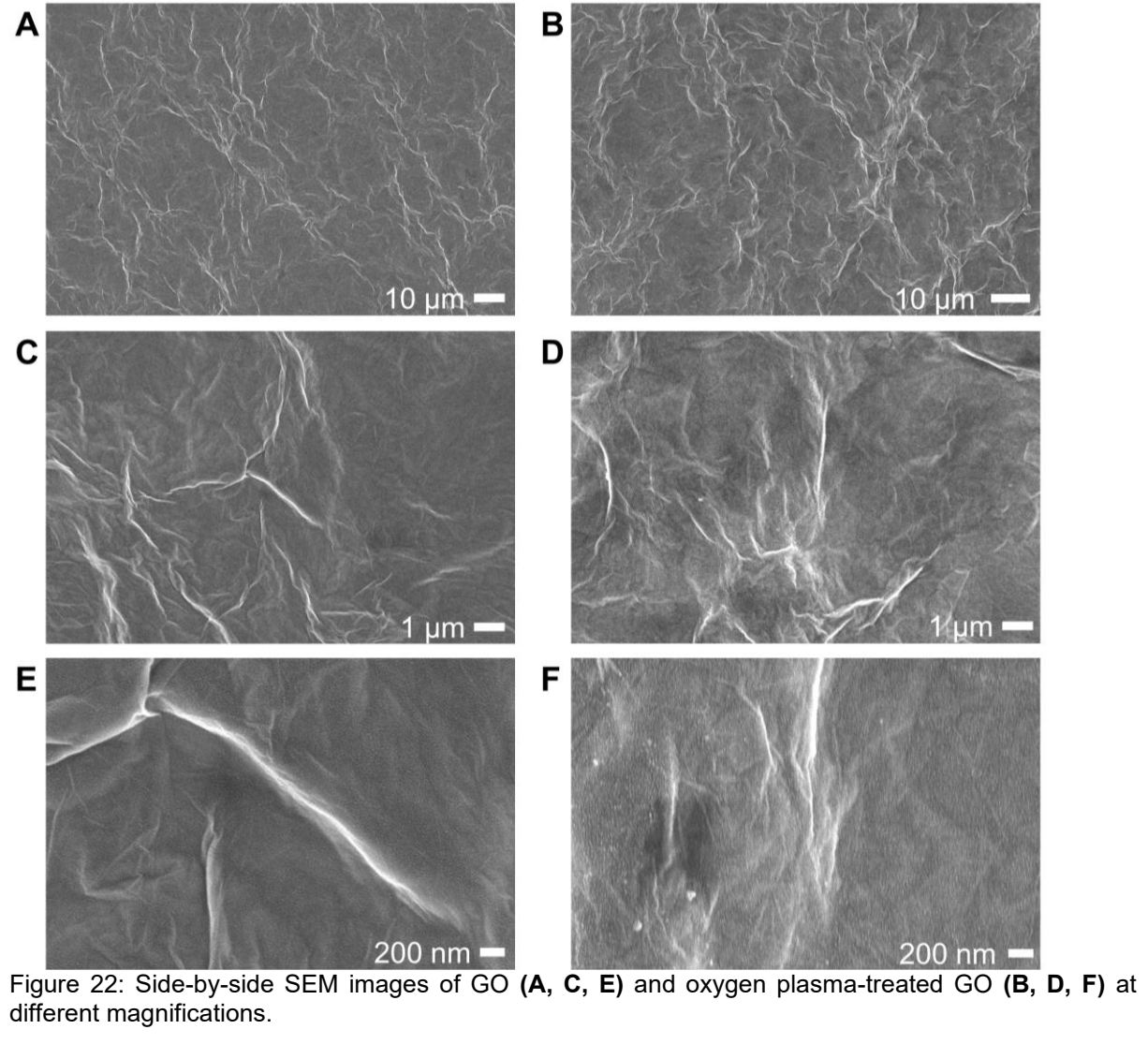


Figure 21: FT-IR spectra of pristine GO, oxygen plasma treated GO and GO, polyurethane (PU) and Pluronic ® F-127 composite.



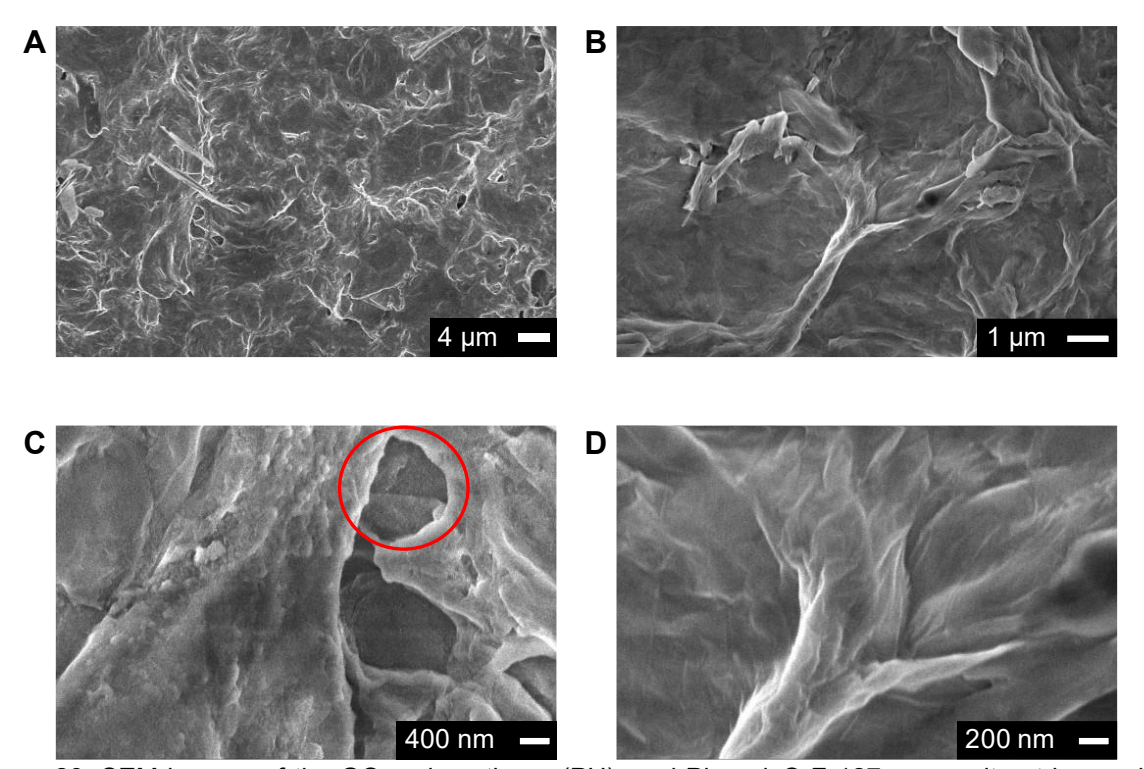


Figure 23: SEM images of the GO, polyurethane (PU), and Pluronic® F-127 composite at increasing magnifications: (A) 4 μ m scale bar, (B) 1 μ m scale bar, (C) 400 nm scale bar, and (D) 200 nm scale bar. The red circle in (C) highlights pore formation in the composite.

2.2.3.3 Electrochemical Measurements

CV scans of the pristine GO showed an asymmetrical peak shape, where the oxidation peak current did not reach the reduction peak current as shown in Figure 24A. This provides evidence that between CV scans, electrochemical reduction was occurring, changing the properties of the working electrode material. Furthermore, the asymmetry is further shown by the different oxidation peak voltage relative to the reductive peak voltage locations. On average, the reductive peak voltage occurred two times after the oxidative peak in the negative voltage in each pH solution, indicating irreversibility (Figure 24A). The peak current is directly proportional to the square root of the scan rate indicating a degree of reversibility (Figure 24E) however, there is a shift in the peak potential with the scan rate showing signs of irreversibility (Figure 24B). It is likely that the pure GO electrode behaves as a quasi-reversible system. A linear relationship can be seen between the oxidative peak voltage showing a sensitivity of -6.80 mV/pH with an R² value of 0.8887 (Figure 24C). There is also a linear relationship exhibited between the oxidative peak current and pH with a slope of -22.59 µA/pH and an R² value of 0.8651 (Figure 24D).

CV scans of the plasma-treated GO also exhibited asymmetrical peaks, with the oxidation peak current falling short of the reduction peak current, as illustrated in

Figure 25A. This suggests that electrochemical reduction was also likely occurring between scans, altering the working electrode material. The asymmetry is further indicated by the differing voltages of the oxidation and reduction peaks. Typically, the reduction peak appeared at around twice the negative potential after the oxidation peak in each pH solution, signalling irreversibility (Figure 25A). Although the peak current's proportionality to the square root of the scan rate suggests some reversibility (Figure 25E), the shift in peak potential with varying scan rates points to irreversibility (Figure 25B). Thus, the plasma-treated GO electrode likely functions as the pure GO in a quasi-reversible system. A linear relationship between the oxidation peak voltage and pH was observed, with a sensitivity of -6.92 mV/pH and an R² value of 0.8718 (Figure 25C). Similarly, the oxidative peak current also showed a linear relationship with pH, having a slightly higher slope of -26.64 μA/pH (relative to pristine GO) and an R² value of 0.8310 (Figure 25D). This increased peak current is likely due to the increased conductivity of the GO following plasma-treatment.

Figure 26 shows the CV results of the GO and PU composite. The scans show relatively increased symmetry in peak shapes with the peak potentials of the oxidative and reductive sweeps occurring at approximately the same locations, indicating increased reversibility (Figure 26A). Asymmetry, however, remains with the peak reductive current exceeding that of the peak oxidative current (Figure 26A). Figure 26B shows increased agreement between the scan rate and the and the peak potential, with the same proportionality between the peak current to the square root of the scan rate (Figure 26E). shown indicating a degree of reversibility. The composite showed increased pH sensitivity in with peak potential (Figure 26C) and increased sensitivity to current (Figure 26D) despite being less conductive than the pristine GO and plasma-treated GO samples. The composite had a sensitivity of approximately - 9.16 mV/pH with an increased R^2 value of 0.9273. Notably, the error bars indicate decreased variability between the scans. The composite had a -44.39 μ A/pH sensitivity with a high R^2 value of 0.9384 (Figure 26D).

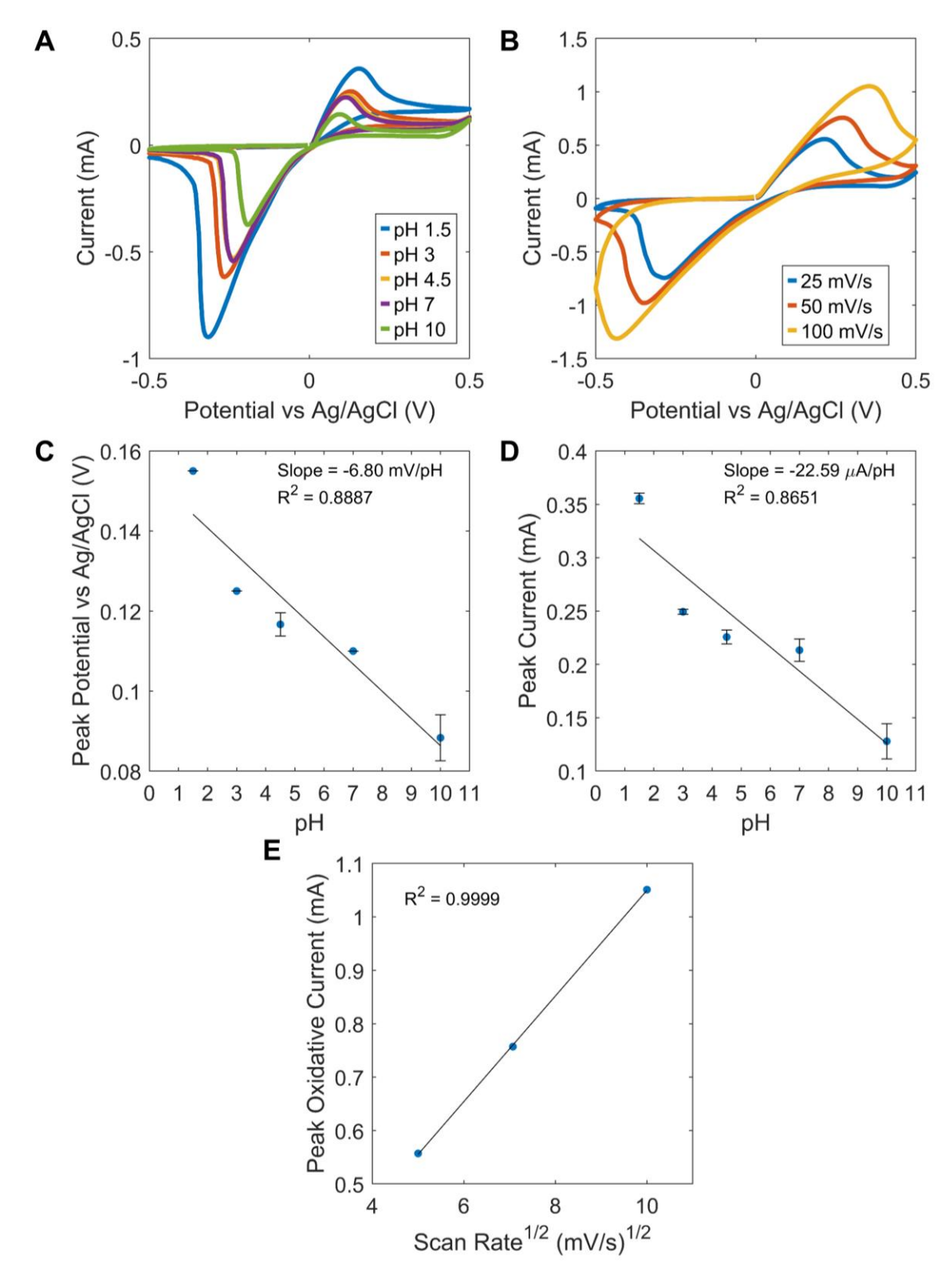


Figure 24: Pristine GO CV results and analysis: (A) CV scans at 5 mV/s in different gastric acid pH solutions, (B) CV at different scan rates in pH 1.5 solution. (C) Mean peak potential vs Ag/AgCl dependence on pH solution. (D) Mean peak current dependence on pH. (E) Peak oxidative current dependence on square root of scan rate.

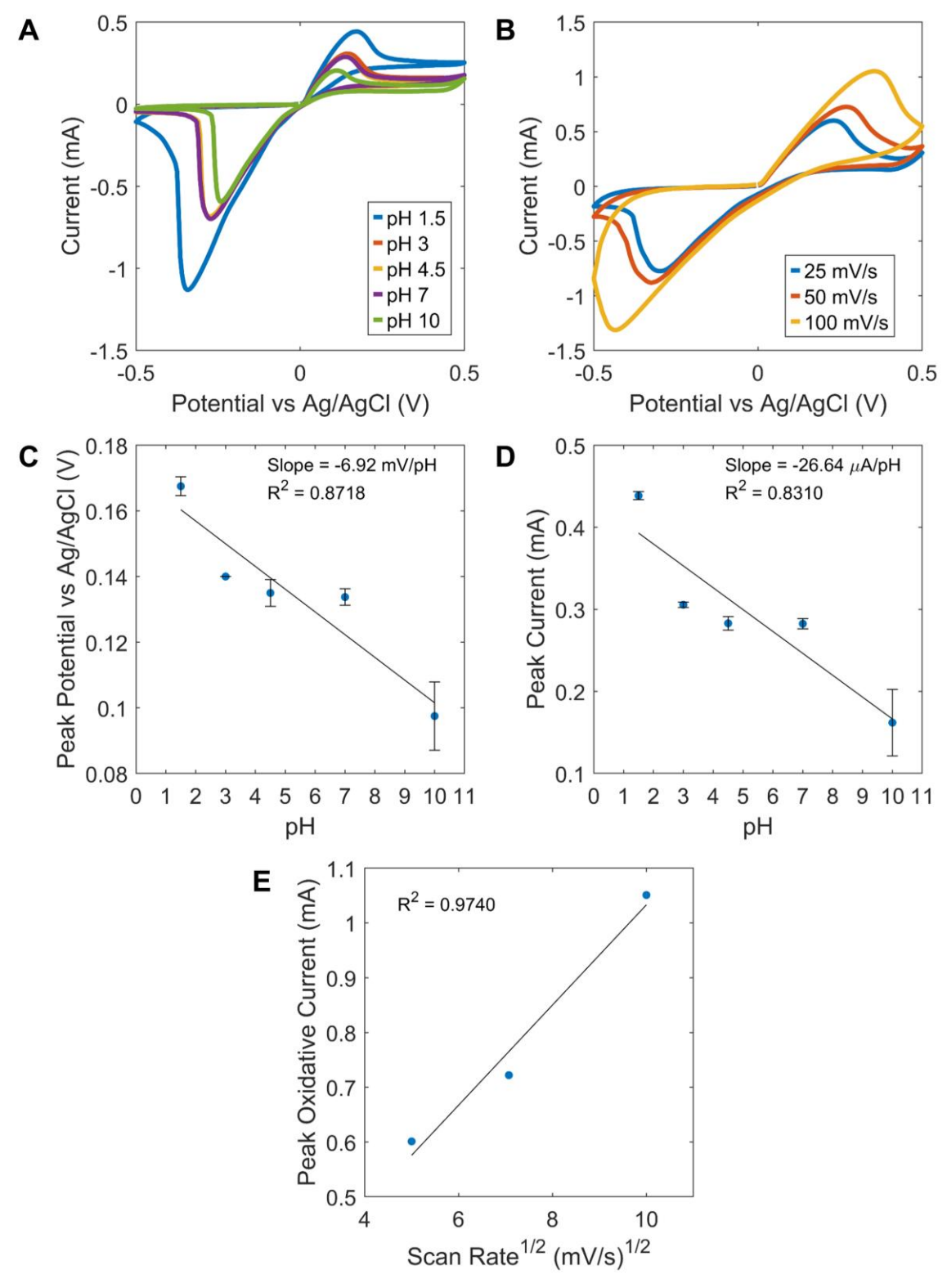


Figure 25: Plasma treated GO CV results and analysis: (A) CV scans at 5 mV/s in different gastric acid pH solutions, (B) CV at different scan rates in pH 1.5 solution. (C) Mean peak potential vs Ag/AgCl dependence on pH solution. (D) Mean peak current dependence on pH. (E) Peak oxidative current dependence on square root of scan rate.

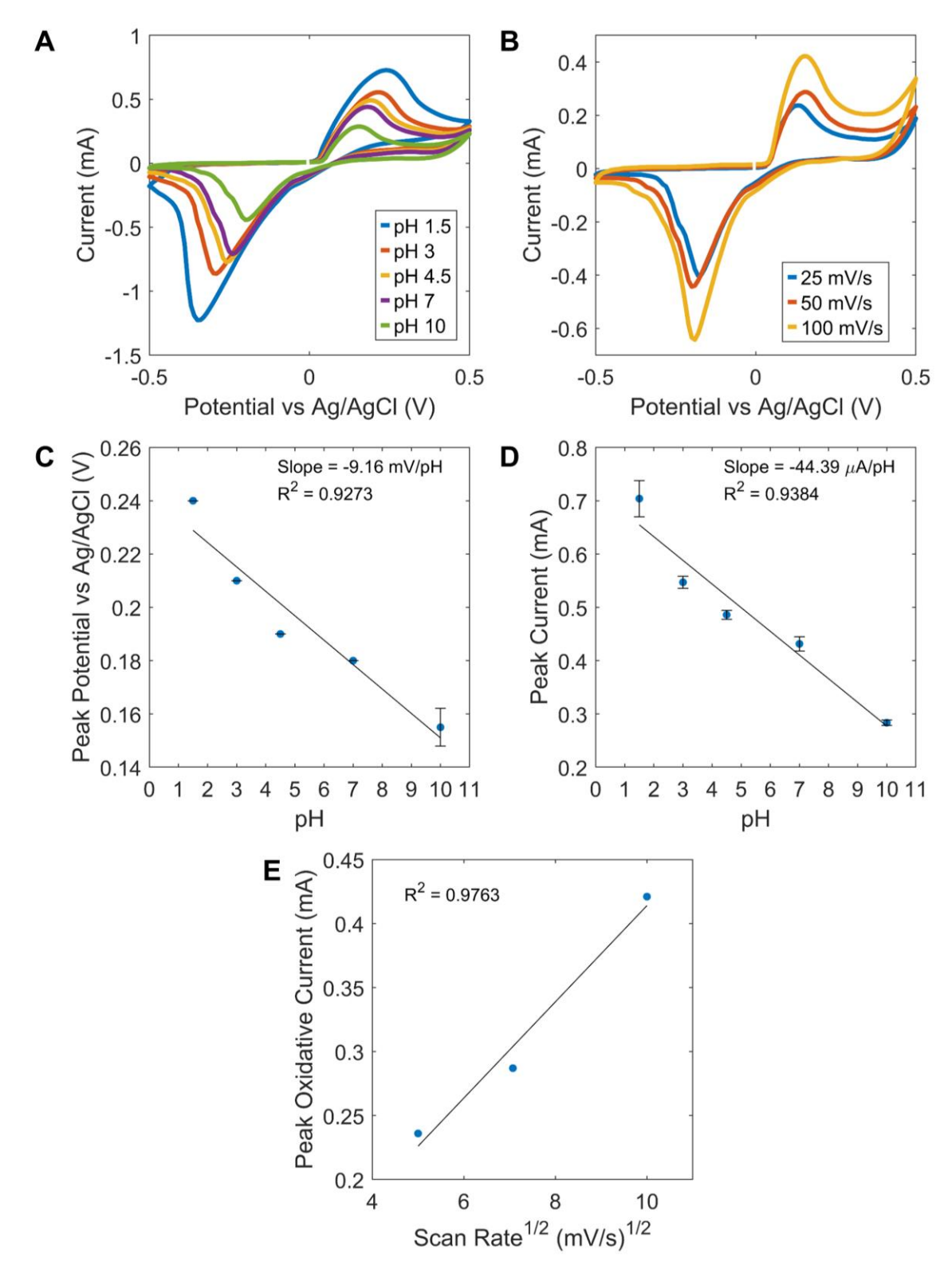


Figure 26: GO and Polyurethane composite (CV) results and analysis: **(A)** CV scans at 50 mV/s in different gastric acid pH solutions, **(B)** CV at different scan rates in pH 10 solution. **(C)** Mean peak potential vs Ag/AgCl dependence on pH solution. **(D)** Mean peak current dependence on pH. **(E)** Peak oxidative current dependence on square root of scan rate.

The OCP of the different working electrodes was also measured with the results shown in Figure 27. Open circuit potential reflects the static state of the system providing

information about the stability of the readings and since negligible currents are used for measurement, no electrochemical reduction or oxidation processes are done. This caused the pH sensitivity in terms of mV/pH to increase, agreeing with values shown in literature. An example of pristine GO with a sensitivity of -21.29 mV/pH is shown (Figure 27A). No improvement in sensitivity could be seen in the plasma treated GO, and there was increased disparity between the increasing and decreasing pH OCP values (Figure 27B). Improved sensitivity was exhibited with the composite, reaching a mean value of -31.75 mV/pH with a higher average R² value (Figure 27D). The R² values are similar to the CV scans, shown in Figure 24-Figure 26, however it can be seen that following exposure to pH 1.5 and pH 10 gastric acid solutions, there is a deviation from the linear relationship. This is particularly prevalent with the plasmatreated GO sample (Figure 27B).

Further analysis was performed to understand the lack of agreement between the CV sensitivity values and the OCP sensitivity by analysing the change in electrical properties with an impedance analyser (Figure 28). It can be seen that prior to the CV scans, the pure GO sample had higher impedance and series resistance values than following the scans (Figure 28A-B). The GO and PU composite had similar impedance results but an increase in the series resistance is exhibited following the CV scans (Figure 28C-D).

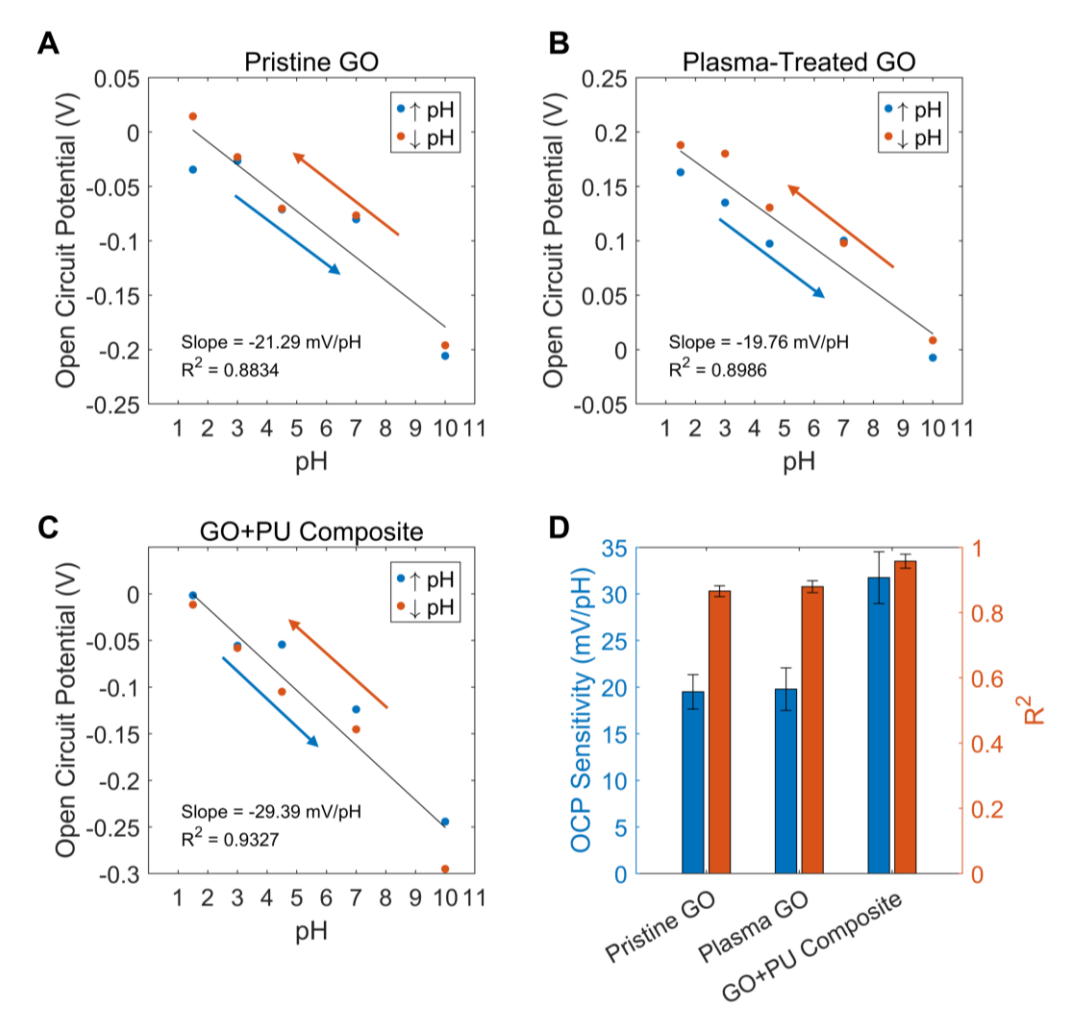


Figure 27: OCP vs pH measurements of representative examples of the three sensor types: **(A)** pristine GO, **(B)** plasma-treated GO, and **(C)** GO+PU composite. **(D)** Variability among three samples of the produced sensors comparing the OCP sensitivity and the R² value.

It is likely that two phenomena occurred during the CV scans on the working electrodes, firstly, electrochemical reduction was occurring on the GO and plasmatreated GO samples leading to an increase in conductivity and a loss of functional groups. This contributed to the lower sensitivity of the two measurement techniques. Secondly, adsorption of the NaCl ions from the gastric acid simulant solution counteracted the reduction while reducing sensitivity. This ion adsorption also explains the asymmetric shape of the CV curves in Figure 24–Figure 26, as surface-bound ions can distort capacitive currents and shift anodic/cathodic symmetry without indicating full irreversibility. The GO+PU composite, having a lower concentration of GO, and being intrinsically less conductive due to the inclusion of a non-conducting polyurethane adhesion-promoting polymer, was more affected by the adsorption causing an increase in resistance following the CV scans.

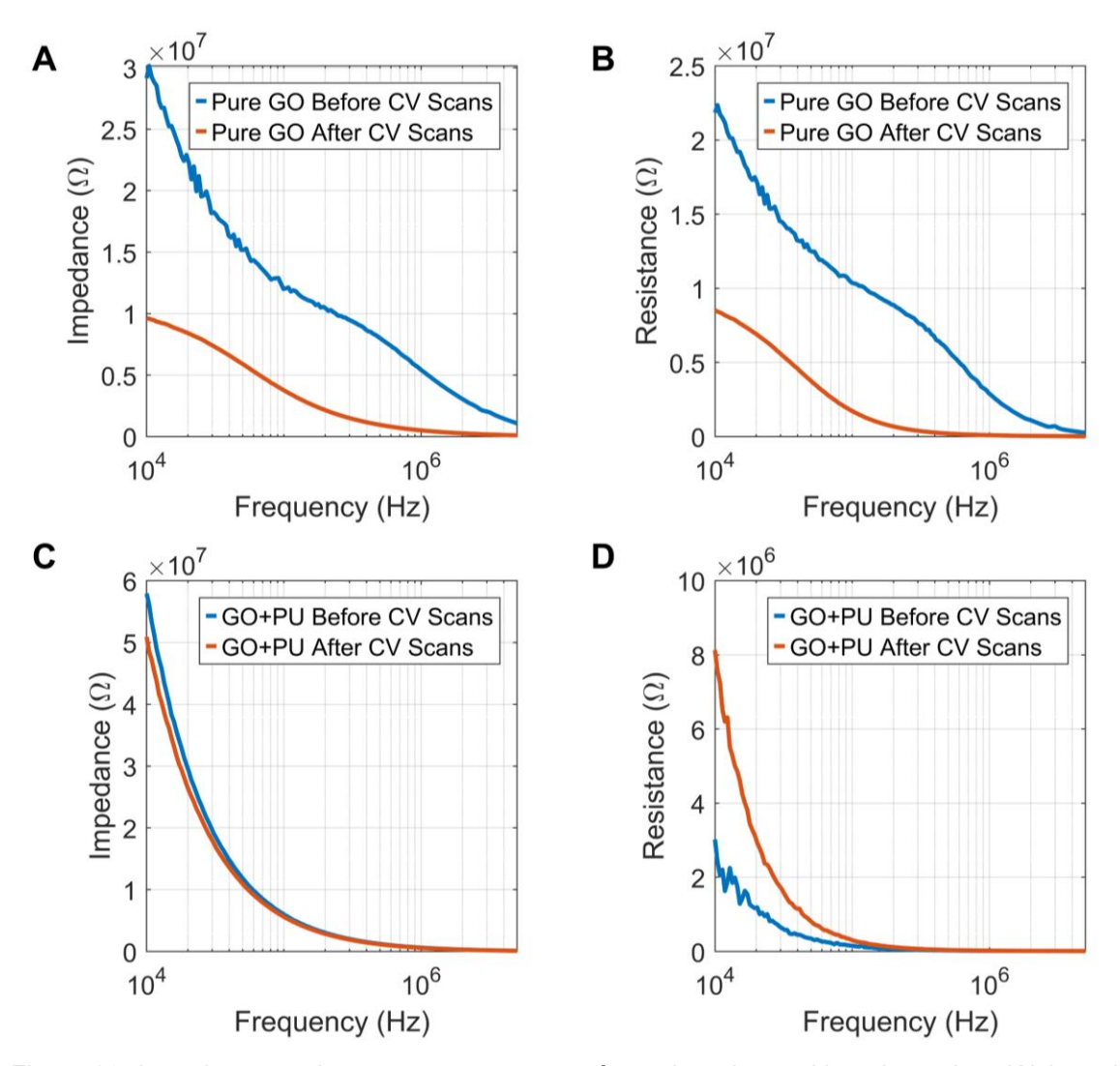


Figure 28: Impedance analyser measurements performed on the working electrodes. (A) impedance and (B) series resistance measurements on the pure/pristine GO WE. (C) Impedance and (D) series resistance measurements on the GO and PU composite WE.

It could be seen visually that the GO and GO-plasma sensors would degrade following both CV and OCP tests, with a loss of nanosheets from the bulk material (Figure 29). This likely caused a decrease in the sensitivity due to the change in the physical properties of the sensor. The polyurethane and GO composite, shown by the SEM images, would sandwich between GO flakes causing less loss of material during the tests and increasing the stability of the sensor particularly in acidic mediums. The decreased flake size that occurred during the synthesis of the composite ink, likely lead to increased surface area and active sites concentration where protonation and deprotonation can occur. This is further confirmed by the FTIR scans where an increased variety of oxygen functional groups are shown. The printing improvements

had a qualitatively stark effect on the quality of the electrodes and their robustness upon subjection to mechanical deformation with a decreased presence of macrocracks.

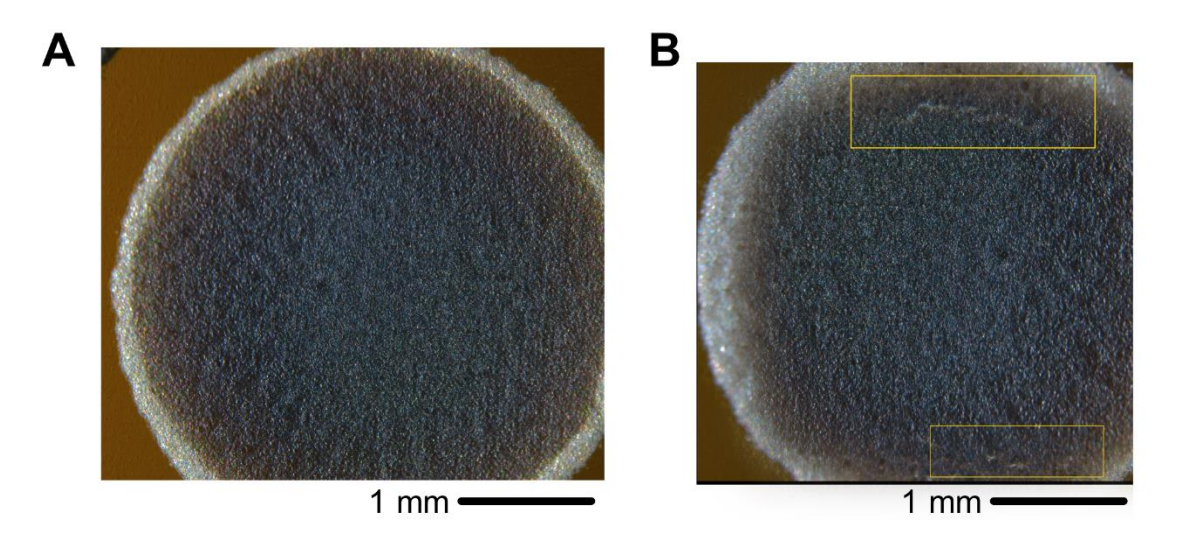


Figure 29: **(A)** Representative example of GO covered working electrode prior to pH sensitivity testing. **(B)** Representative example of GO following pH testing with yellow boxes showing loss of material from silver substrate.

Figure 30 compares the OCP between two unused GO and GO+PU sensors to check for stability in pH 1.5 gastric acid solution. There is a stark improvement in the overall stability of the sensor with a standard deviation of only 3.15 mV observed in 6 hours of testing. Moreover, the pristine GO exhibited more pronounced periodic oscillations compared to the more stable GO+PU composite.

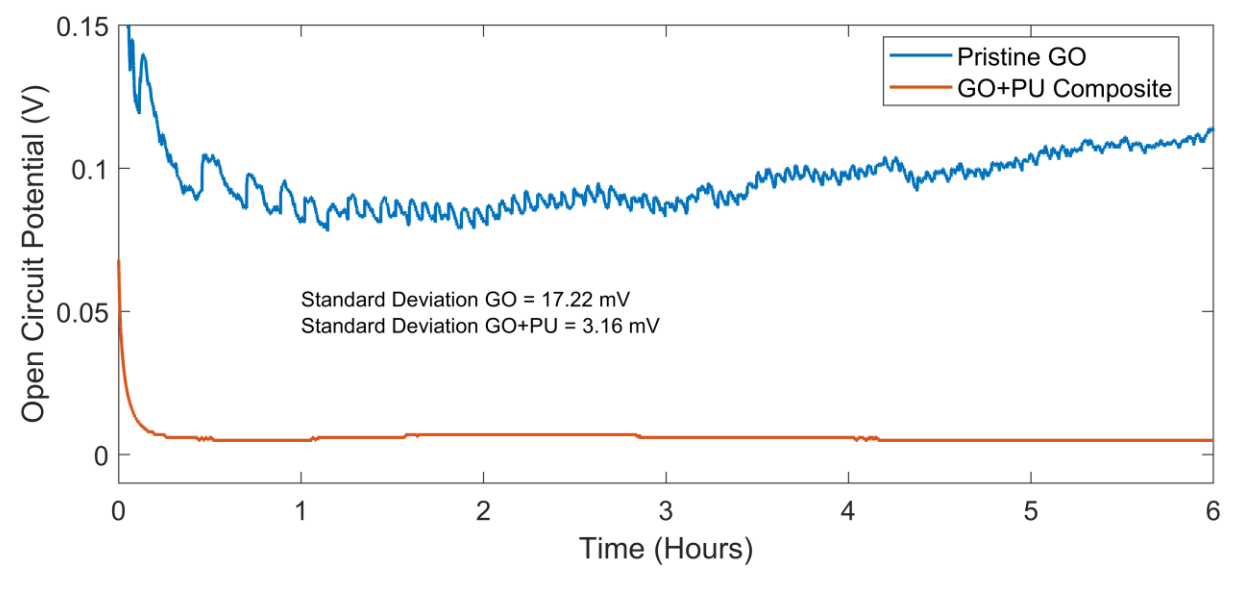


Figure 30: Comparison of open circuit potential stability of the pristine GO and the GO+Polyurethane composite in pH 1.5 solution.

2.2.4 Conclusion

This study aimed to evaluate GO-based electrodes as electrochemically sensitive materials for monitoring acid reflux, with a specific focus on pristine GO, plasmatreated GO, and a GO-polyurethane composite. The investigation sought to address key challenges exhibited in this environment, including sensor stability, sensitivity, and reproducibility, while laying the groundwork for practical and scalable fabrication methods. The performance of each material was assessed using CV and OCP measurements. The results highlighted several key findings and opportunities for improvement, shaping the foundation for future iterations of this technology.

Pristine GO in literature has a high variability in its pH sensitivity, which is strongly linked to the method of preparation and the specific oxygen functional groups present on the surface. The presence of these functional groups on the GO sheet is central to its electrochemical activity, as these groups serve as active sites for protonation and deprotonation reactions. However, the synthesis process and subsequent handling can significantly alter the density and distribution of these functional groups. This variability led to inconsistent pH response across pristine GO samples, which posed a challenge for reproducibility.

To address these issues, plasma treatment was explored as a means of increasing the functional group density, particularly oxygen-containing groups, on the GO surface. Oxygen plasma treatment introduces additional groups, such as hydroxyl and carboxyl, through surface oxidation, with the aim of improving the material's proton sensitivity and overall electrochemical performance [131]. However, the study revealed that while plasma treatment may have initially increased the density of oxygen functional groups, these groups were not stable under prolonged exposure to acidic environments [131]. In gastric acid simulant solutions, the plasma-treated GO exhibited comparable performance to pristine GO, as the added oxygen groups were rapidly reduced or detached. This aligns with literature, as FTIR has confirmed the disappearance of carbonyl groups following CV scans as shown in [138]. This degradation not only diminished the material's sensitivity but also weakened its adhesion to the electrode surface, further contributing to signal drift. These findings underscored the inherent limitations of both pristine and plasma-treated GO for applications requiring prolonged stability in harsh conditions.

Recognising these limitations, a GO-polyurethane composite was developed to improve stability and performance. The incorporation of polyurethane acted as a binding agent, promoting adhesion between GO flakes and preventing their detachment during testing. This structural reinforcement significantly improved the composite's durability in gastric acid simulants, allowing it to maintain functionality for longer durations compared to pristine or plasma-treated GO. Furthermore, the polyurethane matrix facilitated the formation of micro-pores between GO flakes, effectively increasing the surface area available for electrochemical interactions. This enhancement improved the composite's sensitivity to pH changes by providing more active sites for protonation and deprotonation reactions, even as it reduced the material's overall conductivity. These findings highlight the value of polymer-based composites in addressing the limitations of standalone GO for electrochemical sensing applications.

Another major advancement was the optimisation of the sensor fabrication process through direct-write printing techniques. Variability in sensitivity measurements was a recurring challenge in the early stages of this research, partly due to inconsistencies in the deposition and curing of GO-based inks. By implementing direct-write printing, the precise deposition of GO-polyurethane inks onto flexible substrates was achieved, leading to greater uniformity and reduced variability in the electrochemical response. This consistency was reflected in the low standard deviation observed across multiple sensors, demonstrating the reliability of the fabrication method. Additionally, the use of flexible substrates aligned with the principles of mucosa-interfacing electronics, ensuring that the sensors could conform to the dynamic environment of the oesophageal mucosa.

Despite these advancements, the study also revealed critical challenges associated with GO-based materials. Both pristine GO and the GO-polyurethane composite exhibited degradation over time under acidic conditions, driven by the reduction of oxygen functional groups. This degradation weakened the material's adhesion to the working electrode and reduced the availability of active sites, directly impacting pH sensitivity. Furthermore, while the GO-polyurethane composite mitigated some of these issues, it did not fully eliminate the problems of material reduction and signal drift, indicating a need for further innovation in material design.

In conclusion, this study demonstrated the potential of GO-based electrodes for acid reflux monitoring, while identifying key limitations that must be addressed to realise their full potential. Variability in GO's sensitivity, influenced by preparation methods and functional group stability, emerged as a critical challenge. Plasma treatment offered an initial improvement but proved insufficient for maintaining performance in acidic conditions. The development of the GO-polyurethane composite marked a significant step forward, providing enhanced stability and sensitivity compared to pristine GO. Additionally, the adoption of direct-write printing improved fabrication consistency, paving the way for scalable and reproducible sensor production. However, challenges related to long-term stability and degradation remain significant barriers. Future research should focus on refining GO-based composites, and potentially exploring advanced materials with more stable functional groups, and further optimising fabrication methods to develop robust, reliable, and clinically viable sensors for GORD diagnosis.

Chapter 3: Covalent Organic Frameworks for Electrochemical Sensing

3.1 Background and Literature Review

3.1.1 History of Covalent Organic Frameworks

Covalent Organic Frameworks (COFs) are an emerging category of materials initially utilised primarily for gas adsorption and storage [139]. However, they have recently gained attention for their potential in catalysis, ultrasensitive sensors, optoelectronics, and various other applications. COFs have been explored as atomically, they are organised into precise organic subunits into two or three dimensional crystalline structures which can allow for advantageous properties such as radical increases in specific surface area [139,140]. Specific surface area increases coupled with control of functional groups present in the material provide significant opportunities for pH sensing, increasing range, stability and sensitivity. Synthesis of COFs requires precise control of conditions to facilitate bond formation and the study of this is known as reticular chemistry [141].

Reticular chemistry is used to describe how discrete chemical entities are linked in space to make extended structures with strong bonds and how it can be done in a controlled fashion [142]. The linking of larger structures allows for the tuning of chemical and physical properties of materials to suit a particular application, effectively adding properties that were previously inaccessible without linking [142]. The foundation of this type of chemistry begun with coordination chemistry, largely pioneered by Werner Complexes. Alfred Werner was able to determine the correct geometry of CoCl₃. NH₃ complexes which was previously incorrectly predicted by the constant valence model. Once a more precise model of geometries could be predicted, Karl A. Hofmann, was able to extend this chemistry into higher dimensions with his formation of Hofmann Clathrates in 1897 [142]. Hoffmann Clathrates are extended 2D crystallised structures comprising of multiple layers; these layers trap or contain molecules within them, often fully encapsulating them in the form of a lattice. The trapped molecules are known as guest molecules, and can be solvents such as benzene, aniline, and pyrrole [142]. The guest molecules serve as templates to form clathrate structures. Upon removal of guest molecules however, the structural collapse of Hofmann clathrates was quite common., which led to the exploration of more robust and versatile frameworks [142].

Reticular chemistry begun when metal ions were linked through strong bonds with organic linkers to create metal-organic frameworks, commonly known as MOFs. MOFs comprise of polynuclear metal clusters bonded to organic linkers and make porous crystalline structures that do not collapse upon the removal of solvents [142]. This was first demonstrated in 1998 when MOF-2 demonstrated proof of permanent microporosity with nitrogen gas adsorption at 77K. This permanent porosity provides increased specific surface area which can significantly increase the surface area, and active sites crucial for electrochemical sensors.

3.1.2 COF Synthesis

In 2005, Arien Côté, Omar Yaghi, and colleagues at the University of California, Berkeley, reported the organic counterparts of MOFs, known as covalent organic frameworks (COFs) [140,141]. COFs are similarly nanoporous materials which are constructed by linking organic molecular building units covalently to form crystalline porous polymer structures [140,141]. There are several types of linkages used to stitch together the molecular building blocks and dependent on the design chosen, these can be categorised into 2-D and 3-D types [140]. The development of COFs would not have been possible without contributions from coordination chemistry, dynamic bond formation, topochemical polymerisation, supramolecular assembly and advanced characterisation of nanostructured material techniques [143].

The formation of COFs was a breakthrough as they have separate challenges to MOFs, largely because for extended structures to form in the pure phase, in a controlled fashion, crystallisation must occur [140,141]. It is largely accepted that crystallisation only occurs when microscopic reversibility, i.e. the formation and deformation of covalent bonds reversibly, can be achieved. The practices of dynamic covalent chemistry (DCC) lead to the formation of bonds which can be formed, broken and reformed by controlling conditions thermodynamically [140]. DCC thus allows for reversible systems which can help ensure that a COF product is thermodynamically stable and has an ordered structure [140].

Another requirement for the formation of COFs is that during the thermodynamically-controlled bond formation process, the organic building blocks must not be destroyed or have their geometry altered [141]. Therefore, COFs should not be formed under extreme pressures or temperatures to avoid compromising the integrity of the building blocks. Therefore, the DCC must be carefully chosen to account for this. On top of

this, the reversible nature of the DCC reactions does not guarantee structural order that constructs the regular pores of COF materials [139]. COF synthesis requires features such as rigidity in structure, symmetric multi-connectivity and suitable synthetic conditions [139]. Long reaction times typically allow for better error correction, increased crystallisation, and precise control of the concentration of reactants and catalysts required in order to obtain crystalline materials [139]. The majority of COF synthesis occurs using condensation reactions where the building blocks interact with each other via functional group present to form extended network structures [139].

Schiff-base reactions are one of the few reactions that fulfil the abovementioned criteria for the formation of thermodynamically stable structures [139]. They are also one of the most employed techniques of DCC as they are reversible and stable at neutral pHs and consequently have been commonly used for synthesising COFs [141]. Schiff-base chemistry typically occurs in 4 stages. Initially, the Schiff-base reaction is initiated by the protonation of a carbonyl group, such as an aldehyde or a ketone, to make the carbon atom in the functional group more electrophilic (resulting in a C=N double bond) [141]. Secondly, the amine group (also known as a nucleophile) attacks the carbonyl carbon to form an unstable intermediate compound known as a carbinolamine

[141]. Thirdly, intramolecular proton transfer occurs within the carbinolamine and finally, as water is removed from this intermediate, a Schiff base is formed, such as imines, hydrazones, squaraines, β -ketoenamines, benzoxazoles, and phenazines [141].

Other synthetic procedures have also been used to synthesise COFs and are briefly explained in the following sections.

3.1.2.1 Solvothermal Methods

Solvothermal methods are the most used COF synthesis techniques and are highly dependent on the building blocks, reaction time, temperature, solvent conditions and catalyst concentrations [144]. This synthesis method notably allows COF preparation on a larger scale [144]. The process generally begins by mixing monomers, catalysts and solvents together in a Pyrex tube and sonicating for even dispersion. This is then followed by freeze-pump-thaw cycles for degassing purposes, and then sealing with a

gas burner. The tube is then kept in an oven for a certain period for the COF formation to occur [144]. The tube is allowed to cool to room temperature and is typically washed with a low/ultra-low surface tension solvent [144]. This step is known as COF activation which is used to remove adsorbed solvent and impurities from the COF while avoiding the collapse of the porous structure to ensure the presence of accessible surface areas [145]. This is particularly important for more fragile COFs as shown in Figure 31.

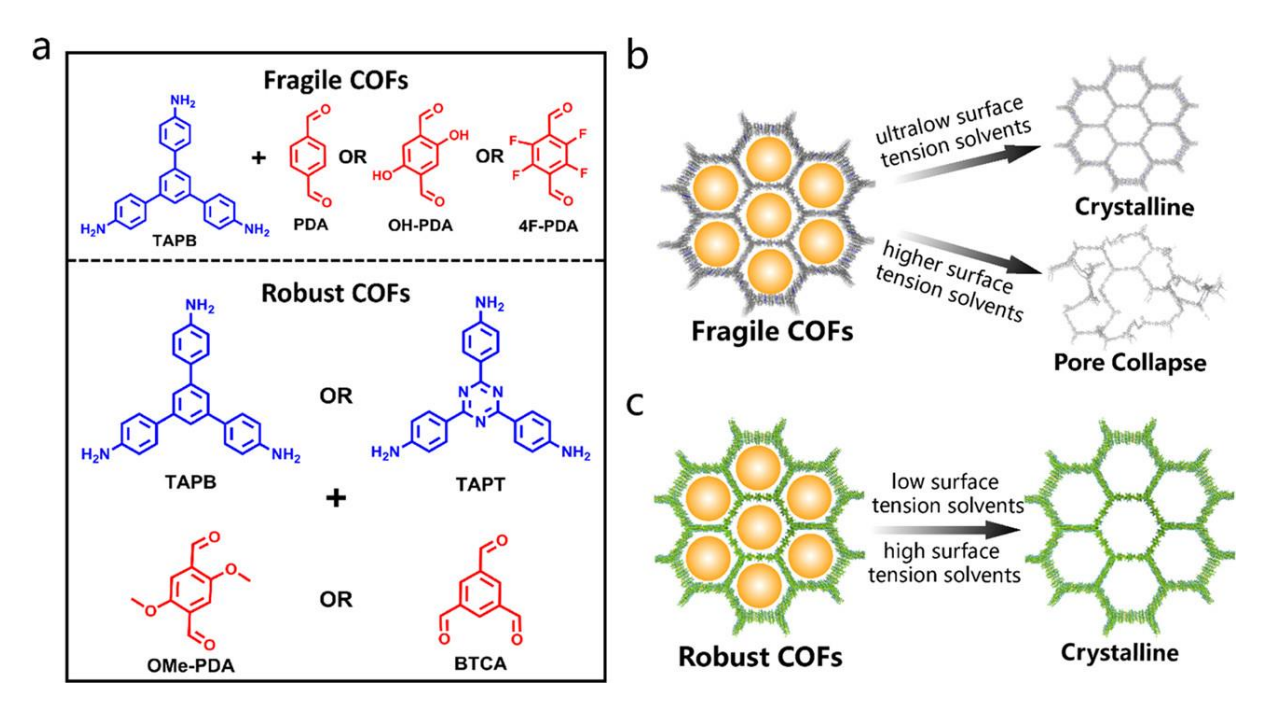


Figure 31: COF activation with ultralow surface tension solvents removes impurities from the COF and results in higher accessible surface area. Adopted with permission of the rights holder from [145].

3.1.2.2 Ionothermal Synthesis

lonothermal synthesis employs ionic liquids as both solvents and reactants for COF synthesis. Ionic liquids solvents are typically defined as organic salts that have low melting points and are comprised of ions in the liquid phase[144,146]. In literature, researchers also define ionic liquids not only as salts that are fluid at near-ambient temperatures (less than ~100 °C) but also any salt that melts below the temperature used in the synthesis of zeolites (150-200 °C), another naturally occurring crystalline porous material [146]. Molten zinc chloride salt is commonly used for creating crystalline porous polytriazines, a subset of COFs, as they show strong Lewis acid-base interactions, and acts as a catalyst for trimerization reaction [147]. A typical synthesis process involves sealing and evacuating the monomer and molten zinc chloride in a Pyrex ampule and heating to 400 °C for 40 hours [144]. The mixture is allowed to cool, grounded to a powder, and thoroughly washed to remove zinc

chloride. To remove the remaining zinc chloride, the powder is put under stirring in a diluted HCl solution for 15 hours before being collected using filtration, washing with water and THF and drying under vacuum [144]. The resulting material presents a sheetlike structure that resembles COF-1 introduced by Côte, Yaghi, et al. [140,141].

3.1.2.3 Room-temperature Synthesis

Room temperature synthesis of COFs is desirable due to its simplicity, easy control, and processability when using fragile building blocks or sensitive substrates [144,148]. Several types of room-temperature synthesis have been shown, for example, Zhang et al. prepared COF nanobars using water containing dissolved CO₂ [149]. Yu et al. synthesised nanoflower morphological HFH-COF using a facile room temperature method which resulted in much higher crystallinity than previous room-temperature synthesis techniques [148]. The synthesis processes differ greatly and can use any of, dissolved gases, vapour-assistance, water-tolerant Lewis acids, etc. for COF formation under ambient pressures and temperatures. The time for synthesis also varies from as short as 10 mins [150] to several days [151] depending on the building blocks and technique used for COF formation.

3.1.2.4 Mechanochemical Synthesis

Mechanochemical synthesis uses mechanical force to drive chemical reactions typically without the need for large quantities of solvents [144,152]. Literature also describes it as a grinding method as the monomers are typically placed in a mortar along with a few drops of a catalyst solvent such as methanol and grinded for approximately 30 minutes allowing for delamination to occur [144,152]. Delamination refers to the separation of layers of COFs such that more reactive sites and surface area can be exposed. Powders that were dispersed in methanol, following TEM imaging, show 100 nm to 1 μm thin graphene-like sheets [152]. Mechanochemical synthesis is considered an environmentally friendly, efficient, and rapid technique and has been used to synthesise COFs such as TpPa-1, TpPa-2, TpPa-NO₂, etc. [144].

3.1.2.5 Interfacial Synthesis

Interfacial methods for COF synthesis are inspired by classic interfacial polymerisation chemistry techniques and allows for well-controlled fabrication of large COF membranes/sheets with high crystallinity and ordered, directional pores [153]. An interface is classified as the phase boundary between two different matters or two different phases of one matter and can range from several angstroms to even

micrometre in size [154]. Naturally, interfacial synthesis can be split into many subtypes, solid/gas, solid/liquid, and liquid/liquid interfacial synthesis.

Gas/solid and liquid/solid interfaces require conditions such as a low density of nuclei, a high diffusion rate and mobility of monomers and a low polymerisation rate for the formation of highly-ordered structures on the solid interface [154]. Experimentally, gas/liquid COFs result in extremely smooth ordered functions with a root-mean-square roughness of about 3 Angstroms. Langmuir-Blodgett is a typical fabrication process used to prepare ultrathin films utilising the gas/solid interface. Zhang et al used this method to prepare a millimetre sized two-dimensional imine-linked covalent organic monolayer [155].

Banarjee's group famously developed a bottom-up interfacial crystallisation technique to fabricate microcrystalline powders as large-scale thin films under ambient conditions using the liquid-liquid approach [156]. In their work they were able to generate highly crystalline COF thin films with thicknesses from ~50-200 nm using the water-dichloromethane interface. Liquid interfacial regions offer a 2D confined space for the lateral mobility of the monomers which allows for the growth of large 2-D structures whilst solid substrates have fixed grain boundaries which generally lead to smaller ordered networks on the surfaces [154].

3.1.2.6 Microwave-Assisted Synthesis

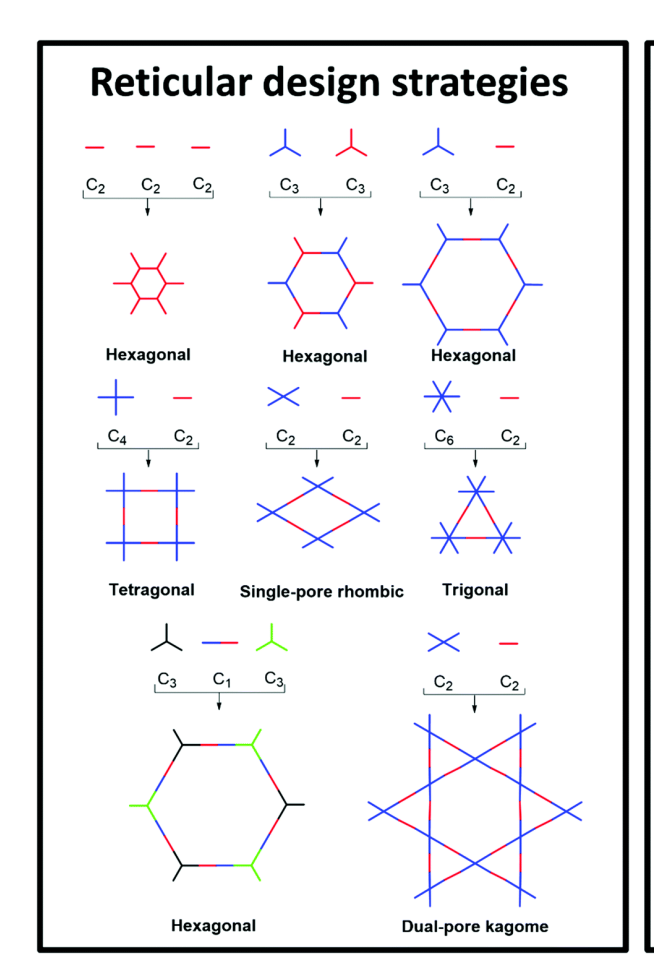
Microwave-assisted synthesis has been used in organic chemistry since 1986 since it can save time, increase yield, and crystallinity [157]. For COF synthesis particularly, higher surface area has been reported when using a microwave [157]. Other advantages of using microwaves come from the energy efficiency as the heat is generated directly within the material in a much faster and more temperature-homogenous way than conventional convection heating techniques [157]. Microwaves used in organic syntheses are characterised by higher synthesis rate, shorter reaction times, homogenous products, higher reproducibility, better properties, higher yields, easier scale-up, lower power consumption, and selective heating. Microwaves have been used to create most major COFs such as boronate ester, imines-, enamines-, azines-, and triazines-based COFs. The drawbacks of this synthesis technique are the need for expensive, specialised equipment and insufficient descriptions of procedures for microwave synthesis.

3.1.3 Advantages of COFs for Chemical Detection

3.1.3.1 Structure Tunability

COFs are highly tuneable, not only in the functional groups present, but also in the structure which affects properties such as pore size, spatial distribution and dimensions [158]. Reticular synthesis of COFs is carried out in five stages [159].

- 1. Selection of a framework topology.
- Vertices evaluation: the precise idealised geometry of the vertices is identified.
 To construct the selected framework, the topologies must be deconstructed into their underlying geometric units.
- 3. Identification of molecular compounds which fit the desired geometry.
- 4. Crystallisation of COF via linkages.
- 5. Characterisation of COFs by crystallographic techniques to confirm geometry formation.



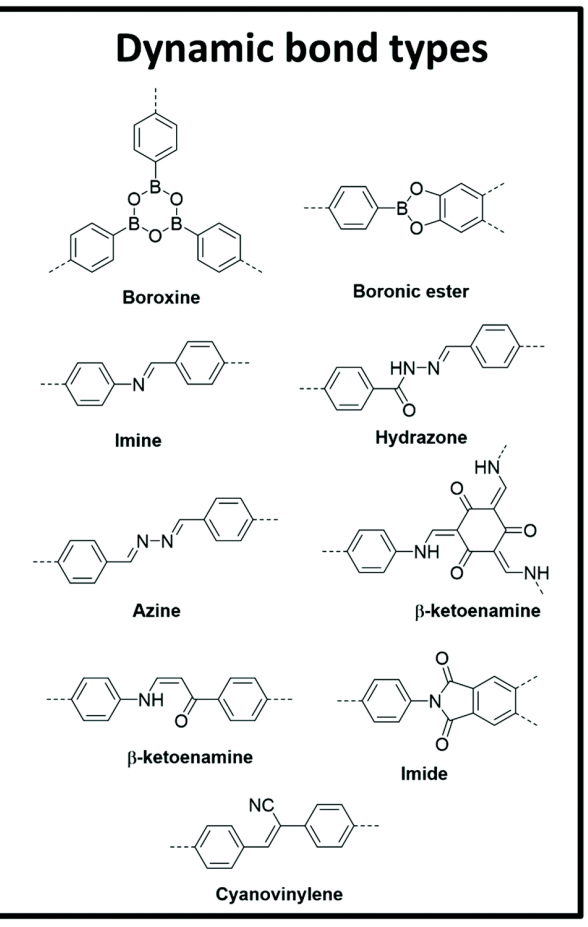


Figure 32: Reticular design strategies used for synthesis of COFs and corresponding most common dynamic bond types used to make COFs. Adopted from with permission of the rights holder [143].

3.1.3.2 Large Specific Surface Area

COF materials, due to their permanent porosity, have very large specific surface areas and low densities [158]. This large specific surface area allows for a high concentration of functional sites which can enable ultrasensitive sensing [158,160]. The functional groups present can allow for selectivity of species such that unwanted species are unable to access the bulk of the active sites, as only the accessible active sites influence their electrochemical activity [160]. The functional sites serve as areas where a target species can be sensed via adsorption allowing for detection via electrochemical techniques [158]. To improve accessibility to electroactive sites, COFs can be exfoliated or prepared in bulk using specialised techniques such as bulk thin films, membranes, or few-layer exfoliated COFs (e-COFs) [160].

3.1.3.3 Tailored Functional Groups

The decoration of COFs with functional electroactive groups has been widely reported in literature. Common functional groups introduced into COFs are —SH, —COOH, — NH₂, —HSO₃ and so on [158,160]. Functional groups' integration into COFs can also influence the hydrophilicity/hydrophobicity of the material [161]. The hydrophilicity of electrode materials, particularly when used in a biomedical context, is extremely important as it can alleviate surface fouling and biofouling [161].

Tailored functional groups also affects the surface charge of the electrode materials and can contribute to the rejection of solutes [161]. Typically, COFs that possess the same positive/negative charge as the species present in the solvent tend to possess good antifouling properties due to the electrostatic repulsion and/or inertness preventing adsorption leading to sensor drift [161].

Functionalised COFs can be prepared using a bottom-up approach where the functional groups are present in the building blocks or using post-synthetic techniques [160,162]. Post-synthetic modifications can be categorised into three subtypes: backbone modification, functional group modifications, and post-synthetic metalation [162]. Backbone modification refers to chemical reactions on the linker to cause covalent linkage modifications or even entire linker-for-linker exchange [162]. Functional group modification refers to the introduction of functional moieties that are generally incompatible with COFs into COF backbones through chemical transformation [162]. Post-synthetic metalation refers to the introduction of single-atom metals, nanoparticles and metal oxides as metal active sites in the COFs. The

metals are added as organic ligands uniformly distributed throughout the polymer structure [143].

3.1.3.4 High Stability

COFs demonstrate higher chemical and thermal stability than MOFs which use relatively weak coordination bonds [158]. The strong covalent bonding present provide structural and active sites' integrity to allow for sensing in even very harsh environments [158,160,163]. The stability can be increased by weakening the polarity of amine bonds, allowing for hydrogen bonding interaction, irreversible enol-to-keto tautomerization, and other techniques [161]. For example, Banerjee's group demonstrated remarkable 2D COF stability in boiling water, 9 N HCl and 9 N NaOH in TpPa-1 COF [43] . This was done by using standard imine chemistry for COF formation, which upon completion, tautomerizes into an irreversible and more inert β-ketoenamine [43,141]. For this TFP chemically to occur, (triformylphloroglucinol) is reacted with PDA (1,4-phnylenediamine) for imine bonds to form between the amines of the PDA with the aldehydes of the TFP [141]. Once three imine bonds form. an irreversible enol-keto tautomerization occurs causing increased stability via the introduction of C=C and C-N stretches confirmed by FTIR spectroscopy [141].

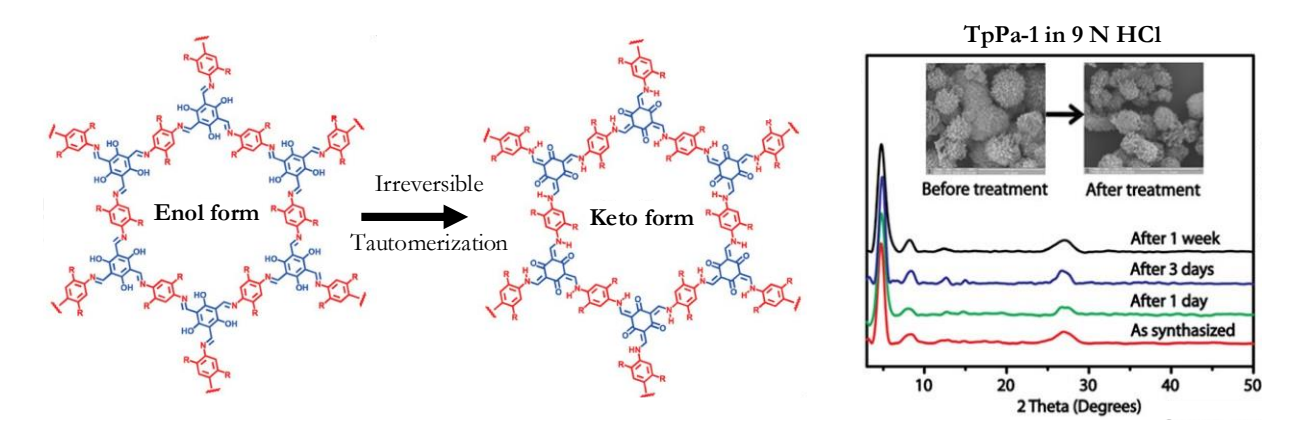


Figure 33: Schematic of the irreversible enol to keto tautomerization that occurs when TFP and PDA combine to form the keto form TpPa-1 or TpPa-2, and PXRD scans showing the stability of the COF in 9 N HCl after 1 week of submersion. Reproduced from [43].

3.1.4 Disadvantages of COFs

For electrochemical detection, general requirements such as a high electron transfer rate, and good conductivity are needed to promote electron transfer between the electrode surface and the solution. COFs typically have low electric conductivity given their polymeric structure [160,162]. COFs also have some processability issues, as

COFs are mostly formed in the form of bulk powders and cannot be dissolved or melted [162]. This limits the ability of the formation of films or membranes which would aid in mass transport through the material which thus allows for accessibility of the abundant active sites present in the material [162]. Therefore, there is a desire to obtain high crystallinity in large structures such that electrochemical properties can be enhanced [162]. These are typically achieved using macroscopically controlled engineering processes as shown in Figure 34. Thin films and membranes can be prepared using strategies such as in situ growth, layer-by-layer stacking, and interfacial polymerisation [162]. Hierarchical porosities, such that a material possesses larger meso or macro pores followed by the primary intrinsic porosity exhibited by COFs can facilitate good mass transport and allow for applications such as electrocatalysis, supercapacitors, batteries, etc. [162]. Hybrid nanostructures in COFs have also been applied during COF synthesis, primarily to alleviate the lack of electrical conductivity in COF networks [162]. So-called terracotta processes have also been used for processing COFs into desired geometrical shapes without the usage of binders or plasticisers [162].

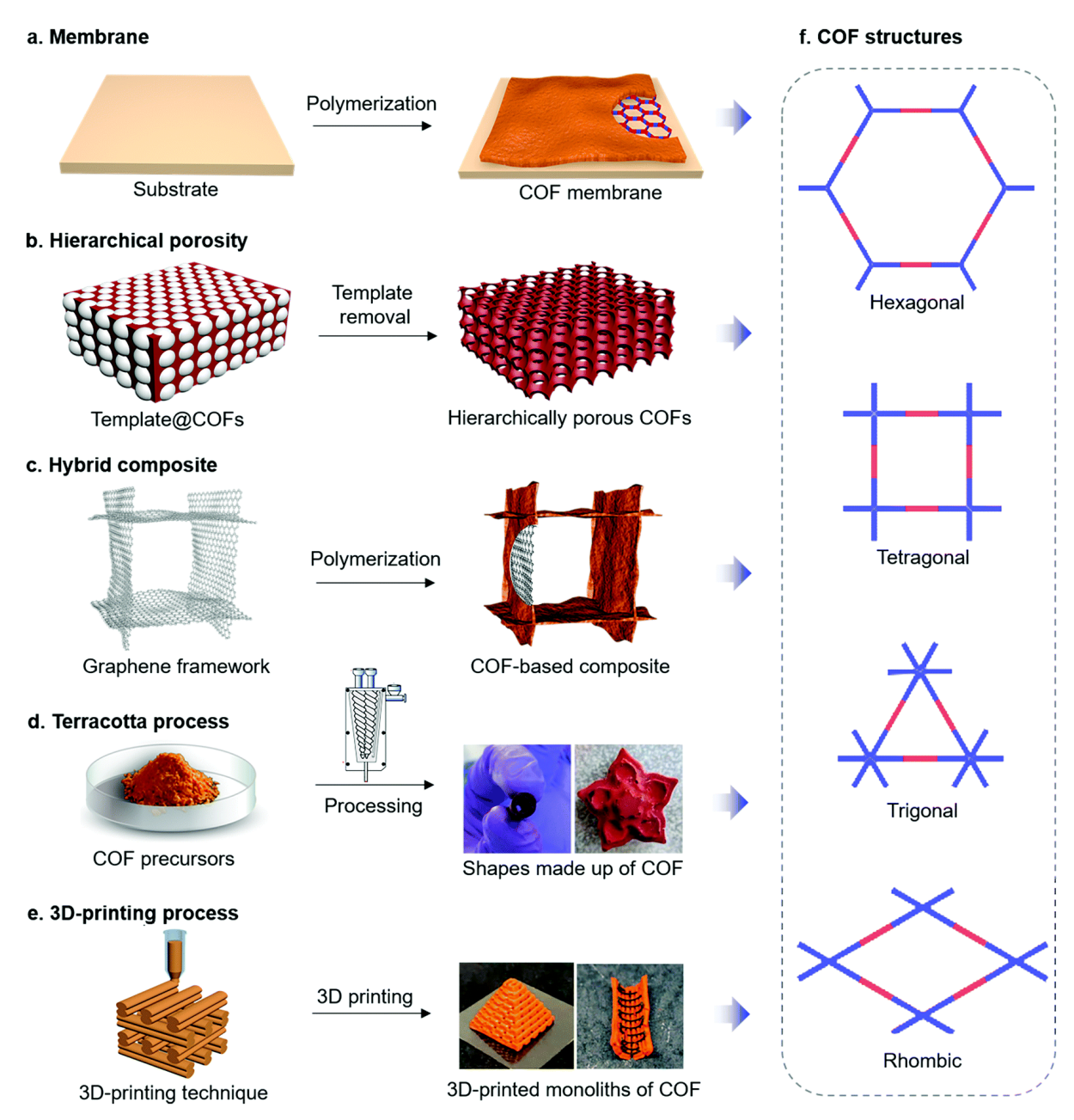


Figure 34: Low processability of COFs leads to macroscopically-controlled engineering strategies for COF synthesis that can facilitate improved electrochemical performance. Sourced from [162].

3.1.5 COF Electrochemical Sensors

Due to the advantages of COFs previously mentioned, COFs have been used for adsorption/separation applications as well as detection and sensing. This is typically performed via incorporating various COFs and MOFs for electrode modification. These advanced materials can exhibit performance improvements in selectivity, sensitivity, working life, and stability [164]. Some of the applications of COF electrochemical sensors such as detection of heavy metal ions, glucose, hydrogen peroxide, drugs, antibiotics, bio-sensing, etc. are shown in Figure 35.

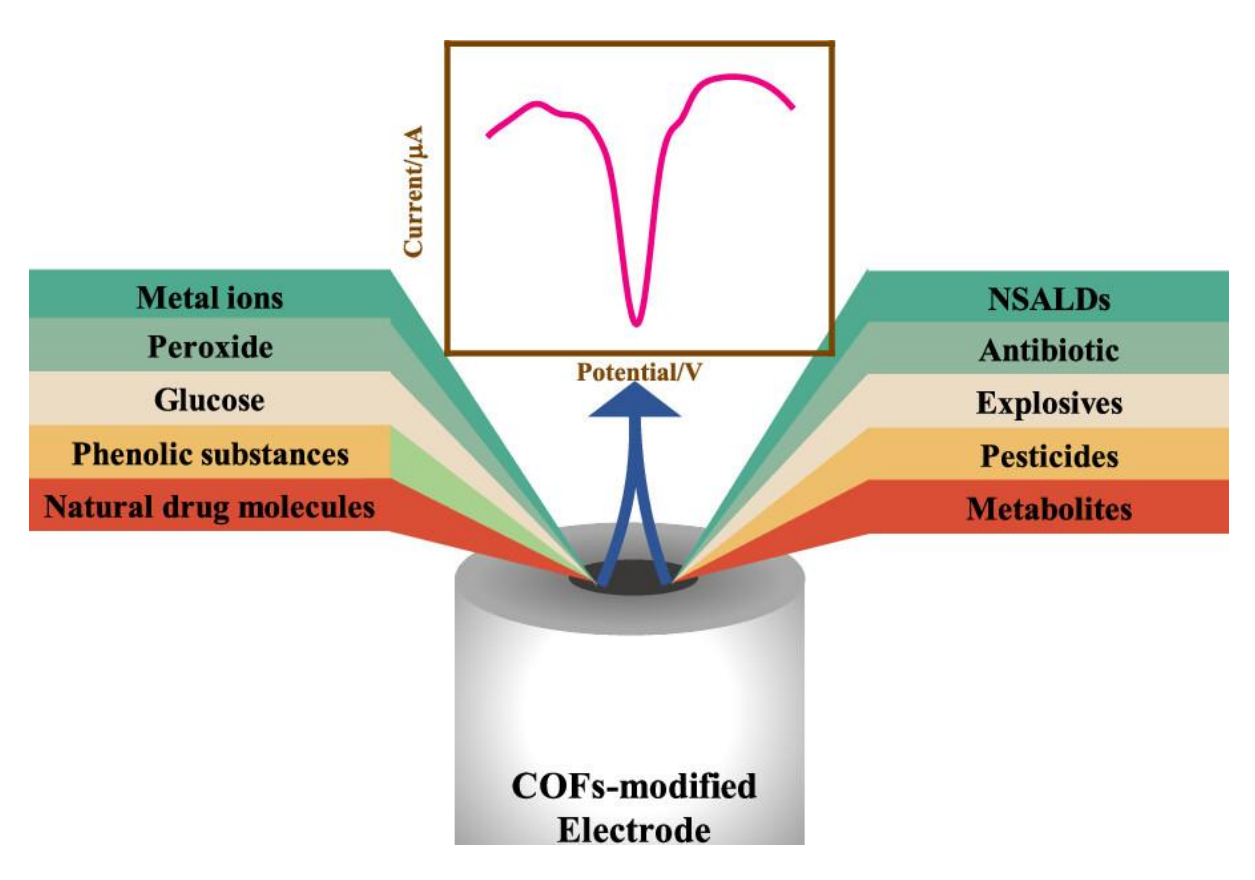


Figure 35: Common electrochemical COF sensors applications. Adopted reproduced with permission of the rights holder, [164].

Due to the low conductivity of COFs previously mentioned, COFs are typically combined with other nanomaterials that can offer improvements in conductivity, electron mobility and other desirable properties [164]. For example, Feng *et al.* created a COF-based nanocomposite named COF/Pt/MWCNT-COOH for the detection of dopamine, a key neurotransmitter in the hypothalamus. In their work, a composite was formed to have a synergistic enhancement of detection, by combining high surface area, high conductivity, and high electron transfer [165]. Geng *et al.* enhanced this work by fabricating a more sensitive dopamine sensor with a much simpler fabrication process via the combination of carbon black in a one-pot solvo-thermal method [166]. At the time of writing, there are more than 100 papers using COFs for electrochemical applications and therefore the focus of the following section is to focus on COFs for pH sensing [164].

3.1.5.1 COF pH Sensing

COF pH sensing is typically performed via one of a few methods, luminescence imaging, colorimetric-based, and electrochemical techniques. Chen *et* al. used luminescent COFs due to their physicochemical stability, and fast response time by

incorporating a pH-sensitive fluorescent group, 8-hydroxyquinoline, into the channels of a 2-D COF [167]. The resultant COF was dubbed COF-HQ and was sensitive in the pH range of 1-5 as shown in Figure 36.

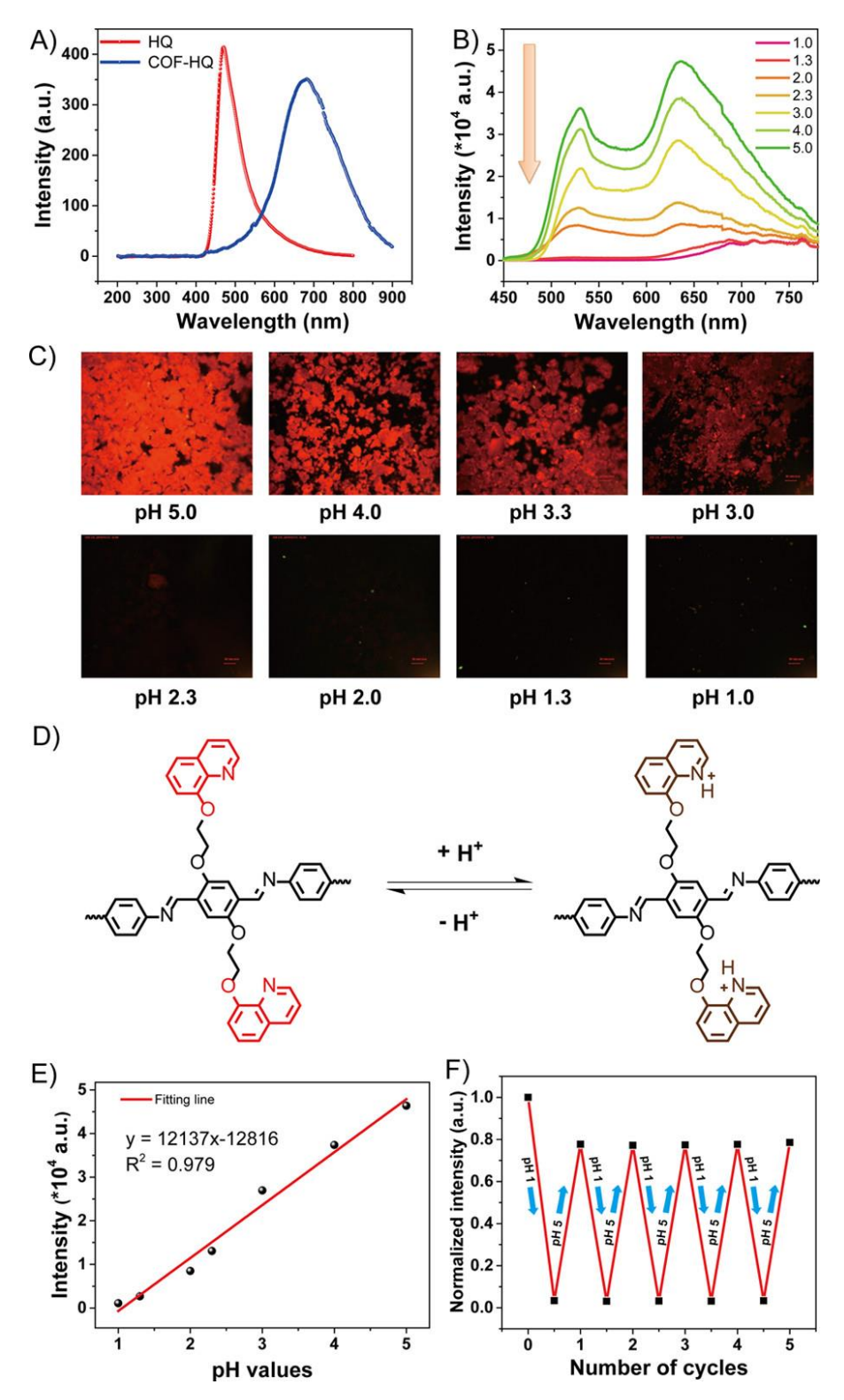


Figure 36: Results of pH sensitive COF-HQ (A) solid state fluorescence spectra of pure 8-hydroxyquinoline (HQ) and formulated COF-HQ. (B) Fluorescence spectra in various acidic solutions. (C) Images of the fluorescence spectra. (D) protonation and deprotonation response of HQ within the

COF-HQ framework. (E) pH and fluorescence intensity plot exhibiting linear relationship. (F) Plot showing repeatability of fluorescence for 5 cycles. Sourced from [167].

Xu *et* al. designed a multiple redox-active state COF to both catalyse H_2O_2 reduction and evaluate pH using voltametric methods [168]. In their work they used 2,5-dihydroxyterethaldehyde and 4,4',4"-(1,3,5-triazine-2,4,6-triyl) trianiline to synthesise COF_{DHTA-TTA} using solvothermal methods to prepare a powder [168]. The subsequent powder was drop cast on a polished glassy carbon electrode with glucose oxidase [168]. pH was determined by identifying the peak potential as signal outputs when performing a voltametric sweep from -0.5 – 0.6 V, where a linear shift of approximately 64.2 mV/pH was exhibited as shown in Figure 37.

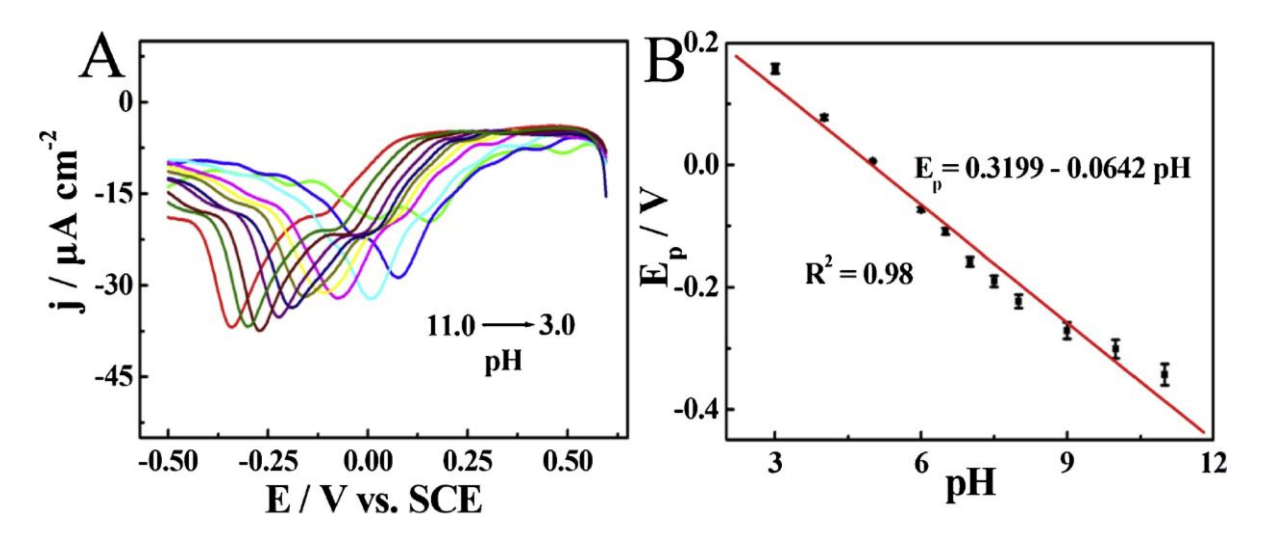


Figure 37: (A) Voltammetric diagram showing pH response of COF_{DHTA-TTA}. (B) Peak voltage extracted from voltammetric response vs pH showing 64.2 mV/pH sensitivity. Sourced from [168].

The same group also used another COF synthesised by linking 1,3,5-benzenetricarboxaldehyde and 5,10,15,20-tetrakis(4-aminophenyl)-21H,23H-porphine to synthesise $COF_{p\text{-por NH2-BTA}}$ and $COF_{p\text{-Fepor NH2-BTA}}$ (following post-synthesis modification) for a similar use. The resultant plot was also linear in the range of 3-9 pH with a reduced sensitivity of 41.2 mV/pH [169].

3.2 pH Sensitive Electrochemical GO+COF Composite

3.2.1 Introduction

Modern electrochemical sensing and biosensing technologies often utilise printed electrodes arranged in two- or three-electrode systems, valued for their simplicity, miniaturisation potential, low cost, and suitability for mass production [168]. The performance of these electrodes is largely influenced by material modifications that affect sensitivity, repeatability, stability, and selectivity. Metal oxides such as iridium oxide and zinc oxide are commonly used due to their high sensitivity and biocompatibility [170]. However, the high cost of iridium oxide limits its large-scale application[171], while the water solubility of zinc oxide in acidic conditions compromises its stability outside neutral pH [172].

Polymer-based sensors, including polyaniline (PANI) and PANI-composites, can achieve near-Nernstian responses (-58 mV/pH). However, their use is restricted by biocompatibility concerns, as precursor materials such as aniline, aniline hydrochloride, and ammonium persulphate exhibit cytotoxicity [170,173]. Furthermore, their sensing range is typically limited to pH values above 2, leading to inaccuracies in detecting highly acidic environments such as gastric acid. These materials often require proton-exchange membranes like Nafion® 115, which raises additional cytotoxicity concerns due to its fluoride content [70]. Similar limitations apply to carbon-based and other conducting polymer sensors, such as polyvinyl alcohol and polypyrrole composites.

Graphene oxide (GO) is a widely used biocompatible pH-sensitive material, but its performance is inconsistent under harsh conditions like strong acids due to the protonation and deprotonation of functional groups[84,99]. At low pH, GO aggregates into a sandwich-like structure with water molecules, while at high pH, it dissolves like a regular salt, leading to instability and unreliable sensing [84]. These limitations make GO unsuitable for continuous GORD monitoring, highlighting the need for more stable alternatives (Figure 38A).

Recent advances have introduced covalent organic frameworks (COFs), a class of porous nanomaterials with a high surface area, excellent biocompatibility, and numerous electroactive sites, enhancing sensitivity [168]. Among various COFs, those that undergo irreversible tautomerization were found to be particularly stable in

extremely acidic environments (e.g., 9 N HCl) and were therefore selected for this study [43]. It was hypothesized that the increased specific surface area and active sites provided by COFs would yield a more stable, sensitive, and consistent pH sensing response. This is because when a polarisable electrode reaches steady state equilibrium, it exhibits the same potential as a capacitor that is charged galvanostatically as shown in equation (28) [174].

$$E = E_0 + i(R + t/C) (28)$$

Here, E is the electrode potential, i is the current, R is the bulk resistance of the electrode, t is time, and C is the electrode capacitance at low frequencies. The time dependence of the electrode potential (potential temporal drift) is then given by equation (29) [174].

Potential drift =
$$\Delta E/\Delta t = i/C$$
 (29)

Equation (29) suggests that a sufficiently large electrode capacitance is necessary for potential stability.

Furthermore, COFs composed of different linkers can incorporate various functional groups, which influence their stability, sensitivity, and response time in different pH environments. As discussed in Section 2.1.5, the sensitivity of GO arises from the protonation and deprotonation of functional groups, specifically amine, carboxyl, and hydroxyl groups [97,99].

Triformylphloroglucinol, used by Kandambeth et al. for acid-stable COFs, contains hydroxyl and formyl groups [43]. It is then combined with p-phenylenediamine (PDA)—which has highly reactive amino groups—to form the COFs. These functional groups inherently in the COF could provide active sites for protonation and deprotonation. P-phenylenediamine, as a base molecule, with an additional carboxyl group is known as 2,5-diaminobenzoic acid. PDA with sulfonic groups, is known as 2,5-diaminobenzene-1,4-disulfonic acid, and can also be used as specialised linkers in COF formation.

When these functionalised COFs are combined with GO, they stack directionally on the GO nanosheets, facilitated by an interfacial COF synthesis technique. This results in π - π stacking, which helps maintain the structural integrity of GO while providing accessible active sites for protonation and deprotonation, as illustrated in Figure 38B.

The resulting GO-COF composites (Figure 38D-F) and were dubbed pristine-COF, carboxyl-COF and sulfonic-COF, corresponding to the functional groups present within the polymer. These COFs exhibit literature-reported pore sizes of approximately 1.8 nm for pristine-COF (TpPa-1 COF) [43], 1.5 nm for carboxyl-COF [175], and 1.4 nm for sulfonic-COF (NUS-10 COF) [176]. The inherently low conductivity of COFs is addressed by using GO, which, through the application of reducing agents and hightemperature synthesis, becomes conductive, enhancing its electrochemical response. Furthermore, the formation of 2D stacked nanopores, acting as nano-channels, increases the capacitive response, generating a significantly larger electrical double layer, as depicted in Figure 38C. The incorporation of functional groups such as SO₃H, also used in Nafion®-117 for selective proton conductivity, may enable a selective double-layer response by preventing other ions from entering the channels. Additionally, the hydrophilic nature of COFs mitigates biofouling by employing water as a physical and energetic barrier against microorganisms and protein binding [177]. To summarise, in this study, GO was combined with directionally stacked COFs synthesised via an interfacial method to promote π - π stacking, facilitating pH sensing [178]. The COF layer preserves GO's structural integrity while offering accessible active sites for protonation and deprotonation. The low conductivity of COFs is counteracted by GO, which, after high-temperature synthesis, becomes conductive, thereby improving electrochemical performance [89]. Additionally, 2D stacked nanopores act as nano-channels, enhancing the capacitive response and contributing to a substantial electrical double layer [163]. Functional groups such as SO₃H, used in Nafion® for selective proton conductivity, allow a selective double-layer response by excluding other ions [163]. Furthermore, the hydrophilic nature of COFs serves as a defence against biofouling by employing water as a protective barrier against microorganisms and protein adsorption [177].

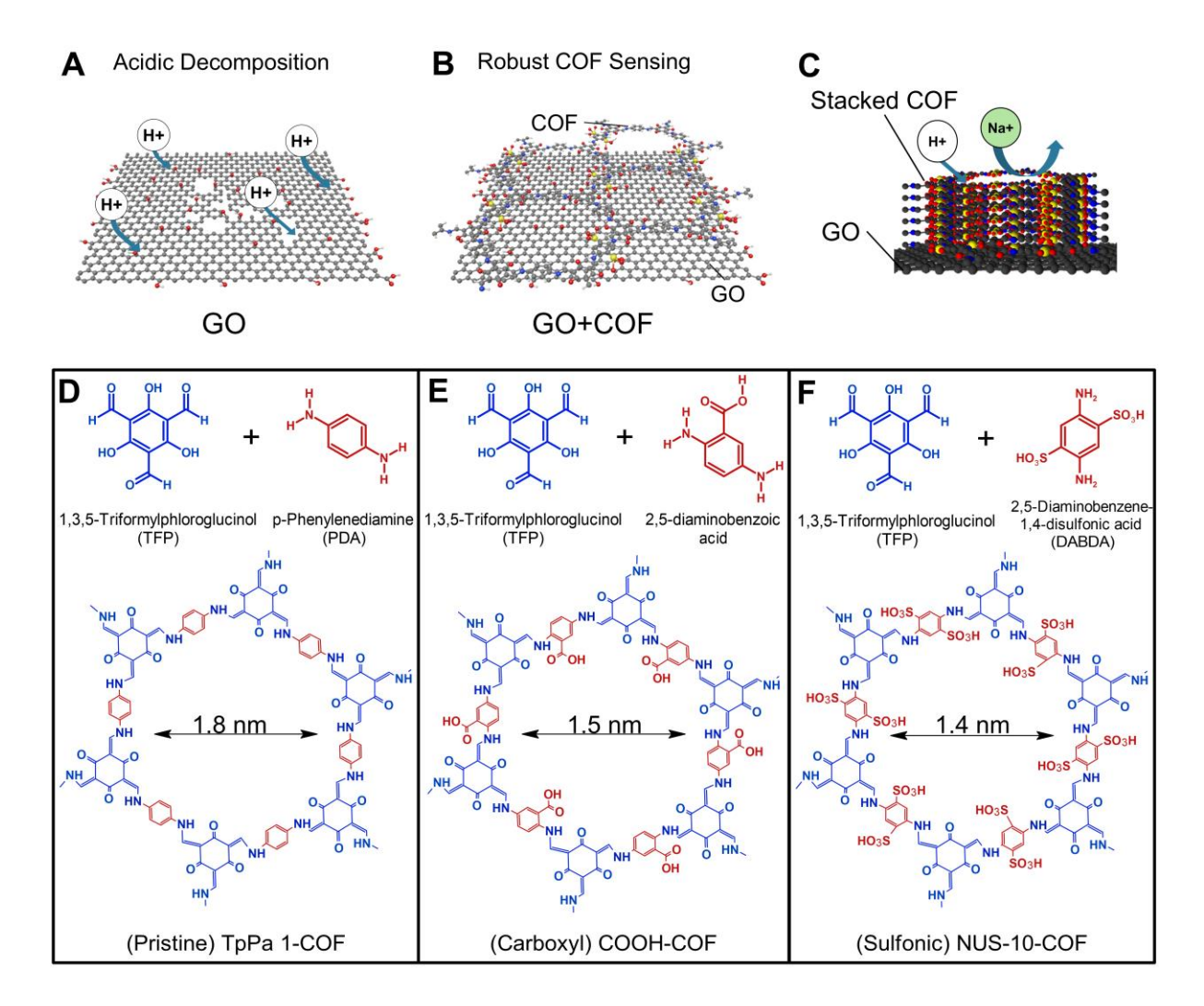


Figure 38: (A) Schematic of protonation and acidic instability of pure GO leading to poor stability. (B) Schematic showing the formation of COF nanopores on the GO adding increased surface area, functional sites, and stability. (C) Schematic showing sulfonic-COF formation of proton-selective nanochannels that cause a pH-selective response. Chemical structure of linkers used to make (D) Pristine TpPa-1 COF, (E) Carboxyl COOH-COF and (F) Sulfonic (NUS-10-COF) showing the difference in functional groups present.

3.2.2 Materials and Methods

3.2.2.1 Materials

Glass slides (75 mm x 50 mm) were purchased from Clarity. All chemicals, reagents and solvents were used without further purification. 3 different COFs were synthesised and compared. All COFs used the following solvents, chemicals and acids for synthesis and were purchased from Sigma Aldrich: octanoic acid, chloroform, N,N-dimethylformamide (DMF), Nafion-117®, and graphene oxide (4 mg/mL) solution. 1,3,5-Triformylphloroglucinol (TFP), purchased from TCI chemicals, was used as a linker for all the COFs synthesised following procedures in literature. For the pristine COF, *p*-phenylenediamine (PDA) was used. For the -SO₃H functionalised COF, 2,5-

diaminobenzene-1,4-disulfonic acid (Pa-SO₃H) was used (Sigma Alrich). For the – COOH functionalised COF, 2,5-diaminobenzoic acid, was ordered from Lab Pro inc.

3.2.2.2 Synthesis Methods

The synthesis of the COF film was based on previously published methods [179] and further processed for application as a COF-based sensor. The overall procedure is illustrated in Figure 39.

Briefly, 10 mg of GO from aqueous solution was freeze dried for 2 days to remove the solvent and stored in glass vials. 10 mL of DMF was added the glass vial and bath sonicated in an ice bath for 2 hours to ensure uniform dispersion. 10 mg of TFP was then added to the glass vial and bath sonicated for 10 mins. A glass slide was put on top of a hot plate heated to 80 °C and the GO+linker solution was pipetted on the glass slide uniformly. 10 mL of octanoic acid was poured into a separate beaker and 10 mg of the second linker, (i.e. Pa-SO₃H, 2,5-diaminobenzoic acid, or PDA) was added to the octanoic acid. This mixture was then bath sonicated for 30 minutes for uniform mixing. The glass slide with GO+linker was then added as shown in Figure 39 to allow for solid-vapour interfacial vapourisation as described by [179]. The beaker was wrapped with aluminium foil to prevent escape of the vapour. To prevent condensation of the vapour onto the glass slide, a solid metal block was added on to the top of the glass slide for sufficient heat transfer via conduction. The setup was placed in an oven at 150 °C for 12 hours for the reaction to occur. Subsequently, the GO-COF film was washed intensely with chloroform to remove impurities and excess reactants and peeled from the glass. The film was then put into a glass vial containing 10 mL of DMF and bath sonicated for 2 hours for liquid exfoliation of the layers of the GO-COF. This step crucially allowed for thinner layers of GO-COF nanosheets to ensure a greater availability of active sites. The solution was then centrifuged to remove the solvent and a solvent transfer into chloroform was performed 3 times to remove all DMF. The new solution was then re-sonicated to uniformly disperse the GO-COF in the solution whilst simultaneously allowing for COF activation as described in [145]. The solution was then drop casted onto the working electrode area of the sensor. The sensor was then placed in a vacuum oven for 12 hours at 80 °C to remove the remaining solvent for COF activation.

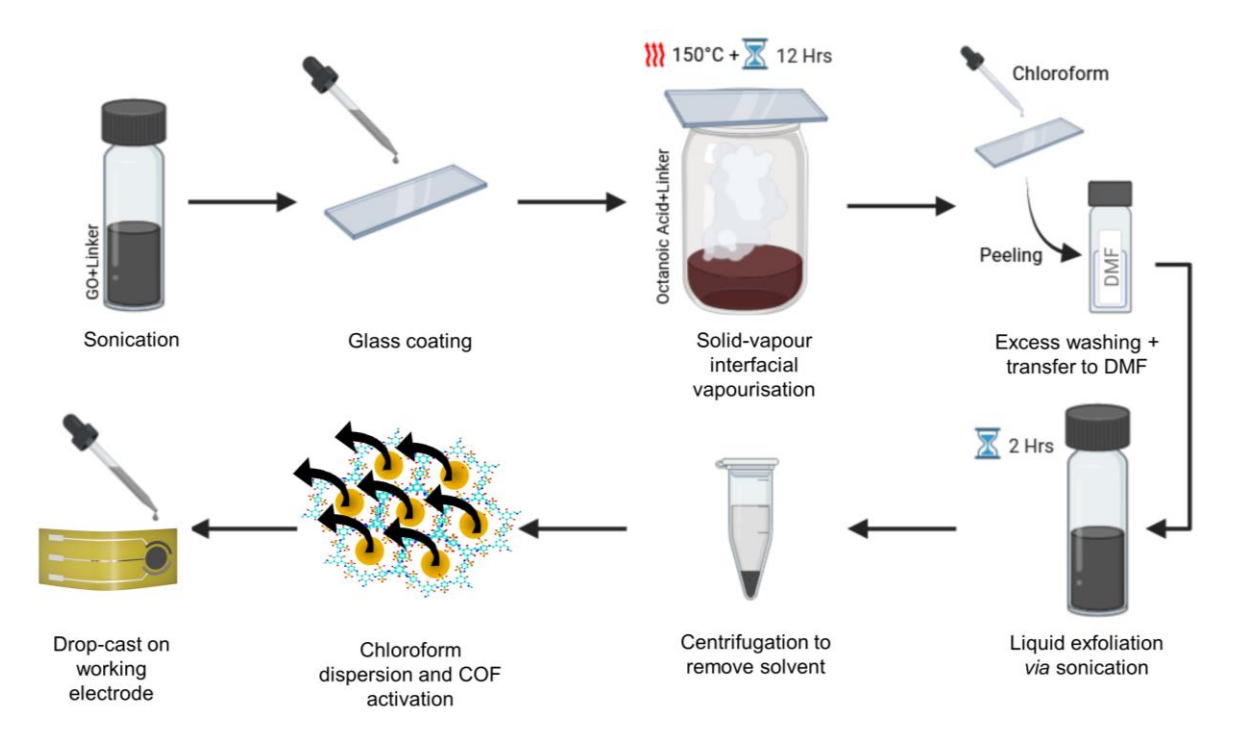


Figure 39: Schematic of method used for synthesising different types of COFs shown in this section.

3.2.2.3 Characterisation Techniques

To characterise the formation of COF, Fourier-Transform Infrared (FTIR) spectroscopy was utilised using a Spectrum Two™, Perkin Elmer spectrophotometer in the region of 400 to 4000 cm⁻¹. The samples were peeled from the glass and placed onto the laser for to minimise interference during the spectroscopy. Analysis of peaks was performed using MATLAB 2023b. The surface morphologies were imaged using scanning electron microscopy (SEM) (ZEISS GeminiSEM 360). Energy dispersive Xray spectroscopy (EDS) was also performed to produce elemental composition maps. The GO+COFs were imaged in two different configurations, (1) following peeling from the glass to obtain thin films and (2) following liquid exfoliation, solvent transfer and COF activation stages detailed in Figure 39. Atomic force microscopy (AFM) was also performed on the glass-coated sample (Bruker MultiMode 8). All COFs were activated prior to imaging and were applied onto a metal stub with double-sided adhesive carbon tape. A thin gold film was sputter coated for improved electron microscopy quality. An in-house goniometer setup was used for performing wettability and contact angle measurements. The setup consists of an adjustable stage, laboratory stand, syringe pump (World Precision Instruments, Aladdin single-syringe infusion pump), light source (Thorlabs, OSL2) and a magnification lens (Thorlabs, MVL7000) fitted to a camera. Videos were recorded to measure the advancing and receding angles and analysis was performed using ImageJ software.

3.2.2.4 Electrochemical measurements

To examine the pH performance of the produced materials, a potentiostat with an integrated impedance analyser (Ivium-n-stat d-module) was employed. This equipment was used to measure the Open Circuit Potential (OCP) and conduct cyclic voltammetry (CV) tests in both 2-electrode and 3-electrode configurations respectively. Impedance and capacitance measurements were conducted using an interdigitated electrode design that discards the reference electrode. Differential pulse voltammetry (DPV) measurements were performed in the 3-electrode configuration with an amplitude and pulse width of 50 mV and 0.2 s respectively.

The sensors were tested while submerged in a gastric acid simulant based on the Riddet Model, excluding pepsin, and following the protocol established by Ferrua and Singh [137]. The pH of the solutions was adjusted with low concentrations of HCl and NaOH. Five distinct solutions with pH levels of 1.5, 3, 4.5, 7, and 10 were prepared to mimic the pH range that the lower oesophagus would experience due to ingested food, beverages, and gastric reflux. For stability testing, the sensor was left in a pH 1.5 gastric acid solution for 12 hours, with OCP readings taken at 1-second intervals.

3.2.2.5 Cytotoxicity Testing

To evaluate the cytotoxicity of the materials, Human Esophageal Epithelial Cells (HEsEpiC) were used, cultured following the supplier's guidelines (Innoprot, Reference: P60152). These cells, isolated from healthy human oesophageal tissue, provide a reliable in vitro model for cytotoxicity studies. Poly-L-lysine and epithelial cell medium were also procured from Innoprot, while six-well cell culture plates were sourced from Costar®.

3.2.2.5.1 Control Samples and Preparation

GO was selected as the control material due to its extensively documented cytotoxicity and biocompatibility. Glass squares (1 cm × 1 cm) were cleaned using acetone, isopropyl alcohol, and deionised water. Oxygen plasma treatment (Diener Femto device) was performed at 0.1 mBar and 30W for 4 minutes to further purify the surfaces. Ethanol rinsing followed to minimise microbial contamination and static charge from the plasma treatment.

For coating, solutions of GO and the GO+COF composite were prepared at equal concentrations (0.1 mg/mL), dispersed in water and chloroform, respectively. Each

glass slide was coated by drop-casting 40 µL of the respective solution, followed by air-drying. The GO+COF-coated slides were further treated in a vacuum oven at 80°C for 12 hours to remove residual chloroform from nanopores and activate the COF.

3.2.2.5.2 Cell Culture, Seeding and Passage

Pre-coating of six-well cell culture plates was performed using poly-L-lysine for enhanced cell attachment. Briefly, the poly-L-lysine coating was applied and allowed to rest overnight. This was followed by removal of excess coating and then washed 3 times with sterile water. The cell culture plates were stored in 4°C for storage prior to seeding. Coated glass samples containing the material, were also coated with poly-L-lysine following the same procedure with one additional pre-processing step, which was to rinse thoroughly with ethanol to ensure sterility.

Preparation of coated glass samples was required before cell seeding.

HEsEpiC cells were seeded at densities of 50,000 and 100,000 cells per well and incubated in epithelial cell medium at 37°C for 7 days. Media changes were performed every three days, replacing half the volume of the medium in each well.

For passaging, approximately 1/5th of the cells were used for passaging. Briefly, a detachment solution was prepared by diluting TrypLE express Enzyme was diluted with PBS in a 1:1 ratio. The solution (4 mL) was added to the cell culture plate (4mL total), and incubated for 3-5 minutes to allow cell detachment. Detaced cells were collected and the TrypLE was then neutralised by adding 8 mL of epithelial cell medium. The cell suspensions were gently mixed to ensure even distribution before reseeding.

3.2.2.5.3 Cytotoxicity Assessment

Cytotoxicity was assessed using a live/dead viability assay following a 7-day incubation period. The assay utilized fluorescent dyes, calcein-AM and ethidium homodimer-1, to stain live and dead cells, respectively. The staining solution was prepared by adding 5 µL of calcein-AM (Component A) and 20 µL of ethidium homodimer-1 (Component B) to 10 mL of DPBS, ensuring thorough mixing for homogeneity. This procedure was conducted using the L3224 ThermoFisher Live/Dead Viability/Cytotoxicity Kit, strictly adhering to the manufacturer's instructions. The prepared dye solution was applied to the cell culture wells and incubated for 30 minutes at room temperature (20–25°C). Fluorescence microscopy (Axio Observer

Zeiss microscope) was employed to visualize and quantify the cells, with excitation/emission wavelengths of 494/517 nm for calcein-AM (green fluorescence for live cells) and 528/617 nm for ethidium homodimer-1 (red fluorescence for dead cells).

Cell viability was further assessed using PrestoBlue™ and PrestoBlue™ HS Cell Viability Reagents (ThermoFisher, A13262) to evaluate metabolic activity. High fluorescence intensity indicated metabolically active, living cells, while low fluorescence intensity corresponded to dead or metabolically inactive cells. PrestoBlue was diluted 1:10 in culture medium, and 400 µL of the solution was added to each well of the cell culture plate. The plate was then incubated for 30 minutes at room temperature (20–25°C). Technical triplicates were prepared, with 100 µL from each well transferred to a black-walled plate for measurement. Fluorescence intensity was recorded using a plate reader (Tecan Infinite 200 Pro) at excitation and emission wavelengths of 560 nm and 590 nm, respectively. Background fluorescence was determined using PrestoBlue without cells and subtracted from the experimental readings to calculate net fluorescence.

3.2.2.5.4 Image Analysis and Quantification

Cell viability was calculated as the percentage of live cells (calcein-AM positive) relative to the total cell population (live + dead). An automated image analysis protocol was developed using MATLAB-2023a® for high-throughput quantification. Cellular images were converted into binary maps using thresholding to distinguish cells from the background. A seeded watershed-based algorithm was applied to identify cell boundaries, with over-segmentation corrected using the MATLAB Image Processing Toolbox. The protocol, validated against manual counting, achieved >99% correlation, ensuring reliable and reproducible results.

3.2.3 Results and Discussion

3.2.3.1 Characterisation

For characterisation, FTIR spectra of the pristine GO, GO with the TFP, and the GO+COFs are shown in Figure 40. Chemical structures of COFs were confirmed using FTIR showing specific peaks at 1306 cm⁻¹ indicating (C—N) stretching and (C=C) stretching ~1617 cm⁻¹ aligning with literature [43,163,179].

Figure 42 shows the EDS mapping of the sulfonic COF which was used to confirm the formation of COF *via* solid-vapour interfacial polymerisation on GO nanosheets. The EDS shows that the major elements detected are carbon, oxygen, nitrogen and sulphur following intense washing of unreacted linkers with chloroform indicating the bonding of the linkers.

Figure 41A presents a free-standing film of GO+COF with a metallic-like lustre after being peeled from glass substrate, with all three synthesized GO+COF materials exhibiting similar optical properties. The formation of the film indicates the formation of COF between GO layers bonded GO together. This was further confirmed by SEM images before and after liquid exfoliation (Figure 41B-D). Figure 41B shows the structural integrity of the GO+COF coatings prior to liquid exfoliation. After exfoliation, the micro-sized flakes of GO+COF composites were formed (Figure 41C-E). Figure 41E specifically highlights the multi-layer stacking structure within the flakes providing insight into the structural integrity and layer separation achieved by the liquid exfoliation process likely increasing the active sites present for pH detection. On the surface of the flakes, a standard nanohierarchical morphology of COFs with small bumps (~ 45 nm) were found through atomic force microscopy (Figure 41F and Figure 41G) which show similar patterns as pure smooth COF coatings on glass in literature [179], suggesting successful coating of COFs on GO sheets without defects. Figure 41H shows the advancing contact angle (θ_{adv}) and the wetting properties of the exfoliated material, indicating a predominantly hydrophilic nature, which contributes to the material's anti-biofouling properties. Figure 43 confirms the successful formation of COF on GO, as evidenced by the surface roughness of the COF/GO composite increasing by more than an order of magnitude compared to the smooth pristine GO indicating a more textured surface due to COF deposition. This increased nanoscale roughness correlates with a larger effective interfacial area. The crystalline structure and the composition of the composites were confirmed by X-ray diffraction (XRD), showing patterns consistent with previously reported results [180], as illustrated in Figure 44.

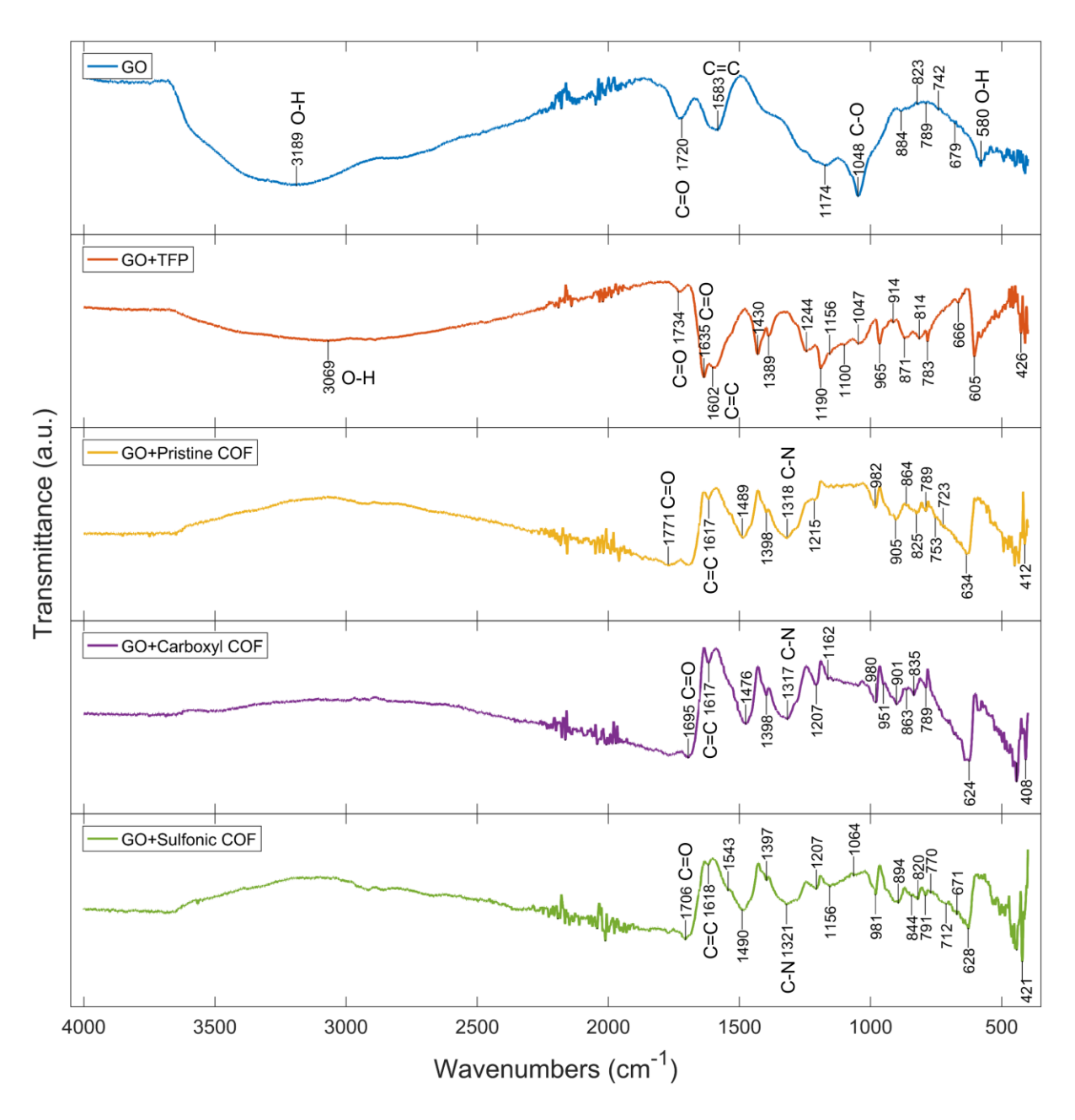


Figure 40: FTIR spectra of GO, GO+2,4,6-triformylphloroglucinol (TFP), and the different GO+COF mixtures: pristine, carboxyl, and sulfonic.

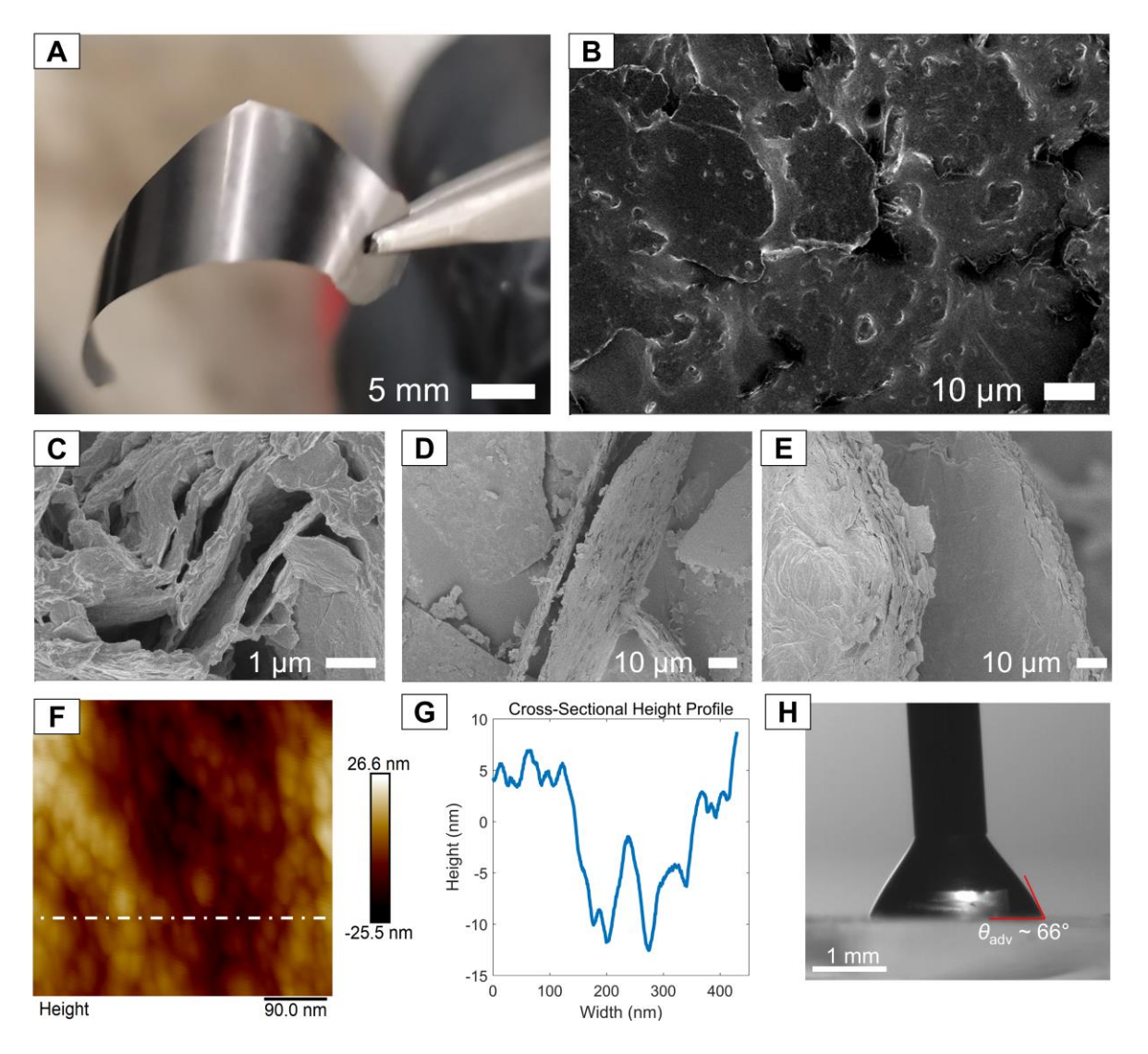


Figure 41: (A) Photograph of peeled GO+Sulfonic COF film showing a metallic-like lustre. (B) SEM image of the stacked structure of the GO+Sulfonic COF film prior to exfoliation. (C) Cross-sectional SEM image following liquid exfoliation showing the layers of the flakes. (D) Cross-sectional SEM image of larger flakes present in the sample following liquid exfoliation. (E) SEM image of layers within flakes following liquid exfoliation. (F) AFM image of the sample following liquid exfoliation. White dashed line indicates cross-sectional line with height profile shown in (G). (H) Advancing contact angle (θ_{adv}) of GO-COF sprayed on glass showing hydrophilic properties.

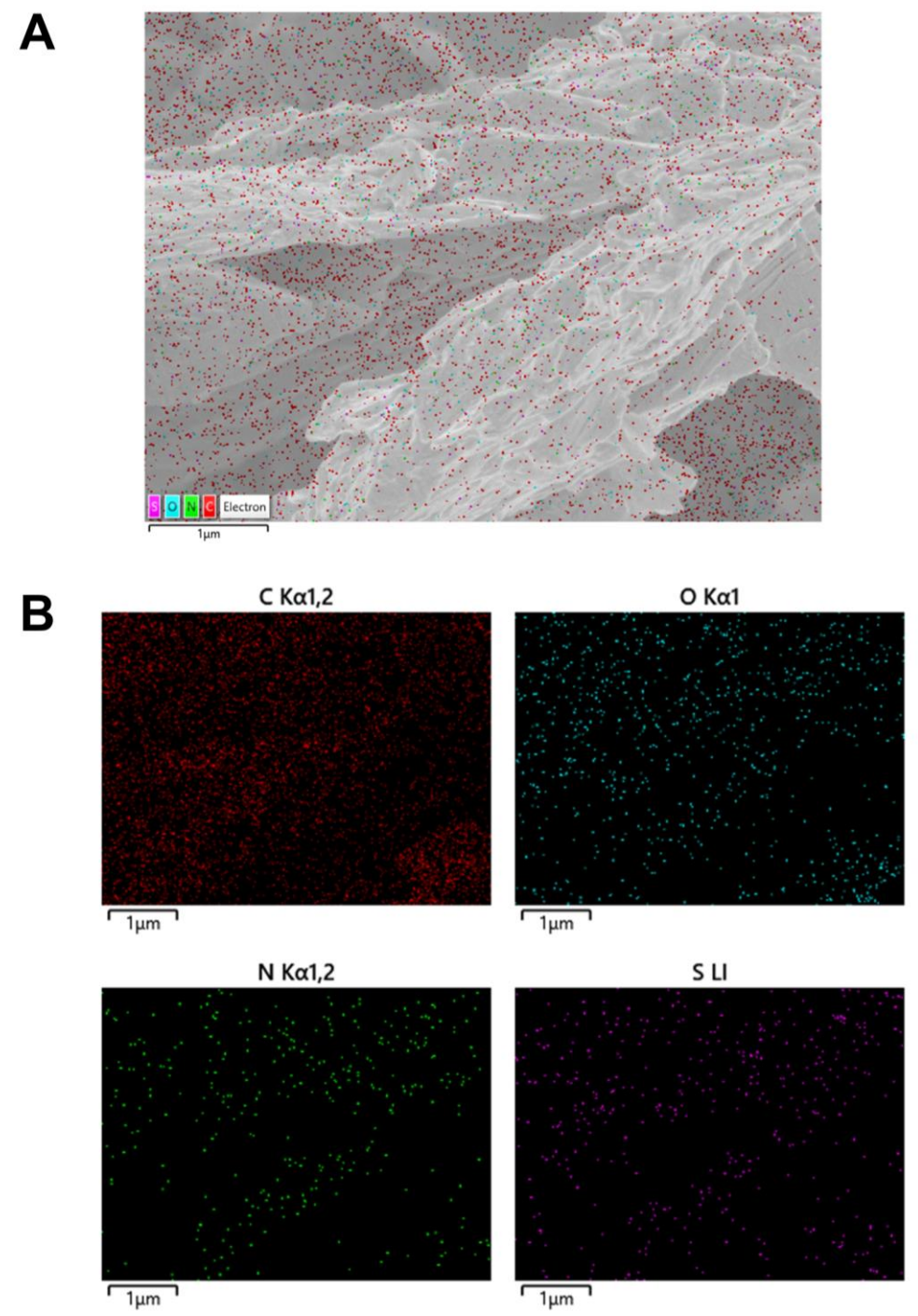


Figure 42: Energy dispersive X-ray spectroscopy (EDS) mapping of elemental composition on sulfonic COF to confirm COF formation. (A) SEM image and (B) Major elements detected and their locations: carbon (C), oxygen (O), nitrogen (N) and sulphur (S).

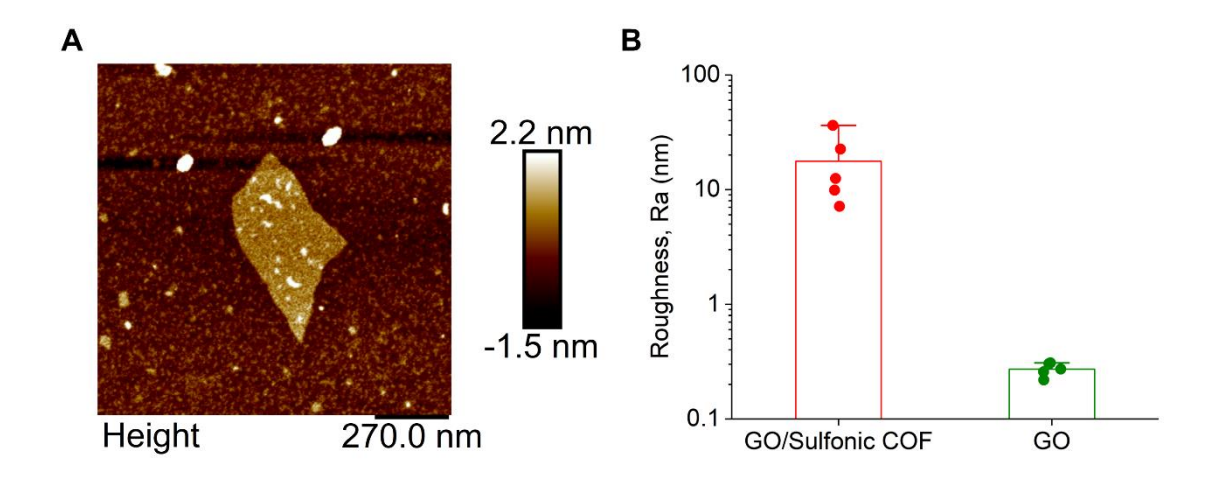


Figure 43: (A) AFM images on single GO sheet and (B) Surface roughness of GO/COF and GO, quantified through AFM scanning.

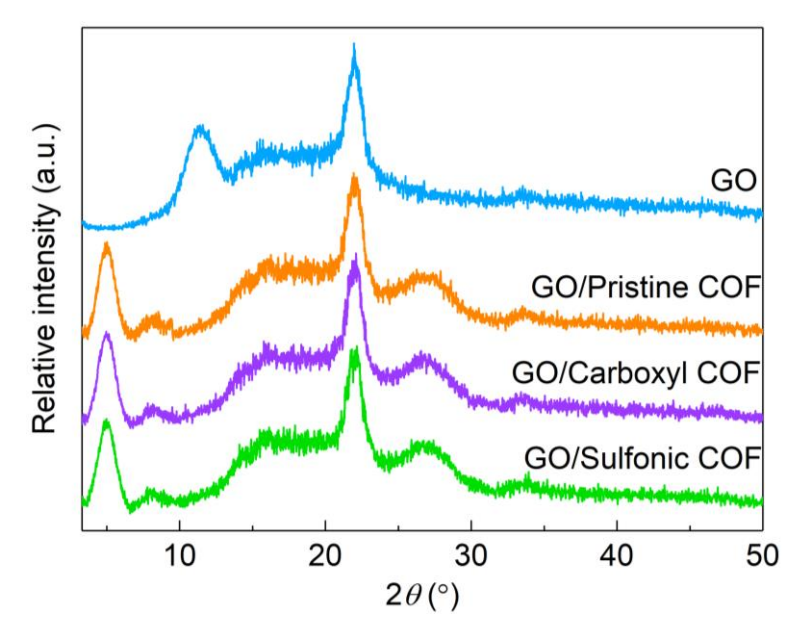


Figure 44: XRD patterns of GO and GO/COF composites, confirming successful synthesis and crystallinity of the materials.

3.2.3.2 Electrochemical Measurements

The electrochemical double layer is formed by the adsorption of ions onto the electrode surface in response to an applied potential, and this effect is particularly pronounced in materials with high surface areas, such as COFs. A faradaic response, characterised by electron transport coupled with proton (H⁺) transfer, is observed in the DPV measurements depicted in Figure 45. The pristine COF and GO composite exhibited the weakest pH electrochemical response, likely due to the lower concentration of electrochemically reactive oxygen functional groups within its structure.

A linear pH response was observed in the range of 1.5–10, which aligns with the physiological pH variations found in the oesophagus of patients with GORD, influenced by ingested food, beverages, and reflux events. The pristine COF and GO composite demonstrated a sensitivity of -13.86 mV/pH (Figure 13B). However, the introduction of carboxyl groups significantly enhanced both the sensitivity and linearity of the carboxyl COF and GO composite's pH response, as shown in Figures 13C-D. The DPV-derived sensitivity of the composite increased to -23.82 mV/pH, with a high degree of linearity (R² = 0.97) (Figure 45D). Additionally, a prominent reductive peak was observed in the negative potential range, which also exhibited pH sensitivity.

The sulfonic acid-functionalised COF and GO composite (sulfonic COF) exhibited a reduced reductive peak but a markedly stronger pH response, with a sensitivity of 27.2 mV/pH and the highest linearity (R² = 0.9755) among the COF composites tested (Figures 13E-F). The sulfonic COF possesses a high density of ordered onedimensional nanochannels, with sulfonic acid groups (-SO₃H) on the pore walls [176]. These groups acted as proton sources, facilitating proton hopping via the deprotonated sulfonate groups (-SO₃⁻) and their subsequent re-protonation. This mechanism enabled a selective buildup of H⁺ ions, contributing to increased capacitance due to the accumulation of protons in the electrical double layer. Consequently, the pH-sensitive response of this composite arose from mechanisms distinct from those described for pure GO by Angizi et al. [97,99]. This is evidenced by the distinct response of the sulfonic COF and GO composite at pH 1.5, where the proton hopping nanochannels, effectively lowered the resistance of the working electrode surface much more significantly than the other COF composites. Other COFs do not have this preferential proton affinity, so their measured resistance is dominated by the gastric acid solution's resistance. At pH 3, the effect diminishes as proton concentration decreases, and the resistance of the electrode becomes comparable to the solution, like the behaviour of the other COF composites.

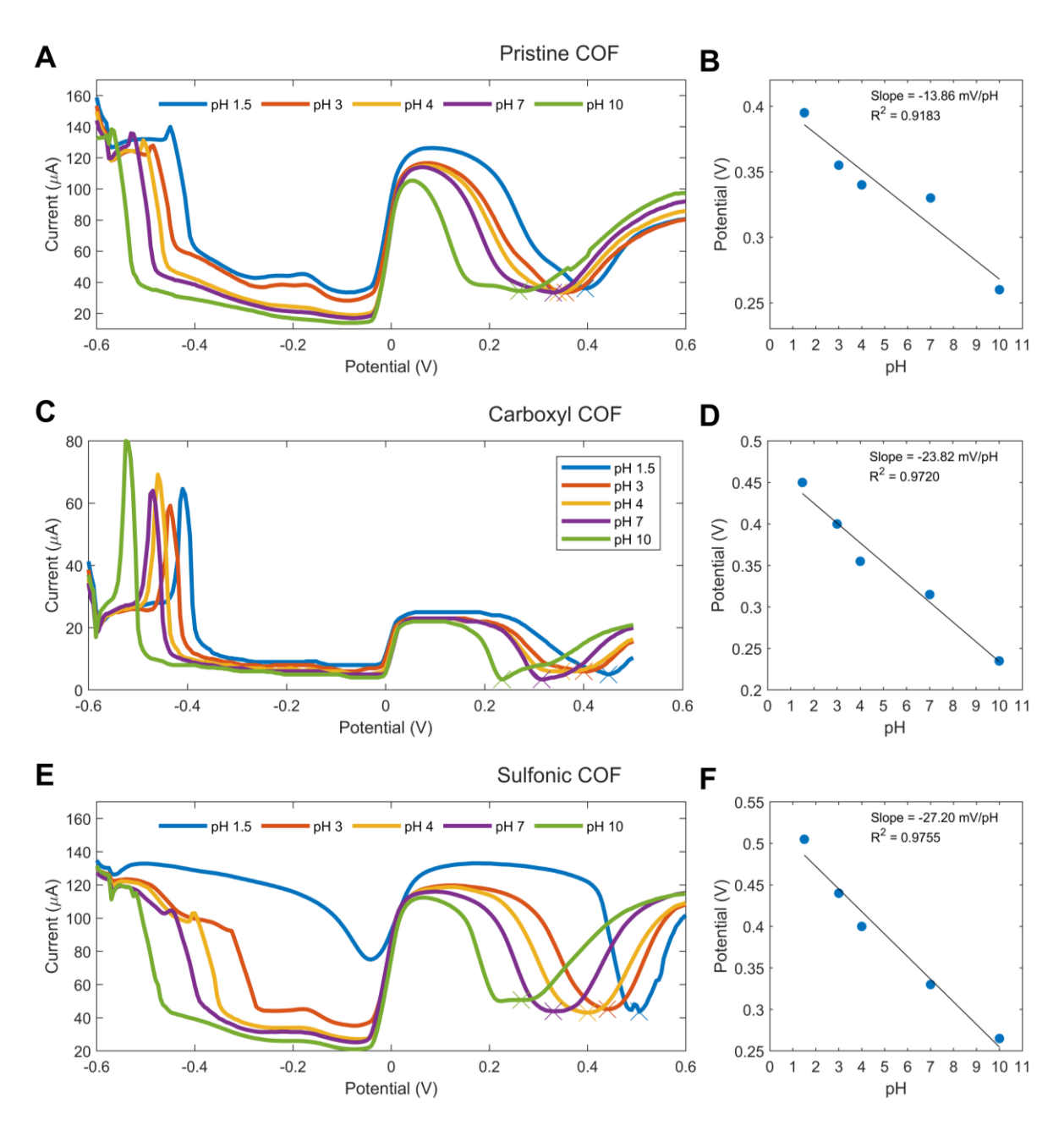


Figure 45: (A) DPV response of Pristine COF in gastric acid simulant solution at different pHs. (B) Calibration curve between oxidative peak and pH. (C) DPV Response of Carboxyl COF and corresponding pH calibration curve (D). (E) DPV Response of Sulfonic COF and corresponding pH calibration curve (F).

Following the promising results from the DPV measurements of the sulfonic COF and GO composite, the primary focus of the measurements presented in the main text is on this composite. The pH responses of all COF composites were characterised using CV and OCP measurements (Figure 46A-B). As anticipated, the CV measurements exhibited reduced linearity and sensitivity due to the lower signal-to-noise ratio compared to the DPV technique. DPV inherently minimises background charging

currents and unnecessary capacitive currents. However, CV remains valuable for understanding the kinetic transfer properties of the electrochemical pH response.

Interestingly, the linear pH range of the pristine COF is significantly reduced to only pH 1-7 (Figure 46C). In basic solutions, the response consistently becomes non-linear. This phenomenon is not observed in the carboxyl and sulfonic COF composites, where the linear pH range extends up to pH 10, the upper limit tested. The OCP response of the sulfonic COF composite, similar to that of pure GO detailed in Chapter I, resulted in a higher sensitivity of 43.5 mV/pH (Figure 46C). The mass ratio of COF to GO was also varied to determine the optimal response, which was found to be at a 1:1 ratio, as shown in Figure 43C.

Selectivity measurements, conducted using the Fixed Interference Method (FIM) in a simulated gastric acid environment, demonstrated high selectivity for commonly ingested interfering ions, including magnesium (Mg²⁺), potassium (K⁺), and calcium (Ca²⁺) ions (Figure 43D). Among these, magnesium ions exhibited the most significant potential shift, particularly at concentrations exceeding 10⁻³ M. However, this effect is unlikely to compromise sensor performance in gastric acid sensing, as the typical dietary intake of magnesium is relatively low, resulting in only trace amounts being present in the stomach [137].

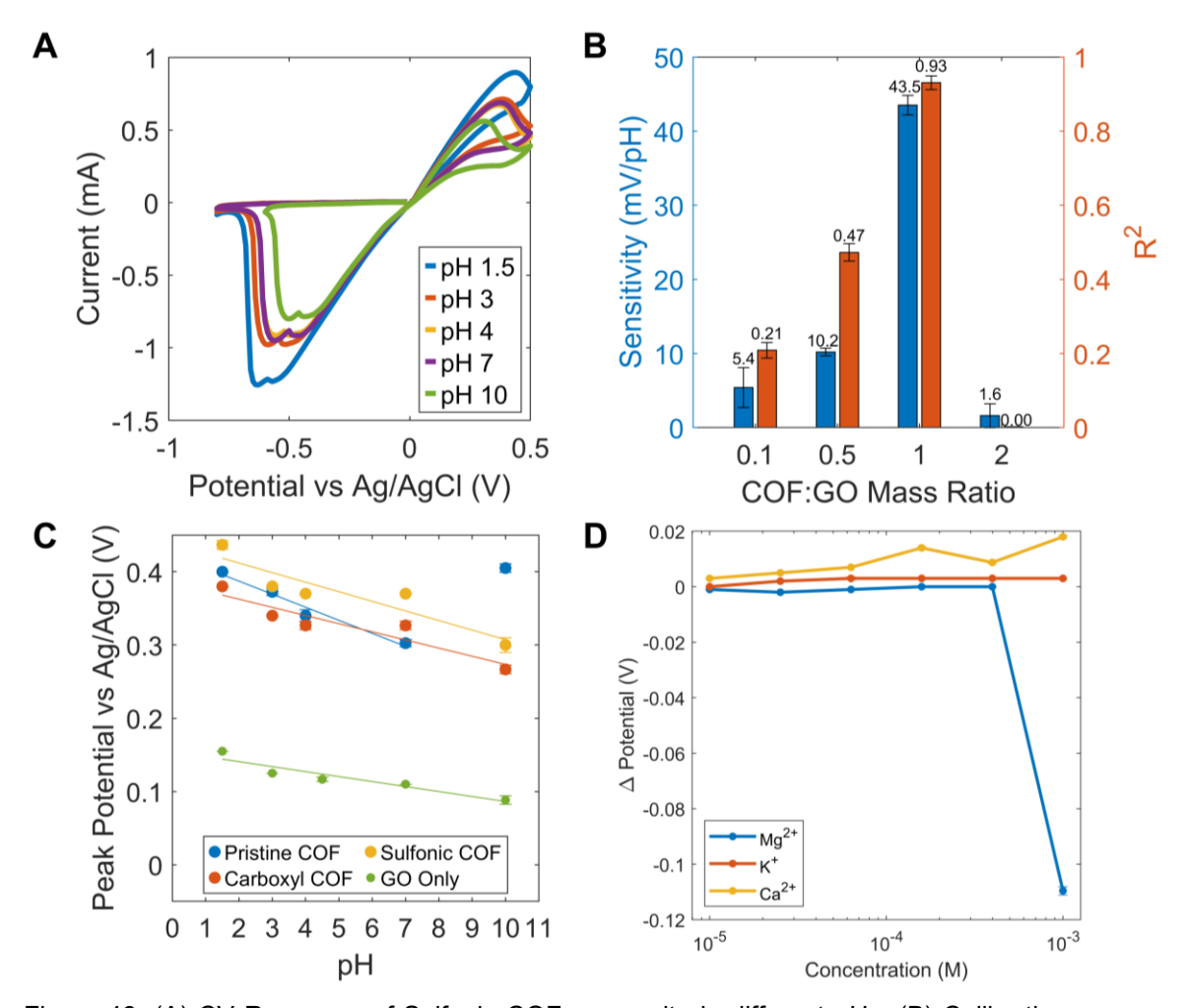


Figure 46: (A) CV Response of Sulfonic COF composite in different pHs. (B) Calibration curve peak oxidative peak against pH derived from CV scans of the different COFs. (C) OCP sensitivity and linearity of Sulfonic COF composite, in different COF:GO mass ratios (n=3). (D) OCP measurements against varying commonly ingested interfering ions to check for sensor selectivity.

The high sensitivity and linearity of the sensor's response were critically dependent on a thorough pre-treatment of the electrodes. Without this essential step, the sensor's response was highly unpredictable, and the OCP measurements lacked reproducibility. The pre-treatment process involved two key stages. First, a layer of Nafion® 117 was drop-cast onto the Ag/AgCl reference electrode and left to desiccate at room temperature overnight before testing. This step was crucial in stabilising the reference electrode, maintaining electrical contact, and ensuring consistent performance, and is standard practice in the literature [70].

Second, the two-electrode version of the sensor underwent an acid or a combined acid-base pre-treatment. For the acid pre-treatment, the sensor was submerged for 8 hours in a gastric acid solution with a pH of 1.5. In the acid-base pre-treatment, the sensor was additionally submerged in a separate gastric acid simulant with a pH of 10

for 8 hours. This prolonged exposure allowed any unstable reactions to occur prior to actual testing, thereby stabilising the sensor's response.

The importance of this pre-treatment is clearly demonstrated in Figure 47. With only acid pre-treatment, the sensor exhibited a linear response; however, significant hysteresis was observed after each measurement cycle, with a noticeable shift in potential following submersion in basic solutions. This behaviour is consistent with the findings of Banerjee et al., who reported reduced stability of these types of COFs in alkaline media [43]. The pre-treatment effectively mitigates these issues, ensuring the sensor delivers a stable and reliable performance across a range of pH conditions.

Although the pre-treatment led to a more stable response, no significant differences in pH stabilisation time were observed (Figure 47C-D). The pH response was fastest in acidic media, likely due to the increased rate of proton hopping and the reduced ion exchange compared to the larger OH⁻ ions present in basic media. This behaviour aligns with that of glass pH electrodes, which also commonly exhibit prolonged stabilisation times in basic environments. While the initial pH response occurred rapidly, full stabilisation—defined as a change in potential of 0 mV over a 10-second period—took up to 80 seconds.

A noteworthy reduction in hysteresis was observed, as shown in Figure 47E-F, which depict the OCP over time following stabilisation. While the sensor displayed some degree of hysteresis when subjected to acid pre-treatment only, this effect was significantly mitigated after the combined acid and base pre-treatment. The hysteresis, which persisted throughout the measurement cycles with acid pre-treatment alone, was nearly eliminated with the additional base pre-treatment, resulting in a more consistent and reliable pH response across varying conditions.

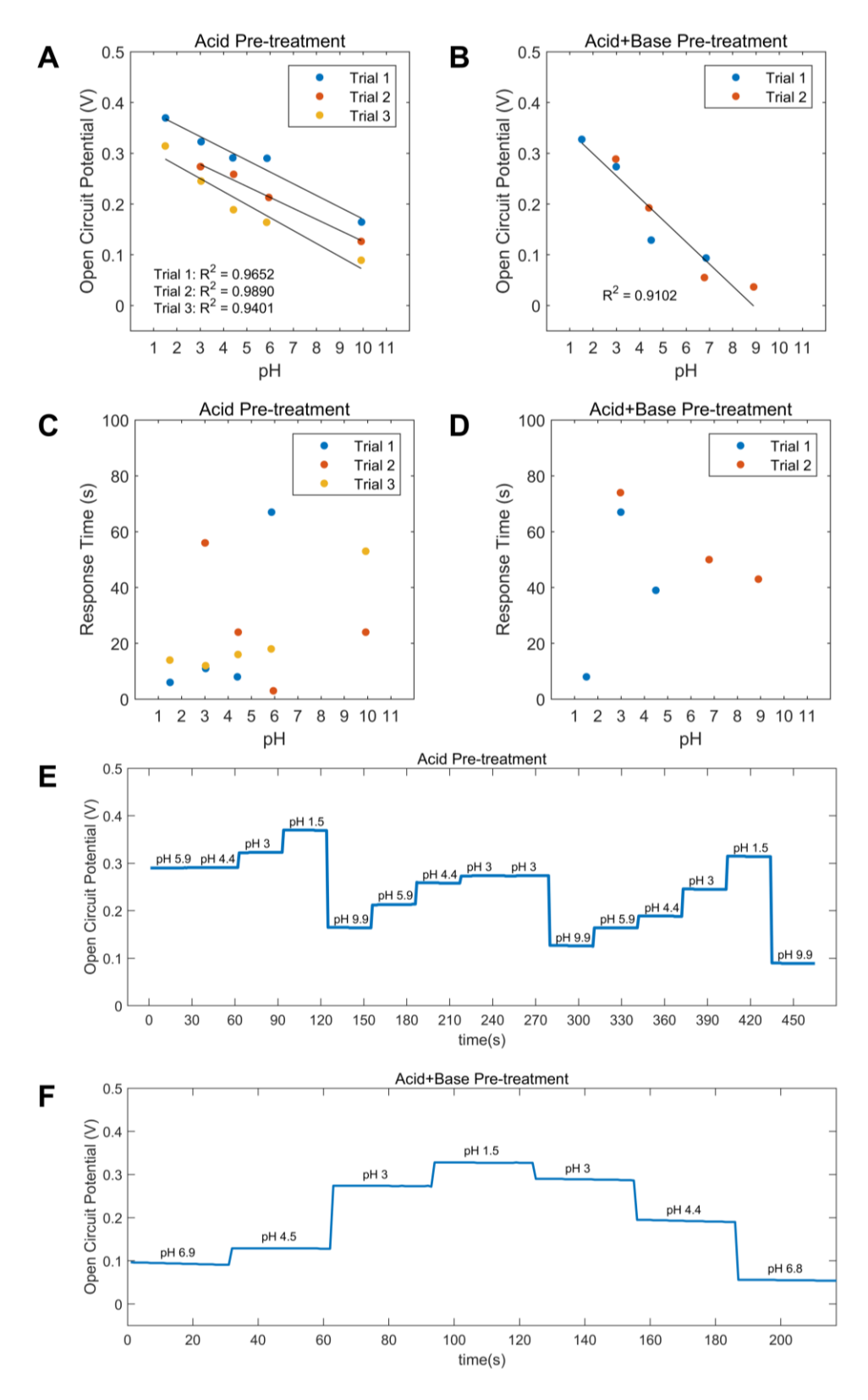


Figure 47: Effect of pre-treatment on Sulfonic-COF. (A) OCP response to pH with acid pre-treatment only. (B) with acid+base pretreatment. (C) Response time (90% of mean final value) of acid pretreatment only and (D) acid+base preteatment. (E) OCP with time in different pH gastric acid simulant solutions with acid pretreatment and (F) acid+base pre-treatment.

The stability assessment of the Sulfonic COF composite demonstrated exceptional resilience under highly acidic conditions (pH 1.5) for an extended duration, following pre-treatment in both acidic and basic environments (Figure 48). This indicates the material's robust structural integrity and electrochemical stability, essential for long-term performance in harsh physiological conditions such as gastric acid. Notably, the Sulfonic COF composite far outperformed GO alone, which exhibited significant potential drift within the first 30 minutes, underscoring the superior stability of the composite material.

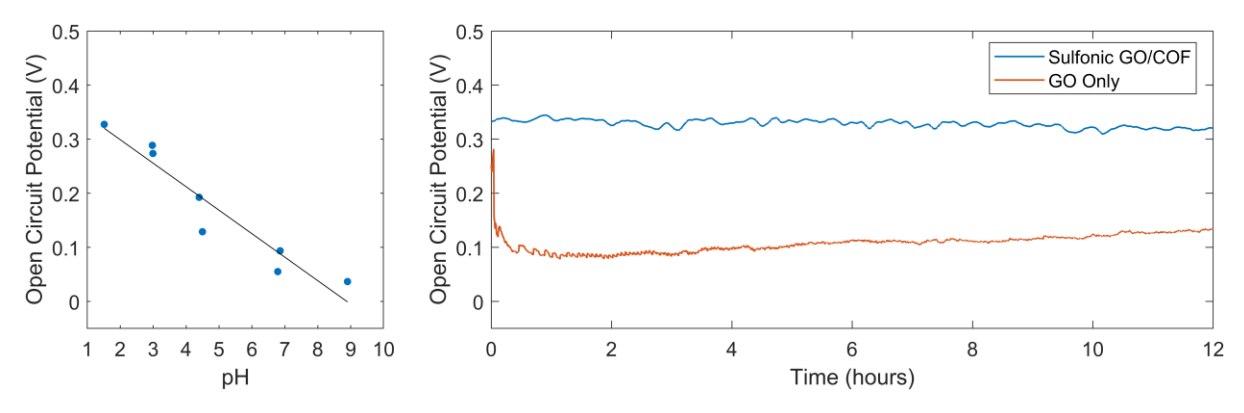


Figure 48: (A) OCP plotted against pH to create a calibration curve. (B) OCP of the sensor submerged in pH 1.5 for several hours demonstrating remarkable stability.

Further long-term stability of the Sulfonic GO/COF sensor was evaluated under both acidic and basic conditions over a 12-hour continuous operation using OCP measurements, as shown in Figure 49. The results demonstrate that the sensor maintains stable potential across this pH range, highlighting its robustness and reliability. Such stability is particularly important for practical applications in physiological and environmental contexts, where exposure to both acidic and basic conditions is common, such as in gastrointestinal monitoring or other biomedical and environmental sensing scenarios.

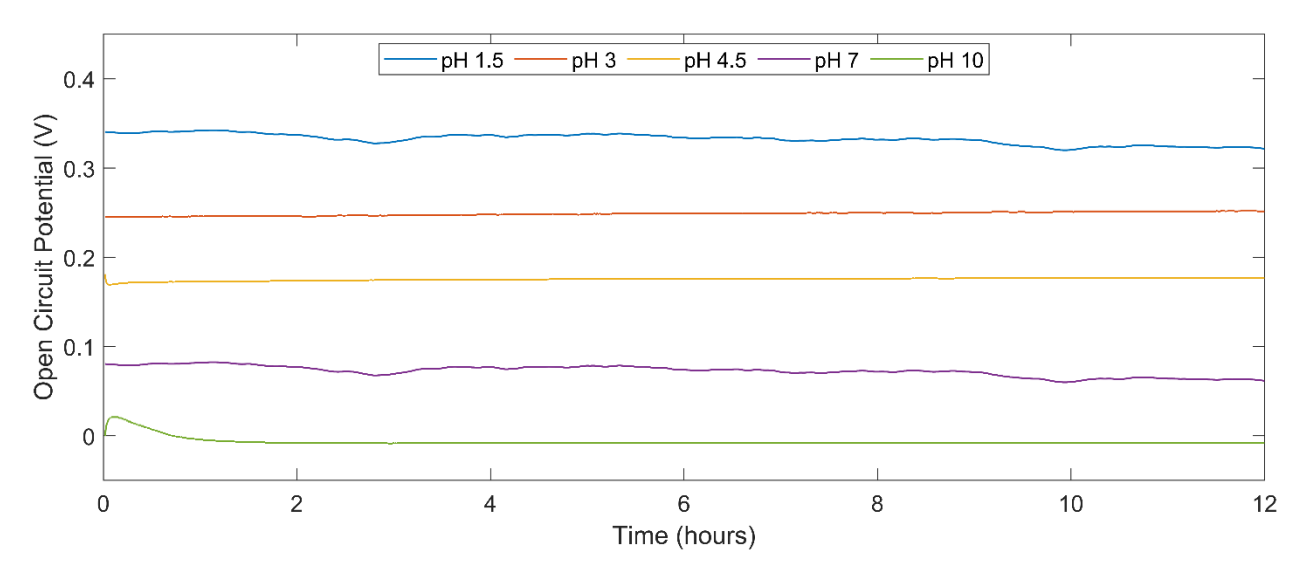


Figure 49: Open-circuit potential (OCP) stability of the GO/Sulfonic COF sensor over 12 hours at various pH conditions (pH 1.5, 3, 4.5, 7, and 10).

To investigate the mechanism behind the OCP response of the sulfonic COF and GO composite, particularly focusing on the role of H⁺ ions in modulating the electrical double layer capacitance, a specialized interdigitated electrode design was implemented, deliberately omitting the reference electrode to focus on the capacitance effects of the material. Capacitance measurements were conducted across a frequency range of 10² - 3x10⁵ Hz in different pH solutions, with the results depicted in Figure 50A. The corresponding pH calibration curve, shown in Figure 50B, demonstrates a highly linear relationship, indicating that the composite's response is predominantly influenced by proton-hopping mechanisms and the presence of ordered channels. These findings strongly suggest that H⁺ ions are the primary contributors to the observed capacitance behaviour, thereby confirming the critical role of proton dynamics in the electrical properties of the sulfonic COF and GO composite. This allows the Sulfonic COF composite to behave as a highly predictable capacitive pH sensor.

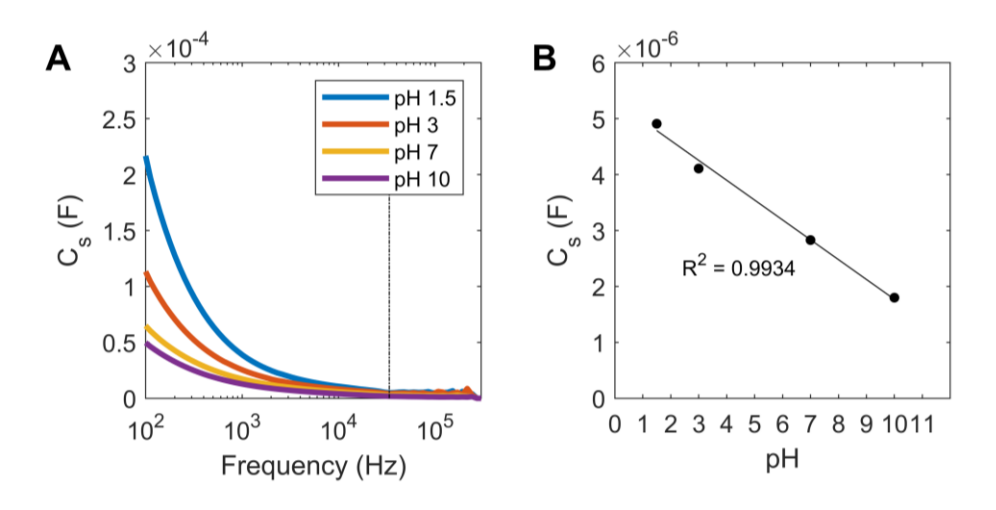


Figure 50: Capacitance response of the Sulfonic COF and GO composite in pH solutions, demonstrating that protons are the primary factor influencing the electrical double layer capacitance. (B) Calibration curve of capacitance to pH at indicated dashed line shown in (A).

3.2.3.3 Cytotoxicity Testing

The cytotoxicity evaluation of the GO+COF composite demonstrated excellent biocompatibility with HEsEpiC cells, supporting its potential use in medical applications. Throughout the 7-day incubation period, epithelial cells adhered consistently to the coated slides, showing robust proliferation with no adverse effects observed. Cell viability remained consistently high, exceeding 93.5% under all tested conditions, independent of initial seeding densities (50,000 or 100,000 cells/well). Importantly, no statistically significant differences (p > 0.05) in live cell percentages were found when comparing untreated controls, GO controls, and GO+COF composite samples across passages 4–6 (Figure 51).

Interestingly, in Figure 51C, an increase in cell viability was observed in the GO+COF-treated samples compared to controls. While the exact mechanism of this enhancement is unclear, the increased viability do not suggest cytotoxic effects.

The live/dead staining assay revealed a negligible presence of dead cells, confirming that the GO+COF composite is non-cytotoxic under the tested conditions. These results were further corroborated by Prestoblue fluorescence assays (Figure 52), which demonstrated comparable fluorescence intensity across all groups (p > 0.05). Notably, Prestoblue measurements were taken at multiple time points (2, 5, and 7 days), exceeding the anticipated monitoring timeline. The consistent absence of cytotoxicity over an extended period highlights the material's stability and suitability for longer-term applications.

These findings position the GO+COF composite as a promising material for use in biomedical devices, particularly in diagnosing gastro-oesophageal reflux disease (GORD). Its ability to maintain high cell viability, even in prolonged exposure, indicates that it could be safely integrated into diagnostic platforms. The potential for the material to enhance cell proliferation, as observed in GO+COF samples, may also offer additional advantages in applications requiring long-term device-patient interactions.

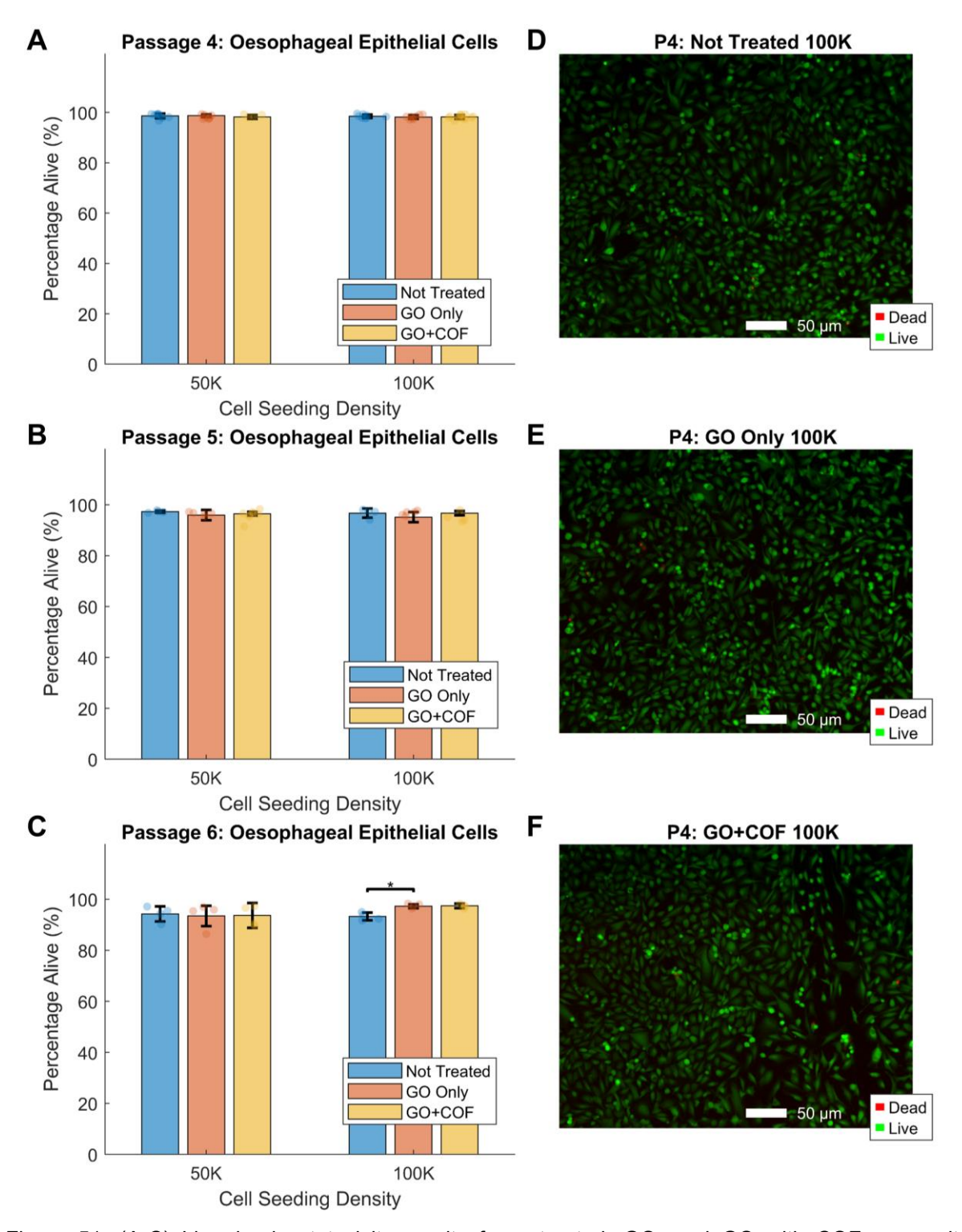


Figure 51: (A-C) Live-dead cytotoxicity results for untreated, GO, and GO with COF composite (GO+COF) at passages 4-6, shown as the percentage of live cells (calcium green-stained) relative to total cells, including ethidium homodimer-stained dead cells. Representative fluorescent images of passage 4 cells at 100K seeding density are shown for (D) untreated sample, (E) GO only, and (F) GO+COF composite.

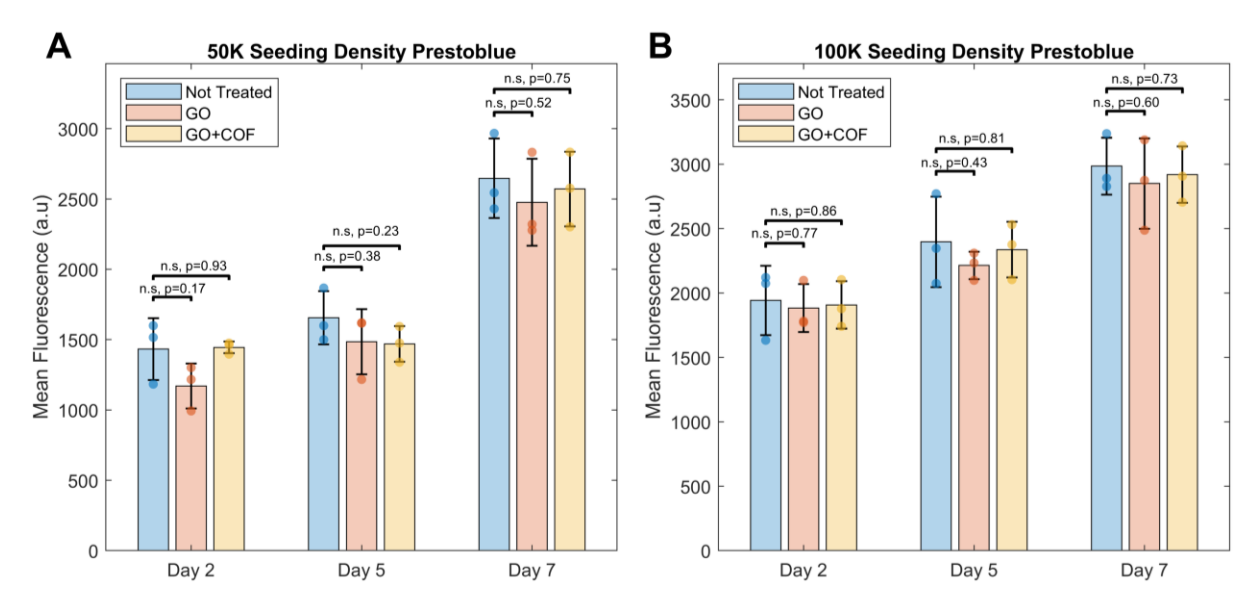


Figure 52: Mean fluorescence of HEsEpiC cells stained with Prestoblue dye of not-treated control samples, GO and GO+COF composite samples for seeding densities of (A) 50K cells/well and (B) 100K cells/well.

3.2.4 Conclusion

This study demonstrated the potential of GO/Sulfonic COF composites as high-performance materials for GORD diagnosis pH sensing. The sulfonic COF variant exhibited superior sensitivity (~43.5 mV/pH in OCP), excellent reproducibility, and rapid response times, particularly in acidic environments. Its capacitive sensing mechanism eliminated the need for a reference electrode, simplifying sensor architecture while reducing cytotoxicity concerns associated with Nafion-based systems. Additionally, electrochemical impedance spectroscopy confirmed a stable and predictable capacitive pH response, further enhancing its reliability.

Biocompatibility tests with human oesophageal epithelial cells showed no adverse effects, supporting its potential for in vivo applications. The removal of Ag/AgCl reference electrodes further reduced cytotoxicity risks, making the composite more suitable for long-term biomedical use.

By addressing the limitations of conventional GO-based sensors, this study establishes GO/Sulfonic COF composites as a promising alternative for flexible, printed pH sensors. Their stability, biocompatibility, and scalability pave the way for improved gastrointestinal monitoring. Future studies should focus on in vivo validation and long-term stability assessments to further advance their clinical applicability.

Chapter 4: Wireless Signalling and Sensing

4.1 Background and Literature Review

Point-of-care (PoC) testing, which involves medical diagnostic testing at or near the site of patient care, is rapidly evolving with the integration of communication technologies [181]. This transition is pivotal for advancing digital healthcare and enabling more seamless and efficient diagnostics [181]. Wireless sensor networks, which can transmit physiological data directly to end users without requiring substantial infrastructure, have gained significant traction in the consumer market [181]. However, their adoption in hospital environments remains limited, largely due to challenges associated with power consumption and data security [181].

Most current approaches rely on battery-powered systems, including Bluetooth and Zigbee-based technologies, which, despite being designed for ultra-low power consumption, still operate at the milliwatt (mW) level [182]. Capsule-based GORD diagnostic devices and other similar systems often employ strategies such as reducing data collection frequency or incorporating energy-harvesting mechanisms to extend sensor lifespan [181,182]. Nonetheless, energy storage systems, such as batteries or supercapacitors remain essential for powering these devices, introducing several drawbacks. Batteries, while convenient, increase device size and complexity, making integration into compact medical devices more challenging [181]. Additionally, the toxic elements commonly found in batteries raise concerns in clinical settings due to potential biocompatibility issues and environmental risks. Improper disposal and recycling of batteries exacerbate these concerns, with hazardous materials often leaching into water systems, posing threats to ecosystems and public health [181]. Additionally, powered devices require dedicated network infrastructure and strict adherence to data security protocols due to their long-range data transmission capabilities.

A promising alternative to battery-powered systems is the use of passive radio frequency identification (RFID) tags, which rely on electromagnetic signals from a reader to power the sensor, eliminating the need for an internal power source [181]. This not only reduces the size and toxicity concerns of the device but also aligns with sustainable and environmentally friendly design principles. A subset of RFID, near-field communication (NFC), offers an additional advantage in clinical settings due to its short-range communication. Rather than being a limitation, this restricted range enhances security by minimising the risk of unauthorised data interception and

ensuring that interactions only occur between deliberately close-proximity devices. Furthermore, NFC is cost-effective and widely integrated into modern smartphones, making it particularly well-suited for PoC testing, where secure, battery-free data transmission is essential.

The following sections delve deeper into the use of passive RFID technology, with a particular focus on near-field communication (NFC) systems, exploring their potential to transform PoC testing by providing reliable, battery-free data transmission solutions [181].

4.1.1 Passive NFC Sensing Working Principle

Near-field communication (NFC) is a subset of radio-frequency identification (RFID) and operates as a short-range communication system, most commonly utilising the 13.56 MHz RFID band [183]. Although NFC technology has existed for over a decade, its widespread adoption only began with the introduction of secure contactless payment systems, enabling consumers to perform transactions with a single tap [183]. In recent years, there has been growing interest in applying NFC technology to wearable healthcare devices, particularly in biosignal sensing, thermal monitoring, and cardiovascular signal applications [184]. NFC is increasingly recognised as a cost-effective solution for transmitting signals in devices that prioritise miniaturisation and wireless functionality. This makes it a compelling alternative to Bluetooth systems, which, although offering longer ranges, rely on built-in batteries. These batteries result in bulkier and heavier device designs that may compromise user comfort [181,183,184].

Batteryless NFC-based devices have been proposed to enhance wearer comfort due to their compact and simple designs. They have been widely demonstrated in the literature for applications ranging from physiological sensing to pacemaker technology [53,185–188]. Their fundamental operational mechanism is based on electromagnetic induction, primarily using inductive and resonant coupling [189].

The basic principle of NFC operation is derived from Faraday's law of induction, which describes a current passing through a coil generates a magnetic field, and conversely, a time-varying magnetic field induces an electromotive force (EMF) in a nearby coil. This mutual inductance enables energy transfer between the transmitter and receiver coils [189].

For higher efficiency, resonant coupling is used, where a resonator is created by pairing a coil (inductor L) with a capacitor (C) to form a resonant LC circuit. Energy transfer is optimised when the resonance frequencies of the transmitter and receiver coils are matched (Figure 53) [184].

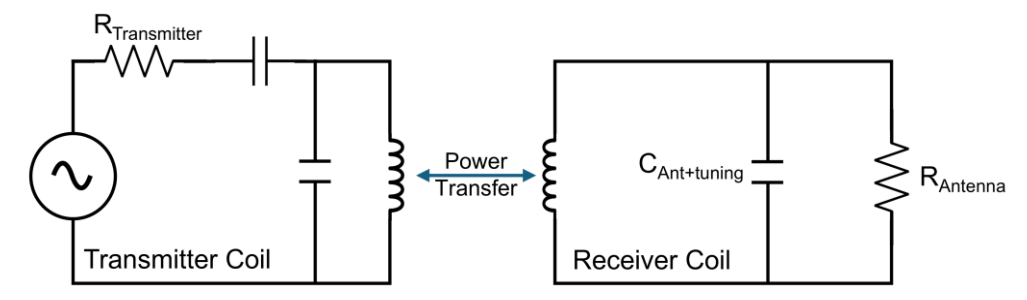


Figure 53: Equivalent circuit diagram of the transmitter and receiver coils demonstrating NFC operation. Recreated from [181,183,189].

The efficiency of this process depends on factors such as the alignment of the coils, their geometry, and the resonance frequency. These design parameters balance power transfer efficiency and device miniaturisation, a critical consideration for wearable and implantable medical devices.

In contrast to near-field method, RFID far-field wireless power transfer utilises radiated electromagnetic waves rather than magnetic coupling [189]. This approach involves antennas instead of coils and can transmit power over significantly longer distances. However, far-field methods are less efficient for power transfer due to higher energy dissipation and lower power density. While suitable for low-power applications like IoT sensors, far-field techniques are generally not ideal for slightly more energy-intensive medical implants or continuous monitoring systems.

4.1.1.1 Coil Geometry

The power induced depends directly on the inductance of the coils, which is determined by their geometry. Consequently, designers face a trade-off between device miniaturisation and power transfer efficiency [184]. The relationship between inductance and coil parameters is described by the equation:

$$L_c = \frac{N^2 \mu A}{I} \tag{30}$$

where L_c is the inductance f the coil, N is the number of turns in the coil, μ is the permeability of material, l is the length of the solenoid coil and A is the area of the coil [184]. This equation indicates that increasing the number of turns (N) has the most

significant impact on inductance. However, increasing the area (A) can also improve power transfer, provided it remains within the limits of the resonant frequency. The resonant frequency, at which maximum power transfer occurs, is defined as:

$$f_{res} = \frac{1}{2\pi\sqrt{L_C C_C}} \tag{31}$$

where C_C is the total capacitance of the device. For biomedical implants, the design must adhere to European implantable biomedical standards, which allow frequency bands up to 2500 MHz for active medical implants [190]. However, lower frequency bands are more commonly used for deep-implanted devices due to better tissue penetration and less signal attenuation.

Another key parameter in NFC design is the quality factor (Q), which determines the sharpness of the resonance peak. It is expressed as:

$$Q = \frac{1}{R_C} \sqrt{\frac{L_C}{C_C}} \tag{32}$$

Where R_C is the coil resistance. The quality factor plays a crucial role in assessing the efficiency of power transfer and signal clarity, particularly in biomedical applications where precision and reliability are critical.

The physical principle for NFC communication is rooted on the mutual inductance (M) between the two inductively coupled coils and which quantifies how effectively magnetic flux from the transmitter coil links to the receiver. Mutual inductance is directly related to the inductances of the two coils (L_1 and L_2) and coupling coefficient k, as expressed by Equation (33) [191].

$$M = k\sqrt{L_1 L_2} \tag{33}$$

Here, k is a dimensionless parameter ranging between 0 (no coupling) and 1 (perfect coupling), dependent on the geometric alignment, spacing, and orientation of the coils.

k can be determined by using electromagnetic field theory which involves solving for M using Neumann's equation [191,192]. For coils with only a few windings that are concentric and parallel with distance (d), M can be reasonably approximated using

$$M \approx \frac{\mu \pi n_1 n_2 a^2 b^2}{\sqrt{(a+b)^2 + d^2} \left[(a-b)^2 + d^2 \right]}$$
 (34)

where a and b are the radii of the two coils; n_1 and n_2 are the windings of the two coils, μ is the permeability of free space. A schematic is included to visualise the parameters leading to the calculation of M (Figure 54).

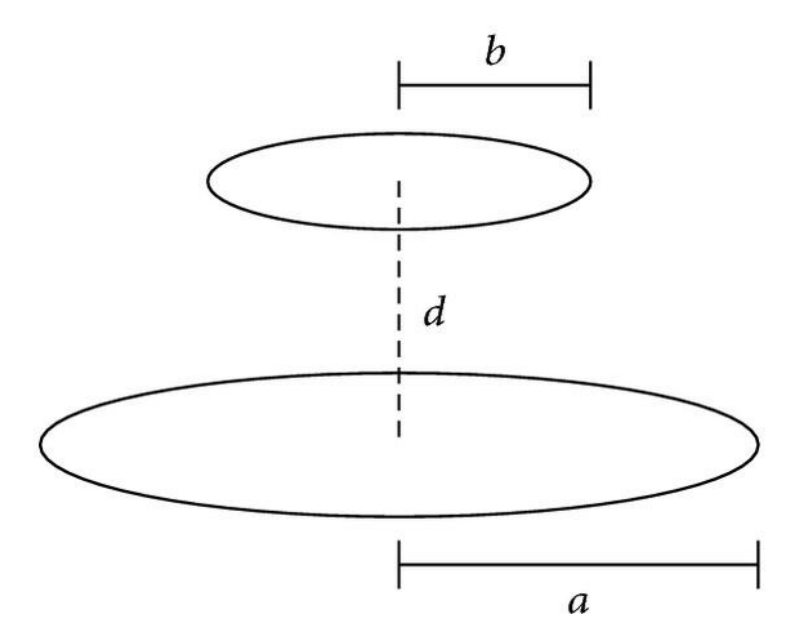


Figure 54: Coaxial coils depicting parameters used to calculate mutual inductance.

4.1.2 Chipped vs Chipless NFC Tags

4.1.2.1 Chipped NFC Sensors

Traditional NFC tags rely on a silicon chip (integrated circuit, IC) for standardised communication procedures. These tags typically transmit data via an I²C (Inter-Integrated Circuit) bus to the NFC IC, following the NFC Data Exchange Format (NDEF). NDEF is a widely adopted standard compatible with most commercial NFC readers, including smartphones, making these systems user-friendly and versatile [181]. A typical setup includes several key components:

- Antenna/Coil: Used to establish communication and induce power from the external NFC reader.
- NFC IC: Responsible for converting the RF signals from the reader into usable power for the tag. It also manages data transmission and often incorporates a microcontroller (MCU) for additional functionality.
- Microcontroller (if external): Used for processing data, interfacing with sensors, and controlling the flow of information. In some designs, the MCU is integrated directly into the NFC IC to reduce size and complexity.

- Sensor interface: Collects analogue signals from the connected sensor and converts them into a format suitable for digital communication.
- Chipped NFC tags offer robust performance but come with inherent limitations.

Data is stored electronically in the chip's memory and allows for increased data storage and more advanced features such as encryption for privacy [181]. A significant challenge is their current consumption, typically requiring currents ranging from hundreds of microamperes to a few milliamperes per reading [193]. This in turn limits the range of the NFC as the mutual inductance required is high to power it.

4.1.2.2 Chipless NFC Sensors

Recent advancements in passive RFID technology have led to the development of chipless passive RFID sensors, which eliminate the integrated chip typically found in traditional RFID systems. Instead, these systems rely on metallic resonators to facilitate communication and sensing. This innovation has made chipless sensors not only more cost-effective but also more robust in operation, particularly in applications requiring large-scale deployment or operation in challenging environments [181,194].

Chipless RFID sensors operate by leveraging changes in the physical or electromagnetic properties of the resonators in response to specific environmental parameters. These resonators are often printed metallic structures designed with two intrinsic characteristics: effective permittivity and effective length. Effective permittivity governs the interaction between the resonator and surrounding electromagnetic fields, while effective length determines the resonant frequency and overall performance of the device [194].

In practice, the reader emits an interrogation signal, typically an oscillating current carrying electromagnetic energy, which interacts with the sensor tag [194]. This interaction generates a backscattered signal whose properties, such as resonant frequency, quality factor, amplitude, or phase, are modulated by environmental conditions like temperature, humidity, or pressure [194]. These modulated signals are then detected and interpreted using tools such as vector network analysers or impedance analysers, providing calibrated data about the sensed parameter [194].

One of the most significant advantages of chipless design is its energy efficiency. By eliminating the chip, which traditionally consumes power, chipless sensors can operate over much greater distances without significant power losses [181,194]. This

extended range, combined with reduced energy demands, makes chipless systems particularly attractive for applications requiring long-range sensing [181,194]. Additionally, the absence of a chip reduces manufacturing costs and simplifies the design, making these systems ideal for cost-sensitive and large-scale implementations [181,194]. The durability of metallic resonators also enhances the reliability of these sensors in demanding environments, further broadening their applicability [194].

While chipless RFID sensors offer significant advantages in terms of cost, energy efficiency, and long-range capabilities, they come with notable challenges that complicate their real-world deployment. One major issue is the increased signal processing complexity required on the reader side. Unlike chipped systems, which rely on integrated circuits for signal handling, chipless systems require sophisticated algorithms to interpret the backscattered signal. This complexity arises from the need to decode subtle modulations in parameters like resonant frequency, amplitude, or phase, which can be influenced by environmental noise and interference [194]. Signal interference is particularly problematic in environments with multiple overlapping electromagnetic sources, making precise calibration essential for reliable operation.

Structural robustness of the sensor itself is another critical concern. Chipless sensors typically employ metallic resonators printed on flexible substrates, which makes them susceptible to bending, stretching, or cracking. Such mechanical deformations can alter the intrinsic properties of the resonators, including effective permittivity and length, leading to poor selectivity and potentially false readings [194]. This is especially problematic in applications requiring repeated handling or exposure to dynamic forces.

Additionally, the quality of the conductive ink used for printing resonators and the encapsulation methods employed to protect the sensor play pivotal roles in determining device performance and durability [194]. Variations in the conductivity of the ink, insufficient adhesion, or suboptimal encapsulation can degrade the sensor's functionality, particularly in harsh sensing environments such as extreme humidity or temperature fluctuations [194].

Another critical challenge lies in calibration for specific environments. Chipless sensors are highly sensitive to their surroundings, which can lead to variations in signal response under different operational conditions [194]. Ensuring accurate calibration

across diverse environments is vital to maintaining the reliability of the sensing data. However, achieving this consistency can be resource-intensive and time-consuming, particularly for large-scale deployments [194].

Finally, chipless systems face limitations in data security and privacy, especially in medical applications where encryption and authentication are critical [181,194]. Unlike chipped systems, which often incorporate advanced encryption algorithms, chipless systems inherently lack these capabilities [181,194]. While adding ID bits to each tag can provide a rudimentary form of identification, this approach is insufficient for meeting stringent privacy requirements in sensitive applications like healthcare.

4.1.3 Potentiometric pH Sensing Using NFC

Devices for pH measurement come in various forms and operate based on distinct measurement principles, as discussed earlier in this thesis. One notable class includes colorimetric devices, which determine pH by analysing shifts in the HSV colour space. These systems have been integrated with NFC technology to enable batteryless operation, offering a compact and efficient solution for pH sensing [193]. Another significant category includes potentiometric sensors, which often employ screen-printed inks tailored for applications such as wound monitoring [186]. These sensors frequently use polyaniline as the working electrode due to its favourable electrochemical properties [70,71,186]. Potentiometric devices have been demonstrated on diverse substrates, including polymers [54], textiles & fabrics [195], temporary tattoos [70], and paper [40,62], showcasing their versatility. Many of these have been paired with NFC technology through various strategies, adopting either chipped or chipless configurations to facilitate wireless data transmission and enhance usability.

A noteworthy example is the work by Bhadra et al., who employed a standard glass pH electrode for remote pH monitoring via a chipless coupled coil sensor-interrogator system [196]. In this system, the sensor's capacitance varied as a function of the potential difference generated by the glass electrode in response to pH changes. The resonant frequency (f_{res}) was given by

$$f_{res} = \frac{1}{2\pi\sqrt{L_C C(V_{pH})}} \tag{35}$$

where $L_{\mathcal{C}}$ is the inductance of the coil, and $\mathcal{C}(V_{pH})$ is the capacitance of the resonant sensing circuit dependent on the open-circuit potential (V_{pH}) [196]. An impedance analyser was used to measure the resonant frequency, as depicted in the block diagram (Figure 55).

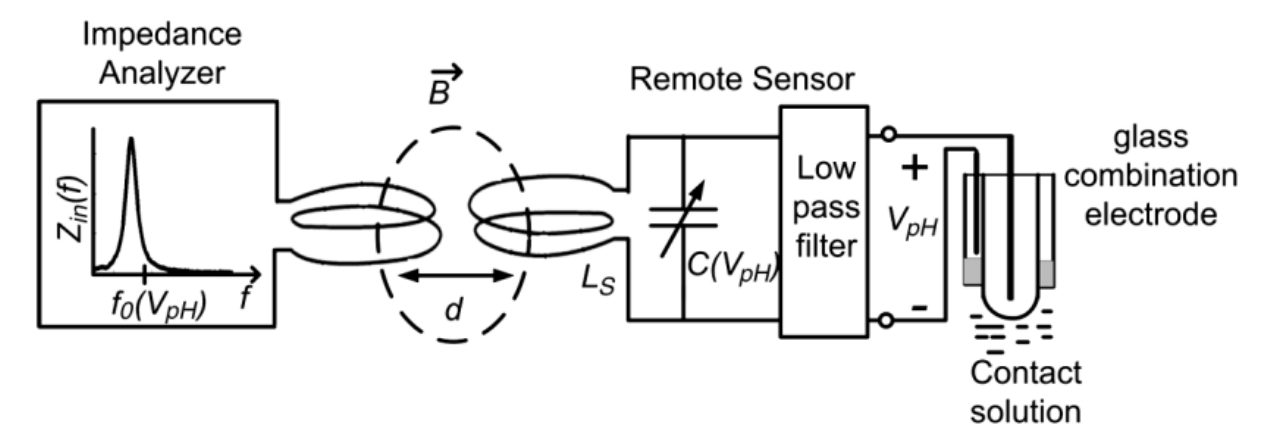


Figure 55: Block diagram of a wireless, chipless, NFC-based pH sensor, demonstrating frequency variation with pH. Figure sourced from [196].

In Bhadra et al.'s design, the sensor coil had a diameter of 6.7 cm, while the interrogator coil was 5.1 cm, operating at approximately 28 MHz. Although these dimensions and operating frequencies are unsuitable for compact GORD sensing applications, the system demonstrated a working range of up to 18 cm. This exceeds the range required for such applications, highlighting its potential for future adaptation and optimisation.

4.1.4 Batteryless, implantable pH sensors using NFC

Batteryless pH sensors leveraging NFC technology have been demonstrated, wherein a reader (transponder) interprets radio-frequency signals using a design similar to that of Bhadra et al., termed the Batteryless Endoluminal Sensing Telemeter (BEST) device by Cao *et al.* [196–198]. In it they improved on the design of Bhadra et al. by incorporating operational amplifiers to convert variations in capacitance and open-circuit potential into a frequency-varying output via relaxation oscillator circuitry. Specifically, the electrical potentials generated by the sensor result in an increase in the output frequency of the relaxation oscillator for acidic solutions and a corresponding decrease for alkaline solutions [198]. Figure 56b depicts how the frequency response was described by equation

$$f_{pH} \propto \frac{1}{R_1 \times C_1 \times V_{\text{pH}}} \tag{36}$$

Where R_1 and C_1 are the resistor and capacitors of the IC, and $V_{\rm pH}$ denotes the voltage generated by the iridium oxide sensor, ranging from +0.5 V to -0.1 V. This resulted in a monotonically decreasing frequency response with increasing pH from 30.95 kHz (at pH 1) to 24.25 kHz at (pH 12).

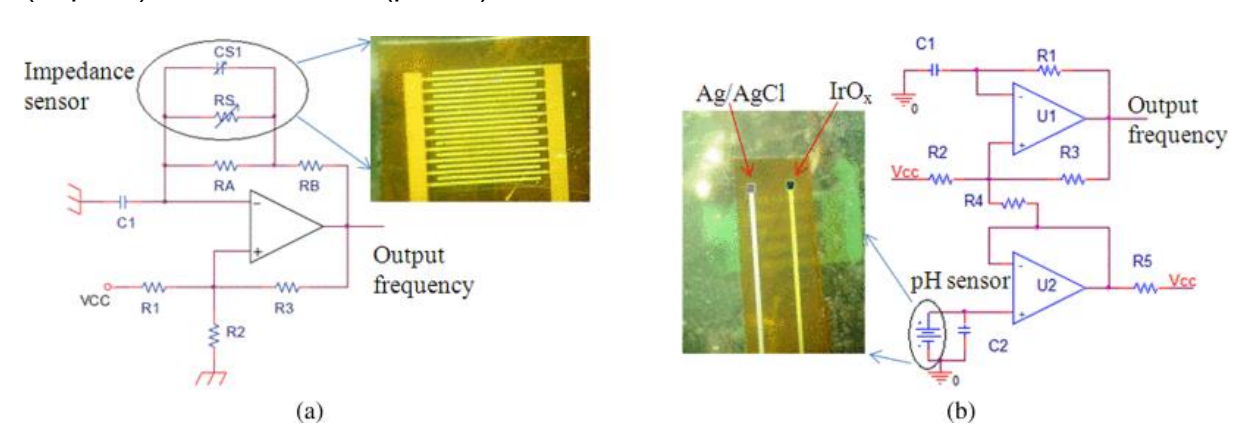


Figure 56: Relaxation oscillator circuitry for the BEST sensors: (a) impedance sensor and (b) pH sensor, as developed by Cao et al. (Sourced from [198]).

The design comprised an implant constructed using 34-AWG magnet wire coiled to achieve an inductance of 22 μ H. The reader unit featured a power amplifier for energy transmission and a 12 × 12 cm coil antenna with an inductance of 17 μ H, coupled with a wireless module capable of transmitting data to a transceiver located up to 35 metres away [198]. After encapsulation in polydimethylsiloxane (PDMS), the implant had a final size of 0.4 cm × 0.8 cm × 3.8 cm [198]. They were able to achieve readings of up to 12 cm between the coils with a drain voltage of 9 V at the reader site.

Li et al. advanced this field by developing passive, wireless sensors for continuous pH monitoring within a fully bioresorbable package [53]. Their design utilised a pH-responsive hydrogel that swells upon exposure to acidic conditions. The coil, fabricated from high-purity zinc thin-sheet material, was laser-cut into a serpentine geometry and encapsulated within the hydrogel. A parallel-plate capacitor, constructed using bioresorbable polymers and enclosed in wax, functioned as a fixed tuning capacitor [53]. The swelling of the hydrogel induced a physical expansion of the coil, thereby increasing its inductance and producing a pH-dependent inductance response [53]. The total diameter of the device was 1 cm, and the corresponding change in real impedance was done by performing a sweep with a vector network

analyser from 10-25 MHz [53]. The drawbacks of this device were that the pH sensing range was limited to pH 5-8 and that the response time was approximately 1 hour [53].

4.2 Turning the sensors into a standalone biomedical device

4.2.1 Introduction

Following the successful fabrication of a robust, biocompatible, and pH-sensitive working electrode, efforts were directed towards developing a portable, standalone sensing device. This development aligns with the overarching aim of this work: to construct an implantable diagnostic tool tailored for gastro-oesophageal reflux disease (GORD) diagnosis. While the BEST capsule has shown efficacy in its extended sampling time, range, and ability to detect non-acidic reflux events, it shares a critical limitation with the Bravo® capsule—reduced patient comfort and tolerability [44,197,198]. As detailed earlier in this thesis, patient comfort is pivotal for improving diagnostic accuracy. Enhanced comfort reduces the likelihood of patients altering their lifestyle habits during the monitoring period, a factor that can compromise the reliability of collected data.

Key improvements to patient comfort stem from using soft, flexible materials and optimising the affixing mechanism to the oesophageal epithelial lining. The validation of the affixing methodology was presented in Chapter 5 (*Biocompatible Mucoadhesives*), addressing a significant component of this challenge. However, the remaining hurdle involves integrating flexible, biocompatible materials into the sensing device's design to enhance tolerability and ensure continuous, accurate monitoring.

An initial active design utilising a Bluetooth Low Energy (BLE) framework is presented in the Appendix. While this design demonstrates potential in addressing data transmission requirements, it fails to meet the essential criteria of being soft and flexible—qualities necessary for enhancing patient comfort and achieving minimally invasive, long-term monitoring.

4.2.1.1 Requirements and Design Challenges

After consulting with gastroenterologists, a detailed list of device requirements was established to ensure clinical applicability. These include:

1. Dimensional Constraints:

The device must fit within the working channel of a standard endoscope, which typically ranges from 2.8–3.2 mm in diameter, with an upper limit of 3.8 mm. The device's length is more flexible but must accommodate ease of insertion and removal.

2. Sampling Frequency:

The device should be capable of recording pH measurements at intervals of 7 seconds or less, ensuring high-resolution data collection.

3. Operational Duration:

The device must function continuously for a minimum of 48 hours and ideally up to 96 hours, accommodating prolonged diagnostic periods.

4. Biocompatibility:

All components in contact with the body must be inert, non-toxic, and biocompatible to minimise adverse tissue responses.

5. Data Transmission:

The device must transmit data effectively through human tissue over distances exceeding 8 cm, to account for variations in patient size and anatomy.

These requirements present significant engineering challenges, particularly regarding miniaturisation, ultra-low power operation, and advanced fabrication techniques. The need for ultra-low power consumption is particularly critical, as batteryless or energy-efficient solutions are preferred to achieve a compact design while ensuring adequate device performance. Furthermore, achieving reliable wireless communication at the required transmission range necessitates optimising the device's antenna or communication protocols to overcome attenuation caused by human tissue.

This work presents the development of a wireless, batteryless, pH sensor for *in vivo* monitoring of reflux events. The implant uses printed coils constructed from flexible inks to achieve a fully flexible and soft design.

4.2.2 Design and Fabrication

The system was designed to have a fixed inductor that is connected to a variable capacitor in series as shown in Figure 57. The variable capacitor connected in series forms an LC circuit that resonates at a frequency (f_{res}) described by

$$f_{res} = \frac{1}{2\pi\sqrt{LC(\text{pH})}}\tag{37}$$

where L is the inductance, C is the capacitance of the interdigitated electrode design which is dependent on pH as shown in the previous chapter. The interdigitated capacitor design ensures that its dielectric properties are modulated by pH, enabling the system to detect reflux events accurately. The resonant frequency (f_{res}) serves as the readout parameter, allowing wireless interrogation through magnetic coupling.

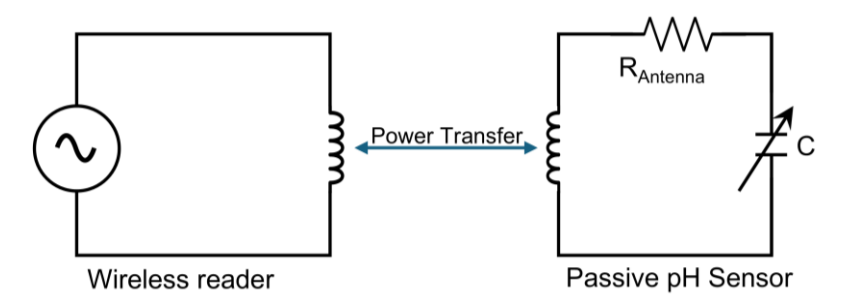


Figure 57: Operating principle of the flexible, batteryless device.

4.2.2.1 Coil and Sensor Fabrication

Four sensor designs were evaluated for the coils, with a primary focus on minimising both DC and AC resistance to maximise the quality (Q) factor. The Q factor, a critical parameter for enhancing the potential reading distance, is defined as:

$$Q = \frac{1}{R} \sqrt{\frac{L}{C}} \tag{38}$$

where L is the inductance, C is the capacitance, and R is the resistance of the coils.

4.2.2.2 Coil Configurations and Design Parameters

The first design featured a single-sided coil layout comprising 19 turns with a spacing of 198 μm and a coil width of 300 μm (Figure 58A). In contrast, the second design adopted a two-sided configuration with the same number of turns but included via-thru holes for interlayer connectivity (Figure 58B). This design employed a larger coil width of 600 μm and a spacing of 295 μm . Both configurations were optimised to produce an inductance of approximately 3.1 μH , determined via Finite Element Analysis simulations in ANSYS Maxwell. The simulations assumed a coil height of 100 μm , achievable through layer-by-layer direct-write ink printing, as described in earlier sections of this thesis.

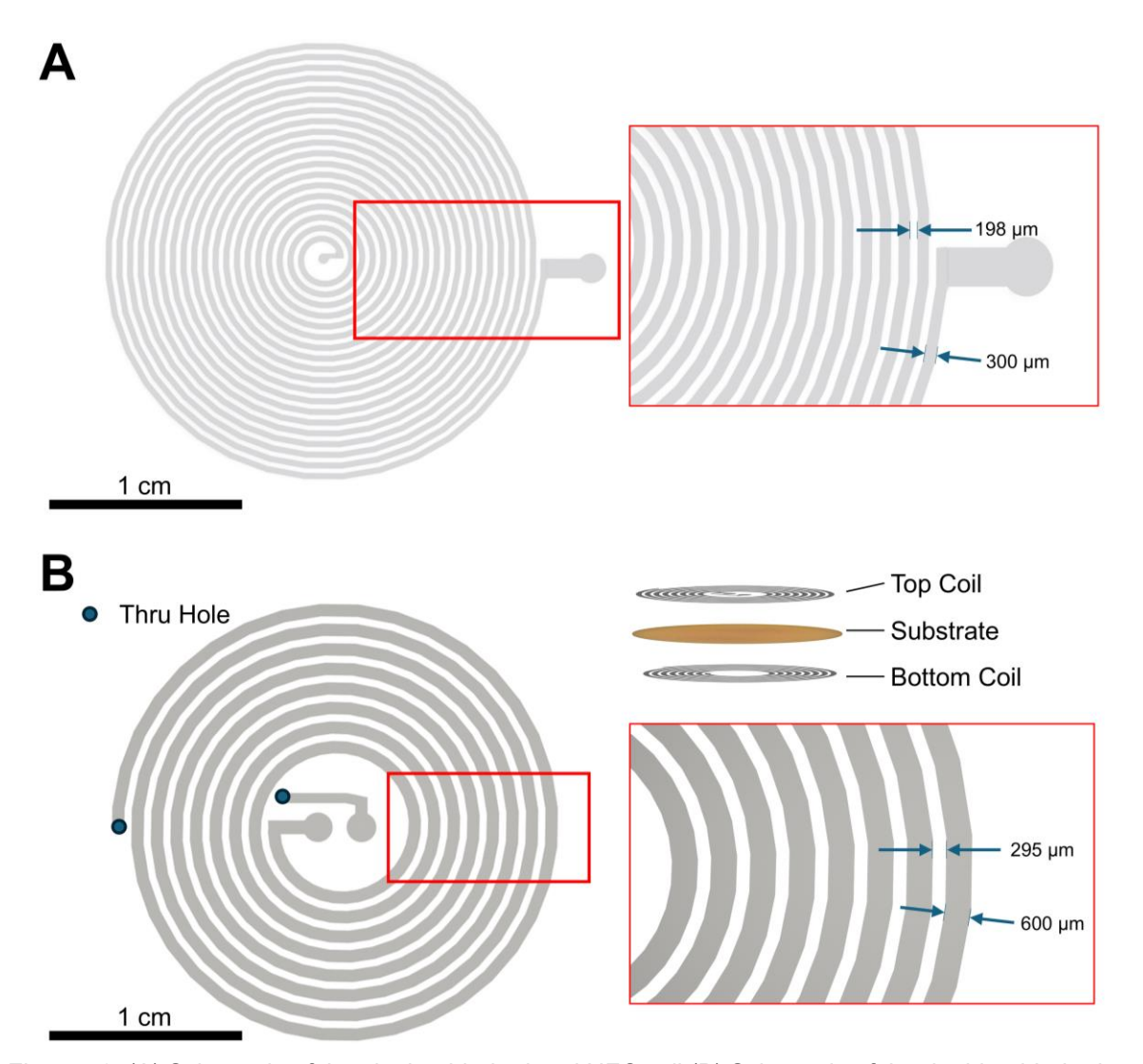


Figure 58: (A) Schematic of the single-sided printed NFC coil (B) Schematic of the double-sided printed NFC coils with via Thru holes connecting both sides to form one larger NFC coil.

4.2.2.3 Material Selection for Improved Performance and Durability

Two additional designs addressed material considerations, focusing on either a single conductive ink or a dual-ink approach:

- 1. The single-ink design employed a silver electronic screen-printable ink (DM-SIP-2005) from Dycotec Materials. This ink was selected due to its favourable properties, including high conductivity, excellent adhesion, and flexibility. These characteristics made it suitable for creating reliable and mechanically stable conductive tracks on the polyimide substrate.
- Dual-Ink Design: Combined two inks to address the limitations of each. The base layer used a silver nanoparticle ink (30% in ethylene glycol, Sigma Aldrich) sintered at 240°C for 4 hours to achieve a resistivity of ≤7 µΩ-cm. This layer

was encapsulated with the Dycotec screen-printable polymer silver ink. The dual-layer strategy improved crack resistance during bending and enhanced adhesion to the polyimide substrate (100 µm thickness, Goodfellow UK). The top layer acted as a bridge to maintain conductivity in the event of micro-cracks, leveraging the robust polymer matrix of the screen-printable ink.

The dual-ink design required precise alignment between layers. After sintering the silver nanoparticle ink, the substrate was realigned using reference markers on a direct-write printer. The screen-printable ink was then deposited, increasing the overall height of the coil to further reduce resistance and enhance robustness against mechanical stress.

Further optimisation involved exploring variations in the width of the silver nanoparticle tracks within the dual-ink coils to determine their effect on overall resistance. The cross-sectional and top-view designs used in the coil fabrication process are shown in Figure 60. The encapsulating polymer layer provided enhanced robustness, functioning as a protective barrier to prevent degradation from mechanical or chemical stresses. All designs were then fully encapsulated in biocompatible polydimethylsiloxane (PDMS) SLYGUARD-184 using direct-write printing.

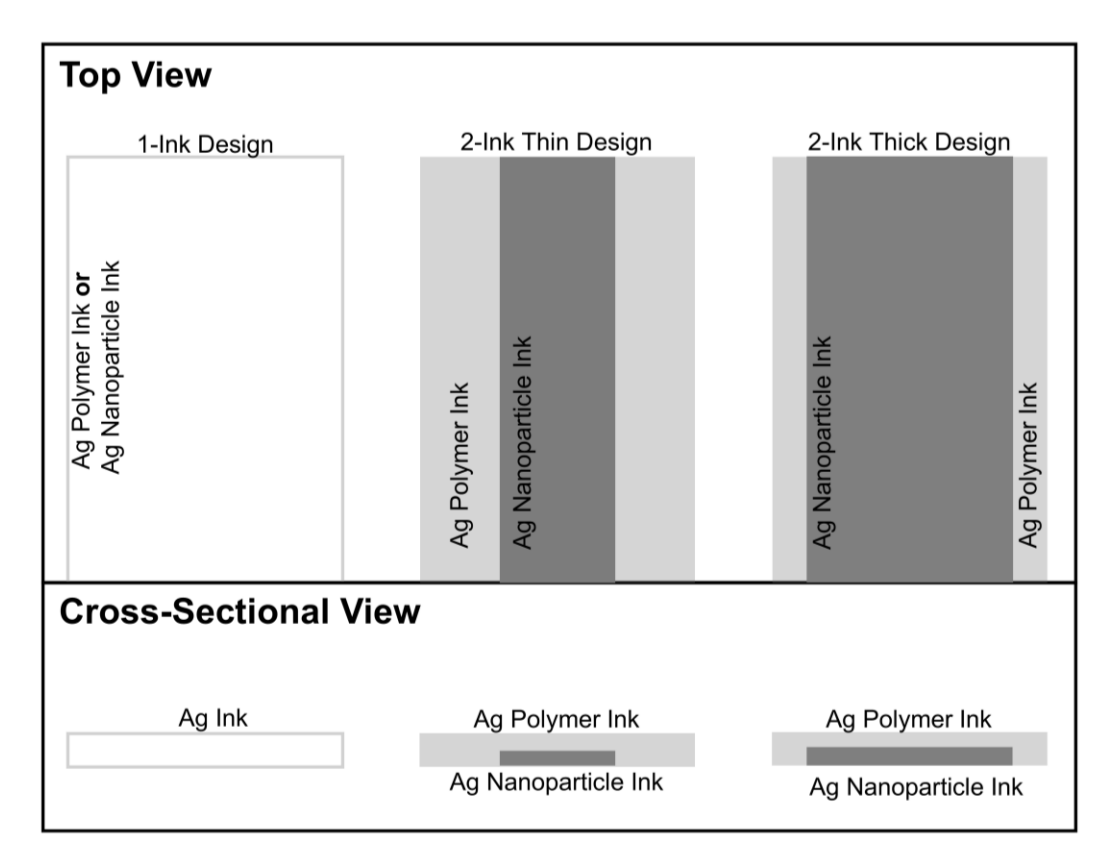


Figure 59: Different coil fabrication strategies using 1-ink, 2-ink (thin silver nanoparticle design) and 2-ink (thick nanoparticle design).

4.2.2.4 Measurement Protocol

The sensor employed a frequency-based pH detection mechanism. Measurements were performed using an impedance analyser that swept the frequency range from 1 MHz to 20 MHz at a speed of 2 MHz per second. The impedance $(Z_{in}(f))$ of the system is described by

$$Z_{in}(f) = Z_1 + Z_T = R_1 + j2\pi f L_1 + \frac{(2\pi f)^2 M^2}{Z_s}$$
 (39)

where Z_1 represents the primary coil in isolation which includes resistive losses (R_1) and inductive reactance $(j2\pi f L_1)$. Z_T refers to the impedance contribution from the coupled secondary coil which represents the effect of energy transfer through magnetic coupling which is described by the last term of Equation (39). Z_s represents the impedance of the secondary coil, which modulates this term.

M is redescribed here for clarity purposes.

$$M = k\sqrt{L_1 L_2} \tag{33}$$

Simulated data, generated using Equations (33), (37) and (39), demonstrates the impact of reducing the resistance of the sensor coil (R_2) while keeping all other parameters constant, emphasising the importance of minimising resistance (Figure 60). At approximately 50 ohms for (R_2), the resonance frequency becomes indistinct (Figure 60A). The parameters for the simulation are detailed in Table 5.

A low coupling coefficient (k=0.1) was intentionally selected to represent a scenario with minimal mutual inductance. The tuning capacitor value (C_1) was chosen based on empirical measurements conducted with the impedance analyser over a frequency range of 1–20 MHz, scanned at a rate of 2 MHz per second. For these measurements, the sensor was physically connected to the impedance analyser using wires. Lower scan rates introduced greater variability in capacitance values at different frequencies, which was unsuitable for the intended measurement type. Supporting data from these experiments are provided in the appendix.

Table 5: Simulation parameters for wireless sensing

Parameter	Value
Primary coil resistance R ₁ (impedance analyser)	10 Ω
Secondary coil resistance R ₂ (sensor)	10-100Ω
Primary coil inductance L_1	3.1 µH
Secondary coil inductance L_2	3.1 µH
Couling coefficient k	0.1
Primary coil capacitance C_1	170 pF

From the supporting data, frequencies below the resonant frequency exhibited relatively stable capacitance values, which varied according to pH. This behaviour was consistent with expectations and is depicted in Figure 60B, where the resistance of the secondary coil was fixed at 10 Ω for clarity. Variations in resonant frequency, as predicted by Equation (37), are evident from the simulated data, enabling accurate pH differentiation based on the resonance response observed during frequency sweeps.

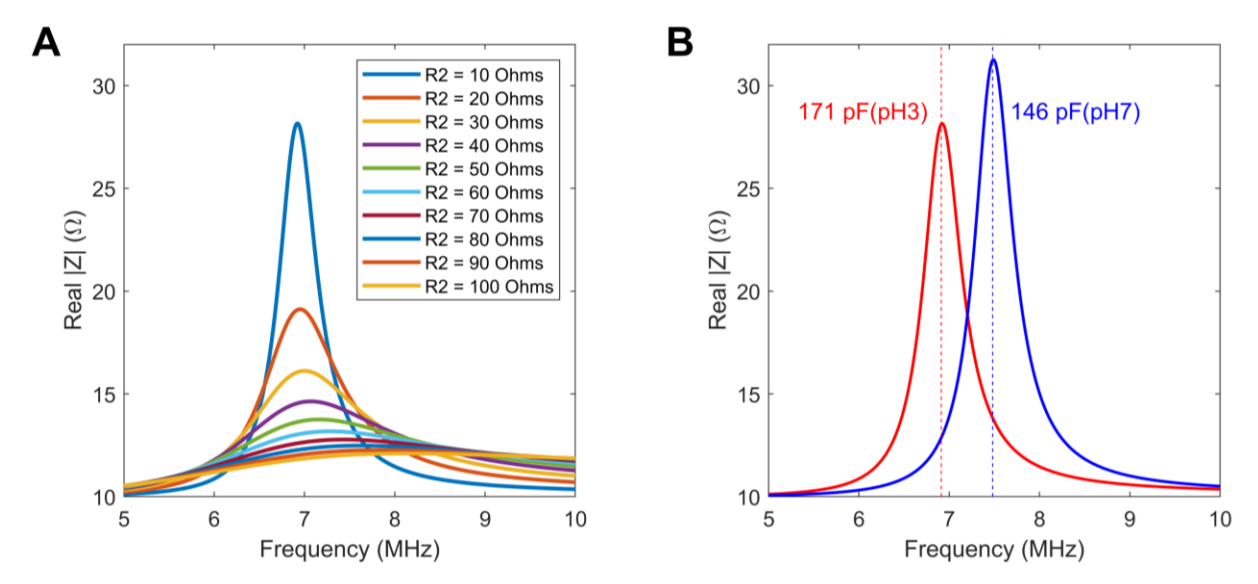


Figure 60: **(A)** Simulated impedance analyser data showing resonance frequency for a 3.1 μ H inductor with varying sensor coil resistances (R_2) at a reference capacitance corresponding to pH 3. Higher R_2 values lead to indistinct resonance peaks, highlighting the importance of minimising resistance. **(B)** Simulated frequency shifts based on empirical capacitance values measured for pH levels 3 and 7, demonstrating the clear relationship between capacitance changes and resonant frequency as predicted by Equation (37).

The capacitance range of the sensor can also be tailored by modifying the physical and material properties of the interdigitated electrodes (IDE) [199]. This is described by:

$$C_{IDE} \propto \frac{\varepsilon L t \alpha \beta N}{d} \tag{40}$$

where the effective permittivity (ε), represents the combined dielectric properties of the materials in the sensor package, such as PDMS, polyimide, and air. The length of the electrode fingers (L) contributes to the charge accumulation area, directly affecting the capacitance [199]. The thickness of the conductive tracks (t) made from the silver ink influences the electric field distribution. Additionally, the gap (d) between adjacent electrode fingers is a critical parameter, as smaller gaps increase capacitance while introducing fabrication challenges [199]. Increasing the number of finger pairs (N) enhances the overlap of the electric fields, which increases capacitance [199].

To account for secondary effects, correction factors α and β are introduced. The factor α captures the influence of polymer thickness on the electric field, with thicker polymer layers modifying how the electric field interacts with the dielectric material [199]. The factor β accounts for fringe effects, which describe the extension of electric fields

beyond the immediate boundaries of the electrode fingers [199]. These fringe effects become more prominent with wider finger spacing or thicker dielectric layers. By adjusting these parameters, the IDE sensor can be optimised for specific applications, ensuring precise control of its capacitance range [199].

Finally, the experimental setup used to measure the magnetic field received at the antenna is depicted in Figure 61. It consists of a primary reading coil connected to an impedance analyser (Wayne Kerr electronics-6500B), which facilitates the transmission and monitoring of signals. A linear track mechanism is employed to precisely adjust the distance between the primary coil and the secondary coil (sensor), enabling controlled measurements of the coupling and field strength at varying separations. The secondary coil is integrated with a capacitive load to emulate the behaviour of the sensor circuit.

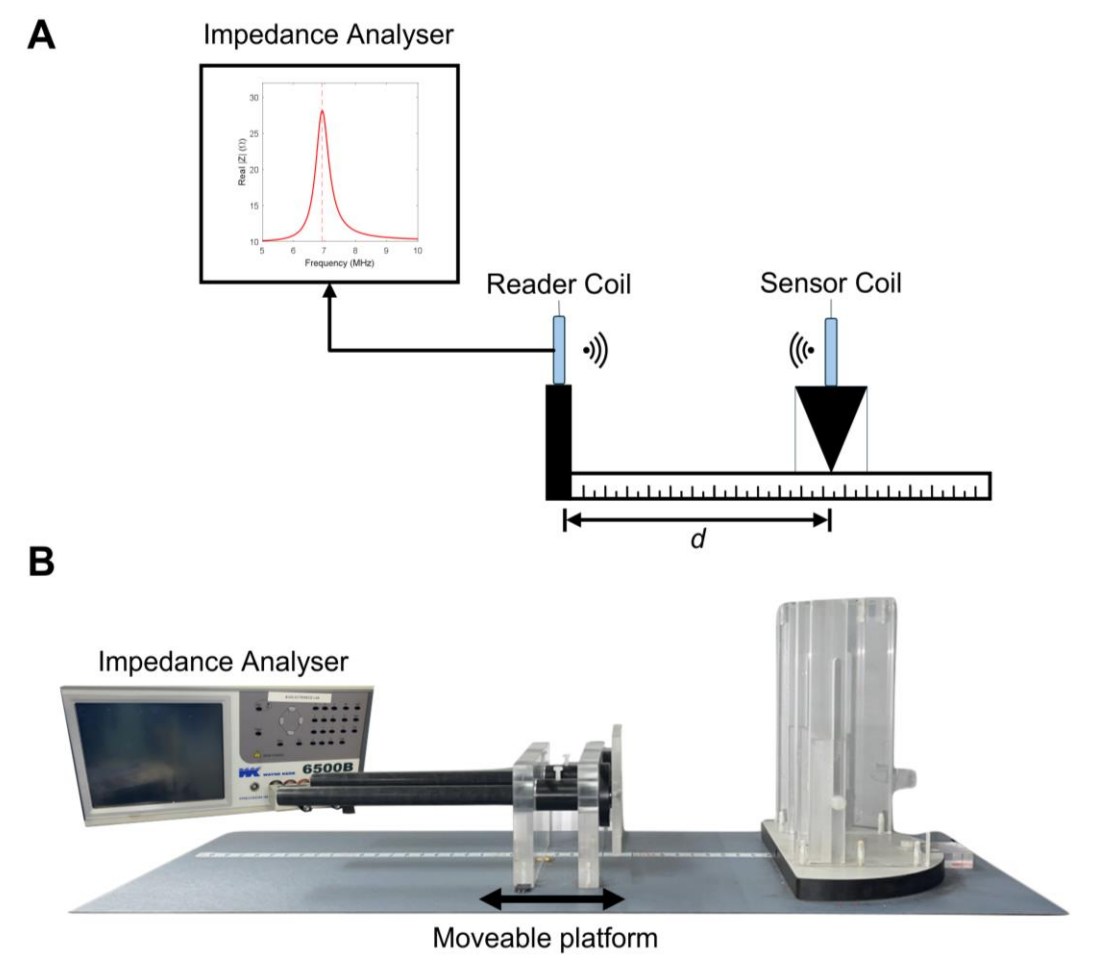


Figure 61: Schematic (A) and image (B) of apparatus to measure the magnetic field with an impedance analyser with a built-in voltage supply.

4.2.3 Results

4.2.3.1 Design and Fabrication

For easier identification of the fabrication differences and results, the results are presented on a case-based basis where the ink(s) used and designs used varies as presented in Table 6.

Table 6: Fabrication designs identifiable by case numbers.

Case	1-Sided / 2-Sided Design	Ink(s) used	Design used
1	1-Sided	Ag Polymer Ink	Thick
2	1-Sided	Ag Nanoparticle Ink	Thick
3	1-Sided	Ag Nanoparticle + Ag Polymer Ink	Thin Nanoparticle, Thick Polymer
4	1-Sided	Ag Nanoparticle + Ag Polymer Ink	Thick Nanoparticle, Thick Polymer
5	2-Sided	Ag Polymer Ink	Thick
6	2-Sided	Ag Nanoparticle Ink	Thick
7	2-Sided	Ag Nanoparticle + Ag Polymer Ink	Thin Nanoparticle, Thick Polymer
8	2-Sided	Ag Nanoparticle + Ag Polymer Ink	Thick Nanoparticle, Thick Polymer

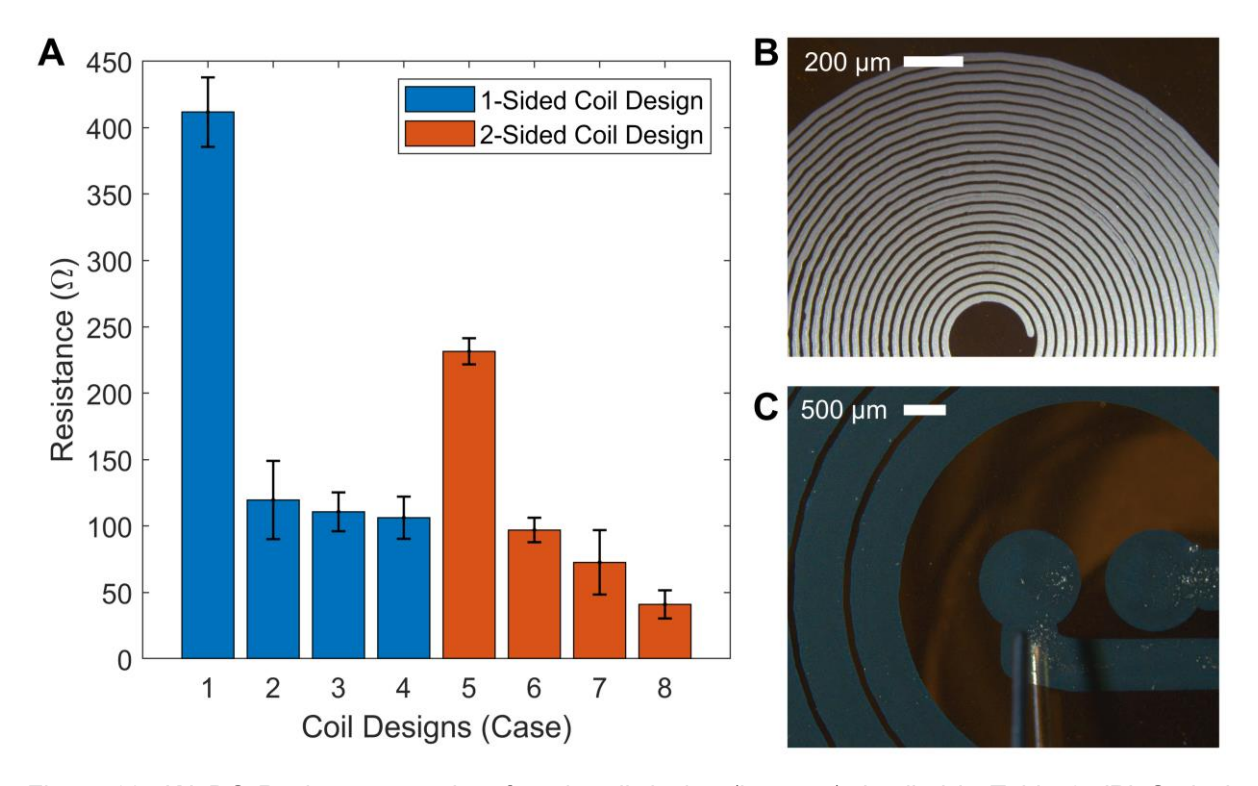


Figure 62: **(A)** DC Resistance results of each coil design (by case) detailed in Table 6. **(B)** Optical microscope images showing the 1-sided coil design vs the 2-sided coil design **(C)**.

Case 8, which incorporates the use of two conductive inks in a thicker configuration, demonstrates superior performance compared to other designs (Figure 62A). This configuration was the only one capable of achieving sufficiently low resistance values to enable discernible frequency shifts in response to capacitance changes introduced by the GO+COF interdigitated electrode composite, as shown in Figure 60. The use of thicker conductive layers enhances current-carrying capability and minimises resistive losses, critical for achieving the sensor's operational requirements.

Additionally, the results highlight the importance of overall track length in resistance optimisation (Figure 62A). The 2-sided coil design significantly shortens the total track length compared to the 1-sided design, further contributing to reduced resistance. As indicated in Figure 62, the shorter path length inherent to the 2-sided design minimizes resistive contributions due to track geometry, improving its overall performance.

While the 1-sided coil design (Figure 62B) demonstrates lower resistance values in some configurations, the enhanced width and thickness of the 2-sided coil (Figure 62C) offer a more effective reduction in DC resistance when combined with the dual-ink approach. This outcome aligns with Pouillet's Law (Equation (41)), which relates resistance (R) to the length (l) and cross-sectional area (A) of the conductive material:

$$R = \rho \frac{l}{A} \tag{41}$$

Here, ρ is the resistivity, an intrinsic property of the material. Increasing the cross-sectional area or reducing the length of the conductive path directly decreases the resistance. The 2-sided design's larger cross-sectional area and reduced track length thus result in improved conductivity and reduced resistive losses.

Impedance analyser measurements of the Case 8 samples revealed consistent inductance values between samples within the frequency range of 1–10 MHz, indicating that the design achieved the expected performance criteria (Figure 63A). The inductance, primarily influenced by the number of coil turns, remained relatively stable around 3.1 μ H in the frequency range of 1–4 MHz. Beyond this range, the inductance increased gradually, reaching approximately 4.5 μ H at 10 MHz. This

increase can be attributed to frequency-dependent magnetic field interactions and parasitic effects inherent in the coil design.

An increase in resistance and inductance was also observed at higher frequencies (Figure 63B). This behaviour can be explained by the combined effects of skin and proximity effects, which become more pronounced as the frequency increases. The skin effect reduces the effective cross-sectional area of the conductor at higher frequencies, leading to a rise in AC resistance. The proximity effect, caused by magnetic field interactions between adjacent coil turns, induces circulating currents within the conductor, further increasing resistance and influencing the effective inductance.

The use of screen-printed conductive inks introduces additional considerations, particularly the percolation effect associated with the silver nanoparticle ink. Conductivity in such inks depends on the formation of a conductive network through particle-to-particle contact. At higher frequencies, localised impedance mismatches within the printed layer may disrupt this network, leading to uneven current distribution and exacerbating resistive losses. This underscores the importance of achieving uniform ink deposition and maintaining sufficient nanoparticle density during fabrication to ensure optimal performance.

The quality factor, or Q-factor, exhibited a steady increase up to approximately 7.5 MHz before declining. This trend reflects the interplay between inductance, resistance, and reactance, with the Q-factor peaking where the ratio of inductive reactance to resistance is most favourable. The subsequent decrease in Q-factor at higher frequencies corresponds to the increased resistive losses observed. The impedance measurements similarly showed a consistent rise, exceeding 300 ohms at higher frequencies, which aligns with the resistance trends depicted in Figure 67A. The Q-factor also aligned with similar values as ones reported in literature, despite the significantly increased relative number of turns [200].

Despite these frequency-dependent challenges, the overall results were satisfactory and closely matched the simulated values. The inductance stability across much of the measured frequency range, coupled with reasonable Q-factor and impedance behaviour, confirms the viability of the Case 8 design and supports its progression to further testing.

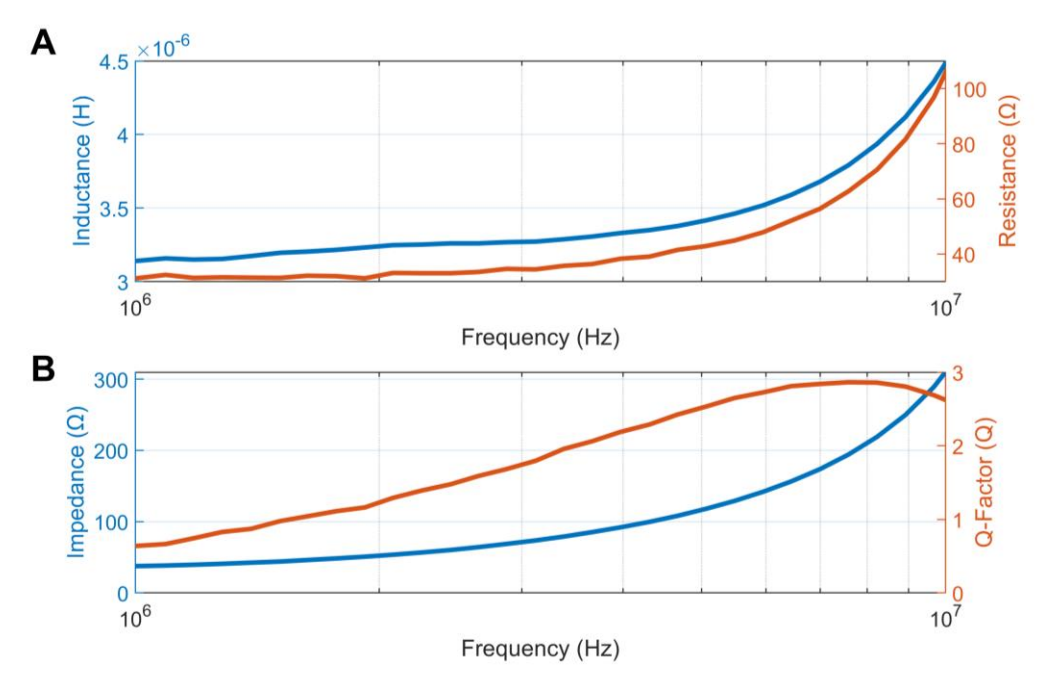


Figure 63: (A) Inductance and resistance values measured from an exemplar Case 8 sample across the frequency range. (B) Impedance and Q-factor values measured from the same Case 8 sample, highlighting the frequency-dependent behaviour of the design.

The GO and COF composite, as developed and detailed in Chapter 3, functions as a selective pH-sensitive capacitive sensor. When integrated with the Case 8 coil, this sensor operates as a tuning capacitor, producing a response consistent with the simulated results presented in Figure 60. This behaviour demonstrates the ability of the GO+COF composite to detect pH changes via capacitance modulation, making it an integral component of the overall sensor design.

To implement this system, the Case 8 coil was designed with interdigitated electrodes (IDE) and integrated with a sprayed-on layer of the GO+COF composite, as shown in Figure 64. The sprayed application method allowed for a uniformly thin coating.

To protect the sensor from environmental and operational challenges, the coils were encapsulated in a layer of polydimethylsiloxane (PDMS) applied via direct-write printing. The PDMS served multiple critical functions. First, it acted as a biocompatible encapsulant, shielding the printed conductive tracks from exposure to the acidic pH solution and ensuring long-term durability. Second, it provided mechanical stability, helping the printed ink tracks adhere securely to the flexible polyimide substrate, even under wet or corrosive conditions.

Additionally, the PDMS encapsulation served a makeshift droplet reservoir. This design ensured that the acidic solution (in this case the simulated gastric acid)

uniformly covered the GO+COF sheet, maintaining consistency in the capacitive measurements. By facilitating full coverage of the sensor surface, the PDMS reservoir eliminated inconsistencies that could arise from variations in droplet shape or size. This approach ensured that the capacitive response was influenced primarily by the proton concentration in the solution, rather than by the extent of the sensor surface exposed to the droplet.

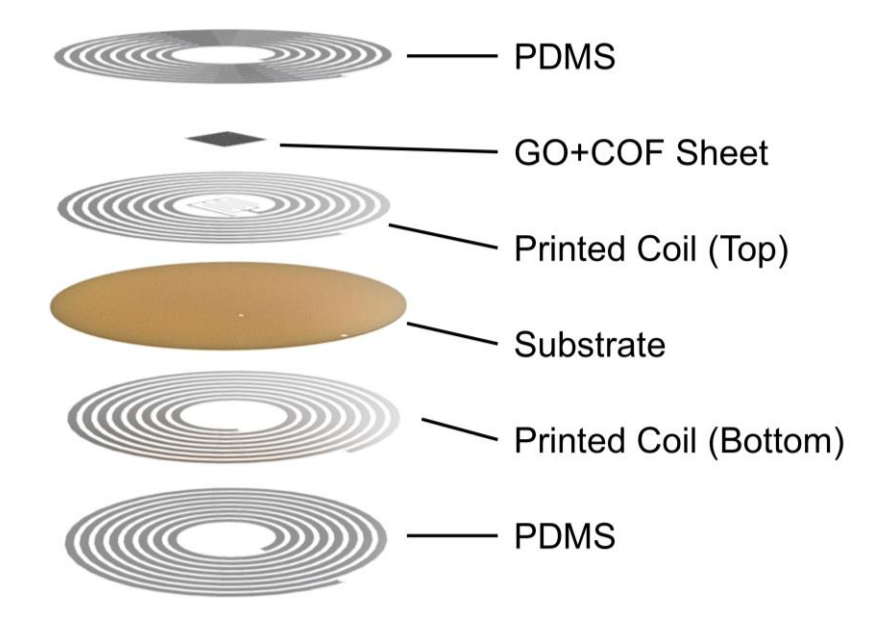


Figure 64: Capacitive pH Sensor with NFC coils.

The sensor was coupled with a standard wire coil, empirically measured to have an inductance of 3.1 µH. The coil was subsequently connected to ceramic capacitors for resonance tuning, enabling the identification of resonant frequencies through impedance analysis. Two configurations were investigated: using two ceramic capacitors in parallel (Capacitor 1), achieving a nominal capacitance of 534 pF and one using a single ceramic capacitor (Capacitor 2), nominally rated at 500 pF.

An impedance analyser was employed to sweep the frequency range from 1 MHz to 5 MHz, capturing the impedance behaviour of the coil-capacitor system. The results, displayed in Figure 65A, show the raw impedance analyser data for the two configurations. In this figure, distinct peaks are observed, corresponding to the resonant frequencies of the coil-capacitor system.

To enhance clarity and mitigate artifacts caused by impedance contributions at higher frequencies—such as those shown earlier in Figure 63—the data was processed using a simple moving mean subtraction technique. This filtering step effectively removed the baseline increase in impedance and isolated the peaks associated with resonance. The processed results are shown in Figure 65B, where the resonant frequencies are more clearly identified.

From the filtered data, the measured resonant frequencies for Capacitor 1 and Capacitor 2 were found to be 3.793 MHz and 3.918 MHz respectively. These frequencies correspond to effective capacitances of 569 and 532 pF respectively for capacitor 1 and capacitor 2, which includes intrinsic capacitances from the coil itself.

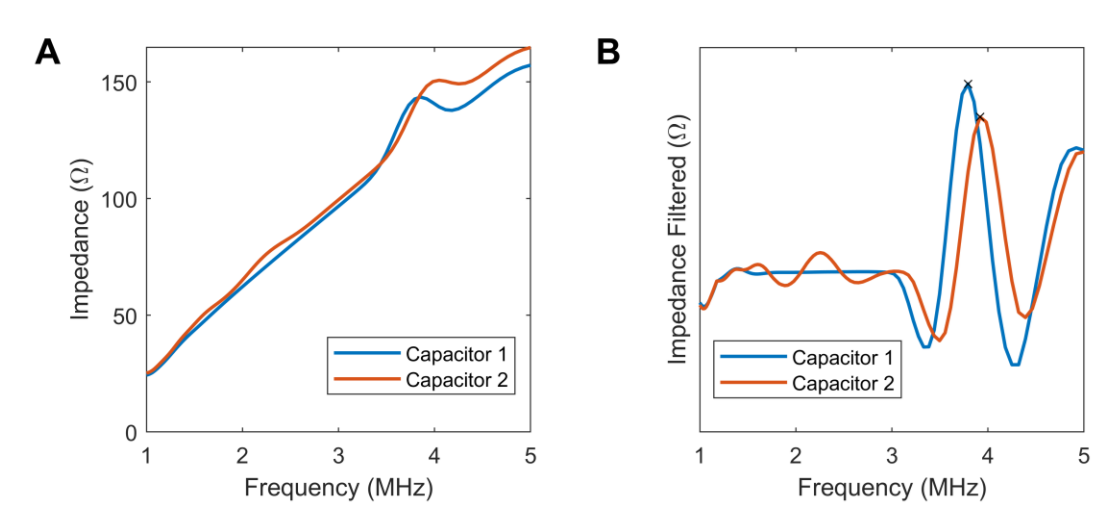


Figure 65: (A) Raw impedance analyser data showing the frequency response of the coil-capacitor system for Capacitor 1 (530 pF) and Capacitor 2 (500 pF). (B) Processed data after moving mean subtraction, highlighting the resonant frequencies of 3.793 MHz and 3.918 MHz for Capacitor 1 and Capacitor 2, respectively.

4.2.4 Conclusion

This chapter demonstrated the potential of leveraging the capacitive response of the GO-COF composite within a wireless, batteryless sensor system designed for gastroesophageal reflux monitoring. The integration of printed electronics principles allowed the development of a flexible, miniaturised coil optimised for medically approved frequencies, while the GO-COF composite served as a tuning capacitor to modulate resonant frequencies in response to pH changes. Proof-of-concept results using static capacitors validated the system's design, highlighting its promise for wireless pH sensing.

However, replicating stable performance with the GO-COF composite tuning capacitor proved challenging due to inconsistent capacitance measurements influenced by droplet variability, surface coverage issues, and unstable flow dynamics. These limitations highlight the need for a more controlled microfluidic system. In particular, designs incorporating droplet reservoirs and capillary action channels can help regulate droplet volumes and ensure consistent wetting of the sensor surface. Such structures facilitate automated expulsion or redistribution of droplets over time, stabilizing the local environment and improving the reproducibility of capacitance measurements. Implementing these features, as demonstrated in related literature [201], would significantly enhance the reliability and long-term performance of GO-COF composite-based sensors under varying operational conditions.

Mechanical deformation of the coil influences its Q-factor, causing a reduction in signal quality and sensitivity [202]. While the GO-COF tuning capacitor itself remains stable under bending, physical changes in the coil geometry alter its inductance and resistance, degrading performance. Design strategies, such as incorporating slight structural rigidity while maintaining overall flexibility, can help mitigate this effect.

Furthermore, limitations in power output from the impedance analyser and suboptimal magnetic coupling between coils constrained the system's robustness. Future iterations should incorporate a dedicated waveform generator and power amplifier to enhance signal strength and coupling efficiency.

The lack of in-vivo validation was another critical limitation, as current ex-vivo experiments did not account for the complexities of biological environments, such as oesophageal motion or coil misalignment. Testing in large animal models would provide crucial insights into the sensor's real-world performance and reliability during prolonged monitoring. Additionally, to transition this system into clinical use, a portable, wearable module must be developed. Incorporating low-power microcontrollers, efficient RF amplifiers, and rechargeable power systems could enable continuous pH monitoring over extended periods.

While this work established a strong foundation for wireless pH monitoring, future efforts should address these limitations to refine the system's stability, scalability, and clinical viability.

Chapter 5: Biocompatible Mucoadhesives

5.1 Background and Literature Review

With the rise of portable and miniaturised electronics, medical diagnostics are shifting away from large, stationary devices toward continuous monitoring in everyday settings with minimal pain or discomfort for the patient [35]. To achieve this, the electronics must integrate seamlessly with the patient, requiring physical properties such as flexibility, stretchability, and softness [35]. As a large proportion of the anatomy is covered by mucosa including the digestive, respiratory, reproductive and urinary systems, electronics that can attach and adhere comfortably to these areas would be required for sensing across the entire human body [35]. The GORD diagnosis medical device being investigated in this thesis should have these properties in order to overcome the shortcomings of the current diagnostic devices and ideally should become as seamless as current commercial skin-interfacing electronics. For example, Nan et. al. argue that mucosa-interfacing electronics should have a form factor where they can be integrated into capsules or catheters for delivery and then become thin films once securely attached to the mucosa layer for seamless integration [35].

To integrate effectively into the mucosal layer, it is crucial to understand the nature of mucosal surfaces and their challenging environment. Mucosal surfaces are curvilinear, regenerative, and dynamic, with complete turnover occurring every 5-8 days in the oesophageal epithelium and every 2-6 days in the gastrointestinal tract [46,203]. These surfaces are composed of 90%-98% water, serving multiple functions such as lubrication, physical barrier formation, microbial trapping, and providing a matrix rich in antimicrobial molecules [204–206]. Mucus, a viscoelastic mucin hydrogel produced by epithelial cells, covers the mucosal layers and varies in thickness depending on the location [35]. This mucus consists of high-molecular-weight glycoproteins linked by peptide bonds and disulphide bridges, typically carrying a net negative charge due to carboxylate groups [204]. In a normal oesophagus, the mucus layer averages about 95 μm in thickness with a turnover rate ranging from minutes to hours [35,207].

Devices designed for mucosal interaction must address challenges related to retention and localisation, given the rapid cellular turnover and wet environment [35]. There needs to be a balance between retention time and ease of removal to prevent inflammatory responses [35]. The tissue-sensor interface is critical and must exhibit

properties such as resistance to biofouling and the ability for long-term bonding, ideally through covalent bonds or other stable interactions [35].

While implantable biomedical devices have been widely used since the development of the cardiac pacemaker in the 1960s—expanding to treatments for neurological disorders and hearing loss — only a limited number have been designed specifically for short- to long-term diagnostic applications [208]. This gap is particularly evident in mucosal diagnostics, where most available technologies remain non-invasive self-testing kits, such as vaginal pH swabs, GORD diagnostic tools, or smart capsules [35]. Smart capsules, which measure parameters such as pH, pressure, or gas concentrations in the gastrointestinal tract, have limited sensing times corresponding to the digestion period [185,209]. To date, the GORD diagnostic techniques have been the primary examples of anchored, implantable sensors interfacing with the mucosa, though they come with their own set of drawbacks [35].

A notable exception to the scarcity of long-term implantable diagnostic devices is the Eversense continuous glucose monitoring (CGM) system, developed by Ascencia[™], which is implanted subcutaneously for up to 90 days in the USA and 180 days in Europe [210]. Although this device is implanted subcutaneously, it does not interface with mucosal surfaces [210]. This distinction highlights the need for further innovation in implantable mucosal diagnostics, where long-term retention, stability, and biofouling resistance remain key challenges.

Various strategies have been explored to implement mucosa-interfacing electronics, including mucus-adhering methods, mucus-penetrating techniques, and mechanical anchoring systems [35]. The following literature review will discuss these mechanisms and the traditional bioadhesives currently in clinical use.

5.1.1 Adhesive Types

Two materials that are adhered together are known as adherends, and the adhesion is commonly facilitated by a third substance known as an adhesive [206]. When an adhesive is employed within or on the body, it is referred to as a bioadhesive. Numerous commercial bioadhesives are available, each designed for specific applications, though most are primarily used for wound sealing, healing, and preventative measures [47]. This is largely because trauma-induced uncontrollable bleeding remains a leading cause of death in surgical procedures [47]. Tissue binders

and sealants are extensively used to ensure complete sealing of wounds following surgical incisions and are increasingly being utilised in medical device implantation [47]. The market for surgical sealants and adhesives was valued at \$2.7 billion in 2020 and is projected to reach \$5.16 billion by 2030, reflecting a compound annual growth rate of 6.7% [211].

Bioadhesives are broadly classified into two categories: natural bioadhesives and synthetic/semi-synthetic bioadhesives. Each type employs different mechanisms of adhesion to remain fixed within the body, but all must meet certain criteria, including biodegradability, flexibility, affordability, and adhesion resistibility [47]. However, commercial bioadhesives generally perform poorly in wet, dynamic environments [47]. The following section will detail the various mechanisms that facilitate adhesion in these challenging conditions.

5.1.2 Adhesion Mechanisms

5.1.2.1 Physical connection adhesion - Bonding types

Tissue surfaces contain functional groups such as amino, carboxyl, hydroxyl, and sulfhydryl, which serve as bonding sites for adhesives.[47]. Adhesives can then form chemical bonds in the form of covalent, non-covalent complexes, hydrogen, polymer chains interdiffusion, polymer networks, or nanoparticles [35,47]. As mucus is waterrich, typical mucoadhesive mechanisms rely primarily non-covalent interactions such as hydrophobic interactions, electrostatic interactions, and mechanical interlocking [35]. Mucoadhesion can also use dual/multiple adhesion mechanisms where water is moved away from the hydrated mucus surface and an initial non-covalent interaction is used for adhesion. Then a covalent bond is formed for increased strengthening of the bonding [35,206]. The chemical bonds are summarised in Table 7 below.

Table 7: Chemical bonds across the interface. Consolidated from [45].

Bonding Type	Description
lonic bonds	lonic bonds are created by the electrostatic attraction of oppositely charged ions.
Covalent bonds	Bonded atoms share electrons to fill each other's orbitals. Can be static or dynamic.
Hydrogen bonds	Covalently bonded hydrogen atoms to electronegative atoms have a small positive charge. This charge attracts other electronegative atoms where the hydrogen is shared between atoms.
Van-der-Waals bonds	Weak bonds that result from dipole-dipole and dipole-induced dipole attractions in polar molecules; occurs as dispersion forces in non-polar molecules as well.

Hydrophobic	When non-polar groups are present in an aqueous solution, indirect bonds can
bonds	form. Hydrogen bonds between nearby water molecules and non-polar groups reduce system entropy. As a result, non-polar groups are more likely to join with
	one another in order to lessen this effect. Commonly described as the hydrophobic effect.

Mucoadhesion typically involves two stages of bonding: the contact stage and the consolidation stage [45]. During the contact stage, the adhesive makes contact with the adherend, and immediate bonds are formed to initiate adhesion [45]. In the consolidation stage, which occurs more gradually, various physicochemical interactions strengthen these initial bonds, resulting in longer-term adhesion [45]. Figure 66 from Yang et al. provides a comprehensive overview of the different chemistries of bonds involved in tissue adhesives [206].

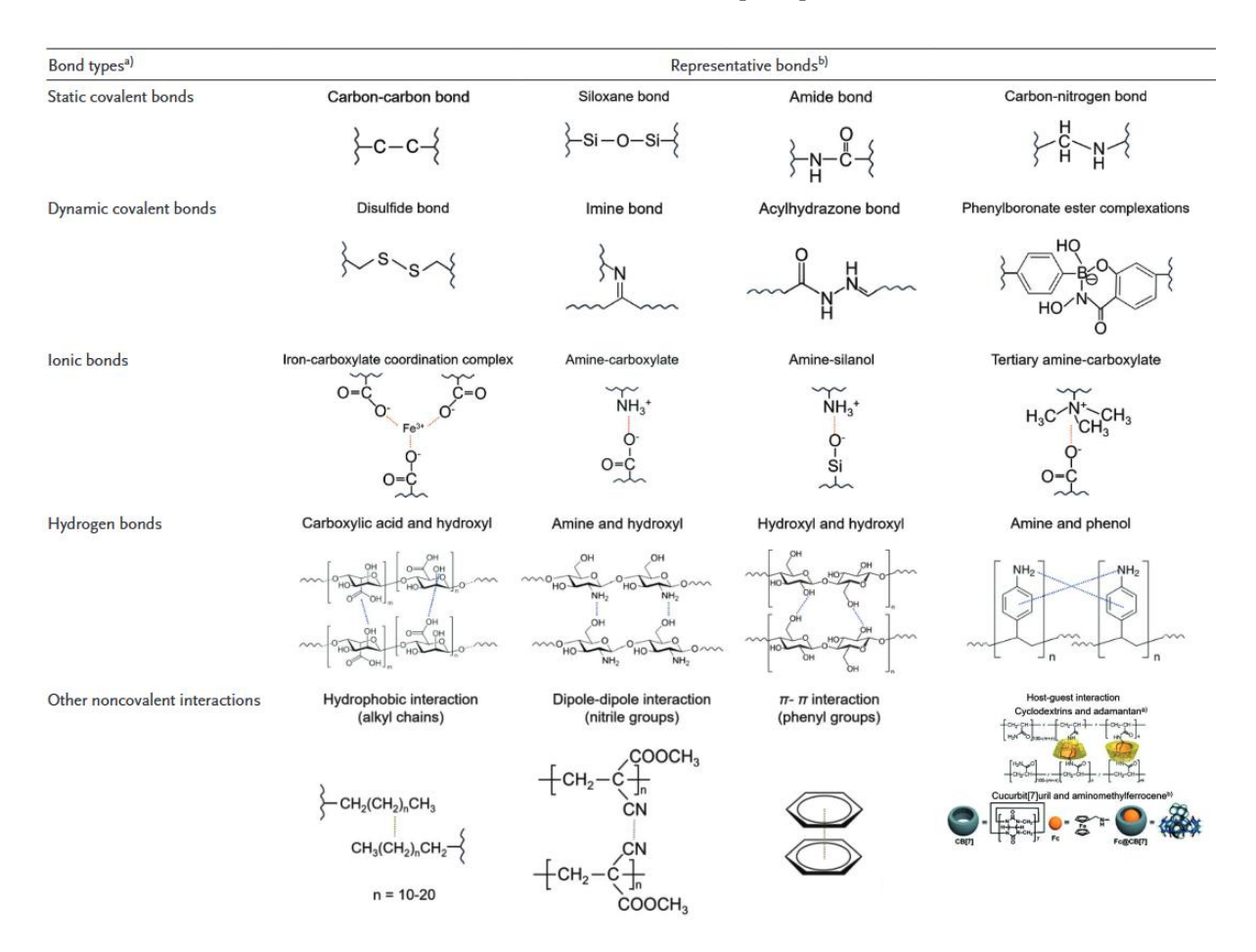


Figure 66: Bond types in tissue adhesives. Figure sourced from [206].

5.1.3 Hydrogel Adhesion

Hydrogels are increasingly utilised in diverse applications such as personal care products, biomaterials, coatings, and plant fertilisers [212]. They are now being explored for advanced uses in sensing, drug delivery, soft robotics, and bio-interfacing

applications due to their ability to mimic the properties of soft tissues chemically, mechanically, and electrically [206,212]. Hydrogels are defined as dilute, cross-linked systems that do not flow in a steady state and use water as the primary swelling agent [212]. They are typically classified into three types: macromolecular hydrogels, supramolecular hydrogels, and supramacromolecular hydrogels, each employing different mechanisms and molecules for cross-linking [212]. Among these, supramolecular hydrogels are particularly notable for their adhesive properties, including mucus-penetrating and mechanical adhesion [35,47,206].

Supramolecular hydrogels are created by using low-molecular weight molecules, polymers, or oligomers that self-assemble into relatively ordered structures over time. These structures are then cross-linked through various techniques to form the gel [212]. The mechanical properties of these hydrogels are influenced by the degree of cross-linking, which can vary depending on environmental factors, processing steps, and polymerisation/gelation kinetics [212].

In hydrogels, water, the primary constituent, contributes minimally to adhesive forces. Instead, adhesion is facilitated by the minority constituents, which bond with the tissue surface topology [35,206]. For effective tissue adhesion, the bonding interface must remain flexible and stretchable, preventing the hydrogel from hardening. The water in the hydrogel acts as a liquid medium that can dissolve and transport various molecules, including encapsulated drugs, allowing for controlled spatial and temporal drug release [206]. For instance, hydrogels can be designed to release anti-inflammatory drugs in a targeted manner.

The polymer network within the hydrogel behaves as a deformable solid that maintains cross-links during deformation. One proposed mechanism of adhesion is the stitch-bond topology, where molecules within the hydrogel are intertwined with the polymer network and form bonds with the tissue surface [206]. Despite this, mucoadhesion remains a complex phenomenon, and existing theories—summarised in Table 8— do not fully capture the entire process when applied individually. Instead, it is likely the result of a combination of these theories [204].

Table 8: Theories of mechanisms of mucoadhesion. Consolidated [45,204].

	Theory	Description
E	Electronic	Electrostatic attraction between oppositely charged surfaces.

Adsorption	Molecules within the bioadhesive induce hydrogen and van der Waals forces to occur. It also considers chemisorption where covalent bonds are formed between the adherends.
Diffusion	Revolves around the penetration and interdiffusion of macromolecules from the bioadhesive into the mucus causing the formation of an interpenetration layer.
Fracture	The difficulty of separation of adhesive bonds is calculated using fracture theory. It relates the adhesive strength to the forces required for detachment.
Mechanical	Interlocking of a liquid adhesive into irregularities on a rough surface or from increased surface area contact on a rough surface.

That said, diffusion and adsorption are commonly described as the primary mechanisms of mucoadhesion where the molecular chains of the hydrogel interpenetrate to the mucin glycoproteins to generate an interpolymer complex that penetrates to a thickness of nanometres or micrometres [206].

5.1.4 Natural Bioadhesives

Polymer materials from natural sources such as chitosan, sodium alginate, gelatine, and fibrin are commonly used for bioadhesives as they are naturally biocompatible. They typically however have poor bonding strength and can suffer from biotic or viral contamination.

5.1.4.1 Chitosan-based

Chitin, a structural element found in crustaceans and the cell walls of fungi, can be converted into chitosan through deacetylation. Chitosan is a semi-crystalline polysaccharide known for its biocompatibility, low toxicity, biodegradability, anti-fouling properties, and non-antigenic nature [47]. Its solubility can be enhanced by modifying it with various functional groups, making it adaptable to different pH environments [213].

Chitosan has shown promise in various applications. For instance, Balakrishnan et al. highlighted its potential as an injectable adhesive scaffold for cartilage tissue regeneration, although the study did not address its effectiveness for mucosal layers [214]. Zeng et al. demonstrated the utility of chitosan in hydrogels, noting its superior adhesion strength compared to commercially available fibrin glues when tested on gelatine-coated glass and rat skin [213]. However, this research did not explore the suitability of chitosan for mucoadhesion specifically. Yuk et al. explored using chitosan and gelatine-based polymer matrices and incorporating with acrylic acid and an

poly(acrylic acid) grafted with N-hydroxysuccinimide ester (PAAc-NHS ester) for adhesion to wet-surfaces [215].

5.1.4.2 Alginate-based

Sodium alginate, an anionic linear polysaccharide extracted from brown algae such as *Laminaria hyperborea*, *Macrocystis pyrifera*, and *Ascophyllum nodosum*, is well-regarded for its biocompatibility, low toxicity, mucoadhesion, and excellent cross-linking capabilities [47,216]. Typically utilised in hydrogel formulations, sodium alginate can interact with peptides, gelatine, collagen type I, and tricalcium phosphate, making it versatile for various applications [47].

Despite these advantages, sodium alginate has limitations, including low biodegradability and inferior mechanical properties [47]. To overcome these drawbacks, it is often combined with other polymers to enhance its mechanical performance for tissue adhesion [217]. Sodium alginate has demonstrated effectiveness as an injectable adhesive in treating haemorrhages in bleeding mouse models [217] and shows promise for drug delivery in mucoadhesive environments [216].

However, sodium alginate is sensitive to pH variations. The carboxylic acid groups, which contribute to the molecule's electronegativity, become insoluble and lead to increased electrostatic repulsion in low pH environments (pH < 3.4). This can result in decreased adhesion in such acidic conditions, potentially limiting its suitability for applications in the oesophagus where the pH can be very low [216]. Additionally, Haugstad et al. noted that alginates perform relatively poorly in mucoadhesion compared to chitosan, highlighting a key limitation for its use in certain medical applications [218]

5.1.4.3 Chondroitin sulphate-based

Chondroitin sulphate (CS) is a glycosaminoglycan sulphate found in human cartilage and other tissues. It consists of alternating chains of sugars and contains hydroxyl, carboxyl, and amide groups, contributing to its unique properties [4,219]. Known for its biocompatibility and biodegradability, CS is widely used in tissue engineering and cartilage repair due to its compressive strength [4,47].

Chondroitin sulphate's excellent cross-linking ability makes it suitable for hydrogel preparation. Dai et al. developed a self-healing bioadhesive metallohydrogel by

combining Fe³⁺ ions with chondroitin sulphate at room temperature. This metallohydrogel demonstrated superior adhesion compared to commercially available fibrin glue [219]. However, it was sensitive to pH changes, undergoing sol-to-gel transformation at high pH and reverting to gel at low pH [219].

Chondroitin sulphate is naturally present in the oesophageal structure [4]. Pecora et al. further demonstrated that commercial formulations containing chondroitin sulphate, tamarind seed extract, and glycerol were effective in adhering to phantom mucus layers, indicating its potential for mucoadhesive applications [4].

5.1.4.4 Hyaluronic acid-based

Hyaluronic acid (HA) is a viscoelastic linear polysaccharide that has gained significant attention as a drug delivery agent since the early 2000s due to some of its remarkable properties [47,220]. As a member of the mucoadhesive polymers group, HA is notable for its ability to adhere to mucosal surfaces. This adhesion is primarily driven by the presence of thiol groups within the polymer, which enable thiolated polymers (such as HA) to rapidly swell in aqueous environments. The swelling facilitates strong attachment to mucus through the formation of covalent disulfide bonds with cysteine-bearing subdomains of mucus glycoproteins [220].

Historically, thiolated polymers, also known as thiomers, faced challenges in maintaining stability at pH levels above 5 due to the oxidation of their thiol groups, which compromised their effectiveness as mucoadhesive agents [220]. However, recent advancements have significantly improved their performance. For instance, Nowak et al. demonstrated the potential of preactivated hyaluronic-acid-L-cysteine ethyl ester (HA-CYS) enhanced with 6-mercaptonicotinamide, creating a mucoadhesive patch that exhibited robust adhesion [220]. Remarkably, this patch remained securely attached in an in-vitro mucosa model for 48 hours under dynamic conditions with a pH of 4.2, highlighting its stability and effectiveness in acidic environments [220].

5.1.4.5 Gelatine-based

Gelatine is a widely used material in pharmaceuticals, derived from the irreversible hydrolysis of collagen from animal sources [47,221]. Its popularity is due to its biodegradability, biocompatibility, non-toxicity, non-immunogenicity, and cost-effectiveness [221]. Gelatine is easily cross-linked, soluble in hot water, and suitable

for use in hydrogels [221]. It is classified into two types: Type A, produced through acid-treatment processes, which is electropositive at neutral pH, and Type B, produced through alkali-treatment, which is electronegative due to a higher percentage of carboxylic groups [221,222].

In drug delivery, Type B gelatine typically shows stronger adhesion, while Type A, due to its higher elastic modulus, is often preferred when combined with other drugs [221]. Gelatine is also used in surgical glues and tissue adhesives. Iwata et al. developed a glue combining gelatine with N-hydroxysuccinimide and activated poly(L-glutamic acid), which demonstrated stronger adhesion than commercial fibrin glue, though mild cytotoxicity from degradation products was noted [223]. Historically, gelatine was combined with resorcinol and formaldehyde for medical glue in 1977, widely used in Europe but never FDA-approved due to formaldehyde's toxicity [224].

To address these concerns, a new formulation using purified bovine serum albumin and glutaraldehyde was created, resulting in the FDA-approved product Bioglue® in 2001, though it has been associated with inflammation and tissue necrosis [224]. Similarly, Progel™, which combines human albumin and a PEG crosslinker, is used clinically but is expensive and lacks haemostatic functionality [225].

In 2017, a multidisciplinary, intercollegiate team optimised the formulation of gelatine methacryloyl sealant dubbed GelMA for use as tissue adhesives in wet environments [225]. The formulation was found to be non-cytotoxic, biocompatible, exhibit high adhesion and shear strengths, and induced high burst resistance when sealing lung defects in porcine and rat models [225]. After 14 days the GelMA was no longer present in the pig model while showing sufficient wound repair [225]. GelMA can be combined with Gel-Dopa (another gelatine-based formulation with mussel-inspired molecules) and prepared into a solid tissue adhesive that only activates following photoinitiation as demonstrated by Pirmoradian et al [226]. For chemical-based cross-linking, Genipen® has been demonstrated as an alternative to aldehyde or epoxy-based cross-linking which are both cytotoxic [226].

5.1.4.6 Mussel-inspired soft tissue adhesive

Marine mussels have inspired the development of bioadhesives due to their remarkable ability to adhere to water-rich surfaces, even in harsh, wet, or bloody environments [47]. The adhesion ability of mussels is attributed to mussel foot proteins

(MFPs), which can rapidly solidify and form strong bonds with various surfaces [47,226]. These proteins are rich in 3,4-dihydroxyphenylalanine (DOPA) and tyrosine residues, which facilitate key chemical interactions and cross-linking. The presence of DOPA is believed to be essential for the adhesive properties, as it not only aids in adsorption but also helps form covalent bonds that cross-link the proteins, giving the MFPs their adhesive strength [227].

DOPA's importance in adhesion is well-documented, with its ability to adsorb proteins onto surfaces and form strong covalent bonds, which solidify the adhesive matrix. This mechanism has inspired several biomedical applications. For example, Hu et al. utilized DOPA in combination with polyvinyl alcohol (PVA) to create a mucoadhesive film designed for drug delivery via wet buccal tissue [228]. The film showed excellent shear strength and required significant force to detach, thanks to the incorporation of multiple bonding mechanisms. These included covalent bonding, adsorption, hydrogen bonding, diffusion, and interpenetration, all working in tandem to create a highly effective adhesive [228]. Figure 67 from [228] shows the film and the various bonding techniques used to which results in the high adhesion.

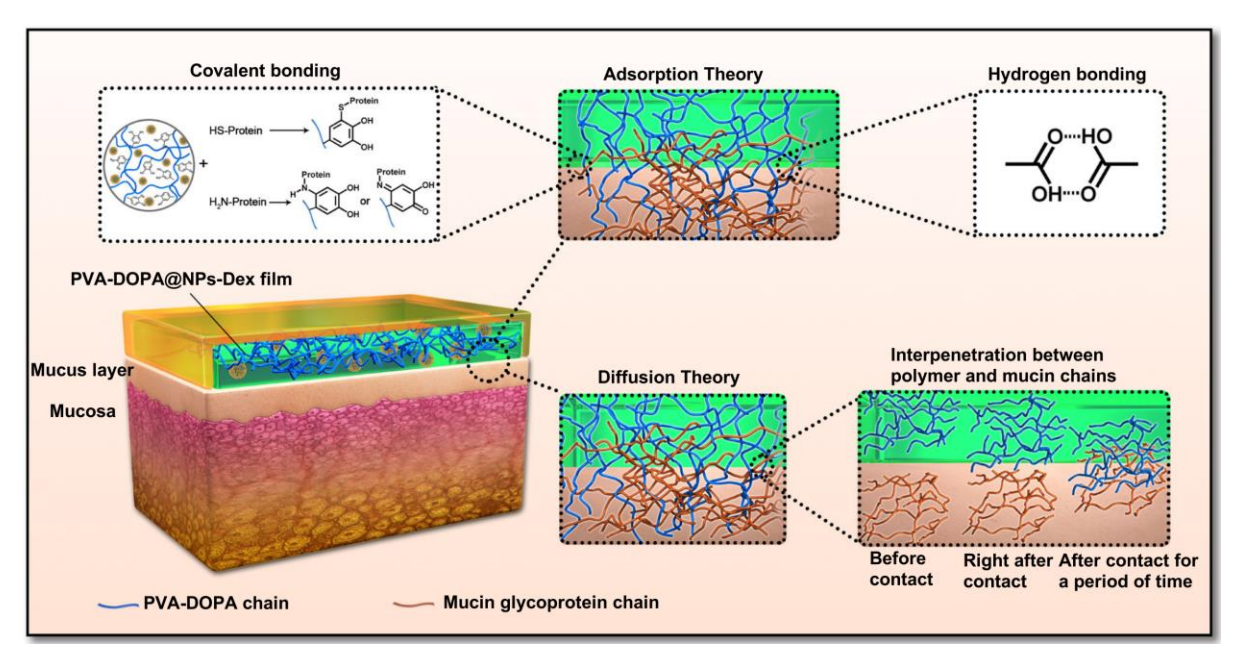


Figure 67: Interactions between PVA-DOPA films with buccal mucosal layers. Figure sourced from [228].

5.1.4.7 Fibrin-based

Fibrin-based glues are one of the two most commonly used tissue adhesives along with cyanoacrylate [47,219]. It is the only FDA approved material for clinical use as a haemostat, sealant and adhesive [229]. This is due to their ability to mimic the final

stages of coagulation in the human body [47,230]. Fibrin-glues are comprised of two components, fibrinogen and thrombin which originates from human plasma [229]. When under the presence of calcium ions, thrombin cleaves the fibrinogen chains to form fibrin monomers. These monomers can then polymerise to form fibrin clots which degrade within 2 weeks [230]. Fibrin has been used for colon sealing, skin transplantation, tumour covering following brain tumour resection, and other various wound closure purposes [47,230]. However, they generally demonstrate poor adhesion and tensile strength and tend to perform best in dry environments [219,229]. Complications can arise due to their human-source in the form of viral transmission, however the risk is considered low and to date no cases have been reported despite widespread use [47,230].

5.1.5 Synthetic and Semi-synthetic Bioadhesives

5.1.5.1 Cyanoacrylate-based

Cyanoacrylates are among the most widely used adhesives in both commercial and medical applications, due to their versatility and strong bonding capabilities. These adhesives are commonly employed for bonding materials such as metals, plastics, rubber, and ceramics, and they are also prominent in tissue adhesion [47,213]. Cyanoacrylates are esters of cyanoacrylic acid, characterized by an acrylate double bond that plays a crucial role in the rapid polymerization and hardening of the adhesive. When applied between two surfaces, with one being tissue, cyanoacrylates polymerize to form a glassy phase that solidifies the interface, establishing covalent bonds with the tissue's polymer networks [206,230].

Despite their widespread use, cyanoacrylates have several limitations, particularly in medical applications. One major drawback is their poor performance in the presence of blood, which can interfere with the adhesive's effectiveness. Additionally, cyanoacrylates can restrict the movement of soft tissues, which is a significant concern in dynamic environments like joints or other areas requiring flexibility [206]. Upon degradation, cyanoacrylates release cytotoxic byproducts, including cyanoacetate and formaldehyde, which raises safety concerns. This issue was somewhat mitigated by recognizing that shorter alkyl chains in cyanoacrylates contribute to higher toxicity, leading to the discontinuation of their use in favour of formulations with longer side chains [47].

In clinical practice, longer-chain cyanoacrylates such as n-butyl-2-cyanoacrylate (NBCA) and octyl-2-cyanoacrylate are now commonly used. These formulations are considered less toxic and have been approved for use in various medical applications. For instance, NBCA-based adhesives are FDA-approved under the name Histoacryl® Flexible for use as a topical adhesive. However, these adhesives are not recommended for use in wet environments due to their exothermic bonding process, which can generate significant heat and potentially cause burns [231]. Indeed, instructions for cyanoacrylate adhesives often recommend drying the application area thoroughly before use [232].

Cyanoacrylates are frequently used for wound closure as an alternative to conventional sutures, but they are generally not preferred over intracutaneous absorbable sutures, which tend to result in better cosmetic outcomes [230]. In wet conditions, the presence of moisture can accelerate the polymerization process, leading to excess heat generation, which is another limitation of these adhesives in such environments [233]. Other commercial cyanoacrylate adhesives, such as Dermabond and Surgiseal, are also widely used, but their degradation products still pose concerns due to their potential carcinogenicity [232].

Overall, while cyanoacrylates offer strong and rapid adhesion, their limitations in wet environments, potential toxicity, and the risks associated with their degradation products make them unsuitable for environments where mucoadhesion is required.

5.1.5.2 PU-based

Polyurethane (PU) has been a staple adhesive across numerous industries for decades, thanks to its versatility and strong bonding properties. Its applications span sectors such as construction, packaging, woodworking, transportation, marine, and electronics [133]. More recently, PU has been adapted for the healthcare sector, where it has been employed in adhesives, artificial organs, medical bone repair, and surgical vascular sutures [134,234]. One notable example is TissuGlu®, a urethane-based surgical adhesive approved by the FDA for use in abdominoplasty. TissuGlu® has been shown to significantly reduce seroma formation—a common complication following abdominoplasty—when compared to control groups, which is largely due to PU's excellent compatibility with blood and tissue, as well as its soft and flexible structure [235].

The healthcare sector has also seen innovations involving PU composites for mucoadhesion. For instance, Ciubotaru and Zaltariov developed a mucoadhesive patch combining polyurethane with chitosan (CS) and hyaluronic acid. Their composite patches exhibited strong attachment forces at both neutral pH and pH 5, highlighting the potential of PU composites in creating effective mucoadhesive products [235].

However, despite its widespread use and advantages, PU is not without its drawbacks. For example, TissuGlu® has been associated with an increased risk of irritation following subcutaneous implantation, and seroma formation was still observed in 22% of patients in one study [232]. Additionally, the degradation products of PU are known to have poor biocompatibility, which raises concerns about long-term safety in medical applications. Moreover, the use of isocyanate-functionalized prepolymers in PU formulations poses significant handling risks due to their toxicity [47].

These challenges highlight the need for careful consideration in the use of polyurethane-based adhesives in medical applications. While PU offers significant benefits, particularly in terms of flexibility and compatibility with biological tissues, its potential for irritation, toxic degradation products, and the risks associated with its chemical components must be balanced against its advantages.

5.1.5.3 **PEG-based**

Poly(ethylene glycol) (PEG) adhesive formulations are among the most widely used adhesives for wet conditions in both in vitro and in vivo applications, with multiple FDA approvals underscoring their clinical reliability [47,225]. PEG-based adhesives are theoretically non-toxic, non-immunogenic, water-soluble, and highly stretchable, making them suitable for a range of medical applications [211,236]. Some of the prominent commercial examples include CoSeal®, DuraSeal™, FocalSeal™, and products from Baxter Healthcare Corporation®, all of which are FDA-approved for surgical use [47,230].

These adhesives are typically prepared in hydrogel form, providing a watertight closure when used in conjunction with sutures, particularly in cranial surgeries [230]. They have demonstrated superior performance compared to fibrin glues, often used as a tide seal, and have also been approved for use in sealing air leaks following pulmonary resections [236]. Unlike cyanoacrylate adhesives, which require a dry

surface for optimal adhesion, PEG-based glues actually benefit from moisture, which enhances their adhesive properties [236].

The adhesion mechanism of PEG-based adhesives is unique in that it does not rely on the formation of covalent bonds. Instead, these adhesives achieve mechanical anchoring by interpolating the sealant into the irregularities of tissue surfaces, providing a secure bond without the need for chemical cross-linking [236].

However, despite their advantages, PEG-based adhesives are not without limitations. One significant drawback is their tendency to swell significantly in wet environments, which can exert unwanted pressure on surrounding tissues, particularly nerves, leading to complications [232]. Additionally, some PEG-based adhesives have been associated with inflammatory responses and increased skin sensitivity, raising concerns about their biocompatibility in certain patients [230,232].

Overall, while PEG-based adhesives offer numerous benefits for surgical applications, particularly in wet environments, their potential for swelling and inducing inflammatory responses must be carefully considered when selecting an adhesive for specific clinical scenarios.

5.1.6 Summary of Bioadhesives Literature and Gaps

To summarise, implantable sensors classified as "active implantable medical devices", designed to adhere to mucosal surfaces using adhesives have not, to my knowledge, been commercialised or received FDA approval. Devices described in the literature often rely on attachment mechanisms such as the Bravo capsule, which utilises mechanical suction, or alternative mechanical clipping techniques to anchor the devices [197]. While these approaches can achieve functionality, they are typically uncomfortable for patients and may not support prolonged use. Current active medical devices intended for long-term implantation, such as continuous glucose monitors, are designed for subcutaneous use and do not interface with mucosal layers [52].

Existing mucosa-interfacing devices are largely limited to technologies like the Bravo capsule, catheter-based systems, or ingestible "smart" capsules. These capsules can traverse the gastrointestinal (GI) tract, monitoring various physiological parameters such as temperature, oxygen, hydrogen, and carbon dioxide concentrations, but they do not remain fixed at a specific location within the GI tract [35].

Adhesives designed for long-term biomedical applications have been widely reported in the literature and, in some cases, commercialised. These adhesives are generally classified into two categories: natural and synthetic/semi-synthetic bioadhesives. Each category has distinct advantages and limitations, as discussed in the literature review. Currently, most bioadhesives approved by health authorities are intended for use as sealants in surgical or post-surgical applications.

However, recent advancements in bioadhesive technologies, particularly mucoadhesives, have shown promise for biomedical device anchoring and implantation. This interest is driven by the diagnostic potential of devices adhering to mucosal surfaces in various organ systems, such as the reproductive, urinary, digestive, and respiratory tracts. Such devices can facilitate in situ monitoring and diagnosis of diseases, ranging from motility disorders and tissue injury to cancers [35].

While this field is still emerging, the potential of mucoadhesive-based biomedical devices is significant, particularly for enabling prolonged, minimally invasive monitoring of physiological parameters in challenging environments such as the gastrointestinal tract.

5.2 Mucoadhesive, biocompatible patches for oesophageal attachment

5.2.1 Introduction

Bioadhesion refers to the phenomenon in which two surfaces, one of which is biological in nature, remain attached at an interface for extended periods [45]. When one of these surfaces is mucus or a mucous membrane, the process is specifically termed mucoadhesion. Mucous membranes are moist surfaces found in various parts of the body, including the gastrointestinal tract, with the oesophagus being of particular interest in this context [45]. Mucoadhesive patches have considerable academic and commercial interest for drug delivery, surgical sealants, biomedical device adhesion, and other healthcare applications [35,215,237]. Recent advances have led to the development of bioadhesives that exhibit rapid and effective adhesion to both dry and wet tissue surfaces. Some modern bioadhesive formulations incorporate active components to mitigate inflammatory responses during wound healing [215,237]. Despite these innovations, the use of mucoadhesives to securely anchor biomedical devices within the oesophagus remains largely unexplored. This represents a

significant opportunity to improve diagnostic and therapeutic devices for GORD and other gastrointestinal conditions.

Current diagnostic devices for GORD, such as the Bravo[™] capsule, rely on mechanical attachment mechanisms, including suction-based or clip-like anchoring. These methods are effective but have several drawbacks. They often cause significant patient discomfort, leading to symptoms such as oesophageal hypertensive spasms or, in severe cases, oesophageal perforation, requiring emergency surgical intervention[10,15,21,30,33,44]. Additionally, these devices are prone to premature dislodgement, which can result in incomplete diagnostic data and missed diagnoses. These challenges highlight the need for alternative attachment mechanisms, such as mucoadhesive patches, which could provide a more comfortable, reliable, and effective solution [35].

The oesophageal lining is composed of three layers: a connective tissue layer, a multilayered epithelial layer, and a mucus layer that maintains moisture [45,238]. The mucus layer, which adheres to the epithelial surface, is a gel-like substance made up of glycoproteins, lipids, inorganic salts, and water—water constituting about 95% of its weight, making it the primary component [45]. This mucus serves as a protective and lubricating layer, and due to its inherent properties, it acts as an anti-adherent, making mucoadhesion particularly challenging.

The mechanisms of mucoadhesion, as detailed in the literature, are not entirely understood but can be explained by six theories: the electronic, adsorption, wetting, diffusion, fracture, and mechanical theories. The electronic theory suggests that mucoadhesion occurs due to electrostatic attraction between oppositely charged surfaces. The adsorption theory involves intermolecular forces such as hydrogen bonding, van der Waals interactions, and covalent bonding [45,204]. The wetting theory relates to the surface tension of the mucus and the mucoadhesive polymer, promoting the spreading of the polymer onto the mucus layer, primarily in liquid mucoadhesive forms [204]. The diffusion theory explains mucoadhesion through the penetration and interdiffusion of macromolecules from the bioadhesive into the mucus, leading to the formation of an interpenetration layer. The fracture theory focuses on the distribution of stress across the adhesive bond, while the mechanical theory attributes mucoadhesion to the physical interlocking of the adhesive material with the mucus layer [45,204].

Hydrophilic macromolecules such as gelatine and acrylic acid contain functional groups—hydroxyl, carboxyl, amine, and methyl—that promote adhesion [45,237]. Formulations containing these macromolecules can be activated by exposure to moisture, initiating the adhesion process via water uptake from the mucous membrane [45,204]. This activation forms the initial contact stage, where the wetting theory is applied, and the mucoadhesive patch begins to swell due to water uptake [239]. Noncovalent physical bonds are then created, leading to the application of adsorption theory. This marks the beginning of the consolidation stage, after which polymer and protein chains interpenetrate and entangle, forming covalent bonds that result in long-term adhesion.

Poly (acrylic acid) is particularly known for its ability to interpenetrate and form strong bonds with glycoproteins present in the mucosa [204,237,240]. Poly(acrylic acid) and its derivatives, which are linear polyacrylate chains, have long been studied for their high mucoadhesive properties. It has been observed that polyanions with high charge density, such as polyacrylic acid, exhibit strong mucoadhesive properties [241]. The high concentration of carboxyl groups within the polymer can form bonds with the mucin layer particularly at lower pHs. At higher pHs however, the mucoadhesive properties decline due to the fact that charge repulsion dominates at pHs higher than 6 and due to the increased swelling at higher pHs, suggesting a lower concentration of polyacrylic acid chains in a given surface area in the swollen state [241]. This drives the conclusion that the swelling and water absorption properties hold a key role in their mucoadhesive properties. Swelling can increase the contact area between the polymer and mucus layer causing increased opportunities for interaction and consequently adhesion. Too extensive water absorption provides no adhesion, however, as the over swollen polymer gel can fail due to insufficient cohesive properties [240]. Finally, following penetration of the polyacrylic acid into the mucus, physical entanglement and secondary bonding (mainly H-bonding and can der Waals attraction) occurs, resulting in the mucoadhesive properties occurring.

The present study investigates the incorporation of (poly)acrylic acid (pAA) into a methacrylated gelatin-based hydrogel matrix to optimise its mechanical and mucoadhesive properties for oesophageal applications. A key focus was on balancing the effects of swelling and cross-linking density, which influence adhesion strength and longevity.

To evaluate the performance of the hydrogel, a series of flow tests were conducted using an ex vivo porcine oesophageal model. The tests simulated real-life conditions, including the consumption of beverages, to determine whether the mucoadhesive patch could maintain adhesion. The study aimed to develop a mucoadhesive patch capable of securely anchoring a pH sensor for GORD diagnosis, overcoming the limitations of existing diagnostic technologies.

This research underscores the importance of optimising the composition and structural properties of mucoadhesive materials for biomedical device integration, particularly in challenging environments like the gastrointestinal tract. By addressing these challenges, this study aims to contribute to the development of more effective and patient-friendly diagnostic solutions for GORD and other conditions.

5.2.2 Materials and Methods

5.2.2.1 Materials

The following materials were ordered from Sigma Alrich without further purification: acrylic acid (AA), gelatine (type A bloom 300 from porcine skin), sodium carbonate, sodium bicarbonate, methacrylic anhydride, hydrochloric acid, acrylic acid N-hydroxysuccinimide ester (AAc-NHS ester), α-ketoglutaric acid. Dialysis membranes (12-14K Dalton) were purchased from Spectrum Labs.

5.2.2.2 Synthesis of Gelatine Methacryloyl (GelMA)

GelMA was synthesised using established protocols. Briefly, 50 mL of 0.25 M carbonate/bicarbonate buffer solution was prepared by dissolving 0.86 g of Na₂CO₃ and 0.88 g of NaHCO₃ under stirring with a magnetic stir bar. Separately 100 mL of 0.1 M HCl solution was prepared. Once dissolved, 5 g of gelatine type A bloom 300 was added under moderate stirring for 10 minutes to facilitate gelatine dissolution. Heat was applied at 55°C while moderate stirring for 30 minutes for gelatine to be fully dissolved and solution became clear. Stirring was increased to 1500 rpm and 159 microlitres of methacrylic anhydride was added drop-wise to the solution while maintaining heating at 55°C. The reaction was allowed to proceed for 1 hour. The reaction was stopped by adding HCl solution until pH reached 7.4 (measured with a pH meter (Hanna Instruments HI-5221) and was subsequently removed from the hot plate. The solution was transferred to a 12-14 KDa dialysis membrane sealed by dialysis clips. The membrane was dialysed against deionised water at 40°C against 5

L of water for 5-7 days changing water daily to remove the methacrylic anhydride. Following this, the gelMA was transferred to a freeze-drying beaker and frozen overnight in a -20°C freezer. The contents were then lyophilised for 4-7 days until completely dehydrated.

5.2.2.3 Bioadhesive preparation

The bioadhesive was prepared by dissolving 10% gelMA (w/w), and varying concentrations of AA (10%, 20%, 30%, 40%) (w/w) in deionised water under 40°C and stirring. The solution was allowed to cool and following this, 1% (w/w) of AAc-NHS ester and 0.2% (w/w) of α-ketoglutaric acid were added and allowed to mix in the solution for 30 minutes. A white-yellowish mixture was obtained as shown in Figure 70D. For the mechanical test samples, the solution was placed in a clear acrylic mould with rectangular prisms of dimensions 20mm x 10mm x 3mm as shown in Figure 70E. The mould was placed in a UV chamber (UVITEC Crosslinker CL-508) for 20 mins at wavelength 312 nm for crosslinking to occur. Three samples were created for each AA concentration. For the lap shear test samples, the solution was spread evenly on polyimide sheets (Goodfellow) and placed in the UV chamber for 20 mins. All samples following crosslinking were allowed to completely dry for 12 hours. The samples for the lap-shear tests were then laser cut (Universal Laser Systems PLS4.75) into (n=3) 20mmx10mm rectangles and were then placed in clear zip-lock bags with silica desiccant packets and placed in a -20°C freezer.

5.2.2.4 Material Characterisation

To characterise the formation of gelMA, Fourier-Transform Infrared spectroscopy was utilised using a Spectrum Two™, Perkin Elmer spectrophotometer in the region of 400 to 4000 cm⁻¹. The as purchased gelatine and final synthesised bioadhesive patch FTIR scans were analysed and compared using MATLAB R2023B.

5.2.2.5 Mechanical Testing

To assess the mechanical properties of the bioadhesive and ensure seamless integration with the surrounding mucosa, a uniaxial tensile test was performed using an Instron machine (model 5969, equipped with a 50 kN load cell) under stretching speed of 1 mm/min at room temperature (23 °C). Prior to loading the bioadhesive, the samples were allowed to swell and equilibrate in a phosphate-buffered solution (PBS) for 10 mins before testing. The bioadhesive was mechanically clamped and loaded as

shown in Figure 68A. The forces were normalised by the original cross-sectional area to obtain the nominal stress values, and measured displacements were normalised against the original length to obtain engineering strain. Each composition consisted of 3 samples.

5.2.2.6 Adhesion Testing

Lap shear testing was selected as the method to measure adhesion because it is used to measure the interfacial shear strength under tension loading and thus provide a shear adhesive strength [242]. This closely mimics the shear forces the sensor would experience *in vivo*, such as those from food, drink, or reflux events. To assess shear strength, laser-cut bioadhesive samples, cured on a polyimide (Kapton™) backing, were affixed to 4 cm × 2 cm acrylic plastic sheets using Gorilla™ Super Glue, as illustrated in the inset of Figure 3B. Oesophageal tissue, harvested from porcine specimens the day before testing, was cut into appropriately sized pieces. The inner oesophageal surface was adhered to the bioadhesive one hour prior to testing to allow for proper equilibration. The tissue was then securely clamped to the Instron testing machine (model 5969, equipped with a 50 kN load cell), while the opposite side was clamped to the acrylic sheet, as shown in Figure 68B. A standard lap shear test was conducted in accordance with ASTM F2255 at a constant tensile speed of 1 mm/min at room temperature (23 °C). Shear strength was calculated by dividing the maximum force recorded during testing by the adhesion area.

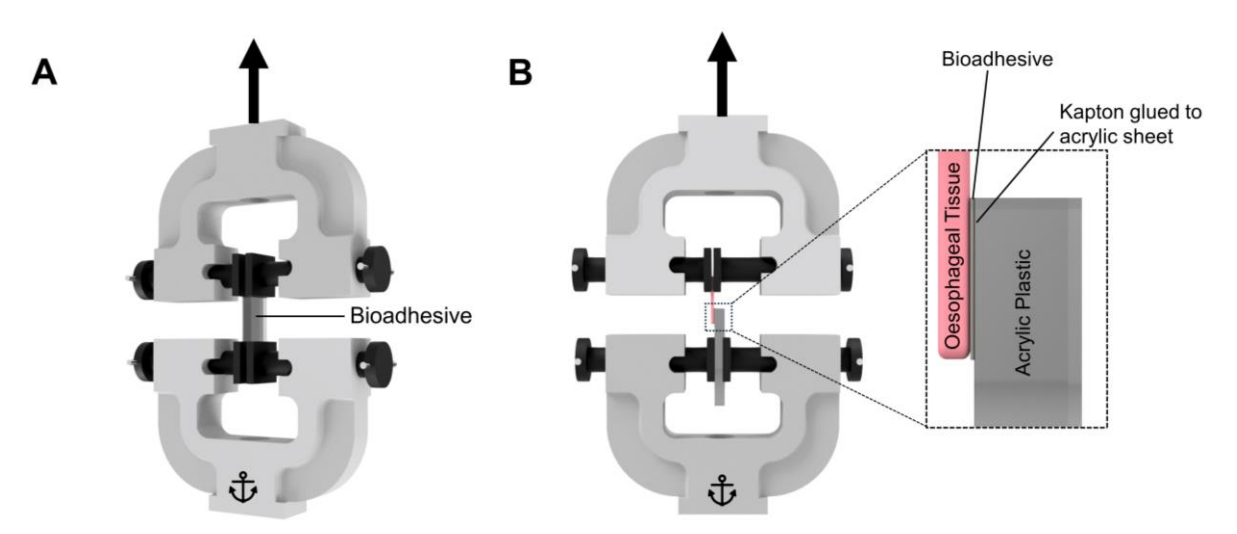


Figure 68: (A) Schematic of the tensile mechanical tests performed on the bioadhesive. (B) Schematic of the lap shear adhesion tests performed on the bioadhesive with the oesophageal tissue.

5.2.2.7 Ex vivo Flow Testing

To assess the suitability of the bioadhesive patch integrated with a sensor for *in vivo* use, initial *ex vivo* testing was conducted as shown in Figure 69. An intact porcine oesophagus and stomach, harvested one day prior, were mounted on a laboratory stand and connected to a pump via a hose, which was set to a flow rate of 180 litres per hour. This rate was estimated to simulate the speed at which a person might quickly drink water, based on internal testing. The hose was secured to the oesophagus using plastic zip-ties, and the duodenum was positioned to allow the 0.9% saline solution to flow into a beaker. An incision was made in the stomach near the duodenum, through which the sensor was carefully rolled up and placed approximately 5 cm above the lower oesophageal sphincter. Light pressure was applied for 5 seconds to adhere the patch to the oesophagus and no flow was conducted for 10 minutes to help ensure robust adhesion and allow for the contact and consolidation stages to occur. The flow test was then conducted for three hours, where saline was pumped, after which a laparoscope was used to image the porcine oesophagus and verify that the sensor remained securely adhered.

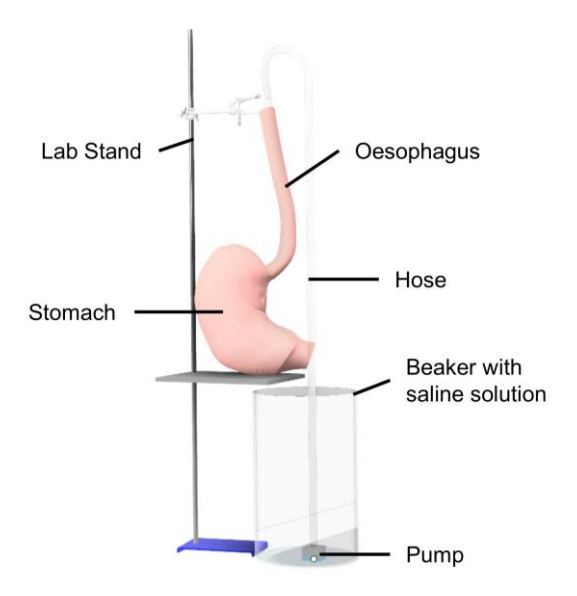


Figure 69: Schematic of the *ex vivo* flow testing apparatus.

5.2.3 Results and Discussion

5.2.3.1 Bioadhesive Design

The bioadhesive patch is thin, highly transparent, and flexible, making it suitable for adhesion to curved surfaces. The transparency of these patches is directly dependent on the degree of cross-linking present in the material. Figure 70A-C show optical

images of a patch made with 10% AA (w/w), where a high degree of transparency is observed when the patch is fabricated on a flat polyimide sheet. However, in Figure 70E, when cross-linking was performed in an acrylic mould for mechanical testing, the 10% AA (w/w) sample turned white and opaque.

This change suggests that the fabrication conditions within the mould increased the cross-linking density, leading to more chemical bonds forming between polymer chains during photo-polymerisation. The confinement effect of the mould likely caused the polymer chains to pack more tightly, resulting in increased cross-linking and the formation of microstructures that scatter light, causing the material to appear opaque.

Additionally, the increased concentration of gelatine in the 10% AA (w/w) sample - relative to the other samples - likely contributed to this effect. Gelatine has longer chains compared to AA, which enhances its ability to form cross-links, thus further increasing the material's opacity. As shown in Figure 70D, the bioadhesive patch solutions exhibited similar translucent and optical properties prior to photopolymerization, indicating that the changes observed post-polymerisation were indeed due to the cross-linking process.

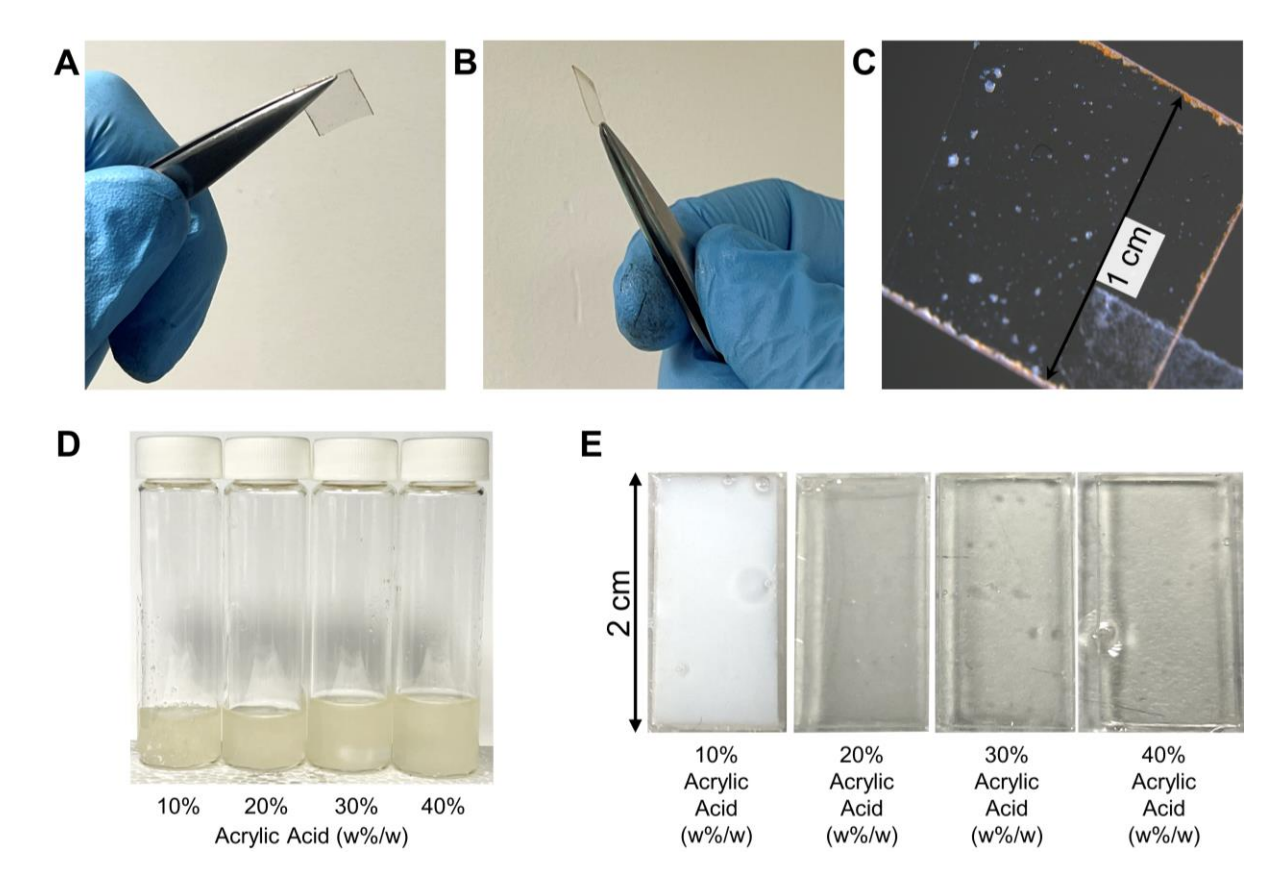


Figure 70: **(A-B)** Optical images of the 10% AA (w%/w) bioadhesive from the front and side. **(C)** Microscope image of the 10% AA (w%/w) bioadhesive showing high transparency. **(D)** Optical image of the bioadhesive formulations prior to UV polymerisation. **(E)** Optical images of the bioadhesive formulations following photopolymerization in 10mm x 20mm x 6mm moulds.

5.2.3.2 Material characterisation

The FTIR spectrum of the gelMA displays the characteristic peaks of the standard gelatine polymer (Figure 71). The typical absorption band around 3285 cm⁻¹ is attributed to the O—H and N—H stretching vibrations. The peaks in the region of 2900–3100 cm⁻¹ correspond to the stretching vibrations of the C–H groups. Notably, in the gelMA, these peaks are more pronounced than in the as-purchased gelatine. The peaks at 1632–1633 cm⁻¹ correspond to the backbone structure of the gelatine, showing the C=O stretching of the amide group. The peaks at 1524–1527 cm⁻¹ correspond to the N—H bending coupled to C—H stretching, and finally, the peaks at 1234–1241 cm⁻¹ correspond to C—N bending and N—H bending, agreeing with literature [66]. Notably, the synthesised bioadhesive sees the introduction of a strong peak at 1241 cm⁻¹ corresponding to the C=O stretching likely because of the polymerised AA. Another peak at 1194 cm⁻¹ corresponds to the introduction of C—O ester group.

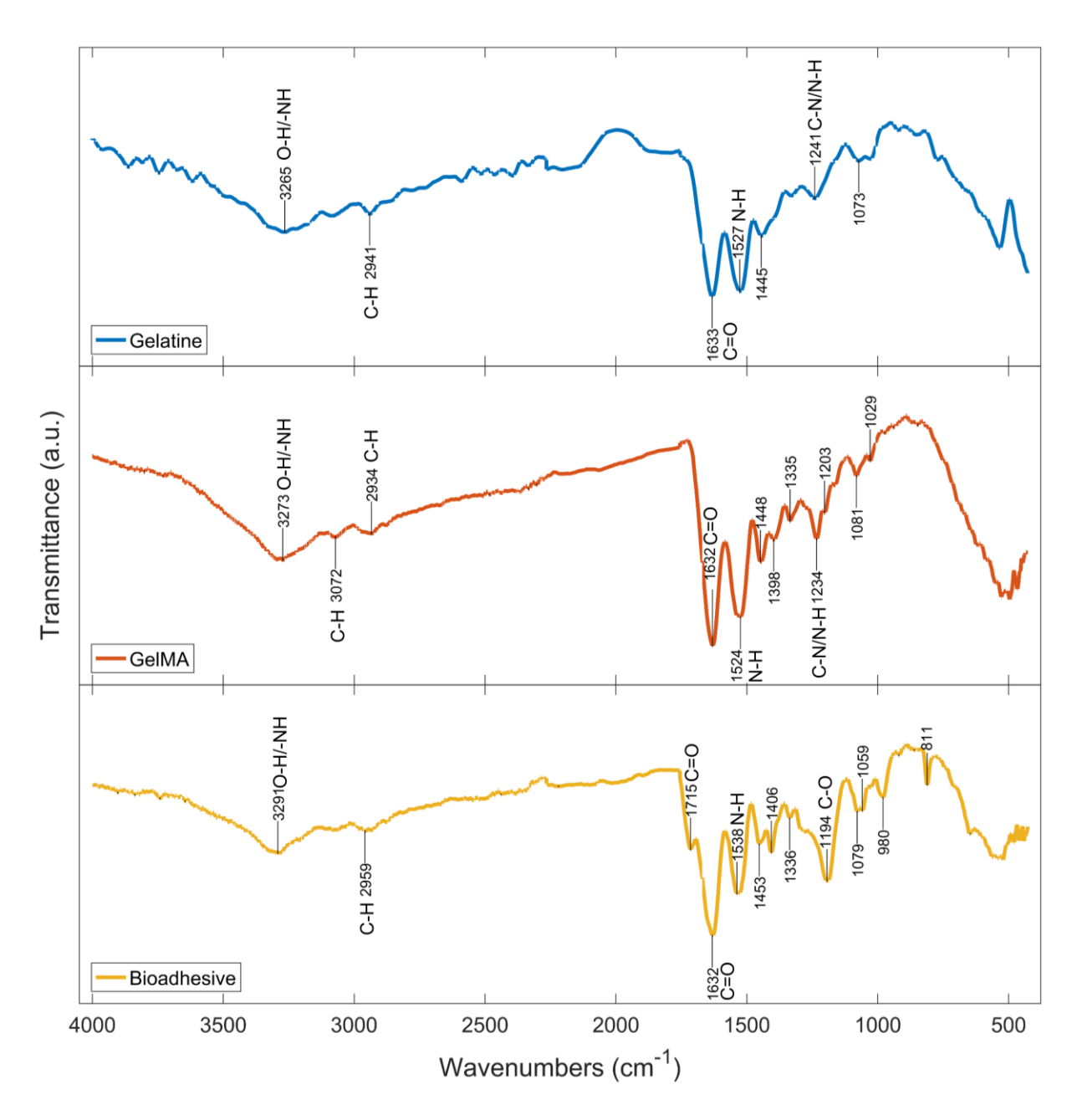


Figure 71: FTIR spectra of as-purchased gelatine, methacrylated gelatine (gelMA) and the synthesised bioadhesive patch.

5.2.3.3 Mechanical Performance

Despite the varying degrees of cross-linking, no significant changes in mechanical stiffness were observed between the 10%, 20%, and 30% (w/w) samples. Before testing, the samples were fully swollen and allowed to equilibrate for 1 hour to ensure consistent conditions. Figure 72L shows an optical image of the patch undergoing tensile stress. The Young's modulus was calculated as the mean value of the linear region of the stress-strain curves by taking the derivative of the stress-strain curves shown in Figure 72A-Figure 72D. The mean Young's modulus of the samples only

incrementally increased from 29 kPa to 33 kPa across the 10-30% AA (w/w) samples, with no major conclusions drawn due to a high p-value (Figure 72I).

However, in the 40% AA (w/w) sample, significant changes in the material properties were observed, with the mean Young's modulus increasing to approximately 110 kPa. The linear (elastic) range of the stress-strain curve was only present up to 45% engineering strain, as indicated by Figure 72H, whereas the elastic region in the other samples ranged from 80% to 400% engineering strain (Figure 72E-Figure 72G).

There were also significant differences in the toughness of the material, which was calculated as the integral of the stress-strain curves up to the failure points (indicated by a cross in Figure 72A-Figure 72D). Toughness increased incrementally up to a maximum in the 30% AA (w/w) sample, after which it began to decrease sharply at 40% (w/w). The initial increase in toughness can be attributed to an optimal degree of cross-linking, which enhances energy dissipation during deformation. At higher AA content, excessive cross-linking leads to a more rigid network, resulting in a higher Young's modulus but lower capacity for plastic deformation, thus reducing toughness. Toughness was calculated as the area under the stress-strain curve up to the failure point, representing the material's ability to absorb energy before fracturing.

However, it should be noted that there were large standard deviations in the toughness measurements. These variations can be attributed to changes in the surface finish of the mould between sample fabrications, with micro-imperfections introduced during the process causing inconsistencies in toughness values. The micro-imperfections can act as stress concentrators leading to earlier failure in some samples. The data for the 30% AA (w/w) sample suggests that this degree of cross-linking allowed for increased sliding of the polymer chains without failure. However, at 40% AA (w/w), the polymer chains were likely further cross-linked, which contributed to the increased Young's modulus and decreased toughness. This suggests that at 30% AA (w/w) increased chain sliding and energy absorption are allowed and beyond this point the materials increase in brittleness. Clear relationships can be observed between the Young's modulus of the individual samples of the 40% AA (w/w) (Figure 72H) and their toughness (Figure 72D), where increased Young's modulus displays increased brittleness.

From a bioadhesive design perspective, these findings are significant. The ability to tune the Young's modulus between 33–110 kPa provides a pathway to optimize the bioadhesive for mechanical compatibility with oesophageal tissue, which has reported Young's modulus values ranging from 6.0–266.0 kPa (longitudinally) and 5.2–62.9 kPa (circumferentially) [238]. Matching the mechanical properties of the bioadhesive to the surrounding tissue is crucial for ensuring seamless integration, reducing discomfort, and maintaining adhesion over time [242].

However, flexibility is another critical factor in bioadhesive performance. While Young's modulus provides insights into stiffness, it does not directly capture flexibility or the material's ability to conform to dynamic tissue movements. The results indicate that increased cross-linking enhances stiffness but reduces elasticity, which may impact long-term adaptability.

Figure 72K presents representative examples of the different samples, illustrating the relationships between cross-linking density, microstructure properties, and mechanical behavior. These results suggest that careful control of AA concentration between 30–40% (w/w) could allow for fine-tuning of the bioadhesive's mechanical properties to balance adhesion strength, toughness, and flexibility for optimal performance in mucosal environments.

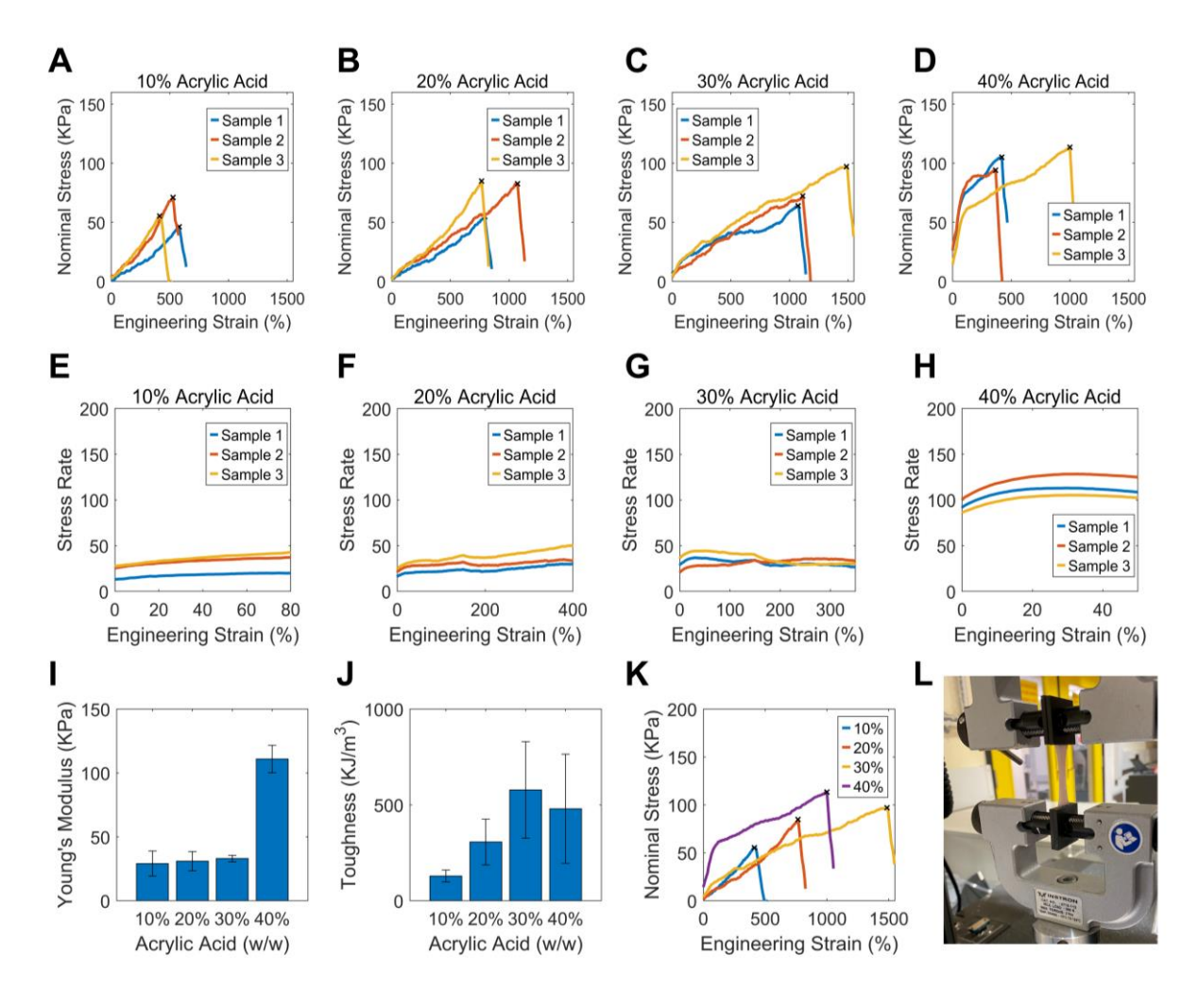


Figure 72: **(A-D)** Nominal stress vs engineering strain of the bioadhesive patches based on AA (w%/w) concentrations (Black cross indicates point of material failure). **(E-H)** Stress rate vs engineering strain used to compute the Young's modulus. **(I)** Young's modulus of the various bioadhesive patches (n=3). **(J)** Toughness of the bioadhesive patches (n=3). **(K)** Representative examples of the patches plotted together **(L)** Image of the patch undergoing tensile stress.

5.2.3.4 Adhesive Performance

The adhesive properties of the GI patch under the slippery conditions of the inner oesophageal tissue were quantitatively analysed using a lap shear test, with three samples tested for each AA concentration. An image of the test setup is shown in Figure 73F. The force-displacement curves exhibited either right or isosceles triangular shapes, depending on the type of detachment observed (Figure 73A-Figure 73D). A sharp decline in the curve following the maximum shear force (indicated by a cross) suggests that detachment occurred in a single swift motion. In contrast, a gradual decline indicates that detachment was incremental, with the contact area between the tissue and bioadhesive decreasing progressively.

The detachment behaviour qualitatively depended on whether separation occurred immediately at the mucosal layer or if the submucosa reattached during the lap shear test. Figure 73E presents the maximum shear stress results as a function of AA concentration (w/w). Initially, the mean shear stress decreases with increasing AA concentration, then incrementally increases as the AA concentration continues to rise. This trend may be attributed to the anatomical characteristics of oesophageal tissue and the slippery nature of the mucosa, which primarily bonds to the mucus-penetrating chains from the AA. These results are consistent with findings from other studies in the literature using similar chemical compositions, though notably, no previous studies have reported shear stress results specifically for oesophageal tissue [215,237].

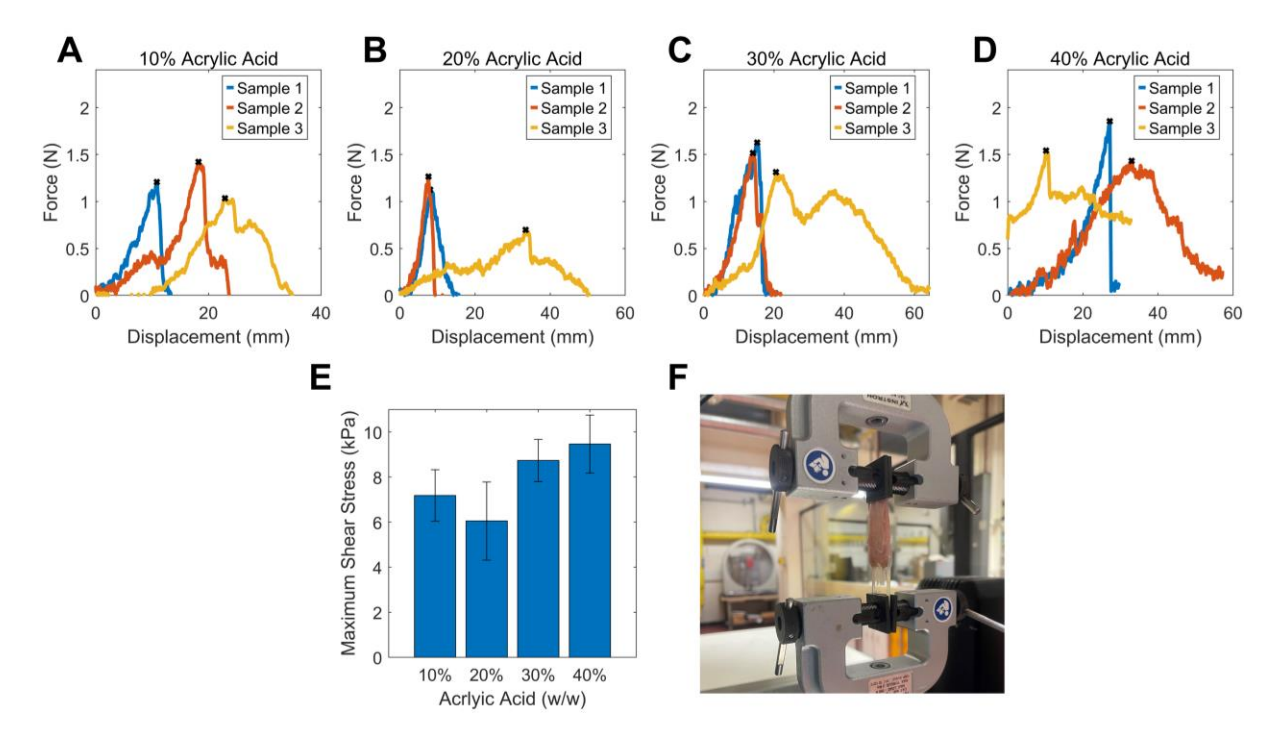


Figure 73: **(A-D)** Force vs displacement plots of the bioadhesive with varying AA (w%/w) concentrations undergoing lap shear stress testing on oesophageal tissue for adhesion measurements. **(E)** Maximum shear stress of the bioadhesive patches (n=3) **(F)** Optical image of the setup used for testing.

5.2.3.5 Flow Testing

To assess the ability of the bioadhesive to adhere to the wet and dynamic surface of oesophageal tissue in conditions simulating *in vivo* acid reflux diagnosis, an *ex vivo* flow test was conducted. The flow test was carried out for 4 hours at a flow rate of 180 L/hour pumping 0.9% saline solution. The flow rate is above typical human drinking rates and was chosen as an accelerated stress condition to challenge the adhesion

and stability of the bioadhesives. This would give a worst-case detachment scenario and identify potentially failure modes rapidly.

Based on the increased maximum shear stress observed in the 40% AA (w/w) sample, this composition was selected as the bioadhesive backing for a potentiometric sensor. The sensor, featuring a silver/silver chloride reference electrode and a carbon-based working electrode, was fabricated on a polyimide substrate with a 2 cm diameter and a 200-micron thickness. The 40% AA (w/w) composition was photopolymerised directly onto the polyimide sheet using the established methodology.

Figure 74A illustrates a schematic of how the sensor, integrated with the bioadhesive, would be mounted using an endoscope. Figure 74B and Figure 74C show different perspectives of a to-scale 3D clear resin-printed model of the lower oesophagus and stomach, demonstrating how the sensor would be mounted when detecting reflux events. Figure 74D provides an optical image of the testing apparatus, where a pump was used to continuously flush a 0.9% saline solution through the oesophagus and stomach. This setup was used to test whether the sensor and the fully swollen adhesive could withstand conditions mimicking food, beverage, and reflux events. The flexible sensor was rolled up and inserted just above the lower oesophageal sphincter via an incision near the duodenum, as depicted in Figure 74E.

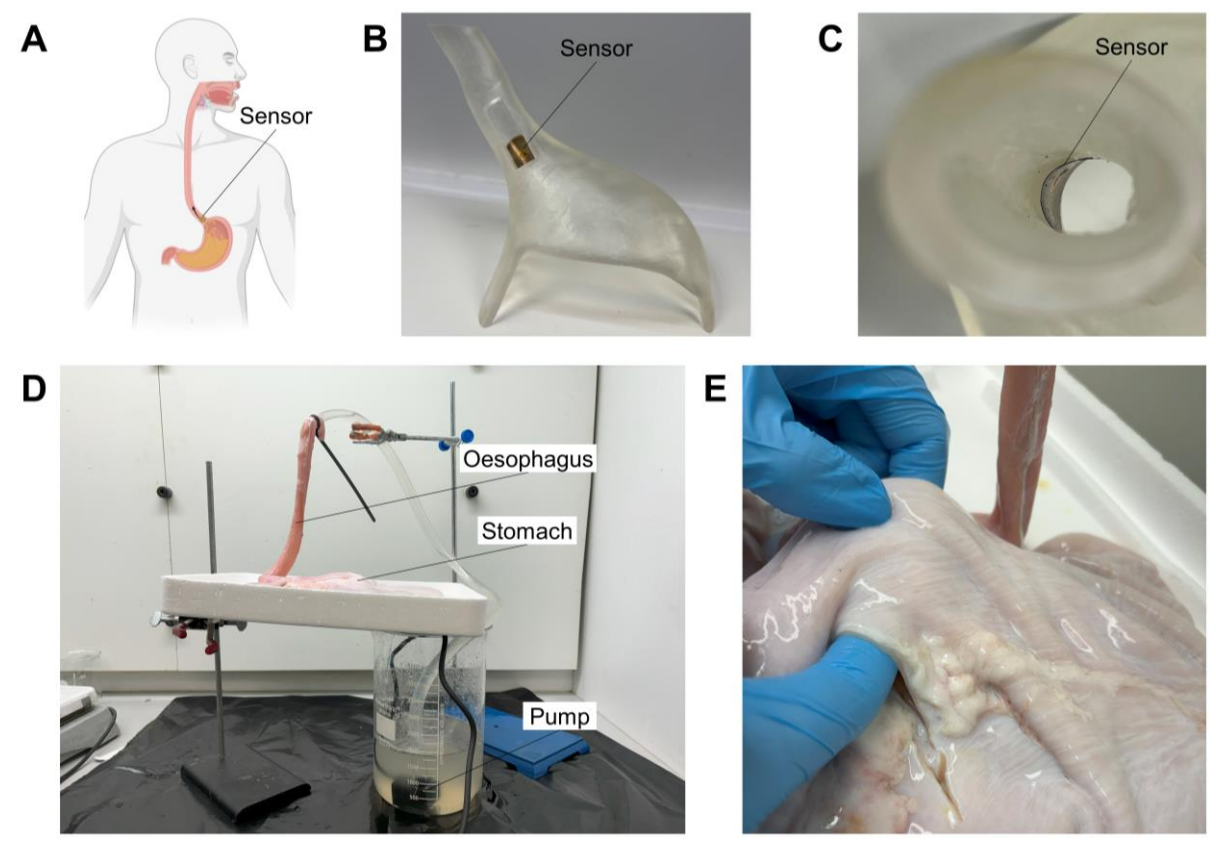


Figure 74: **(A)** Schematic of patient with acid reflux, and where the sensor would be mounted [partially created using biorender.com] **(B)** Optical image of life-sized 3D printed oesophagus and stomach model showing the sensor's mounting and location. **(C)** Image of the model from the top of the oesophageal model showing its conformity to the oesophageal wall. **(D)** Image of the setup flow test model. **(E)** Image of the incision created to implant the sensor for the flow test.

A stiff laparoscope was then used to investigate and qualitatively assess the sensor's adherence following the flow tests. The laparoscope had dual cameras and was initially inserted from the oesophagus and directed through the gastrointestinal tract until reaching beyond the lower oesophageal sphincter and then removed. Figure 75A show laparoscopic and camera views of the oesophagus tissue and the imaging process prior to reaching the sensor which is then visible in Figure 75B. Notably, the sensor remained in place despite shear forces from the laparoscope itself during insertion and removal.

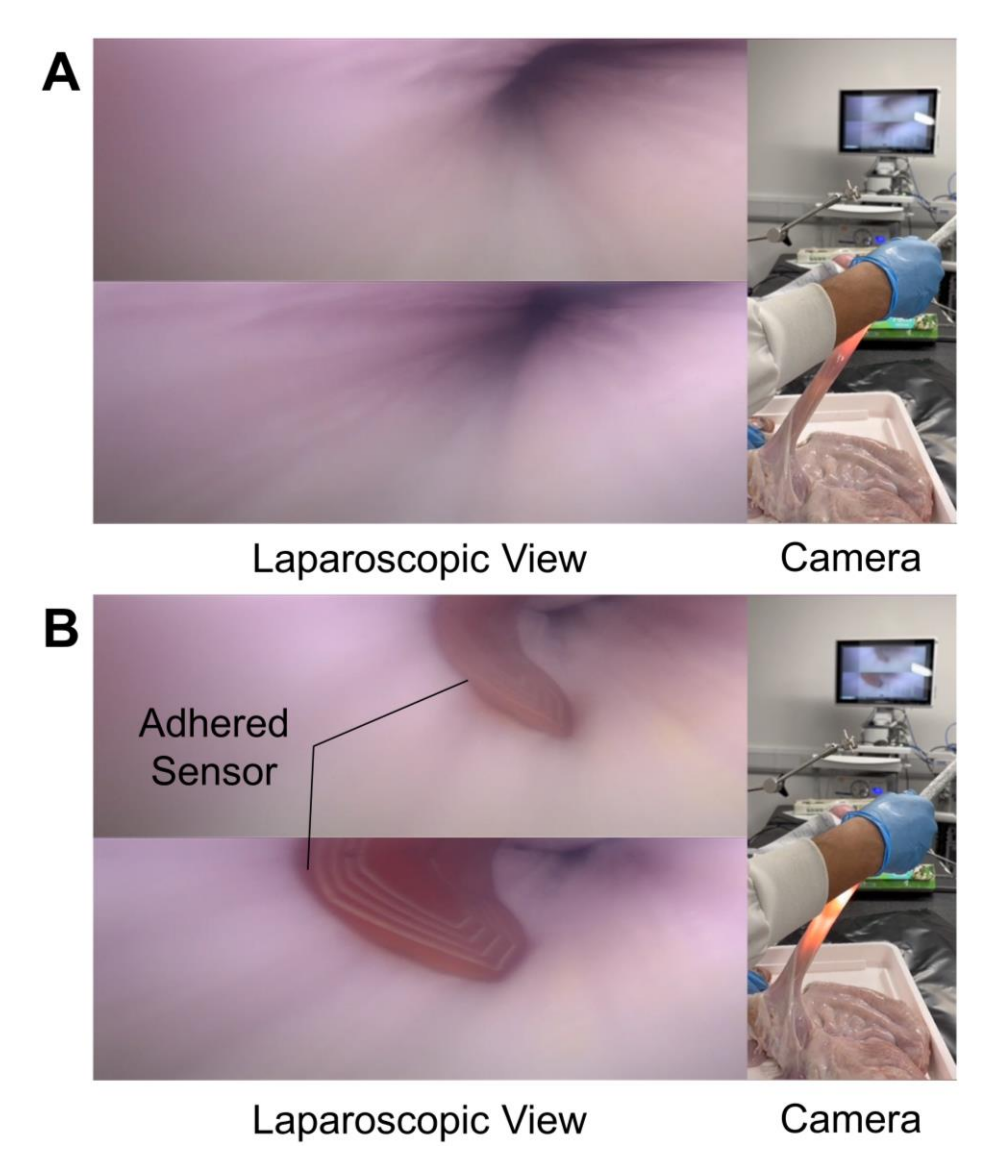


Figure 75: Laparoscope and camera images extracted from a video following the flow testing. (A) laparoscope location in oesophagus prior to lower oesophageal sphincter. (B) Laparoscope at lower oesophageal sphincter showing adhered sensor.

5.2.4 Conclusion

This study explored the variation of poly(acrylic acid) content within a gelatine-poly(acrylic acid) hydrogel matrix to evaluate its suitability for anchoring medical devices to the oesophageal lining. Specifically, the research focused on assessing the mechanical and mucoadhesive properties of the formulations through tensile and lap shear tests. The results highlighted the effectiveness of formulations containing 30% and 40% AA (w/w), which demonstrated appropriate mechanical strength and adhesion properties. These formulations were shown to be capable of being tuned to match the mechanical characteristics of the oesophageal tissue, thereby ensuring seamless integration and minimising discomfort during application.

The 40% AA (w/w) formulation was selected for further application due to its superior performance in adhesion performance and matching mechanical properties. It was coated on the back of a thin-film pH sensor with a polyimide substrate and tested on an *ex vivo* porcine oesophageal model. During this evaluation, continuous saline pumping was employed to mimic the dynamic environment of the oesophagus during beverage ingestion. Notably, the bioadhesive successfully maintained its attachment to the oesophageal lining throughout several hours of testing, as confirmed by laparoscopic imaging. This outcome demonstrates the potential for bioadhesives to overcome the inherent challenges posed by the anti-adherent properties of the oesophageal mucus layer.

The findings of this study present a promising step forward in utilising bioadhesives for seamless healthcare monitoring in challenging environments such as the gastrointestinal tract. The use of bioadhesives for anchoring medical devices in the oesophagus could address key limitations of current mechanical attachment methods, such as discomfort, complications, and early dislodgement.

While the results are encouraging, further research is needed to refine and optimise the bioadhesive formulations for clinical application. A critical area of future work involves ensuring the controlled and safe dislodgement of the bioadhesive following the monitoring period. Additionally, in vivo testing on porcine models will be essential to assess the long-term biocompatibility, safety, and performance of the bioadhesive in dynamic physiological environments, including the effects of peristaltic motion and varying gastric contents. Testing with different fluid viscosities was not possible in the present work due to the need for a specialised pump setup, and conducting full-scale in vivo experiments was beyond the scope and resources of this PhD.

In conclusion, this study demonstrates the feasibility of using bioadhesives to anchor medical devices to the oesophageal lining. The integration of mucoadhesive hydrogels with thin-film sensors offers a compelling approach for advancing healthcare monitoring technologies. By addressing the outlined challenges and conducting further testing, this approach has the potential to be used for diagnostic and therapeutic practices for GORD and beyond.

Chapter 6: Conclusion and Future Work

6.1 Conclusions

This research sought to develop an innovative biomedical diagnostic device for the detection of gastro-oesophageal reflux disease (GORD), addressing the shortcomings of existing technologies. Current diagnostic tools are often uncomfortable, invasive, and limited in their diagnostic accuracy, prompting the need for a more user-friendly, compact, and reliable solution. The proposed device aimed to overcome these challenges by leveraging the design principles of mucosa-interfacing electronics, an emerging and transformative class of in vivo sensing technologies which follows the design principles of skin-interfacing electronics. These devices are designed to integrate seamlessly with the human body, enabling imperceptible, minimally invasive diagnostic capabilities.

To achieve this vision, the research adopted a multidisciplinary approach, drawing on advancements in material science, nanofabrication, bioadhesion, and wireless communication. Fully printed sensors were fabricated to provide precise, robust pH measurements in the low-acidity environment of the oesophagus. Covalent organic frameworks (COFs) were explored as advanced electrochemical composites, offering improved sensitivity, stability, and excellent biocompatibility for real-time sensing applications. Additionally, biocompatible mucoadhesive systems were developed to ensure secure, long-term attachment of the device to the oesophageal mucosa, maintaining stability under dynamic physiological conditions and validated using exvivo testing. Proof-of-concept wireless data transmission was integrated into the system using near-field communication (NFC) technology, enabling real-time, continuous monitoring without the need for implantable batteries or other power sources improving overall patient safety.

This chapter synthesises the key findings of this study, providing an overview of the device's capabilities and the challenges encountered during development. The implications of this work are contextualised within the broader field of biomedical diagnostics, where advancements in nanomaterials, wireless communication, and bioadhesive technologies are driving the next generation of diagnostic devices. The chapter also critically evaluates the significance of the findings, highlighting how they contribute to the growing field of mucosa-interfacing electronics and their potential applications beyond GORD diagnosis. Finally, limitations of the current research are

acknowledged, and opportunities for future development are outlined, including pathways to enhance device reliability, scalability, and clinical viability.

6.2 Contributions

Implantable biomedical devices for in-vivo sensing and other medical applications have been in use for decades, with notable examples including pacemakers, continuous glucose monitors, and implantable cardioverter defibrillators. For the diagnosis of gastro-oesophageal reflux disease (GORD), the only FDA-approved technologies currently available are capsule-based pH sensors and catheter-based systems. While these devices are effective to a degree, their limitations are significant, primarily due to the high levels of patient discomfort and low tolerability associated with their use. This discomfort often forces patients to modify their lifestyles and behaviours during monitoring periods, which undermines the ability to accurately correlate lifestyle factors with reflux events. Since GORD has no definitive cure, identifying such correlations is critical for managing symptoms and improving patient outcomes.

To address these limitations and improve patient comfort, this study explored advanced nanofabrication techniques, focusing specifically on printed electronics. Printed electronics offer numerous advantages, including ease of manufacturing, high resolution, repeatability, and scalability at a low cost. These benefits make the technology particularly suitable for widespread adoption, an important consideration given the already high prevalence of GORD and its increasing incidence due to modern dietary and lifestyle factors. Among the nanofabrication methods available, direct-write printing was selected for its suitability for prototyping and its ability to precisely deposit functional inks.

Graphene oxide emerged as a promising nanomaterial for pH sensing due to its unique properties, such as high sensitivity over a broad pH range (2–12) and excellent selectivity, as reported in the literature. However, significant challenges were encountered with the reproducibility of results. Literature highlighted inconsistencies in pH sensitivity between different batches of GO and variations in results depending on the method of application, such as drop-casting. This variability was linked to the preparation methods of GO, which influence its functional groups, defect density, and nanosheet morphology. Additionally, agglomeration of GO frequently occurred,

altering its surface area and reducing its effectiveness. Practical issues also arose, such as poor adhesion of GO to printed electrodes, particularly under bending and flow conditions, which are critical for in-vivo applications.

To overcome these challenges, GO was combined with polyurethane polymers and a stabiliser to create a novel pH-sensitive direct-write printable ink. This innovative ink demonstrated improved robustness and adhesion, making it suitable for printing and enabling consistent sensor fabrication with reliable performance across sensors. Testing revealed good pH sensitivity over a range of 2–12, with functionality extending to pH 1.5, a critical range for detecting reflux events. Sensor performance was validated using gastrointestinal reflux simulant solutions, chosen to replicate the real-world conditions the device would face.

Despite these advancements, the expected high pH sensitivity reported in literature was not fully achieved with the as-purchased GO from the manufacturer. This limitation highlighted the influence of GO preparation methods and parameters, which significantly affect the material's functional groups, defect density, and nanoscale properties, all of which contribute to its pH sensitivity. Over time as well, the GO was found to reduce during pH sensing leading to reduced sensitivity and increased drift with time. To achieve enhanced sensitivity, consistency, and selectivity, further work was needed which led to the exploration of covalent organic frameworks (COFs) for use.

COFs are a highly versatile class of advanced nanomaterials, offering remarkable tunability in their physical and chemical properties. Their characteristics can vary significantly based on their structure, such as 2D versus 3D frameworks, and their overall stability is heavily influenced by the nature of the bonds between the organic ligands. Highly stable COFs, as demonstrated in the literature, often undergo irreversible tautomerisation, resulting in robust materials with high surface areas and a porous architecture. These features make COFs particularly appealing for applications requiring high sensitivity and functionality.

However, the utility of pure COFs as electrode materials is limited by their inherently low electrical conductivity. To overcome this limitation, composite materials combining COFs with the previously explored GO was explored. During the synthesis of these composites, the thermal treatment required for COF generation transformed the GO

into a deoxygenated form with less oxygen-containing functional groups. The COF however served as a protective and functional layer, interacting with GO via $\pi-\pi$ stacking among the nanosheets. This combination allows for the creation of a hybrid material that is both conductive and retains the high surface area and stability of COFs.

To optimise the pH-sensing performance of these composites, covalent organic frameworks (COFs) with specific functional groups known to undergo protonation and deprotonation were carefully selected. These functional groups were chosen for their ability to interact synergistically with the pH-responsive properties of GO, enhancing the composite's overall sensitivity and selectivity. Among the tested COFs, those incorporating sulfonate (-SO₃⁻) functional groups demonstrated the most promising performance. The inherent proton selectivity of the -SO₃⁻ groups facilitated a highly sensitive and stable capacitive response, making these COFs ideal candidates for capacitive pH sensing applications.

To evaluate the biocompatibility of the COF-GO composite, cytotoxicity testing was performed on human oesophageal epithelial cells using standard viability assays. The results confirmed that the composite material exhibited minimal cytotoxic effects, meeting the critical requirement for safe in-vivo applications. These findings validated the composite's suitability for prolonged contact with the oesophageal mucosa, addressing a key concern for biomedical implantable devices.

The selected COF-GO composite further demonstrated exceptional stability and selectivity under challenging conditions, maintaining a robust capacitive response even in highly acidic gastric acid simulant solutions (pH ~1.5). This performance highlighted its potential for real-world applications, enabling the development of a printed capacitive pH sensor with outstanding reliability, even under the dynamic and harsh conditions of the gastrointestinal environment.

Building on the success of the pH-sensitive electrode materials, efforts were directed toward leveraging the capacitive response of the COF-GO composite as a tuning capacitor in a wireless, batteryless sensor system. In alignment with the principles of printed electronics and mucosa-interfacing device design, various inks were used to create flexible components. The design incorporated a miniaturised 2 cm × 2 cm coil printed on a polyimide substrate, optimised for wireless transmission at medically

approved frequencies. The GO-COF-based interdigitated electrode acted as the tuning capacitor, modulating the resonant frequency in response to pH changes.

The coil's geometry was carefully designed, with a high number of turns to achieve the necessary inductance for operation at frequencies detectable by a standard impedance analyser and within the medically accepted frequency range. The Q-factor of the coil compared favourably with similar works reported in the literature, validating the design [200]. Proof-of-concept operation was demonstrated using standard static capacitors, successfully achieving resonance frequency shifts. However, replicating this performance with the GO-COF composite tuning capacitor proved challenging, as discussed in detail in the limitations and future work sections.

The final component of the device was the integration of a biocompatible mucoadhesive patch to secure the sensor to the oesophageal mucosa. Various formulations of gelatine, methacrylated gelatine, and poly(acrylic acid) matrices were investigated, with an emphasis on optimising mechanical strength and adhesive properties. Following works from literature, the addition of an acrylic acid N-hydroxysuccinimide ester (AAc-NHS ester) further enhanced adhesion by creating strong covalent bonds with mucosal tissues. This formulation was designed for compatibility with the overall device architecture, allowing direct deposition onto the polyimide substrate. The patch was cured using UV irradiation to form a cohesive, integrated system.

To validate the adhesive performance of the mucoadhesive patch, ex-vivo experiments were conducted using porcine oesophageal and gastric tissue. The sensor was implanted into an intact porcine oesophagus and stomach and subjected to flow conditions simulating beverage ingestion to test its ability to maintain adhesion under dynamic, slippery conditions. These experiments demonstrated successful tethering of the sensor to the oesophageal mucosa, providing a reliable mechanism for mucosal attachment. This approach eliminates the mechanical attachment issues faced by current GORD diagnostic devices, significantly improving patient comfort and diagnostic efficacy.

In culmination, this work successfully integrated advanced nanomaterials, flexible printed electronics, wireless communication, and biocompatible adhesives to develop a novel oesophageal diagnostic device for GORD. Proof-of-concept experiments

demonstrated the feasibility of the device, laying the groundwork for further development and clinical validation. The combined efforts in material science, device engineering, and biomedical innovation presented in this thesis represent a significant step toward creating more effective, minimally invasive diagnostic tools for GORD.

6.3 Limitations and Future Work

While the current study successfully demonstrated the feasibility of a printed, mucosainterfacing biomedical device for pH sensing and wireless transmission, several limitations were identified that provide opportunities for future improvement. These challenges span material, design, and implementation aspects, and addressing them will be critical for advancing the proposed technology.

Chapter 2 lacked the level of materials characterisation required to fully verify the oxidation of plasma-treated graphene. Although FTIR and SEM provided useful insights, more advanced techniques such as X-ray photoelectron spectroscopy (XPS) and Raman spectroscopy would have been valuable to confirm the incorporation of oxygen-containing functional groups, quantify oxidation states, and distinguish between carbon bonding environments. Incorporating such analyses in future work would provide a more rigorous understanding of how plasma treatment modifies the graphene surface, thereby strengthening the correlation between material properties and sensor performance.

One major limitation was the inability of the GO-COF composite sheet to reliably function as a tuning capacitor for pH changes. While static capacitors demonstrated consistent resonance frequency shifts, the capacitance of the GO-COF composite was highly unstable, influenced by factors such as droplet size and inconsistent surface coverage. This instability persisted despite careful construction of the droplet reservoir using PDMS and further compounded by uncontrolled flow dynamics. To mitigate this issue, future designs could incorporate a microfluidic system with a defined mixing chamber. Such a system would allow precise control over flow rates and droplet volumes, ensuring consistent capacitance measurements while enabling automated flushing and mixing. These enhancements could reduce signal variability, enabling clearer identification of capacitance shifts in response to pH changes.

The low power output of the impedance analyser used in the current design also presented a significant limitation. The analyser's restricted power likely led to weaker

magnetic coupling between the primary and secondary coils, with the observed coupling coefficient falling below the simulated value of 0.1. Furthermore, the geometry of the secondary coil was not optimised to enhance coupling. In similar systems, larger secondary coils are used to achieve higher inductance and stronger coupling coefficients [187,198]. Future designs could address these issues by employing a dedicated waveform generator paired with a power amplifier, as illustrated in Figure 76. This modification would allow for stronger magnetic coupling, improved signal strength, and enhanced robustness. Notably, published studies using transponder coils with dimensions of 12 cm × 12 cm have reported quality factors as high as 70, providing a benchmark for future optimisation efforts [187,198].

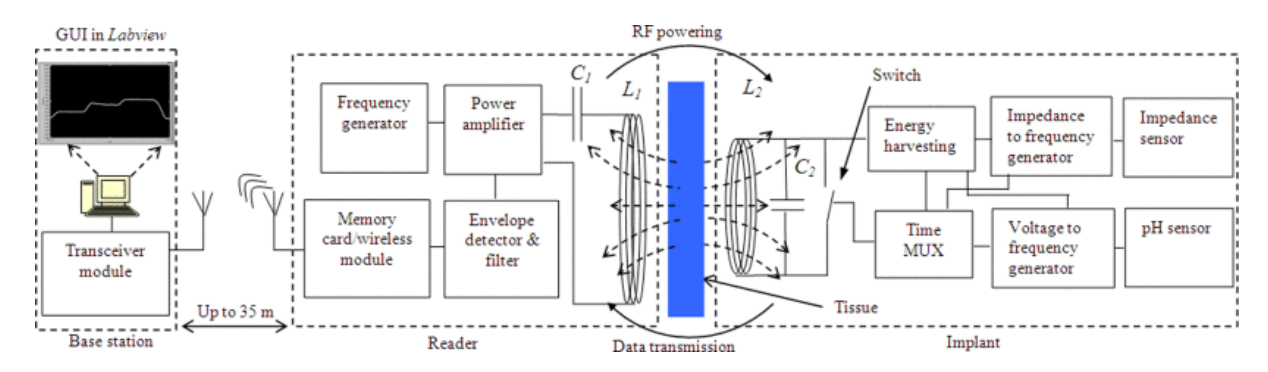


Figure 76: Block diagram of a system which uses a power amplifier, and frequency generator to enhance the RF powering. Adopted from [198].

The absence of validation in animal models represents another significant limitation of this study. While ex-vivo experiments provided valuable insights, they did not replicate the complexities of in-vivo conditions. Testing the sensor in large animal models would allow for a more comprehensive evaluation of its functionality, particularly its ability to detect reflux events and transmit signals reliably over extended periods. Such studies would also provide critical insights into the effects of coil misalignment and oesophageal motion on signal quality. Incorporating animal experiments would offer invaluable data on the sensor's performance in biologically relevant environments, as well as uncover potential challenges that may not arise in controlled laboratory settings.

The current reliance on a benchtop impedance analyser for frequency sweeps also limits the system's practicality. For the sensor to be viable in clinical and real-world applications, a portable and wearable version of the system must be developed. This would involve designing a compact frequency sweep module capable of continuous

operation for at least 48 hours. A low-power microcontroller paired with efficient RF amplifiers could facilitate on-demand frequency sweeps, while rechargeable battery systems could provide a reliable power source. Such innovations would make the sensor more practical for monitoring applications, including long-term pH tracking in medical scenarios.

An exciting avenue for future work lies in the development of bioresorbable versions of the sensor [53]. This approach would eliminate the need for ensuring device exit after use, and electronic waste aligning with growing interest in environmentally sustainable and biocompatible technologies. In bioresorbable designs, materials such as PDMS and polyimide could be replaced with bioresorbable encapsulants like beeswax or chitosan-based composites. Similarly, cytotoxic components like silver nanoparticles could be substituted with biocompatible materials, such as high-purity zinc, which can be laser-cut into precise electrode geometries [53]. Figure 77 presents a conceptual illustration of a proposed bioresorbable sensor. The gelatine-based bioadhesive used in the current design is already biocompatible and could be retained in future iterations. Prior research has demonstrated the efficacy of similar materials in creating non-immunogenic, bioresorbable devices, underscoring the feasibility of this approach.

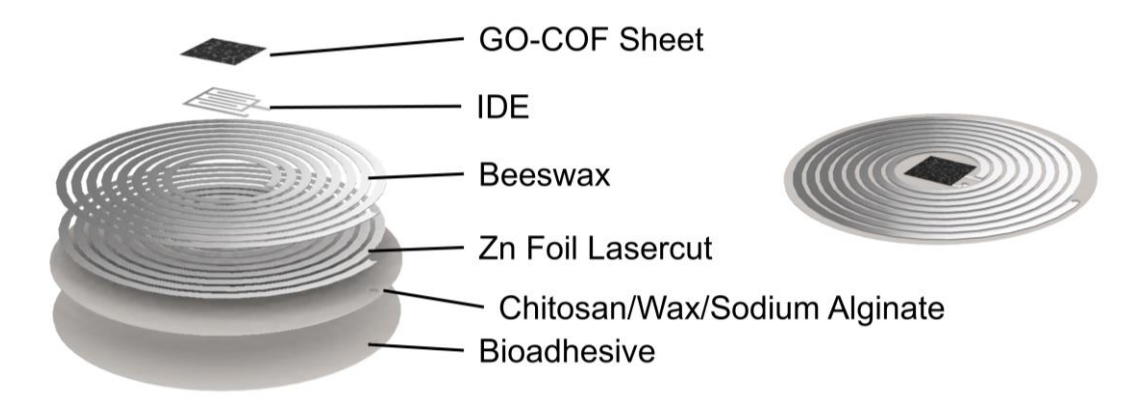


Figure 77: Proposed bioresorbable version of the full sensor design.

In summary, future improvements to the proposed design should focus on stabilising capacitance measurements through microfluidic integration, enhancing magnetic coupling via higher-power systems, optimising coil geometry, validating functionality in animal models, and developing portable and wearable solutions. Additionally, exploring bioresorbable designs could position the technology as a sustainable and

biocompatible solution for biomedical applications. These advancements will be crucial for translating the current design into a practical, reliable, and widely applicable technology.

6.4 Concluding Remarks

6.4.1 Summation of Key Points

This research successfully developed a novel pH-sensing device for GORD diagnosis, combining graphene oxide-based sensors, COF-enhanced sensitivity, gelatine-poly(acrylic acid) bioadhesives, and NFC-enabled wireless communication. The interdisciplinary approach addressed critical challenges in sensor design, bioadhesion, and data transmission, resulting in a device that offers significant advantages over existing technologies.

6.4.2 Broader Implications and Contributions of the Research

Beyond GORD diagnostics, this work provides a foundation for the broader application of mucosa-interfacing electronics in biomedical diagnostics. The integration of advanced materials, bioadhesion, and wireless communication into a cohesive device demonstrates the potential for transformative healthcare technologies that are minimally invasive and highly effective.

6.4.3 Final Thoughts and Future Directions

This study represents a step forward in the development of mucosa-interfacing electronics, paving the way for next-generation diagnostic tools. While challenges remain, the methodologies and findings offer a roadmap for future innovations in in vivo sensing and healthcare monitoring. Continued research and collaboration across disciplines will be essential to realise the full potential of this technology, ultimately improving patient outcomes and quality of life.

References

- [1] L. Frazzoni, M. Frazzoni, N. De Bortoli, M. Ribolsi, S. Tolone, S. Russo, R.L. Conigliaro, R. Penagini, L. Fuccio, R.M. Zagari, E. Savarino, Application of Lyon Consensus criteria for GORD diagnosis: evaluation of conventional and new impedance-pH parameters, Gut 71 (2022) 1062–1067. https://doi.org/10.1136/gutjnl-2021-325531.
- [2] K.D. Bardhan, V. Strugala, P.W. Dettmar, Reflux Revisited: Advancing the Role of Pepsin, International Journal of Otolaryngology 2012 (2012) 1–13. https://doi.org/10.1155/2012/646901.
- [3] J.P. Pearson, S. Parikh, R.C. Orlando, N. Johnston, J. Allen, S.P. Tinling, N. Johnston, P. Belafsky, L.F. Arevalo, N. Sharma, D.O. Castell, M. Fox, S.M. Harding, A.H. Morice, M.G. Watson, M.D. Shields, N. Bateman, W.A. McCallion, M.P. van Wijk, T.G. Wenzl, P.D. Karkos, P.C. Belafsky, Review article: reflux and its consequences—the laryngeal, pulmonary and oesophageal manifestations. Conference held in conjunction with the 9th International Symposium on Human Pepsin (ISHP) Kingston-upon-Hull, UK, 21-23 April 2010., Alimentary Pharmacology & Therapeutics 33 Suppl 1 (2011) 1–71. https://doi.org/10.1111/j.1365-2036.2011.04581.x.
- [4] T.M.G. Pecora, B. Ragazzo, W. Bertin, A. Ragonese, M. Mascagni, P. Maffei, R. Pignatello, Rheological behavior of a new mucoadhesive oral formulation based on sodium chondroitin sulfate, xyloglucan and glycerol, Journal of Functional Biomaterials 12 (2021). https://doi.org/10.3390/jfb12020028.
- [5] J. Dent, H.B. El-Serag, M.A. Wallander, S. Johansson, Epidemiology of gastro-oesophageal reflux disease: A systematic review, Gut 54 (2005) 710–717. https://doi.org/10.1136/gut.2004.051821.
- M.A. Dirac, S. Safiri, D. Tsoi, R.A. Adedoyin, A. Afshin, N. Akhlaghi, F. Alahdab, [6] A.M. Almulhim, S. Amini, F. Ausloos, U. Bacha, M. Banach, A.S. Bhagavathula, A. Bijani, A. Biondi, A.M. Borzì, D. Colombara, K.E. Corey, B. Dagnew, A. Daryani, D.V. Davitoiu, F.M. Demeke, G.T. Demoz, H.P. Do, A. Etemadi, F. Farzadfar, F. Fischer, A.K. Gebre, H. Gebremariam, B. Gebremichael, A. Ghashghaee, U.C. Ghoshal, S. Hamidi, M. Hasankhani, S. Hassan, S.I. Hay, C.L. Hoang, M.K. Hole, K.S. Ikuta, O.S. Ilesanmi, S.S.N. Irvani, S.L. James, F. Joukar, A. Kabir, H.G. Kassaye, T. Kavetskyy, A.P. Kengne, R. Khalilov, M.U. Khan, E.A. Khan, M. Khan, A. Khater, R.W. Kimokoti, A. Koyanagi, A.L. Manda, D. Mehta, V. Mehta, T.J. Meretoja, T. Mestrovic, E.M. Mirrakhimov, P. Mithra, A. Mohammadian-Hafshejani, M. Mohammadoo-Khorasani, A.H. Mokdad, M. Moossavi, G. Moradi, G. Mustafa, M.D. Naimzada, S. Nasseri-Moghaddam, J. Nazari, I. Negoi, C.T. Nguyen, H.L.T. Nguyen, M.R. Nixon, S. Olum, A. Pourshams, H. Poustchi, M. Rabiee, N. Rabiee, A. Rafiei, S. Rawaf, D.L. Rawaf, N.L.S. Roberts, G. Roshandel, S. Safari, H. Salimzadeh, B. Sartorius, A. Sarveazad, S.G. Sepanlou, A. Sharifi, A. Soheili, H.A.R. Suleria, D.B. Tadesse, F.G.G. Tela, B.E. Tesfay, B. Thakur, B.X. Tran, M. Vacante, P. Vahedi, Y. Veisani, T. Vos, K. Vosoughi, A. Werdecker, A.B. Wondmieneh, Y.G. Yeshitila, M. Zamani, K.A. Zewdie, Z.J. Zhang, R. Malekzadeh, M. Naghavi, The global, regional, and national burden of gastro-oesophageal reflux disease in 195

- countries and territories, 1990–2017: a systematic analysis for the Global Burden of Disease Study 2017, The Lancet Gastroenterology and Hepatology 5 (2020) 561–581. https://doi.org/10.1016/S2468-1253(19)30408-X.
- [7] H.B. El-Serag, Time Trends of Gastroesophageal Reflux Disease: A Systematic Review, Clinical Gastroenterology and Hepatology 5 (2007) 17–26. https://doi.org/10.1016/j.cgh.2006.09.016.
- [8] T. Kennedy, R. Jones, The prevalence of gastro-oesophageal reflux symptoms in a UK population and the consultation behaviour of patients with these symptoms, Alimentary Pharmacology and Therapeutics 14 (2000) 1589–1594. https://doi.org/10.1046/j.1365-2036.2000.00884.x.
- [9] J. Mason, A.P.S. Hungin, Review article: gastro-oesophageal reflux disease the health economic implications, Alimentary Pharmacology & Therapeutics 22 (2005) 20–31. https://doi.org/10.1111/j.1365-2036.2005.02606.x.
- [10] N.R. Fajardo, J.L. Wise, G.R. 3rd Locke, J.A. Murray, N.J. Talley, Esophageal perforation after placement of wireless Bravo pH probe., Gastrointestinal Endoscopy 63 (2006) 184–185. https://doi.org/10.1016/j.gie.2005.07.035.
- [11] H. Meyiz, M. El Agheb, A. Lamine, M. El Yousfi, N. Aqodad, D. Benajeh, M. El Abkari, A. Ibrahimi, I. Mellouki, H. Meyiz, M.E. Agheb, A. Lamine, M.E. Yousfi, N. Aqodad, D. Benajeh, M.E. Abkari, A. Ibrahimi, I. Mellouki, The Impact of Gastroesophageal Reflux on the Quality of Life: About a Series of 100 Patients at Fez University Hospital, Open Journal of Gastroenterology 09 (2019) 99–108. https://doi.org/10.4236/ojgas.2019.96012.
- [12] I. Wiklund, Review of the Quality of Life and Burden of Illness in Gastroesophageal Reflux Disease, Digestive Diseases 22 (2004) 108–114. https://doi.org/10.1159/000080308.
- [13] M.J. Shaw, J.A. Crawley, Improving Health-Related Quality of Life in Gastro-Oesophageal Reflux Disease, Drugs 63 (2003) 2307–2316. https://doi.org/10.2165/00003495-200363210-00003.
- [14] P. Maerten, M. Ortner, P. Michetti, G. Dorta, Wireless Capsule pH Monitoring: Does It Fulfil All Expectations?, Digestion 76 (2007) 235–240. https://doi.org/10.1159/000112796.
- [15] M.A. Kwiatek, J.E. Pandolfino, The Bravo[™] pH capsule system, Digestive and Liver Disease 40 (2008) 156–160. https://doi.org/10.1016/j.dld.2007.10.025.
- [16] C.P. Gyawali, The Value of Reflux Monitoring: The Old and the New for the Diagnosis and Assessment of GERD, Foregut 1 (2021) 124–131. https://doi.org/10.1177/26345161211021774.
- [17] C.P. Gyawali, P.J. Kahrilas, E. Savarino, F. Zerbib, F. Mion, A.J.P.M. Smout, M. Vaezi, D. Sifrim, M.R. Fox, M.F. Vela, R. Tutuian, J. Tack, A.J. Bredenoord, J. Pandolfino, S. Roman, Modern diagnosis of GERD: the Lyon Consensus., Gut 67 (2018) 1351–1362. https://doi.org/10.1136/gutjnl-2017-314722.
- [18] J.S. Lee, Is Wireless Capsule pH Monitoring Better Than Catheter Systems?, Journal of Neurogastroenterology and Motility 18 (2012) 117–119. https://doi.org/10.5056/jnm.2012.18.2.117.

- [19] A. Iluyomade, A. Olowoyeye, O. Fadahunsi, L. Thomas, C.N. Libend, K. Ragunathan, J. Fenster, S. Vignesh, Interference with daily activities and major adverse events during esophageal pH monitoring with bravo wireless capsule versus conventional intranasal catheter: a systematic review of randomized controlled trials: Interference with daily activities, Diseases of the Esophagus (2016) n/a-n/a. https://doi.org/10.1111/dote.12464.
- [20] S. Aulakh, S. Ashley, K. Haas, T. Truong, Esophageal pH Capsule Retention, ACG Case Reports Journal 7 (2020) e00383–e00383. https://doi.org/10.14309/crj.000000000000383.
- [21] A. de Hoyos, E.A. Esparza, Technical problems produced by the Bravo pH test in nonerosive reflux disease patients., World Journal of Gastroenterology 16 (2010) 3183–3186. https://doi.org/10.3748/wjg.v16.i25.3183.
- [22] R. Fass, R. Hell, R.E. Sampliner, G. Pulliam, E. Graver, V. Hartz, C. Johnson, P. Jaffe, Effect of Ambulatory 24-Hour Esophageal pH Monitoring on Reflux-Provoking Activities, Digestive Diseases and Sciences 44 (1999) 2263–2269. https://doi.org/10.1023/A:1026608804938.
- [23] Medtronic, DIGITRAPPER PH-Z TESTING SYSTEM, (2023). https://www.medtronic.com/covidien/en-gb/products/reflux-testing/digitrapper-ph-z-testing-system.html#.
- [24] T. Franzén, L.T. Grahn, Reliability of 24-Hour Oesophageal pH Monitoring Under Standardized Conditions, Scandinavian Journal of Gastroenterology 37 (2002) 6–8. https://doi.org/10.1080/003655202753387275.
- [25] M.F. Can, G. Yagci, S. Cetiner, M. Gulsen, T. Yigit, E. Ozturk, S. Gorgulu, T. Tufan, Accurate positioning of the 24-hour pH monitoring catheter: Agreement between manometry and pH step-up method in two patient positions, World Journal of Gastroenterology 13 (2007) 6197–6202. https://doi.org/10.3748/wjg.13.6197.
- [26] N.J. Trudgill, D. Sifrim, R. Sweis, M. Fullard, K. Basu, M. McCord, M. Booth, J. Hayman, G. Boeckxstaens, B.T. Johnston, N. Ager, J. De Caestecker, British Society of Gastroenterology guidelines for oesophageal manometry and oesophageal reflux monitoring., Gut 68 (2019) 1731–1750. https://doi.org/10.1136/gutjnl-2018-318115.
- [27] S. Ayazi, J.C. Lipham, G. Portale, C.G. Peyre, C.G. Streets, J.M. Leers, S.R. DeMeester, F. Banki, L.S. Chan, J.A. Hagen, T.R. DeMeester, Bravo Catheter-Free pH Monitoring: Normal Values, Concordance, Optimal Diagnostic Thresholds, and Accuracy, Clinical Gastroenterology and Hepatology 7 (2009) 60–67. https://doi.org/10.1016/j.cgh.2008.08.020.
- [28] B. Lutsi, I. Hirano, Ambulatory pH Monitoring: New Advances and Indications., Gastroenterology & Hepatology 2 (2006) 835–842.
- [29] J.E. Pandolfino, J.E. Richter, T. Ours, J.M. Guardino, J. Chapman, P.J. Kahrilas, Ambulatory esophageal pH monitoring using a wireless system., The American Journal of Gastroenterology 98 (2003) 740–749. https://doi.org/10.1111/j.1572-0241.2003.07398.x.

- [30] R.M.A. Lawenko, Y.Y. Lee, Evaluation of gastroesophageal reflux disease using the bravo capsule ph system, Journal of Neurogastroenterology and Motility 22 (2016) 25–30. https://doi.org/10.5056/jnm15151.
- [31] G. Wang, D. Filip, M.D. Poscente, C.N. Andrews, M.P. Mintchev, Capsule-Based Measurements of Gastrointestinal Impedance, in: M. Sawan (Ed.), Handbook of Biochips: Integrated Circuits and Systems for Biology and Medicine, Springer New York, New York, NY, 2015: pp. 1–14. https://doi.org/10.1007/978-1-4614-6623-9_17-1.
- [32] R. Dekel, I.B. Malagon, C. Green, R. Fass, Comparison of transnasaly placed wireless pH capsule (BRAVO®) versus traditional 24-hour esophageal pH monitoring-a randomized trial, The American Journal of Gastroenterology 98 (2003) 1. https://doi.org/10.1111/j.1572-0241.2003.07845.x.
- [33] C. Tharavej, J. Hagen, G. Portale, C.-C. Hsieh, T. Gandamihardja, J. Lipham, J. Peters, S. DeMeester, P. Crookes, C. Bremner, T. Demeester, Bravo capsule induction of esophageal hypercontractility and chest pain, Surgical Endoscopy 20 (2006) 783–786. https://doi.org/10.1007/s00464-005-0257-8.
- [34] J.E. Pandolfino, Q. Zhang, M.A. Schreiner, S. Ghosh, M.P. Roth, P.J. Kahrilas, Acid reflux event detection using the Bravo wireless versus the Slimline catheter pH systems: why are the numbers so different?, Gut 54 (2005) 1687–1692. https://doi.org/10.1136/gut.2005.064691.
- [35] K. Nan, V.R. Feig, B. Ying, J.G. Howarth, Z. Kang, Y. Yang, G. Traverso, Mucosa-interfacing electronics, Nature Reviews Materials 7 (2022) 908–925. https://doi.org/10.1038/s41578-022-00477-2.
- [36] K. Fukuda, Y. Takeda, Y. Yoshimura, R. Shiwaku, L.T. Tran, T. Sekine, M. Mizukami, D. Kumaki, S. Tokito, Fully-printed high-performance organic thin-film transistors and circuitry on one-micron-thick polymer films, Nature Communications 5 (2014) 5–12. https://doi.org/10.1038/ncomms5147.
- [37] P. Salvo, B. Melai, N. Calisi, C. Paoletti, F. Bellagambi, A. Kirchhain, M.G. Trivella, R. Fuoco, F. Di Francesco, Graphene-based devices for measuring pH, Sensors and Actuators B: Chemical 256 (2018) 976–991. https://doi.org/10.1016/j.snb.2017.10.037.
- [38] O. Akhavan, E. Ghaderi, E. Hashemi, R. Rahighi, Ultra-sensitive detection of leukemia by graphene, Nanoscale 6 (2014) 14810–14819. https://doi.org/10.1039/c4nr04589k.
- [39] H. Bai, C. Li, X. Wang, G. Shi, A pH-sensitive graphene oxide composite hydrogel, Chemical Communications 46 (2010) 2376–2378. https://doi.org/10.1039/c000051e.
- [40] F. Vivaldi, A. Bonini, B. Melai, N. Poma, A. Kirchhain, D. Santalucia, P. Salvo, F.D. Francesco, A graphene-based pH sensor on paper for human plasma and seawater, Proceedings of the Annual International Conference of the IEEE Engineering in Medicine and Biology Society, EMBS (2019) 1563–1566. https://doi.org/10.1109/EMBC.2019.8856991.
- [41] S. Aabith, R. Caulfield, O. Akhlaghi, A. Papadopoulou, S. Homer-Vanniasinkam, M.K. Tiwari, 3D direct-write printing of water soluble micromoulds for high-

- resolution rapid prototyping, Additive Manufacturing 58 (2022) 103019. https://doi.org/10.1016/j.addma.2022.103019.
- [42] K. Zhang, B. Hu, M. Zhang, L. Meng, H. Liu, Direct Writing Micropatterns with a Resolution up to 1 μm, Advanced Functional Materials 30 (2020) 1907907. https://doi.org/10.1002/adfm.201907907.
- [43] S. Kandambeth, A. Mallick, B. Lukose, M.V. Mane, T. Heine, R. Banerjee, Construction of Crystalline 2D Covalent Organic Frameworks with Remarkable Chemical (Acid/Base) Stability via a Combined Reversible and Irreversible Route, Journal of the American Chemical Society 134 (2012) 19524–19527. https://doi.org/10.1021/ja308278w.
- [44] J.E. Pandolfino, M.A. Kwiatek, Use and Utility of the Bravo[™] pH Capsule, Journal of Clinical Gastroenterology 42 (2008). https://journals.lww.com/jcge/Fulltext/2008/05000/Use_and_Utility_of_the_Bravo pH Capsule.28.aspx.
- [45] J.D. Smart, The basics and underlying mechanisms of mucoadhesion., Advanced Drug Delivery Reviews 57 (2005) 1556–1568. https://doi.org/10.1016/j.addr.2005.07.001.
- [46] J.M. Williams, C.A. Duckworth, M.D. Burkitt, A.J.M. Watson, B.J. Campbell, D.M. Pritchard, Epithelial cell shedding and barrier function: a matter of life and death at the small intestinal villus tip., Veterinary Pathology 52 (2015) 445–455. https://doi.org/10.1177/0300985814559404.
- [47] K. Zheng, Q. Gu, D. Zhou, M. Zhou, L. Zhang, Recent progress in surgical adhesives for biomedical applications, Smart Materials in Medicine 3 (2022) 41–65. https://doi.org/10.1016/j.smaim.2021.11.004.
- [48] A. Fog, R.P. Buck, Electronic semiconducting oxides as pH sensors, Sensors and Actuators 5 (1984) 137–146. https://doi.org/10.1016/0250-6874(84)80004-9.
- [49] M.I. Khan, K. Mukherjee, R. Shoukat, H. Dong, A review on pH sensitive materials for sensors and detection methods, Microsyst Technol 23 (2017) 4391–4404. https://doi.org/10.1007/s00542-017-3495-5.
- [50] R. Yu, Z. Zhang, G. Shen, Potentiometric sensors: aspects of the recent development, (2000) 150–153.
- [51] L. Manjakkal, D. Szwagierczak, R. Dahiya, Metal oxides based electrochemical pH sensors: Current progress and future perspectives, Progress in Materials Science 109 (2020) 100635. https://doi.org/10.1016/j.pmatsci.2019.100635.
- [52] E. González-Fernández, M. Staderini, J.R.K. Marland, M.E. Gray, A. Uçar, C. Dunare, E.O. Blair, P. Sullivan, A. Tsiamis, S.N. Greenhalgh, R. Gregson, R.E. Clutton, S. Smith, J.G. Terry, D.J. Argyle, A.J. Walton, A.R. Mount, M. Bradley, A.F. Murray, In vivo application of an implantable tri-anchored methylene blue-based electrochemical pH sensor, Biosensors and Bioelectronics 197 (2022) 113728. https://doi.org/10.1016/j.bios.2021.113728.
- [53] S. Li, D. Lu, S. Li, J. Liu, Y. Xu, Y. Yan, J.Z. Rodriguez, H. Bai, R. Avila, S. Kang, X. Ni, H. Luan, H. Guo, W. Bai, C. Wu, X. Zhou, Z. Hu, M.A. Pet, C.W. Hammill, M.R. MacEwan, W.Z. Ray, Y. Huang, J.A. Rogers, Bioresorbable, wireless, passive sensors for continuous pH measurements and early detection of gastric

- leakage, Science Advances 10 (2024) eadj0268. https://doi.org/10.1126/sciadv.adj0268.
- [54] P. Salvo, N. Calisi, B. Melai, B. Cortigiani, M. Mannini, A. Caneschi, G. Lorenzetti, C. Paoletti, T. Lomonaco, A. Paolicchi, I. Scataglini, V. Dini, M. Romanelli, R. Fuoco, F. Di Francesco, Temperature and pH sensors based on graphenic materials, Biosensors and Bioelectronics 91 (2017) 870–877. https://doi.org/10.1016/j.bios.2017.01.062.
- [55] S. Levine, A.L. Smith, Theory of the differential capacity of the oxide/aqueous electrolyte interface, Discussions of the Faraday Society 52 (1971) 290–301. https://doi.org/10.1039/DF9715200290.
- [56] D.E. Yates, S. Levine, T.W. Healy, Site-binding Model of the Electrical Double Layer at the Oxide/Water Interface, Journal of the Chemical Society, Faraday Transactions 1: Physical Chemistry in Condensed Phases 70 (1974) 1807–1818. https://doi.org/10.1039/F19747001807.
- [57] J.J. García-Guzmán, C. Pérez-Ràfols, M. Cuartero, G.A. Crespo, Toward In Vivo Transdermal pH Sensing with a Validated Microneedle Membrane Electrode, ACS Sensors 6 (2021) 1129–1137. https://doi.org/10.1021/acssensors.0c02397.
- [58] S.A. Grant, K. Bettencourt, P. Krulevitch, J. Hamilton, R. Glass, In vitro and in vivo measurements of fiber optic and electrochemical sensors to monitor brain tissue pH, Sensors and Actuators B: Chemical 72 (2001) 174–179. https://doi.org/10.1016/S0925-4005(00)00650-X.
- [59] R. Bhardwaj, S. Sinha, N. Sahu, S. Majumder, P. Narang, R. Mukhiya, Modeling and simulation of temperature drift for ISFET-based pH sensor and its compensation through machine learning techniques, International Journal of Circuit Theory and Applications 47 (2019) 954–970. https://doi.org/10.1002/cta.2618.
- [60] L. Liu, J. Shao, X. Li, Q. Zhao, B. Nie, C. Xu, H. Ding, High performance flexible pH sensor based on carboxyl-functionalized and DEP aligned SWNTs, Applied Surface Science 386 (2016) 405–411. https://doi.org/10.1016/j.apsusc.2016.06.058.
- [61] M. Yuqing, G. Jianguo, C. Jianrong, Ion sensitive field effect transducer-based biosensors, Biotechnology Advances 21 (2003) 527–534. https://doi.org/10.1016/S0734-9750(03)00103-4.
- [62] R. Kawahara, P. Sahatiya, S. Badhulika, S. Uno, Paper-based potentiometric pH sensor using carbon electrode drawn by pencil, Japanese Journal of Applied Physics 57 (2018). https://doi.org/10.7567/JJAP.57.04FM08.
- [63] M. Waleed Shinwari, M. Jamal Deen, D. Landheer, Study of the electrolyte-insulator-semiconductor field-effect transistor (EISFET) with applications in biosensor design, Microelectronics Reliability 47 (2007) 2025–2057. https://doi.org/10.1016/j.microrel.2006.10.003.
- [64] J.H. Ahn, J.Y. Kim, M.L. Seol, D.J. Baek, Z. Guo, C.H. Kim, S.J. Choi, Y.K. Choi, A pH sensor with a double-gate silicon nanowire field-effect transistor, Applied Physics Letters 102 (2013) 2–6. https://doi.org/10.1063/1.4793655.

- [65] J. Go, P.R. Nair, B. Reddy, B. Dorvel, R. Bashir, M.A. Alam, Coupled Heterogeneous Nanowire–Nanoplate Planar Transistor Sensors for Giant (>10 V/pH) Nernst Response, ACS Nano 6 (2012) 5972–5979. https://doi.org/10.1021/nn300874w.
- [66] P.K. Ang, W. Chen, A.T.S. Wee, P.L. Kian, Solution-gated epitaxial graphene as pH sensor, Journal of the American Chemical Society 130 (2008) 14392–14393. https://doi.org/10.1021/ja805090z.
- [67] B. Melai, P. Salvo, N. Calisi, L. Moni, A. Bonini, C. Paoletti, T. Lomonaco, V. Mollica, R. Fuoco, F. Di Francesco, A graphene oxide pH sensor for wound monitoring, Proceedings of the Annual International Conference of the IEEE Engineering in Medicine and Biology Society, EMBS 2016-Octob (2016) 1898–1901. https://doi.org/10.1109/EMBC.2016.7591092.
- [68] H. Chung, M.S. Sulkin, J. Kim, C. Goudeseune, H. Chao, J.W. Song, S.Y. Yang, Y. Hsu, R. Ghaffari, I.R. Efimov, J.A. Rogers, Stretchable, Multiplexed pH Sensors With Demonstrations on Rabbit and Human Hearts Undergoing Ischemia, Adv Healthcare Materials 3 (2014) 59–68. https://doi.org/10.1002/adhm.201300124.
- [69] W. Lonsdale, M. Wajrak, K. Alameh, Manufacture and application of RuO2 solidstate metal-oxide pH sensor to common beverages, Talanta 180 (2018) 277– 281. https://doi.org/10.1016/j.talanta.2017.12.070.
- [70] A.J. Bandodkar, V.W.S. Hung, W. Jia, G. Valdés-Ramírez, J.R. Windmiller, A.G. Martinez, J. Ramírez, G. Chan, K. Kerman, J. Wang, Tattoo-based potentiometric ion-selective sensors for epidermal pH monitoring, Analyst 138 (2013) 123–128. https://doi.org/10.1039/C2AN36422K.
- [71] H.J. Park, J.H. Yoon, K.G. Lee, B.G. Choi, Potentiometric performance of flexible pH sensor based on polyaniline nanofiber arrays, Nano Convergence 6 (2019) 9. https://doi.org/10.1186/s40580-019-0179-0.
- [72] J.H. Yoon, K.H. Kim, N.H. Bae, G.S. Sim, Y.-J. Oh, S.J. Lee, T.J. Lee, K.G. Lee, B.G. Choi, Fabrication of newspaper-based potentiometric platforms for flexible and disposable ion sensors, Journal of Colloid and Interface Science 508 (2017) 167–173. https://doi.org/10.1016/j.jcis.2017.08.036.
- [73] L. Santos, J.P. Neto, A. Crespo, D. Nunes, N. Costa, I.M. Fonseca, P. Barquinha, L. Pereira, J. Silva, R. Martins, E. Fortunato, WO₃ Nanoparticle-Based Conformable pH Sensor, ACS Appl. Mater. Interfaces 6 (2014) 12226–12234. https://doi.org/10.1021/am501724h.
- [74] K.S. Novoselov, A.K. Geim, S.V. Morozov, D. Jiang, Y. Zhang, S.V. Dubonos, I.V. Grigorieva, A.A. Firsov, Electric Field Effect in Atomically Thin Carbon Films, Science 306 (2004) 666–669. https://doi.org/10.1126/science.1102896.
- [75] N. Lei, P. Li, W. Xue, J. Xu, Simple graphene chemiresistors as pH sensors: fabrication and characterization, Measurement Science and Technology 22 (2011) 107002. https://doi.org/10.1088/0957-0233/22/10/107002.
- [76] M. Liu, X. Zhang, Graphene benefits, Nature Photonics 7 (2013) 851–852. https://doi.org/10.1038/nphoton.2013.257.

- [77] C.-Y. Lee, K.F. Lei, S.-W. Tsai, N.-M. Tsang, Development of graphene-based sensors on paper substrate for the measurement of pH value of analyte, BioChip Journal 10 (2016) 182–188. https://doi.org/10.1007/s13206-016-0304-7.
- [78] W. Fu, C. Nef, O. Knopfmacher, A. Tarasov, M. Weiss, M. Calame, C. Schönenberger, Graphene Transistors Are Insensitive to pH Changes in Solution, Nano Letters 11 (2011) 3597–3600. https://doi.org/10.1021/nl201332c.
- [79] J. Ristein, W. Zhang, F. Speck, M. Ostler, L. Ley, T. Seyller, Characteristics of solution gated field effect transistors on the basis of epitaxial graphene on silicon carbide, Journal of Physics D: Applied Physics 43 (2010). https://doi.org/10.1088/0022-3727/43/34/345303.
- [80] S. Kanaparthi, S. Badhulika, Solvent-free fabrication of paper based all-carbon disposable multifunctional sensors and passive electronic circuits, RSC Advances 6 (2016) 95574–95583. https://doi.org/10.1039/c6ra21457f.
- [81] S. Stankovich, D.A. Dikin, G.H.B. Dommett, K.M. Kohlhaas, E.J. Zimney, E.A. Stach, R.D. Piner, S.T. Nguyen, R.S. Ruoff, Graphene-based composite materials, Nature 442 (2006) 282–286. https://doi.org/10.1038/nature04969.
- [82] V. Georgakilas, M. Otyepka, A.B. Bourlinos, V. Chandra, N. Kim, K.C. Kemp, P. Hobza, R. Zboril, K.S. Kim, Functionalization of Graphene: Covalent and Non-Covalent Approaches, Derivatives and Applications, Chemical Reviews 112 (2012) 6156–6214.
- [83] H. Wu, W. Lu, J.J. Shao, C. Zhang, M.B. Wu, B.H. Li, Q.H. Yang, pH-dependent size, surface chemistry and electrochemical properties of graphene oxide, Xinxing Tan Cailiao/New Carbon Materials 28 (2013) 327–335. https://doi.org/10.1016/S1872-5805(13)60085-2.
- [84] C.J. Shih, S. Lin, R. Sharma, M.S. Strano, D. Blankschtein, Understanding the pH-dependent behavior of graphene oxide aqueous solutions: A comparative experimental and molecular dynamics simulation study, Langmuir 28 (2012) 235–241. https://doi.org/10.1021/la203607w.
- [85] P. Mostafalu, M. Akbari, K.A. Alberti, Q. Xu, A. Khademhosseini, S.R. Sonkusale, A toolkit of thread-based microfluidics, sensors, and electronics for 3D tissue embedding for medical diagnostics, Microsystems and Nanoengineering 2 (2016). https://doi.org/10.1038/micronano.2016.39.
- [86] A. Simonis, H. Lüth, J. Wang, M.J. Schöning, New concepts of miniaturised reference electrodes in silicon technology for potentiometric sensor systems, Sensors and Actuators, B: Chemical 103 (2004) 429–435. https://doi.org/10.1016/j.snb.2004.04.072.
- [87] S. Ansari, A. Kelarakis, L. Estevez, E.P. Giannelis, Oriented Arrays of Graphene in a Polymer Matrix by in situ Reduction of Graphite Oxide Nanosheets, Small 6 (2010) 205–209. https://doi.org/10.1002/smll.200900765.
- [88] S.K. Ameri, P.K. Singh, S.R. Sonkusale, Three dimensional graphene transistor for ultra-sensitive pH sensing directly in biological media., Analytica Chimica Acta 934 (2016) 212–217. https://doi.org/10.1016/j.aca.2016.05.048.
- [89] M.A. Ceniceros-Reyes, K.S. Marín-Hernández, U. Sierra, E.M. Saucedo-Salazar, R. Mendoza-Resendez, C. Luna, P.J. Hernández-Belmares, O.S. Rodríguez-Fernández, S. Fernández-Tavizón, E. Hernández-Hernández, E.D.

- Barriga-Castro, Reduction of graphene oxide by in-situ heating experiments in the transmission electron microscope, Surfaces and Interfaces 35 (2022) 102448. https://doi.org/10.1016/j.surfin.2022.102448.
- [90] V. Semwal, B.D. Gupta, Highly sensitive surface plasmon resonance based fiber optic pH sensor utilizing rGO-Pani nanocomposite prepared by in situ method, Sensors and Actuators, B: Chemical 283 (2019) 632–642. https://doi.org/10.1016/j.snb.2018.12.070.
- [91] Y.R. Li, S.H. Chang, W.L. Tsai, C.T. Chang, K.Y. Wang, P.Y. Yang, H.C. Cheng, Highly sensitive pH sensors of extended-gate field-effect transistor with the oxygen-functionalized reduced Graphene oxide films on reverse pyramid substrates, IEEE Electron Device Letters 36 (2015) 1189–1191. https://doi.org/10.1109/LED.2015.2477851.
- [92] Y.R. Li, S.H. Chang, C.T. Chang, W.L. Tsai, Y.K. Chiu, P.Y. Yang, H.C. Cheng, High-sensitivity extended-gate field-effect transistors as pH sensors with oxygen-modified reduced graphene oxide films coated on different reverse-pyramid silicon structures as sensing heads, Japanese Journal of Applied Physics 55 (2016) 0–6. https://doi.org/10.7567/JJAP.55.04EM08.
- [93] S. Wang, P.K. Ang, Z. Wang, A.L.L. Tang, J.T.L. Thong, K.P. Loh, High mobility, printable, and solution-processed graphene electronics, Nano Letters 10 (2010) 92–98. https://doi.org/10.1021/nl9028736.
- [94] F. Torrisi, T. Hasan, W. Wu, Z. Sun, A. Lombardo, T.S. Kulmala, G.W. Hsieh, S. Jung, F. Bonaccorso, P.J. Paul, D. Chu, A.C. Ferrari, Inkjet-printed graphene electronics, ACS Nano 6 (2012) 2992–3006. https://doi.org/10.1021/nn2044609.
- [95] F. Kim, L.J. Cote, J. Huang, Graphene Oxide: Surface Activity and Two-Dimensional Assembly, Advanced Materials 22 (2010) 1954–1958. https://doi.org/10.1002/adma.200903932.
- [96] C. Mattevi, G. Eda, S. Agnoli, S. Miller, K.A. Mkhoyan, O. Celik, D. Mastrogiovanni, G. Granozzi, E. Garfunkel, M. Chhowalla, Evolution of Electrical, Chemical, and Structural Properties of Transparent and Conducting Chemically Derived Graphene Thin Films, Advanced Functional Materials 19 (2009) 2577–2583. https://doi.org/10.1002/adfm.200900166.
- [97] S. Angizi, X. Huang, L. Hong, M.A. Akbar, P.R. Selvaganapathy, P. Kruse, Defect Density-Dependent pH Response of Graphene Derivatives: Towards the Development of pH-Sensitive Graphene Oxide Devices, Nanomaterials 12 (2022). https://doi.org/10.3390/nano12111801.
- [98] IEEE, INTERNATIONAL ROADMAP FOR DEVICES AND SYSTEMS [™] 2022 Edition, Executive Summary, IEEE IRDS (2022).
- [99] S. Angizi, E.Y.C. Yu, J. Dalmieda, D. Saha, P.R. Selvaganapathy, P. Kruse, Defect Engineering of Graphene to Modulate pH Response of Graphene Devices, Langmuir 37 (2021) 12163–12178. https://doi.org/10.1021/acs.langmuir.1c02088.
- [100] J. Hong, J.-B. Lee, S. Lee, J. Seo, H. Lee, J.Y. Park, J.-H. Ahn, T. II Seo, T. Lee, H.-B.-R. Lee, A facile method for the selective decoration of graphene defects based on a galvanic displacement reaction, NPG Asia Materials 8 (2016) e262–e262. https://doi.org/10.1038/am.2016.42.

- [101] M.A. Huff, NanoSensor Fabrication An Overview of Some of the Practical Issues Involved, NSF Nanosensor Manufacturing: Finding Better Paths to Products (2017). https://www.nano.gov/sites/default/files/Nanosensor.
- [102] Y. Huang, H. Wu, L. Xiao, Y. Duan, H. Zhu, J. Bian, D. Ye, Z. Yin, Assembly and applications of 3D conformal electronics on curvilinear surfaces, Materials Horizons 6 (2019) 642–683. https://doi.org/10.1039/c8mh01450g.
- [103] J. Liang, K. Tong, Q. Pei, A Water-Based Silver-Nanowire Screen-Print Ink for the Fabrication of Stretchable Conductors and Wearable Thin-Film Transistors, Advanced Materials 28 (2016) 5986–5996. https://doi.org/10.1002/adma.201600772.
- [104] S.B. Walker, J.A. Lewis, Reactive silver inks for patterning high-conductivity features at mild temperatures, Journal of the American Chemical Society 134 (2012) 1419–1421. https://doi.org/10.1021/ja209267c.
- [105] B.Y. Ahn, E.B. Duoss, M.J. Motala, X. Guo, S.I. Park, Y. Xiong, J. Yoon, R.G. Nuzzo, J.A. Rogers, J.A. Lewis, Omnidirectional printing of flexible, stretchable, and spanning silver microelectrodes, Science 323 (2009) 1590–1593. https://doi.org/10.1126/science.1168375.
- [106] A. Eshkeiti, A.S.G. Reddy, S. Emamian, B.B. Narakathu, M. Joyce, M. Joyce, P.D. Fleming, B.J. Bazuin, M.Z. Atashbar, Screen printing of multilayered hybrid printed circuit boards on different substrates, IEEE Transactions on Components, Packaging and Manufacturing Technology 5 (2015) 415–421. https://doi.org/10.1109/TCPMT.2015.2391012.
- [107] M.R. Somalu, A. Muchtar, W.R.W. Daud, N.P. Brandon, Screen-printing inks for the fabrication of solid oxide fuel cell films: A review, Renewable and Sustainable Energy Reviews 75 (2017) 426–439. https://doi.org/10.1016/j.rser.2016.11.008.
- [108] Y.Y. Noh, N. Zhao, M. Caironi, H. Sirringhaus, Downscaling of self-aligned, all-printed polymer thin-film transistors, Nature Nanotechnology 2 (2007) 784–789. https://doi.org/10.1038/nnano.2007.365.
- [109] M.R. Somalu, V. Yufit, I.P. Shapiro, P. Xiao, N.P. Brandon, The impact of ink rheology on the properties of screen-printed solid oxide fuel cell anodes, International Journal of Hydrogen Energy 38 (2013) 6789–6801. https://doi.org/10.1016/j.ijhydene.2013.03.108.
- [110] Eurocircuits, eC Stencil Mate Operator Mnual, 2011.
- [111] J. Mewis, N.J. Wagner, Thixotropy, Advances in Colloid and Interface Science 147–148 (2009) 214–227. https://doi.org/10.1016/j.cis.2008.09.005.
- [112] J.W. Phair, M. Lundberg, A. Kaiser, Leveling and thixotropic characteristics of concentrated zirconia inks for screen-printing, Rheologica Acta 48 (2009) 121– 133. https://doi.org/10.1007/s00397-008-0301-4.
- [113] M.R. Somalu, N.P. Brandon, Rheological studies of nickel/scandia-stabilized-zirconia screen printing inks for solid oxide fuel cell anode fabrication, Journal of the American Ceramic Society 95 (2012) 1220–1228. https://doi.org/10.1111/j.1551-2916.2011.05014.x.

- [114] T.V. Neumann, M.D. Dickey, Liquid Metal Direct Write and 3D Printing: A Review, Advanced Materials Technologies 5 (2020) 2000070. https://doi.org/10.1002/admt.202000070.
- [115] R. Caulfield, F. Fang, M.K. Tiwari, Drops, Jets and High-Resolution 3D Printing: Fundamentals and Applications, in: Droplet and Spray Transport: Paradigms and Applications. Energy, Environment, and Sustainability, Springer, Singapore, 2017. https://doi.org/10.1007/978-981-10-7233-8 6.
- [116] B. Derby, Inkjet printing of functional and structural materials: Fluid property requirements, feature stability, and resolution, Annual Review of Materials Research 40 (2010) 395–414. https://doi.org/10.1146/annurev-matsci-070909-104502.
- [117] H. Yuk, X. Zhao, A New 3D Printing Strategy by Harnessing Deformation, Instability, and Fracture of Viscoelastic Inks, Advanced Materials 30 (2018) 1–8. https://doi.org/10.1002/adma.201704028.
- [118] S. Taushanoff, V.M. Dubin, Photopatternable, Electrochemically Plated Conductive Fabrics, ECS Transactions 77 (2017) 877–885. https://doi.org/10.1149/07711.0877ecst.
- [119] Z. Hou, H. Lu, Y. Li, L. Yang, Y. Gao, Direct Ink Writing of Materials for Electronics-Related Applications: A Mini Review, Frontiers in Materials 8 (2021) 1–8. https://doi.org/10.3389/fmats.2021.647229.
- [120] C. Liu, F. Xu, Y. Liu, J. Ma, P. Liu, D. Wang, C. Lao, Z. Chen, High mass loading ultrathick porous Li4Ti5O12 electrodes with improved areal capacity fabricated via low temperature direct writing, Electrochimica Acta 314 (2019) 81–88. https://doi.org/10.1016/j.electacta.2019.05.082.
- [121] S. Bhattacharya, A. Datta, J.M. Berg, S. Gangopadhyay, Studies on surface wettability of poly(dimethyl) siloxane (PDMS) and glass under oxygen-plasma treatment and correlation with bond strength, Journal of Microelectromechanical Systems 14 (2005) 590–597. https://doi.org/10.1109/JMEMS.2005.844746.
- [122] D. Hegemann, H. Brunner, C. Oehr, Plasma treatment of polymers for surface and adhesion improvement, Nuclear Instruments and Methods in Physics Research, Section B: Beam Interactions with Materials and Atoms 208 (2003) 281–286. https://doi.org/10.1016/S0168-583X(03)00644-X.
- [123] A. Marmur, Hydro-hygro-oleo-omni-phobic? Terminology of wettability classification, Soft Matter 8 (2012) 6867–6870.
- [124] A. Marmur, C. Della Volpe, S. Siboni, A. Amirfazli, J.W. Drelich, Contact angles and wettability: towards common and accurate terminology, Surface Innovations 5 (2017) 3–8. https://doi.org/10.1680/jsuin.17.00002.
- [125] A. Sarycheva, A. Polemi, Y. Liu, K. Dandekar, B. Anasori, Y. Gogotsi, 2D titanium carbide (MXene) for wireless communication, Science Advances 4 (2018) 1–9. https://doi.org/10.1126/sciadv.aau0920.
- [126] H.J. Hettlich, F. Otterbach, C. Mittermayer, R. Kaufmann, D. Klee, Plasma-induced surface modifications on suicone intraocular lenses: chemical analysis and in vitro characterization, Biomaterials 12 (1991) 521–524. https://doi.org/10.1016/0142-9612(91)90153-2.

- [127] M.N. Kirikova, E.V. Agina, A.A. Bessonov, A.S. Sizov, O.V. Borshchev, A.A. Trul, A.M. Muzafarov, S.A. Ponomarenko, Direct-write printing of reactive oligomeric alkoxysilanes as an affordable and highly efficient route for promoting local adhesion of silver inks on polymer substrates, Journal of Materials Chemistry C 4 (2016) 2211–2218. https://doi.org/10.1039/c5tc03497c.
- [128] M. Zhou, Y. Zhai, S. Dong, Electrochemical Sensing and Biosensing Platform Based on Chemically Reduced Graphene Oxide, Analytical Chemistry 81 (2009) 5603–5613. https://doi.org/10.1021/ac900136z.
- [129] S. Chinnathambi, G.J.W. Euverink, Hydrothermally reduced graphene oxide as a sensing material for electrically transduced pH sensors, Journal of Electroanalytical Chemistry 895 (2021) 115530. https://doi.org/10.1016/j.jelechem.2021.115530.
- [130] M.-S. Chae, J. Kim, D. Jeong, Y. Kim, J.H. Roh, S.M. Lee, Y. Heo, J.Y. Kang, J.H. Lee, D.S. Yoon, T.G. Kim, S.T. Chang, K.S. Hwang, Enhancing surface functionality of reduced graphene oxide biosensors by oxygen plasma treatment for Alzheimer's disease diagnosis, Biosensors and Bioelectronics 92 (2017) 610–617. https://doi.org/10.1016/j.bios.2016.10.049.
- [131] F.M. El-Hossary, A. Ghitas, A.M.A. El-Rahman, A.A. Ebnalwaled, M.A. Shahat, M.H. Fawey, Cold RF oxygen plasma treatment of graphene oxide films, Journal of Materials Science: Materials in Electronics 32 (2021) 15718–15731. https://doi.org/10.1007/s10854-021-06123-x.
- [132] M. Asai, S. Honda, N. Isshiki, M. Takesue, A. Hiraishi, M. Yamada, K. Takei, Highly Stable, Flexible ISFET pH Sensor Using Sorted Semiconducting SWNTs in Aqueous Solution, Advanced Materials Technologies 8 (2023) 2300842. https://doi.org/10.1002/admt.202300842.
- [133] D.M. Segura, A.D. Nurse, A. McCourt, R. Phelps, A. Segura, Chapter 3 Chemistry of polyurethane adhesives and sealants, in: P. Cognard (Ed.), Handbook of Adhesives and Sealants, Elsevier Science Ltd, 2005: pp. 101–162. https://doi.org/10.1016/S1874-5695(02)80004-5.
- [134] M. Cui, Z. Chai, Y. Lu, J. Zhu, J. Chen, Developments of polyurethane in biomedical applications: A review, Resources Chemicals and Materials 2 (2023) 262–276. https://doi.org/10.1016/j.recm.2023.07.004.
- [135] G. Sun, J. An, C.K. Chua, H. Pang, J. Zhang, P. Chen, Layer-by-layer printing of laminated graphene-based interdigitated microelectrodes for flexible planar micro-supercapacitors, Electrochemistry Communications 51 (2015) 33–36. https://doi.org/10.1016/j.elecom.2014.11.023.
- [136] B.J. Hong, O.C. Compton, Z. An, I. Eryazici, S.T. Nguyen, Successful stabilization of graphene oxide in electrolyte solutions: Enhancement of biofunctionalization and cellular uptake, ACS Nano 6 (2012) 63–73. https://doi.org/10.1021/nn202355p.
- [137] M.J. Ferrua, R.P. Singh, Human Gastric Simulator (Riddet Model), in: K. Verhoeckx, P. Cotter, I. López-Expósito, C. Kleiveland, T. Lea, A. Mackie, T. Requena, D. Swiatecka, H. Wichers (Eds.), The Impact of Food Bioactives on Health, Springer International Publishing, Cham, 2015: pp. 61–71. https://doi.org/10.1007/978-3-319-16104-4_7.

- [138] W.J. Basirun, M. Sookhakian, S. Baradaran, M.R. Mahmoudian, M. Ebadi, Solid-phase electrochemical reduction of graphene oxide films in alkaline solution, Nanoscale Res Lett 8 (2013) 397. https://doi.org/10.1186/1556-276X-8-397.
- [139] J.L. Segura, M.J. Mancheño, F. Zamora, Covalent organic frameworks based on Schiff-base chemistry: synthesis, properties and potential applications, Chem. Soc. Rev. 45 (2016) 5635–5671. https://doi.org/10.1039/C5CS00878F.
- [140] X. Feng, X. Ding, D. Jiang, Covalent organic frameworks, Chemical Society Reviews 41 (2012) 6010–6022. https://doi.org/10.1039/C2CS35157A.
- [141] Linkages in Covalent Organic Frameworks, in: Introduction to Reticular Chemistry, John Wiley & Sons, Ltd, 2019: pp. 197–223. https://doi.org/10.1002/9783527821099.ch8.
- [142] Emergence of Metal-Organic Frameworks, in: Introduction to Reticular Chemistry, John Wiley & Sons, Ltd, 2019: pp. 1–27. https://doi.org/10.1002/9783527821099.ch1.
- [143] J.L. Segura, S. Royuela, M. Mar Ramos, Post-synthetic modification of covalent organic frameworks, Chem. Soc. Rev. 48 (2019) 3903–3945. https://doi.org/10.1039/C8CS00978C.
- [144] K. Geng, T. He, R. Liu, S. Dalapati, K.T. Tan, Z. Li, S. Tao, Y. Gong, Q. Jiang, D. Jiang, Covalent Organic Frameworks: Design, Synthesis, and Functions, Chemical Reviews 120 (2020) 8814–8933. https://doi.org/10.1021/acs.chemrev.9b00550.
- [145] D. Zhu, R. Verduzco, Ultralow Surface Tension Solvents Enable Facile COF Activation with Reduced Pore Collapse, ACS Applied Materials & Interfaces 12 (2020) 33121–33127. https://doi.org/10.1021/acsami.0c09173.
- [146] E.R. Cooper, C.D. Andrews, P.S. Wheatley, P.B. Webb, P. Wormald, R.E. Morris, Ionic liquids and eutectic mixtures as solvent and template in synthesis of zeolite analogues, Nature 430 (2004) 1012–1016. https://doi.org/10.1038/nature02860.
- [147] P. Kuhn, M. Antonietti, A. Thomas, Porous, Covalent Triazine-Based Frameworks Prepared by Ionothermal Synthesis, Angewandte Chemie International Edition 47 (2008) 3450–3453. https://doi.org/10.1002/anie.200705710.
- [148] Z. Yu, H. Chen, W. Zhang, Q. Ding, Q. Yu, M. Fang, L. Zhang, Room temperature synthesis of flower-like hollow covalent organic framework for efficient enrichment of microcystins, RSC Advances 13 (2023) 4255–4262. https://doi.org/10.1039/D2RA06901F.
- [149] F. Zhang, J. Zhang, B. Zhang, X. Tan, D. Shao, J. Shi, D. Tan, L. Liu, J. Feng, B. Han, G. Yang, L. Zheng, J. Zhang, Room-Temperature Synthesis of Covalent Organic Framework (COF-LZU1) Nanobars in CO2/Water Solvent, ChemSusChem 11 (2018) 3576–3580. https://doi.org/10.1002/cssc.201801712.
- [150] M. Matsumoto, R.R. Dasari, W. Ji, C.H. Feriante, T.C. Parker, S.R. Marder, W.R. Dichtel, Rapid, Low Temperature Formation of Imine-Linked Covalent Organic Frameworks Catalyzed by Metal Triflates, Journal of the American Chemical Society 139 (2017) 4999–5002. https://doi.org/10.1021/jacs.7b01240.

- [151] D.D. Medina, J.M. Rotter, Y. Hu, M. Dogru, V. Werner, F. Auras, J.T. Markiewicz, P. Knochel, T. Bein, Room Temperature Synthesis of Covalent–Organic Framework Films through Vapor-Assisted Conversion, Journal of the American Chemical Society 137 (2015) 1016–1019. https://doi.org/10.1021/ja510895m.
- [152] Nanoscopic and Macroscopic Structuring of Covalent Organic Frameworks, in: Introduction to Reticular Chemistry, 2019: pp. 267–283. https://doi.org/10.1002/9783527821099.ch11.
- [153] L.-Y. Chen, Y.-N. Gai, X.-T. Gai, J. Qin, Z.-G. Wang, L.-S. Cui, H. Guo, M.-Y. Jiang, Q. Zou, T. Zhou, J.-G. Gai, Interfacial synthesized covalent organic framework nanofiltration membranes for precisely ultrafast sieving, Chemical Engineering Journal 430 (2022) 133024. https://doi.org/10.1016/j.cej.2021.133024.
- [154] R. Dong, T. Zhang, X. Feng, Interface-Assisted Synthesis of 2D Materials: Trend and Challenges, Chemical Reviews 118 (2018) 6189–6235. https://doi.org/10.1021/acs.chemrev.8b00056.
- [155] W. Dai, F. Shao, J. Szczerbiński, R. McCaffrey, R. Zenobi, Y. Jin, A.D. Schlüter, W. Zhang, Synthesis of a Two-Dimensional Covalent Organic Monolayer through Dynamic Imine Chemistry at the Air/Water Interface, Angewandte Chemie International Edition 55 (2016) 213–217. https://doi.org/10.1002/anie.201508473.
- [156] K. Dey, M. Pal, K.C. Rout, S. Kunjattu H, A. Das, R. Mukherjee, U.K. Kharul, R. Banerjee, Selective Molecular Separation by Interfacially Crystallized Covalent Organic Framework Thin Films, Journal of the American Chemical Society 139 (2017) 13083–13091. https://doi.org/10.1021/jacs.7b06640.
- [157] B. Díaz de Greñu, J. Torres, J. García-González, S. Muñoz-Pina, R. de los Reyes, A.M. Costero, P. Amorós, J.V. Ros-Lis, Microwave-Assisted Synthesis of Covalent Organic Frameworks: A Review, ChemSusChem 14 (2021) 208– 233. https://doi.org/10.1002/cssc.202001865.
- [158] J. Liu, J. Wang, Y. Wang, Y. Wang, Covalent organic frameworks as advanced materials in the application of chemical detection, Journal of Polymer Science n/a (2022). https://doi.org/10.1002/pol.20220683.
- [159] O.M. Yaghi, M.J. Kalmutzki, C.S. Diercks, Reticular Design of Covalent Organic Frameworks, in: Introduction to Reticular Chemistry, John Wiley & Sons, Ltd, 2019: pp. 225–243. https://doi.org/10.1002/9783527821099.ch9.
- [160] Y. Yusran, Q. Fang, V. Valtchev, Electroactive Covalent Organic Frameworks: Design, Synthesis, and Applications, Advanced Materials 32 (2020) 2002038. https://doi.org/10.1002/adma.202002038.
- [161] S. Yuan, X. Li, J. Zhu, G. Zhang, P. Van Puyvelde, B. der Bruggen, Covalent organic frameworks for membrane separation, Chem. Soc. Rev. 48 (2019) 2665–2681. https://doi.org/10.1039/C8CS00919H.
- [162] X. Zhao, P. Pachfule, A. Thomas, Covalent organic frameworks (COFs) for electrochemical applications, Chem. Soc. Rev. 50 (2021) 6871–6913. https://doi.org/10.1039/D0CS01569E.
- [163] Y. Peng, G. Xu, Z. Hu, Y. Cheng, C. Chi, D. Yuan, H. Cheng, D. Zhao, Mechanoassisted Synthesis of Sulfonated Covalent Organic Frameworks with

- High Intrinsic Proton Conductivity, ACS Applied Materials & Interfaces 8 (2016) 18505–18512. https://doi.org/10.1021/acsami.6b06189.
- [164] R. Xue, Y.-S. Liu, S.-L. Huang, G.-Y. Yang, Recent Progress of Covalent Organic Frameworks Applied in Electrochemical Sensors, ACS Sensors 8 (2023) 2124–2148. https://doi.org/10.1021/acssensors.3c00269.
- [165] S. Feng, M. Yan, Y. Xue, J. Huang, X. Yang, An electrochemical sensor for sensitive detection of dopamine based on a COF/Pt/MWCNT–COOH nanocomposite, Chem. Commun. 58 (2022) 6092–6095. https://doi.org/10.1039/D2CC01376B.
- [166] W.-Y. Geng, H. Zhang, Y.-H. Luo, X.-G. Zhu, A.-D. Xie, J. Wang, D.-E. Zhang, Facile fabrication of carbon-loaded covalent-organic framework composites with enhanced electrochemical performance for dopamine determination, Microporous and Mesoporous Materials 323 (2021)111186. https://doi.org/10.1016/j.micromeso.2021.111186.
- [167] L. Chen, L. He, F. Ma, W. Liu, Y. Wang, M.A. Silver, L. Chen, L. Zhu, D. Gui, J. Diwu, Z. Chai, S. Wang, Covalent Organic Framework Functionalized with 8-Hydroxyquinoline as a Dual-Mode Fluorescent and Colorimetric pH Sensor, ACS Applied Materials & Interfaces 10 (2018) 15364–15368. https://doi.org/10.1021/acsami.8b05484.
- [168] M. Xu, L. Wang, Y. Xie, Y. Song, L. Wang, Ratiometric electrochemical sensing and biosensing based on multiple redox-active state COFDHTA-TTA, Sensors and Actuators B: Chemical 281 (2019) 1009–1015. https://doi.org/10.1016/j.snb.2018.11.032.
- [169] Y. Xie, M. Xu, L. Wang, H. Liang, L. Wang, Y. Song, Iron-porphyrin-based covalent-organic frameworks for electrochemical sensing H2O2 and pH, Materials Science and Engineering: C 112 (2020) 110864. https://doi.org/10.1016/j.msec.2020.110864.
- [170] M.T. Ghoneim, A. Nguyen, N. Dereje, J. Huang, G.C. Moore, P.J. Murzynowski, C. Dagdeviren, Recent Progress in Electrochemical pH-Sensing Materials and Configurations for Biomedical Applications, Chem. Rev. 119 (2019) 5248–5297. https://doi.org/10.1021/acs.chemrev.8b00655.
- [171] D. Jasiński, J. Meredith, K. Kirwan, The life cycle impact for platinum group metals and lithium to 2070 via surplus cost potential, Int J Life Cycle Assess 23 (2018) 773–786. https://doi.org/10.1007/s11367-017-1329-4.
- [172] A. Fulati, S.M. Usman Ali, M. Riaz, G. Amin, O. Nur, M. Willander, Miniaturized pH Sensors Based on Zinc Oxide Nanotubes/Nanorods, Sensors 9 (2009) 8911–8923. https://doi.org/10.3390/s91108911.
- [173] V. Kašpárková, P. Humpolíček, J. Stejskal, Z. Capáková, P. Bober, K. Skopalová, M. Lehocký, Exploring the Critical Factors Limiting Polyaniline Biocompatibility, Polymers (Basel) 11 (2019) 362. https://doi.org/10.3390/polym11020362.
- [174] J. Hu, A. Stein, P. Bühlmann, Rational design of all-solid-state ion-selective electrodes and reference electrodes, TrAC Trends in Analytical Chemistry 76 (2016) 102–114. https://doi.org/10.1016/j.trac.2015.11.004.

- [175] Y. Yang, M. Faheem, L. Wang, Q. Meng, H. Sha, N. Yang, Y. Yuan, G. Zhu, Surface Pore Engineering of Covalent Organic Frameworks for Ammonia Capture through Synergistic Multivariate and Open Metal Site Approaches, ACS Cent Sci 4 (2018) 748–754. https://doi.org/10.1021/acscentsci.8b00232.
- [176] Y. Guo, X. Zou, W. Li, Y. Hu, Z. Jin, Z. Sun, S. Gong, S. Guo, F. Yan, High-density sulfonic acid-grafted covalent organic frameworks with efficient anhydrous proton conduction, J. Mater. Chem. A 10 (2022) 6499–6507. https://doi.org/10.1039/D2TA00793B.
- [177] Z. Huang, H. Ghasemi, Hydrophilic polymer-based anti-biofouling coatings: Preparation, mechanism, and durability, Advances in Colloid and Interface Science 284 (2020) 102264. https://doi.org/10.1016/j.cis.2020.102264.
- [178] H. Wang, M. Wang, Y. Wang, J. Wang, X. Men, Z. Zhang, V. Singh, Synergistic effects of COF and GO on high flux oil/water separation performance of superhydrophobic composites, Separation and Purification Technology 276 (2021) 119268. https://doi.org/10.1016/j.seppur.2021.119268.
- [179] V. Singh, J. Zhang, J. Chen, C.G. Salzmann, M.K. Tiwari, Precision Covalent Organic Frameworks for Surface Nucleation Control, Advanced Materials 35 (2023) 2302466. https://doi.org/10.1002/adma.202302466.
- [180] W. Li, Q. Wang, F. Cui, G. Jiang, Covalent organic framework with sulfonic acid functional groups for visible light-driven CO₂ reduction, RSC Adv. 12 (2022) 17984–17989. https://doi.org/10.1039/D2RA02660K.
- [181] A. Lazaro, R. Villarino, M. Lazaro, N. Canellas, B. Prieto-Simon, D. Girbau, Recent Advances in Batteryless NFC Sensors for Chemical Sensing and Biosensing, Biosensors 13 (2023) 775. https://doi.org/10.3390/bios13080775.
- [182] D. Yogev, T. Goldberg, A. Arami, S. Tejman-Yarden, T.E. Winkler, B.M. Maoz, Current state of the art and future directions for implantable sensors in medical technology: Clinical needs and engineering challenges, APL Bioengineering 7 (2023) 031506. https://doi.org/10.1063/5.0152290.
- [183] A. Lazaro, R. Villarino, D. Girbau, A Survey of NFC Sensors Based on Energy Harvesting for IoT Applications, Sensors 18 (2018) 3746. https://doi.org/10.3390/s18113746.
- [184] M.H. Kang, G.J. Lee, J.H. Yun, Y.M. Song, NFC-Based Wearable Optoelectronics Working with Smartphone Application for Untact Healthcare, Sensors 21 (2021) 878. https://doi.org/10.3390/s21030878.
- [185] E. De la Paz, N.H. Maganti, A. Trifonov, I. Jeerapan, K. Mahato, L. Yin, T. Sonsaard, N. Ma, W. Jung, R. Burns, A. Zarrinpar, J. Wang, P.P. Mercier, A self-powered ingestible wireless biosensing system for real-time in situ monitoring of gastrointestinal tract metabolites, Nature Communications 13 (2022) 7405. https://doi.org/10.1038/s41467-022-35074-y.
- [186] R. Rahimi, U. Brener, M. Ochoa, B. Ziaie, Flexible and transparent pH monitoring system with NFC communication for wound monitoring applications, in: 2017 IEEE 30th International Conference on Micro Electro Mechanical Systems (MEMS), IEEE, Las Vegas, NV, USA, 2017: pp. 125–128. https://doi.org/10.1109/MEMSYS.2017.7863356.

- [187] H. Lyu, M. John, D. Burkland, B. Greet, A. Post, A. Babakhani, M. Razavi, Synchronized Biventricular Heart Pacing in a Closed-chest Porcine Model based on Wirelessly Powered Leadless Pacemakers, Sci Rep 10 (2020) 2067. https://doi.org/10.1038/s41598-020-59017-z.
- [188] H. Jeong, L. Wang, T. Ha, R. Mitbander, X. Yang, Z. Dai, S. Qiao, L. Shen, N. Sun, N. Lu, Modular and Reconfigurable Wireless E-Tattoos for Personalized Sensing, Adv Materials Technologies 4 (2019) 1900117. https://doi.org/10.1002/admt.201900117.
- [189] M. Boada, A. Lazaro, D. Girbau, R. Villarino, Battery-less nfc sensors for the internet of things, ISTE Ltd / John Wiley and Sons Inc, Hoboken, 2022.
- [190] M.M. Soliman, M.E.H. Chowdhury, A. Khandakar, M.T. Islam, Y. Qiblawey, F. Musharavati, E. Zal Nezhad, Review on Medical Implantable Antenna Technology and Imminent Research Challenges, Sensors 21 (2021) 3163. https://doi.org/10.3390/s21093163.
- [191] C. Degen, Inductive coupling for wireless power transfer and near-field communication, J Wireless Com Network 2021 (2021) 121. https://doi.org/10.1186/s13638-021-01994-4.
- [192] R. Mendes Duarte, G. Klaric Felic, Analysis of the Coupling Coefficient in Inductive Energy Transfer Systems, Active and Passive Electronic Components 2014 (2014) 1–6. https://doi.org/10.1155/2014/951624.
- [193] M. Boada, A. Lazaro, R. Villarino, D. Girbau, Battery-Less NFC Sensor for pH Monitoring, IEEE Access 7 (2019) 33226–33239. https://doi.org/10.1109/ACCESS.2019.2904109.
- [194] S.R. Patre, Passive Chipless RFID Sensors: Concept to Applications—A Review, IEEE J. Radio Freq. Identif. 6 (2022) 64–76. https://doi.org/10.1109/JRFID.2021.3114104.
- [195] L. Manjakkal, W. Dang, N. Yogeswaran, R. Dahiya, Textile-Based Potentiometric Electrochemical pH Sensor for Wearable Applications, Biosensors 9 (2019). https://doi.org/10.3390/bios9010014.
- [196] S. Bhadra, G.E. Bridges, D.J. Thomson, M.S. Freund, Electrode Potential-Based Coupled Coil Sensor for Remote pH Monitoring, IEEE Sensors J. 11 (2011) 2813–2819. https://doi.org/10.1109/JSEN.2011.2170563.
- [197] H. Cao, S. Rao, S. Tang, H.F. Tibbals, S. Spechler, J.-C. Chiao, Batteryless implantable dual-sensor capsule for esophageal reflux monitoring, Gastrointestinal Endoscopy 77 (2013) 649–653. https://doi.org/10.1016/j.gie.2012.10.029.
- [198] Hung Cao, V. Landge, U. Tata, Young-Sik Seo, S. Rao, Shou-Jiang Tang, H.F. Tibbals, S. Spechler, J. Chiao, An Implantable, Batteryless, and Wireless Capsule With Integrated Impedance and pH Sensors for Gastroesophageal Reflux Monitoring, IEEE Trans. Biomed. Eng. 59 (2012) 3131–3139. https://doi.org/10.1109/TBME.2012.2214773.
- [199] H. Cao, S.K. Thakar, T. Fu, M. Sheth, M.L. Oseng, V. Landge, Y. Seo, J.-C. Chiao, A wireless strain sensor system for bladder volume monitoring, in: 2011 IEEE MTT-S International Microwave Symposium, IEEE, Baltimore, MD, USA, 2011: pp. 1–4. https://doi.org/10.1109/MWSYM.2011.5972653.

- [200] J.F. Salmerón, F. Molina-Lopez, D. Briand, J.J. Ruan, A. Rivadeneyra, M.A. Carvajal, L.F. Capitán-Vallvey, N.F. De Rooij, A.J. Palma, Properties and Printability of Inkjet and Screen-Printed Silver Patterns for RFID Antennas, Journal of Elec Materi 43 (2014) 604–617. https://doi.org/10.1007/s11664-013-2893-4.
- [201] K. Kuruvinashetti, A. Komeili, A. Sanati Nezhad, Autonomous wearable sensing enabled by capillary microfluidics: a review, Lab Chip 25 (2025) 3879–3920. https://doi.org/10.1039/D5LC00536A.
- [202] N. Mohd Faudzi, A.R. Razali, A. Abdul Manaf, N.H. Abd Rahman, A.A. Aziz, A. Ibrahim, A.M. Mozi, Analysis of Flexible Silver-printed NFC Tag Antenna on Miniaturization and Bending Effect, EAJ 19 (2023) 54–67. https://doi.org/10.24191/esteem.v19iMarch.21262.
- [203] R.C. Orlando, Esophageal mucosal defense mechanisms, GI Motility Online (2006).
- [204] V.V. Khutoryanskiy, Advances in Mucoadhesion and Mucoadhesive Polymers, Macromolecular Bioscience 11 (2011) 748–764. https://doi.org/10.1002/mabi.201000388.
- [205] S.K. Linden, P. Sutton, N.G. Karlsson, V. Korolik, M.A. McGuckin, Mucins in the mucosal barrier to infection., Mucosal Immunology 1 (2008) 183–197. https://doi.org/10.1038/mi.2008.5.
- [206] J. Yang, R. Bai, B. Chen, Z. Suo, Hydrogel Adhesion: A Supramolecular Synergy of Chemistry, Topology, and Mechanics, Advanced Functional Materials 30 (2020) 1901693. https://doi.org/10.1002/adfm.201901693.
- [207] J. Dixon, V. Strugala, S.M. Griffin, M.R. Welfare, P.W. Dettmar, A. Allen, J.P. Pearson, Esophageal mucin: an adherent mucus gel barrier is absent in the normal esophagus but present in columnar-lined Barrett's esophagus, The American Journal of Gastroenterology 96 (2001) 2575–2583. https://doi.org/10.1016/S0002-9270(01)02721-6.
- [208] G.C. Sedenho, A.R. Pereira, K.C. Pagnoncelli, J.C.P. de Souza, F.N. Crespilho, Implantable Enzyme-Based Biofuel Cells, in: K.B.T.-E. of I.C. Wandelt (Ed.), Elsevier, Oxford, 2018: pp. 248–260. https://doi.org/10.1016/B978-0-12-409547-2.13709-6.
- [209] K. Kalantar-Zadeh, K.J. Berean, N. Ha, A.F. Chrimes, K. Xu, D. Grando, J.Z. Ou, N. Pillai, J.L. Campbell, R. Brkljača, K.M. Taylor, R.E. Burgell, C.K. Yao, S.A. Ward, C.S. McSweeney, J.G. Muir, P.R. Gibson, A human pilot trial of ingestible electronic capsules capable of sensing different gases in the gut, Nature Electronics 1 (2018) 79–87. https://doi.org/10.1038/s41928-017-0004-x.
- [210] S.K. Garg, D. Liljenquist, B. Bode, M.P. Christiansen, T.S. Bailey, R.L. Brazg, D.S. Denham, A.R. Chang, H.K. Akturk, A. Dehennis, K.S. Tweden, F.R. Kaufman, Evaluation of Accuracy and Safety of the Next-Generation Up to 180-Day Long-Term Implantable Eversense Continuous Glucose Monitoring System: The PROMISE Study, Diabetes Technology & Therapeutics 24 (2021) 84–92. https://doi.org/10.1089/dia.2021.0182.
- [211] T. Divyani, S. Swampna, O. S, Surgical Sealants and Adhesives Market, Allied Market Research, 2022.

- [212] R. Eelkema, A. Pich, Pros and Cons: Supramolecular or Macromolecular: What Is Best for Functional Hydrogels with Advanced Properties?, Advanced Materials 32 (2020) 1906012. https://doi.org/10.1002/adma.201906012.
- [213] Z. Zeng, X.M. Mo, C. He, Y. Morsi, H. El-Hamshary, M. El-Newehy, An in situ forming tissue adhesive based on poly(ethylene glycol)-dimethacrylate and thiolated chitosan through the Michael reaction, Journal of Materials Chemistry B 4 (2016) 5585–5592. https://doi.org/10.1039/c6tb01475e.
- [214] B. Balakrishnan, N. Joshi, A. Jayakrishnan, R. Banerjee, Self-crosslinked oxidized alginate/gelatin hydrogel as injectable, adhesive biomimetic scaffolds for cartilage regeneration, Acta Biomaterialia 10 (2014) 3650–3663. https://doi.org/10.1016/j.actbio.2014.04.031.
- [215] H. Yuk, C.E. Varela, C.S. Nabzdyk, X. Mao, R.F. Padera, E.T. Roche, X. Zhao, Dry double-sided tape for adhesion of wet tissues and devices, Nature 575 (2019) 169–174. https://doi.org/10.1038/s41586-019-1710-5.
- [216] L. Agüero, D. Zaldivar-Silva, L. Peña, M. Dias, Alginate microparticles as oral colon drug delivery device: A review, Carbohydrate Polymers 168 (2017) 32–43. https://doi.org/10.1016/j.carbpol.2017.03.033.
- [217] C.K. Song, M.K. Kim, J. Lee, E. Davaa, R. Baskaran, S.G. Yang, Dopa-Empowered Schiff Base Forming Alginate Hydrogel Glue for Rapid Hemostatic Control, Macromolecular Research 27 (2019) 119–125. https://doi.org/10.1007/s13233-019-7026-3.
- [218] K.E. Haugstad, A.G. Håti, C.T. Nordgård, P.S. Adl, G. Maurstad, M. Sletmoen, K.I. Draget, R.S. Dias, B.T. Stokke, Direct determination of chitosan-mucin interactions using a single-molecule strategy: Comparison to alginate-mucin interactions, Polymers 7 (2015) 161–185. https://doi.org/10.3390/polym7020161.
- [219] C. Dai, Z. Zhou, Z. Guan, Y. Wu, Y. Liu, J. He, P. Yu, L. Tu, F. Zhang, D. Chen, R. Wang, C. Ning, L. Zhou, G. Tan, A Multifunctional Metallohydrogel with Injectability, Self-Healing, and Multistimulus-Responsiveness for Bioadhesives, Macromolecular Materials and Engineering 303 (2018) 1–9. https://doi.org/10.1002/mame.201800305.
- [220] J. Nowak, F. Laffleur, A. Bernkop-Schnürch, Preactivated hyaluronic acid: A potential mucoadhesive polymer for vaginal delivery, International Journal of Pharmaceutics 478 (2015) 383–389. https://doi.org/10.1016/j.ijpharm.2014.11.048.
- [221] M. Jovanović, N. Tomić, S. Cvijić, D. Stojanović, S. Ibrić, P. Uskoković, Mucoadhesive Gelatin Buccal Films with Propranolol Hydrochloride: Evaluation of Mechanical, Mucoadhesive, and Biopharmaceutical Properties, Pharmaceutics 13 (2021). https://doi.org/10.3390/pharmaceutics13020273.
- [222] G. Tan, L. Zhou, C. Ning, Y. Tan, G. Ni, J. Liao, P. Yu, X. Chen, Biomimetically-mineralized composite coatings on titanium functionalized with gelatin methacrylate hydrogels, Applied Surface Science 279 (2013) 293–299. https://doi.org/10.1016/j.apsusc.2013.04.088.
- [223] H. Iwata, S. Matsuda, K. Mitsuhashi, E. Itoh, Y. Ikada, A novel surgical glue composed of gelatin and N-hydroxysuccinimide activated poly(L-glutamic acid):

- Part 1. Synthesis of activated poly(L-glutamic acid) and its gelation with gelatin., Biomaterials 19 (1998) 1869–1876.
- [224] H. Feier, P. Deutsch, M. Gaspar, S. Ursoniu, The influence of albumin/glutaraldehyde sealant in early results after acute type a aortic dissection, Revista de Chimie 70 (2019) 2032–2035. https://doi.org/10.37358/rc.19.6.7269.
- [225] A. Assmann, A. Vegh, M. Ghasemi-Rad, S. Bagherifard, G. Cheng, E.S. Sani, G.U. Ruiz-Esparza, I. Noshadi, A.D. Lassaletta, S. Gangadharan, A. Tamayol, A. Khademhosseini, N. Annabi, A highly adhesive and naturally derived sealant, Biomaterials 140 (2017) 115–127. https://doi.org/10.1016/j.biomaterials.2017.06.004.
- [226] M. Pirmoradian, T. Hooshmand, F. Najafi, M. Haghbin Nazarpak, S. Davaie, Design, synthesis, and characterization of a novel dual cross-linked gelatinbased bioadhesive for hard and soft tissues adhesion capability, Biomedical Materials (Bristol) 17 (2022). https://doi.org/10.1088/1748-605X/ac9268.
- [227] K.A. Burke, D.C. Roberts, D.L. Kaplan, Silk Fibroin Aqueous-Based Adhesives Inspired by Mussel Adhesive Proteins, Biomacromolecules 17 (2016) 237–245. https://doi.org/10.1021/acs.biomac.5b01330.
- [228] S. Hu, X. Pei, L. Duan, Z. Zhu, Y. Liu, J. Chen, T. Chen, P. Ji, Q. Wan, J. Wang, A mussel-inspired film for adhesion to wet buccal tissue and efficient buccal drug delivery, Nature Communications 12 (2021). https://doi.org/10.1038/s41467-021-21989-5.
- [229] W.D. Spotnitz, Fibrin Sealant: The Only Approved Hemostat, Sealant, and Adhesive-a Laboratory and Clinical Perspective., ISRN Surgery 2014 (2014) 203943. https://doi.org/10.1155/2014/203943.
- [230] A. Lauto, D. Mawad, L.J.R. Foster, Adhesive biomaterials for tissue reconstruction, Journal of Chemical Technology & Biotechnology 83 (2008) 464–472. https://doi.org/10.1002/jctb.1771.
- [231] B. Jamnadas-Khoda, M.A.A. Khan, G.P.L. Thomas, S.J. Ghosh, Histoacryl glue: A burning issue, Burns 37 (2011) e1–e3. https://doi.org/10.1016/j.burns.2010.09.005.
- [232] M.J. Brennan, B.F. Kilbride, J.J. Wilker, J.C. Liu, A bioinspired elastin-based protein for a cytocompatible underwater adhesive, Biomaterials 124 (2017) 116–125. https://doi.org/10.1016/j.biomaterials.2017.01.034.
- [233] Q.A. Service, Trauma/Skin closure Histoacryl topical skin adhesive, State of Queensland, Queensland, 2020. https://www.ambulance.qld.gov.au/docs/clinical/cpp/CPP_Skin.
- [234] M. Xue, Y. Ji, J. Ou, F. Wang, C. Li, S. Lei, W. Li, Surface wettability and strong adhesion of medical polyurethane elastomer porous films by microphase separation, AIP Advances 9 (2019) 75309. https://doi.org/10.1063/1.5107459.
- [235] B.-I. Ciubotaru, M.-F. Zaltariov, L. Verestiuc, D. Filip, D. Macocinschi, Mucoadhesive Composites Based on Polyurethane/AgNPs for Urinary Catheter Application, in: 2019 E-Health and Bioengineering Conference (EHB), 2019: pp. 1–4. https://doi.org/10.1109/EHB47216.2019.8970045.

- [236] D.F. Torchiana, Polyethylene Glycol Based Synthetic Sealants:, Journal of Cardiac Surgery 18 (2003) 504–506. https://doi.org/10.1046/j.0886-0440.2003.00305.x.
- [237] P. Chansoria, A. Chaudhari, E.L. Etter, E.E. Bonacquisti, M.K. Heavey, J. Le, M.K. Maruthamuthu, C.C. Kussatz, J. Blackwell, N.E. Jasiewicz, R.S. Sellers, R. Maile, S.M. Wallet, T.M. Egan, J. Nguyen, Instantly adhesive and ultra-elastic patches for dynamic organ and wound repair, Nature Communications 15 (2024) 4720. https://doi.org/10.1038/s41467-024-48980-0.
- [238] C. Durcan, M. Hossain, G. Chagnon, D. Perić, L. Bsiesy, G. Karam, E. Girard, Experimental investigations of the human oesophagus: anisotropic properties of the embalmed muscular layer under large deformation, Biomech. Model. Mechanobiol. 21 (2022) 1169–1186.
- [239] D.F.S. Fonseca, P.C. Costa, I.F. Almeida, P. Dias-Pereira, I. Correia-Sá, V. Bastos, H. Oliveira, C. Vilela, A.J.D. Silvestre, C.S.R. Freire, Swellable Gelatin Methacryloyl Microneedles for Extraction of Interstitial Skin Fluid toward Minimally Invasive Monitoring of Urea, Macromolecular Bioscience 20 (2020) 2000195. https://doi.org/10.1002/mabi.202000195.
- [240] H.T. Lam, O. Zupančič, F. Laffleur, A. Bernkop-Schnürch, Mucoadhesive properties of polyacrylates: Structure Function relationship, International Journal of Adhesion and Adhesives 107 (2021) 102857. https://doi.org/10.1016/j.ijadhadh.2021.102857.
- [241] H. Park, J.R. Robinson, Mechanisms of Mucoadhesion of Poly(acrylic Acid) Hydrogels, Pharmaceutical Research 4 (1987) 457–464. https://doi.org/10.1023/A:1016467219657.
- [242] M. Singh, D.L. Teodorescu, M. Rowlett, S.X. Wang, M. Balcells, C. Park, B. Bernardo, S. McGarel, C. Reeves, M.R. Mehra, X. Zhao, H. Yuk, E.T. Roche, A Tunable Soft Silicone Bioadhesive for Secure Anchoring of Diverse Medical Devices to Wet Biological Tissue, Advanced Materials 36 (2024) 2307288. https://doi.org/10.1002/adma.202307288.
- [243] S.M. Bidoki, D.M. Lewis, M. Clark, A. Vakorov, P.A. Millner, D. McGorman, Ink-jet fabrication of electronic components, Journal of Micromechanics and Microengineering 17 (2007) 967–974. https://doi.org/10.1088/0960-1317/17/5/017.
- [244] B.K.P. Horn, H.M. Hilden, S. Negahdaripour, Closed-form solution of absolute orientation using orthonormal matrices, Journal of the Optical Society of America A 5 (1988) 1127. https://doi.org/10.1364/josaa.5.001127.
- [245] U.B. Irurzun, V. Dutschk, A. Calvimontes, R. Akkerman, Generation of microsized conductive lines on glass fibre fabrics by inkjet printing, Autex Research Journal 12 (2012) 55–61. https://doi.org/10.2478/v10304-012-0011-y.
- [246] H. Shahariar, I. Kim, H. Soewardiman, J.S. Jur, Inkjet Printing of Reactive Silver Ink on Textiles, ACS Applied Materials and Interfaces (2019). https://doi.org/10.1021/acsami.8b18231.
- [247] Y. Huang, N. Bu, Y. Duan, Y. Pan, H. Liu, Z. Yin, Y. Xiong, Electrohydrodynamic direct-writing, Nanoscale 5 (2013) 12007–12017. https://doi.org/10.1039/C3NR04329K.

[248] Y. Jiang, C. Wu, L. Li, K. Wang, Z. Tao, F. Gao, W. Cheng, J. Cheng, X.Y. Zhao, S. Priya, W. Deng, All electrospray printed perovskite solar cells, Nano Energy 53 (2018) 440–448. https://doi.org/10.1016/j.nanoen.2018.08.062.

Appendix I

High-Resolution Inkjet Printing

Another widely used technique for the fabrication of printed electronics is via inkjet printing. Similarly to screen printing, it has shown to effectively print on plastic, textile, paper and glass substrates showing effectiveness regardless of porosity of the substrate [104]. Inkjet printing from a high-level perspective can be narrowed down to three steps: (1) generation of droplets, (2) positioning of the droplets on to a given substrate (3) using a solidification mechanism to dry the droplets on the substrate to produce a solid deposit [116]. Typically, the ink is loaded into a syringe with a needle which can vary in length and diameter. The drop generation is performed and either the stage or the needle is digitally actuated pneumatically or electronically to the desired location to deposit the ink with sub-micron precision on the chosen substrate.

Drop generation is performed via two methods typically, continuous inkjet printing (CIJ) and drop-on-demand (DOD) printing [116]. The key difference is how the dropping rate is electronically controlled. CIJ produces a continuous stream where charged deflectors can be activated to stop the stream such that a gutter collects it [116]. DOD uses a mechanical or thermal actuator to generate droplets. The actuator used is dependent on the ink type and allows for full control of when droplets should be generated.

The difficulty with inkjet printing is then the selection of suitable inks by analysing the ink rheology as with screen printing [243]. Conversely to screen printing, which typically requires thick paste that can crack and lose functionality when mechanically deformed, inkjet printing requires low-viscosity inks in order to not clog the needles [104,244]. For ink-jet printing, to prevent clogging of the ink in the nozzle, all particles within the ink, including dispersed molecules or nanoparticles, must be at least 1/50 of the nozzle diameter or smaller which prevent agglomerates and general printing instability [94]. Surface tension is also a crucial parameter as ink must be held inside the nozzle without dripping [245]. The inks typically contain a mixture of binders, dispersants, adhesion promoters in an aqueous solution depending on the application [243].

One drawback of the high percentage of binders is the reduction of electrical performance and spillage when printing ultra-fine features, however it does still typically outperform screen-printing inks [118]. This requires suitable wettability of the ink relative to the substrate chosen to minimise spreading while printing [245]. Organic inks typically have low conductivity while metallic inks require high annealing temperatures (>200 °C) which limits the substrates that can be used [104]. Another drawback is that inkjet printing is considered slow for mass production, although it does produce less wasted ink and requires less preparation than screen printing [118]. Following selection of a suitable ink and substrate, the remaining optimisation parameters are droplet sizes, actuation speed and nozzle-to-substrate distance [246]. Derby mentions the need for a suitable nozzle-to-substrate distance such that drops do not combine mid-air [116]. For CIJ systems this is accounted for in a region where drop generation rates of 20-60 kHz is common while for DOD systems this is typically between 1-20 kHz [116]. Citations in literature have also shown that on rougher surfaces and for fine lines, several passes of the nozzle on the substrate are required to decrease cracks and discontinuities while improving electrical conductivity [246]. Behaviour of droplets upon impacting a solid surface causing spreading has been reported by Derby as an issue that ink and substrate selection must account for [116]. Further, Derby also reported that drop spacing in both frequency and distance can cause instabilities such as beading, bulging and discontinuities [116].

Electrohydrodynamic Printing

Electrohydrodynamic (EHD) printing is largely considered to be the next generation printing technique as it uses electric fields to eject ink through nozzles [102,115]. This printing technique requires the ink to reach the tip of the nozzle where surface tension causes it to form a meniscus and hold its shape just as in direct-write printing [115]. To reach the tip of the nozzle, a pneumatic backpressure device can be used to force the ink to the tip. For EHD, an electric field is then applied which causes movement of the ions in the ink to move towards the surface of the meniscus and increases stress in the area in what is known as the Maxwell stress. As the electric field increases, the Maxwell stress acts against the surface tension force and forms a pointed shape that is smaller than the diameter of the nozzle it is housed in [115]. Reports of print fibres 10-1000 times smaller than nozzle size has been widely reported [102]. Once the Maxwell stress overcomes the surface tension stress, the ink is ejected and deposited

on the substrate [115]. This printing technique has been described qualitatively to "pull" the fluids rather than "push" them highlighting one of the main differences between it and the other printing techniques mentioned [102]. The electric field parameters can be controlled to deliver droplets of different viscosities and volumes onto the substrate [102].

EHD printing has the advantage of using inks with much higher viscosities than other printing techniques operating at a range of 1-10,000 cps as opposed to inkjet's 5-20 cps [102]. Further, it has been shown to achieve resolutions of 0.1-10 μm quite regularly in various applications applicable to the present work such as electrode structures, rGO transistors, and metal-network electrodes [102]. Inks used commonly include molten metal ink, polymer ink, graphene-based ink, rGO-based ink, etc. [102].

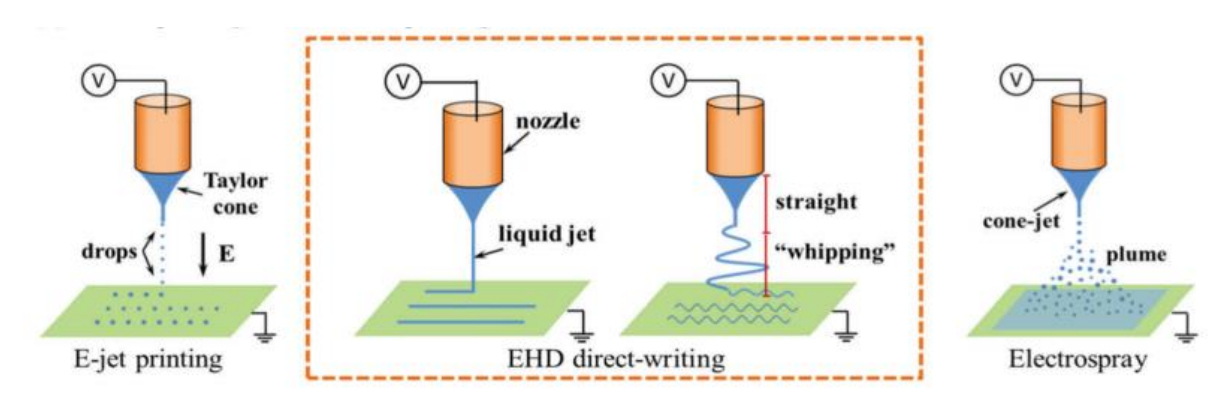


Figure 78: Schematic of EHD printing using the three most common modes, e-jet, EHD direct-writing, and electrospray. Figure sourced from [102].

There are three main EHD techniques used today, e-jet printing, EHD direct-writing and electrospray with Figure 78 showing a schematic of the three techniques [102]. The printing techniques differ by the liquid ejection rate which is controlled by the ink feed rate, the applied field strength and the ink properties [115]. E-jetting is when the ink is applied with Maxwell stresses, induced by the electrical field, much higher than the surface tension stress which causes the meniscus to become sharply conical in what is known as a Taylor cone [115]. Figure 78 shows that despite the use of the word jet, implying a continuous stream, upon closer inspection the jet is made up of discrete larger droplets released in rapid succession [115]. As the electric field strength and the flow rate increases the droplet size and frequency increases which leads to EHD direct writing where a true continuous stream is present. EHD direct-write is based off of another nano-sensor manufacturing technique, electrospinning,

where in the presence of an electric field or a centrifugal force the jet extends into a straight line for a certain distance [247]. Beyond this line, there is bending instability that leads to a spiral like path with increasing circumference which leads to the "whipping" action shown in Figure 12 [247]. Finally, EHD electrospray was developed by inducing atomisation on the ink. This is performed by using an electric field to produce uniformly charged droplets where the Coulombic attraction forces between the droplets cause the jet to atomise [248]. While this may produce a uniform spray, the print quality and uniformity are largely dependent on the adhesion of the ink to the substrate.

Self-Assembled Layers

SAL layers are thick, uniformly-covered layers applied to substrates [127]. SALs have rich chemistry which causes the formation of oxygen, nitrogen, or sulphur containing functional groups to chemically inert surfaces [127]. These groups allow particles from inks to bind to the polymer even after curing and causes better retention of the inks despite application of bending, twisting or other mechanical deformations to the substrate [127].

SALs are deposited using many techniques such as vapour phase deposition (which is slow and typically chemically dangerous), via spin coating (for uniform layers), or inkjet printing for very localised adhesion improvement [127]. OMPMS (oligo(3-mercaptopropyl)(methoxy)siloxane) was demonstrated by Kirikova et al. to be an effective promoter of adhesion of silver nanoparticle inks increasing retention following a tape test by 90-100% (remaining silver area following test).

Appendix II

Cyclic Voltammetry Scans - COF/GO Composite

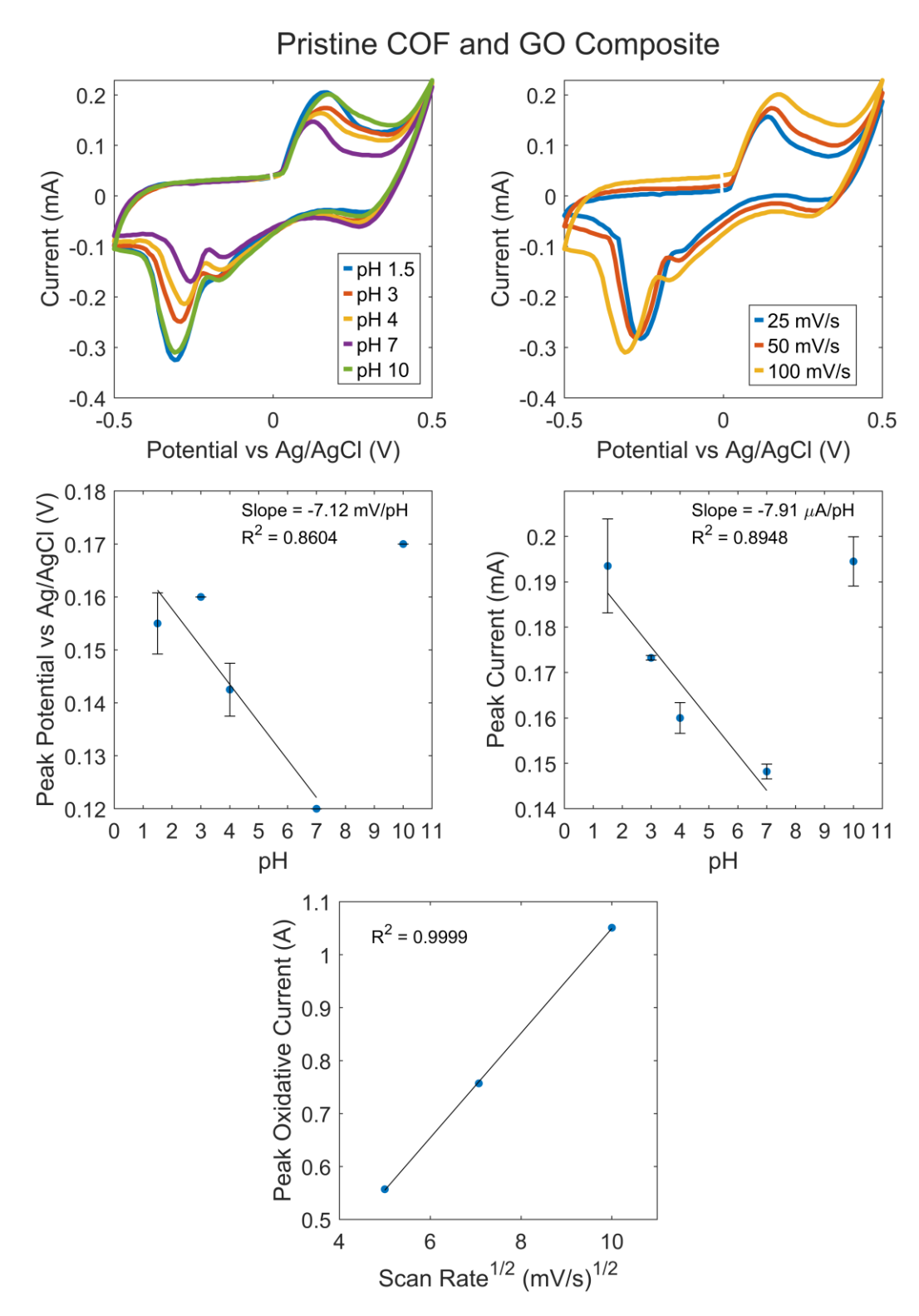


Figure 79: Cyclic Voltammetry results of pristine COF and GO composite.

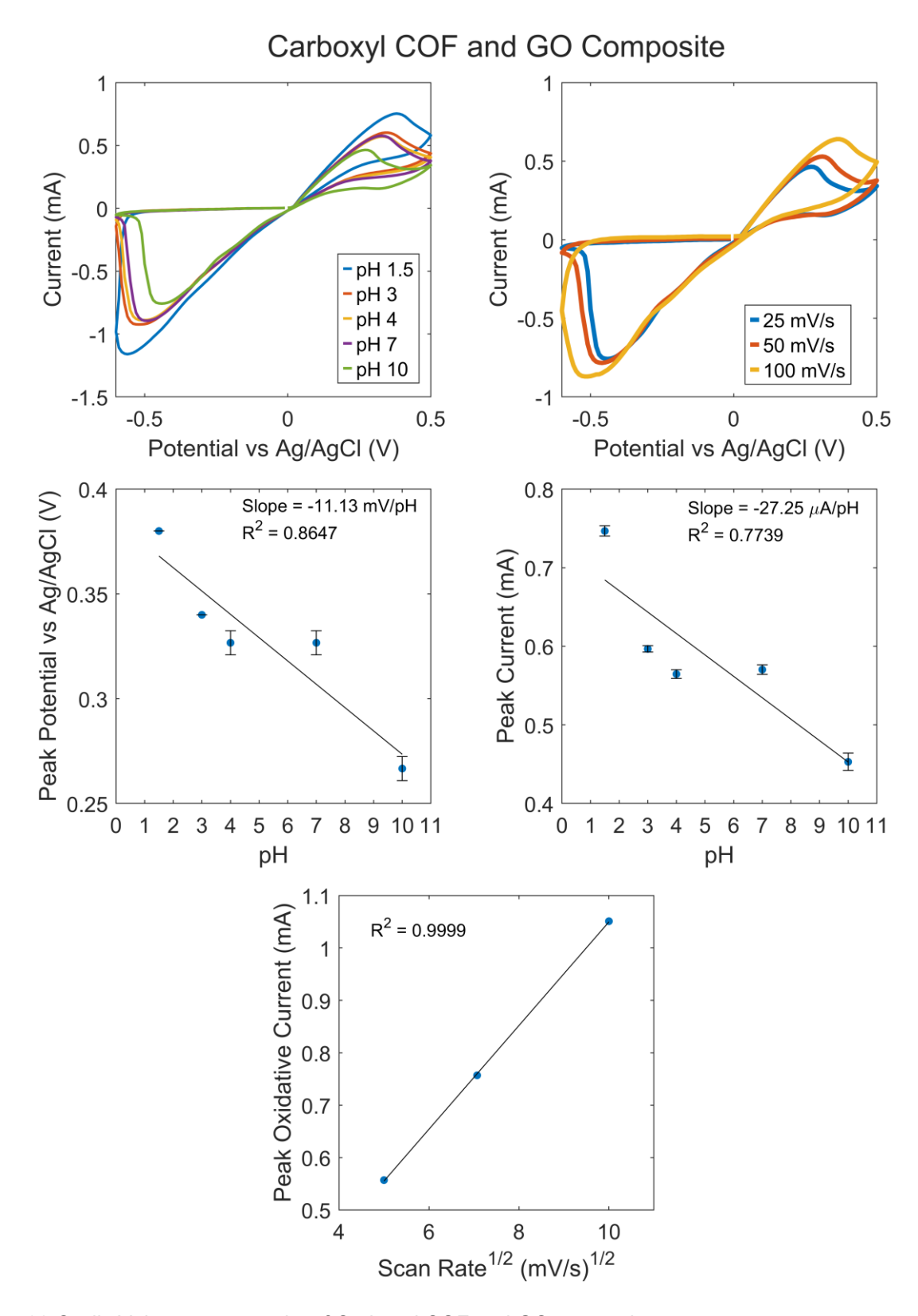


Figure 80 Cyclic Voltammetry results of Carboxyl COF and GO composite.

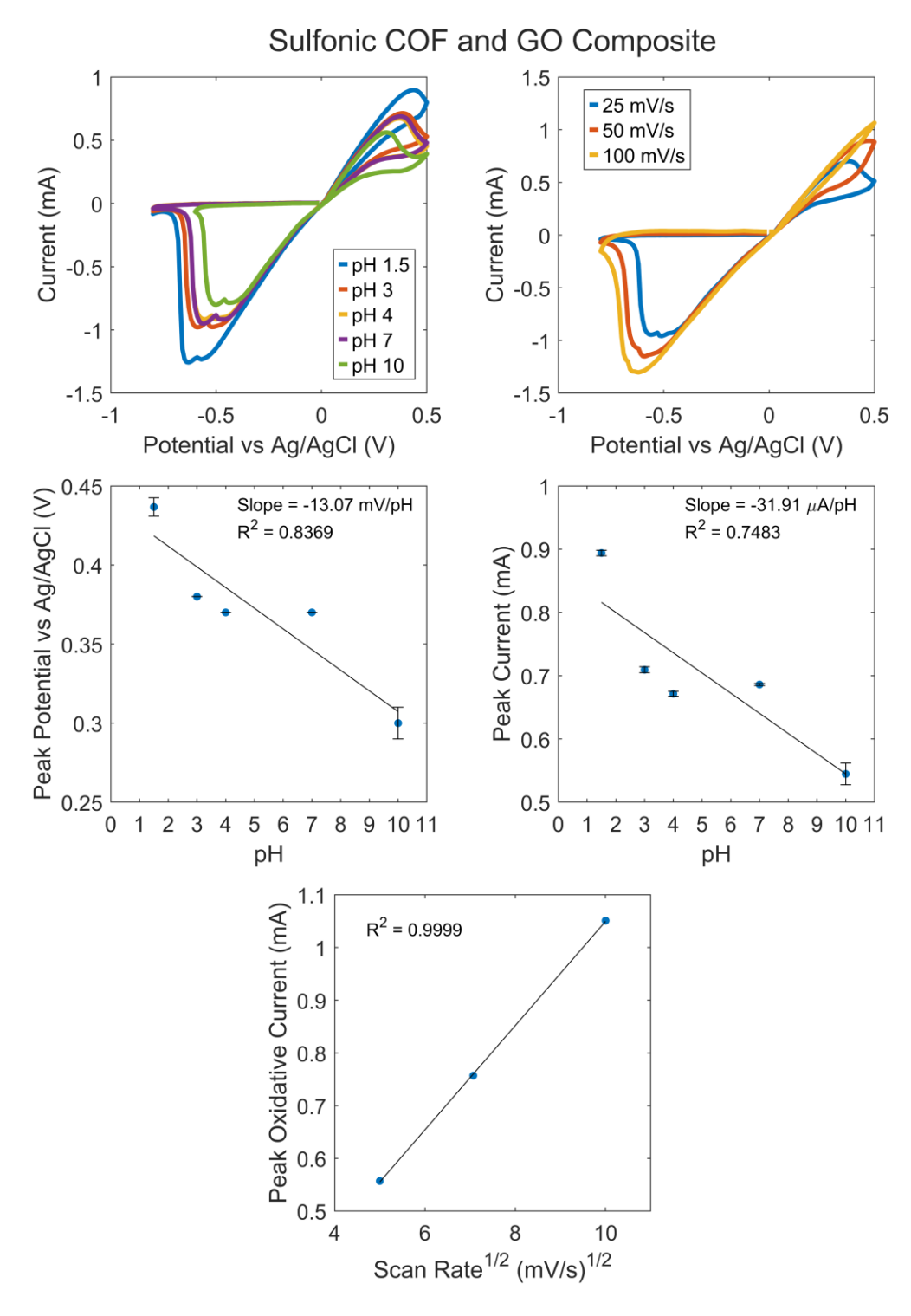


Figure 81: Cyclic Voltammetry results of Sulfonic COF and GO composite.

Impedance Analyser Scans

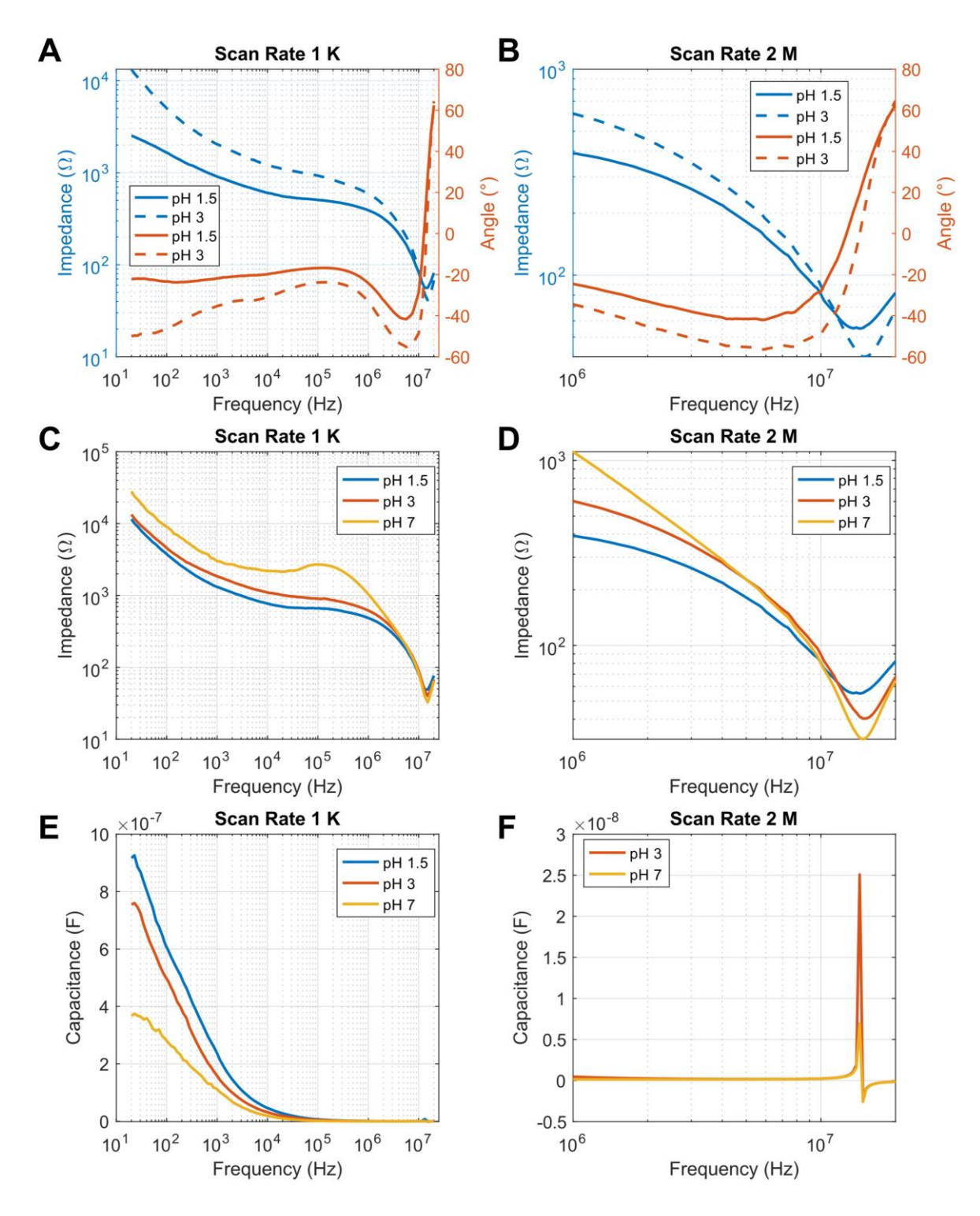


Figure 82: Impedance analyser results showing changes in impedance, phase, and capacitance in different pHs.

Appendix III

Cell Viability Analysis Procedure

Details of the analysis method developed on MATLAB for Cell Viability Fluorescent labelling with Live/Dead cells.

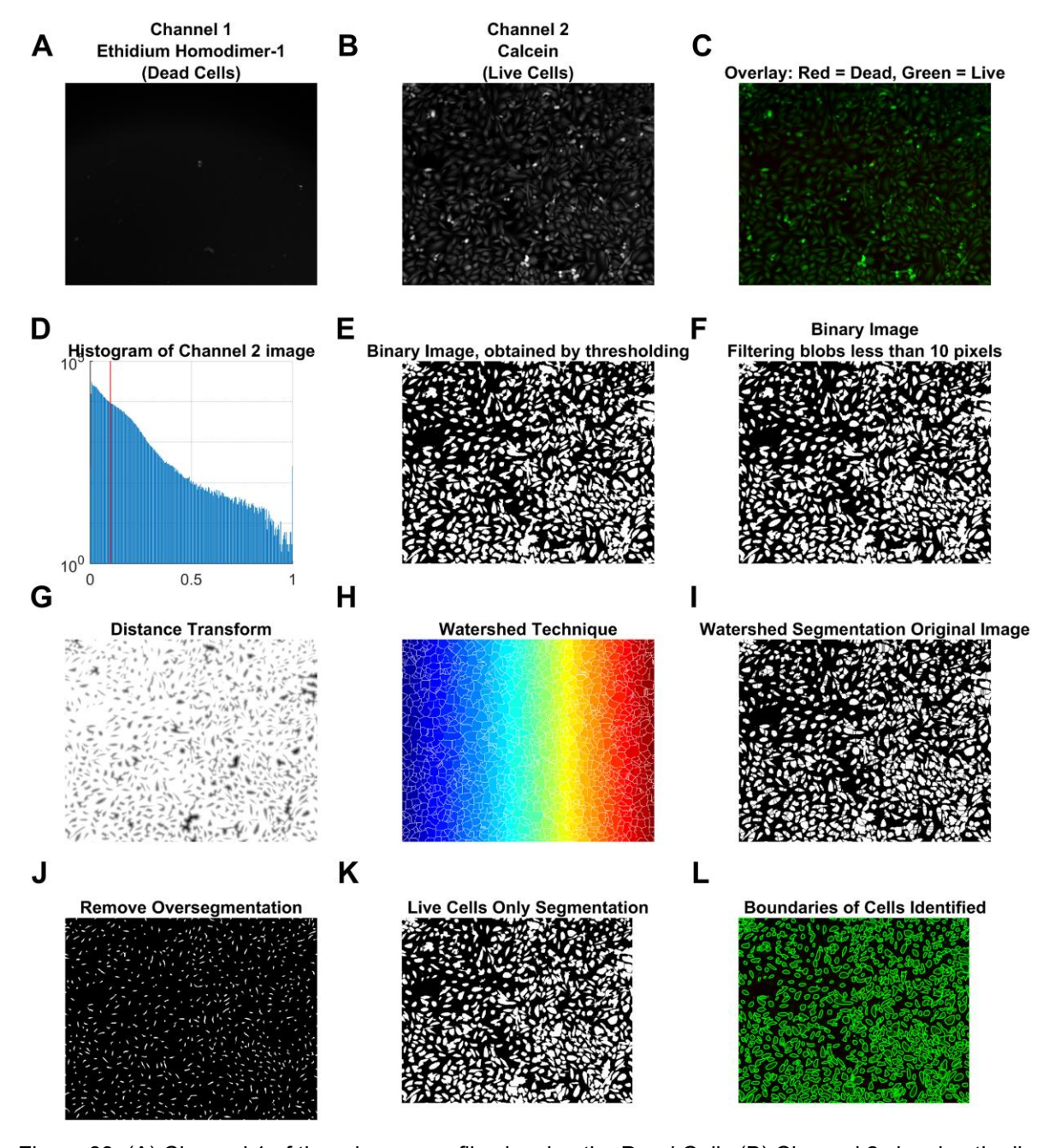


Figure 83: (A) Channel 1 of the microscope file showing the Dead Cells (B) Channel 2 showing the live cells in grayscale image (C) Overlay of the channels showing their original colours. (D) Histogram of Channel 2 image used for thresholding the Binary image shown in (E). (F) Applying filters to remove noisy data less than 10 pixels in size. (G) Applying a distance transform performed by Matlab image processing toolkit. (H) Applying the watershed technique to identify the boundaries of the cells. (I) Using the identified boundaries to segment the original image. (J) Removing oversegmentation by identifying minimum segmented distance (K) Image following full segmentation (L) Highlighted boundaries of live cells identified by function (shown in green).

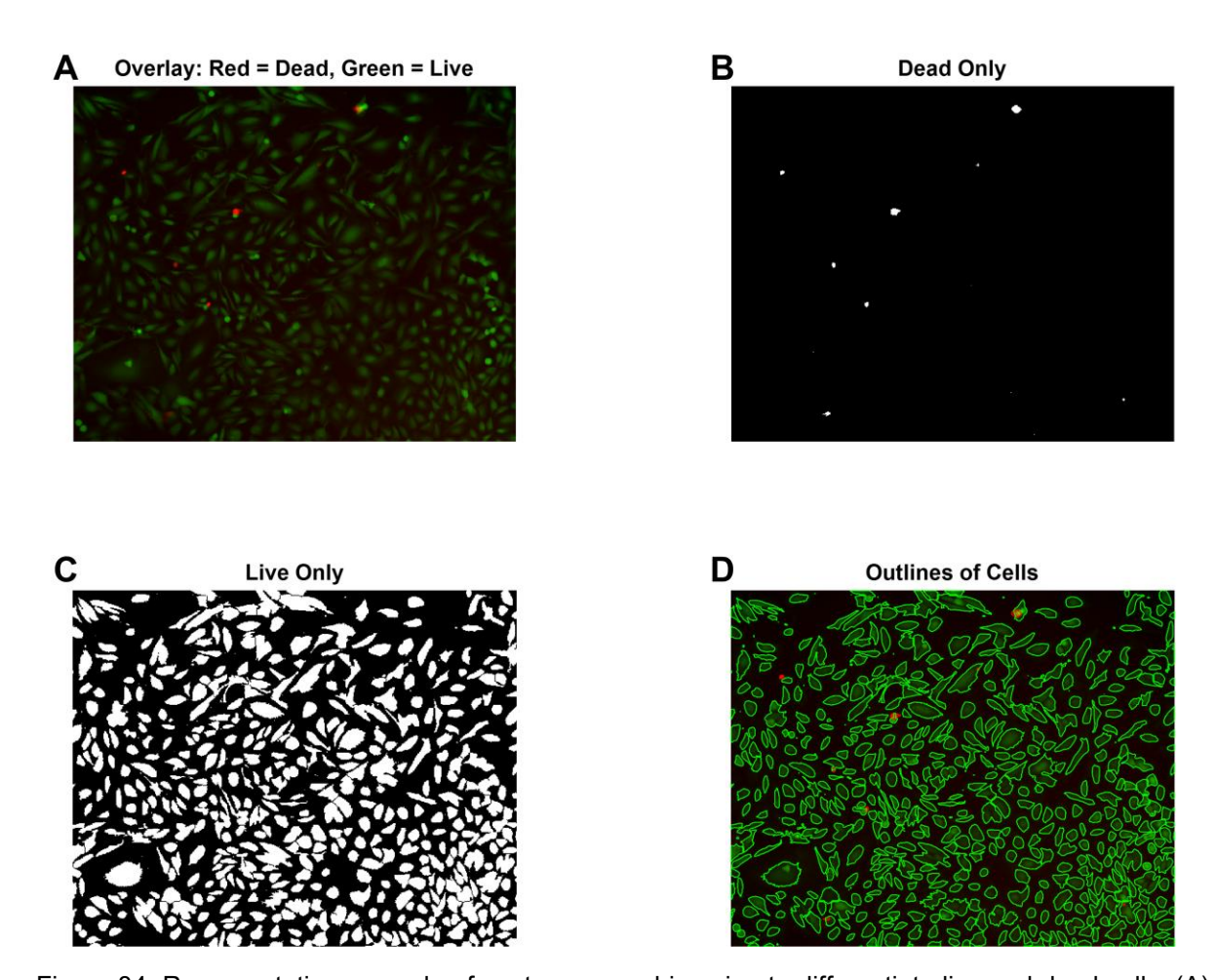


Figure 84: Representative example of post-processed imaging to differentiate live and dead cells. (A) Original image with overlaid colours for context. (B) Channel 1: Processed image highlighting dead cells. (C) Channel 2: Processed image highlighting live cells. (D) Segmented boundaries of live cells (green) and dead cells (red) for enhanced visualisation.

Matlab Code of Example to identify Live/Dead Cell Viability Based off: https://blogs.mathworks.com/steve/2013/11/19/watershed-transformquestion-from-tech-support/ basefileName = char("co only 10x 4.czi"); % Load the BioFormats image bfr = BioformatsImage(basefileName); % Get Ethidium Homodimer-1 (dead cells) and Calcein (live cells) Channel1 = getPlane(bfr, 1, 1, 1); % Channel 1: Ethidium Homodimer-1 Channel2 = getPlane(bfr, 1, 2, 1); % Channel 2: Calcein % Normalize both channels for better visualization Channel1 = mat2gray(Channel1); % Normalize to [0,1] Channel2 = mat2gray(Channel2); % Normalize to [0,1] % Create an RGB image with Red for Channel 1 (dead cells) and Green for Channel 2 (live cells) RGB_Image = cat(3, Channel1, Channel2, zeros(size(Channel1))); % Red = Channel1, Green = Channel2, Blue = 0 hFig1 = gcf; t=tiledlayout(4,3,"TileSpacing","tight","Padding","compact"); nexttile(1); imshow(Channel1, []); title({'Channel 1', 'Ethidium Homodimer-1', '(Dead Cells)'}); nexttile; imshow(Channel2, []); title({'Channel 2', 'Calcein', '(Live Cells)'}); nexttile; imshow(RGB Image); title('Overlay: Red = Dead, Green = Live'); nexttile; axis square; hold on; [pixelCount, grayLevels] = imhist(Channel2,256); bar(grayLevels, pixelCount); title('Histogram of Channel 2 image'); xlim([0 grayLevels(end)]); % Scale x axis manually. grid on; set(gca, 'YScale', 'log'); thresholdValue = 0.1; binaryImage = Channel2 > thresholdValue; % Bright objects will be chosen if you use >. binaryImage = imfill(binaryImage, 'holes'); maxYValue = vlim; line([thresholdValue, thresholdValue], maxYValue, 'Color', 'r'); text(double(thresholdValue + 50), double(0.94 * maxYValue(2)), 'Foreground', 'FontSize', 10, 'Color', [0 0 .5]);

nexttile;

imshow(binaryImage);

```
title('Binary Image, obtained by thresholding');
nexttile;
bw2 = ~bwareaopen(~binaryImage, 10);
imshow(bw2)
title({'Binary Image', 'Filtering blobs less than 10 pixels'});
nexttile;
D = -bwdist(~binaryImage);
imshow(D,[])
title('Distance Transform');
nexttile;
Ld = watershed(D);
imshow(label2rgb(Ld))
title('Watershed Technique');
nexttile;
bw2 = binaryImage;
bw2(Ld == 0) = 0;
imshow(bw2);
title('Watershed Segmentation Original Image');
nexttile;
mask = imextendedmin(D,2);
imshow(mask);
title('Remove Oversegmentation');
nexttile;
hold on;
title("Live Cells Only Segmentation");
D2 = imimposemin(D,mask);
Ld2 = watershed(D2);
bw3 = binaryImage;
bw3(Ld2 == 0) = 0;
imshow(bw3)
nexttile;
hold on;
title("Boundaries of Cells Identified");
imshow(RGB_Image);
props = regionprops(labeledImage, 'all');
numberOfBlobs = numel(props);
boundaries = bwboundaries(bw3);
numberOfBoundaries = size(boundaries, 1);
hold on;
for k = 1 : numberOfBoundaries
      thisBoundary = boundaries{k}; % Get boundary for this specific blob.
      x = thisBoundary(:,2); % Column 2 is the columns, which is x.
      y = thisBoundary(:,1); % Column 1 is the rows, which is x.
      plot(x, y, 'g-', 'LineWidth', 0.5); % Plot boundary in green.
end
hold off;
```

Appendix IV

As a first prototype, the decision was taken to produce a proof-of-concept device which utilises ultra-low power, miniaturised components and can detect pH accurately.

Bluetooth-Based Communication Device

Potentiometric Sensor Components

Typically, miniaturised components are designed for ultra-low power use. It was determined that for the sensing portion of the prototype two components would be required, a potentiostat chip, a microcontroller unit (MCU). A voltage regulator/energy harvesting circuit to power the components would also be needed but is not considered here. For the potentiostat chip, two options are used by industry, the AD5940/AD5941 designed by Analog Devices®, and the AFE4410/AFE4500 designed by Texas Instruments®. Both devices can be configured for ultra-lower power use and include 12-bit DACs for voltage bias definition and 16-bit ADC for sufficient resolution measurement of voltage potential. They can operate at below freezing temperatures and up to 85°C. The AD series is 3.6mm x 4.2 mm whereas the AFE series can come in 3 mm x 2.6 mm packages. This makes the AFE series more suitable due to the size requirements detailed earlier. However, Analog Devices® offers an evaluation board for the AD5940 which is user friendly and can connect directly to any Arduino-based microcontroller framework. For this reason, the AD5940 was chosen for the proof-of-concept device.

MCUs are manufactured by numerous competitors in industry and can reach sub 2 mm dimensions with high resolution and low power requirements. Although they can be classified into 3 core types, in practice, their ease of compatibility for performing tasks using various components is highly linked to the manufacturer. This is due to a variety of reasons not discussed here. For user-friendliness in this prototyping stage, the manufacturer-recommended ARM Cortex M3 MCU was chosen in the form of the EVAL-ADICUP3029, a MCU wireless evaluation board. It has an ADuCM3029 microcontroller manufactured by Analog Devices. This evaluation board is designed for ultra-low power programming uses and includes transmitters, battery/power input, specialised debugging software and example codes by the manufacturer.

Communication Method

Bluetooth low energy (BLE) uses the classic 2.4 GHz frequencies as classic Bluetooth but uses a different modulation technique considerably reducing power requirements while maintaining range. This method of communication was chosen despite the drawbacks of the 2.4 GHz band for implantable electronics communication, as this was a first prototype and would not be implanted.

Sensor Design

As mentioned, the aim of the first prototype was to show a proof-of-concept rather than create a full-fledged miniaturised device that could meet the requirements of the sensor. The ability of the sensor to correctly sense pH and successfully transmit the readings to a reader device using miniaturised components would be considered successful. For this first-prototype, the sensor code and integration of the components was prioritised.

However, a CAD design was made using CAD Software (Fusion 360, Autodesk ®). The design was scaled such that the width of the square sensors were ~15.5 mm and would comfortably fit the components of the sensor. Exploded and assembled views are shown in Figure 85 without the interconnects on the substrate for clarity purposes. The power requirements of the device are not shown here, this was because the device would likely require a flexible solid-state battery which are not commercially available and would have to be fabricated following approaches shown in literature. This was decided to be out of scope of the current prototype and a simple battery system could be used instead for power. It should be reiterated however, that this design was not fabricated, and was only created to be a part of future work.

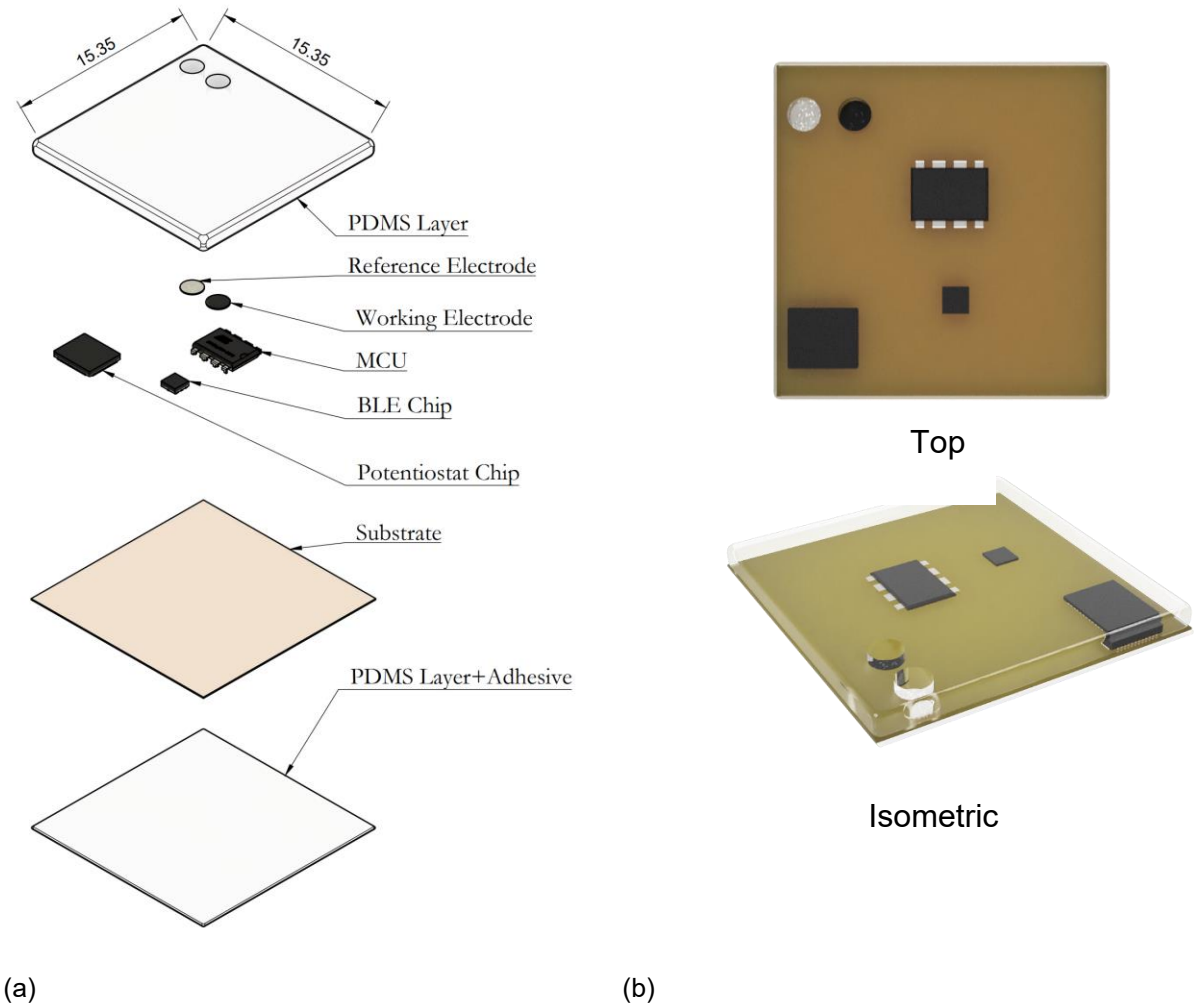


Figure 85: Exploded **(a)** and assembled **(b)** views of the proposed battery-powered sensor. (Dimensions in mm)

Software Design

The core functions of the sensor were adapted from the example code provided by the manufacturer and were integrated in a bespoke manner to suit the application required. In this section there are two components, the sensor itself, which comprises of the integration of the MCU, potentiostat chip and the BLE chip, and the GUI designed to display the measurements from the sensor on an Android® mobile device.

Sensor Device

There are six different algorithms which are described at a high-level to perform the required application. Briefly, initially the MCU is initialised, and the communication platform between the potentiostat device is initialised. Following this, the AD5940 switch matrix is configured to perform the measurement mode required, and then calls for measurements to be taken. Then the MCU initialises the BLE chip, a connection

algorithm is called, and once connection is established, measurements are continuously sent to the receiver. The different algorithms are explained in further detail (from a high-level perspective) below, where any libraries used, inputs and outputs are indicated.

Algorithm 1 MCU Initialisation

Input: (void)

Include: ADICUP3029 manufacturer library

1: Initialise MCU pin multiplexer

2: Initialise core clock

3: Initialise peripheral clock

4: Set power mode: (Ultra-Low Power Mode)5: Set Debug message output to UART

Output: MCU Initialised

Initially, the MCU must be initialised and set to the correct configuration where the clocks, multiplexer and mode are set. The MCU is used to configure the remaining components, and the clocks of the AD5940 and BLE are set using the MCU clock type. The AD5940 is controlled through SPI (Serial-Programming Interface) communication type by the MCU which requires the SPI and GPIO (General Purpose In/Out) pins to be correctly configured.

Algorithm 2 Communication Initialisation between MCU and AD5940

Input: (void)

Include: ADICUP3029 manufacturer library, AD5940 manufacturer C++ and header files.

1: Initialise SPI peripheral and GPIO pins

2: Enable master mode on MCU

3: Enable SPI mode on MCU

4: Assign GPIO pin for input from AD5940

Output: Communication Established

Once configured, the AD5940 must be initialised as described by algorithm 2 and then configured to use potentiometric measurements as described in algorithm 3. The appendix has the functional block diagram provided by the manufacturer which was configured for potentiometric measurements, it can be seen that the low bandwidth AFE loop is similar to a standard potentiostat circuit.

For the potentiometric measurements, there is a default configuration where the switches, resistance values and biases are set such that the program can run. However, the algorithm is designed to check for a user-friendly editable configuration file such that these values can be overridden to suit the purpose. These values are set dependent on the range of the potential measurements required [121].

```
Algorithm 3 AD5940-Configuration
Input: (void)
Include: AD5940 manufacturer C++ and header files.
1: Run AD5940 platform configuration: clock, FIFO and sequencer, assign GPIO pins, etc.
2: Configure Potentiometric measurements (Ultra-Low Power configuration)
        Use low power transimpedance amplifier
3:
4:
           Activate necessary switches
5:
        Set resistor values for measurements (dependent on potential range)
        If (default values override = True) {Use custom config file}
6:
        Configure low-power DAC for RE voltage set
7:
        Configure multiplexer switches
8:
        Configure ADC gain values
10: Run Potentiometric measurements continuously
Output: Measurement Results
```

Following output of the measurement results as desired, the MCU is called to activate and utilise the BLE chip to broadcast the results to a compatible BLE receiver device. The clocks and radio are initialised using the MCU. Then the algorithm waits for a connection to be established. Following connection, the measurement results are broadcasted to the receiver device at the same specified frequency of the measurement results.

```
Algorithm 4 BLE broadcasting
Input: Measurement results
Include: Bluetooth low energy library
1: Initialise BLE
        Configure core and peripheral clocks
2:
3:
        Initialise radio
4:
        Register device name
        Initialise data exchange profile
5:
        Wait for connection
7: If (connection established = True) {
        Print (Connected Message) to UART
        Broadcast (Measurement results)
9:
10:
11: If (connection established = False) {
        Print (Disconnected Message) to UART }
13: If (connection lost = True) {
        Attempt auto re-connect sequence()}
15: Switch off to conserve power
Output: Measurement results broadcasted
```

The algorithms have been set to run continuously until an interrupt function is triggered from the receiver device or until a continuous disconnection state is exhibited.

Mobile GUI

The GUI was designed using MIT App Inventor® due to the user-friendly block-based programming interface for Android phones. Figure 86 shows the GUI and the different buttons are described in Table 9. Android was chosen over IOS due to the lack of development of BLE functionality for IOS on MIT App Inventor. The GUI displays the potential values, the corresponding pH value (following calibration) and the connection status. The GUI also plots the potential with respect to time.

Table 9: Details of buttons and their function.

Button	Function
Scan	Begin Bluetooth scan on mobile device.
	List all detected Bluetooth devices and arrange by signal strength.
Stop Scanning	Stop scanning for new devices and arrangement by signal strength. Wait for User's selection of Bluetooth device to connect to.
Disconnect	Following connection, disconnect to stop readings.
Calibrate	Used to calibrate the sensor for potentiometric measurements. Submerge sensor into 2 known pH buffer solutions, generate the linear relationship between pH and potential.

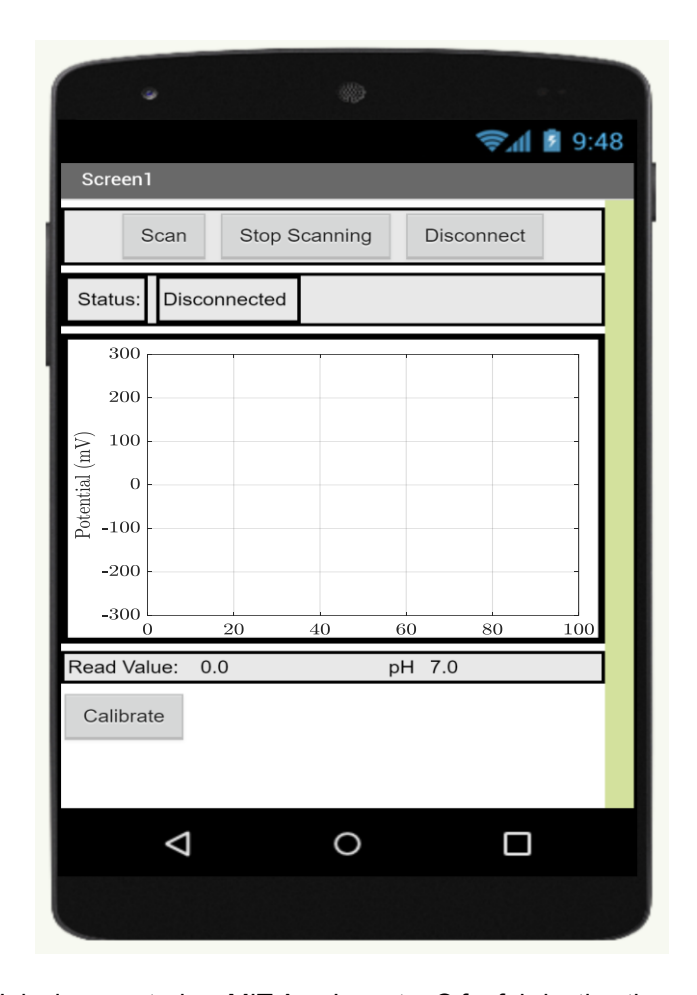


Figure 86: Mobile GUI design created on MIT App Inventor ® for fabricating the proof-of-concept device.

Results and Discussion

The results are expressed in terms of practicality as a proof-of-concept device and accuracy of the potentiostat compared to a professional grade potentiostat (Ivium-n-stat, q-module). In terms of practicality, the sensor performed as designed. The sensor was able to connect to the mobile device and provide measurements. However, the length of time of connection was variable, seemingly at random. At times, it would run for 1 hour or longer, and at other times it would run for only a few measurements before a fatal interrupt would occur at the MCU side. The device had a high range (>10m) and was able to reconnect upon connection drop at a much higher rate than the sampling rate specified at 5 s.

In terms of accuracy compared to the professional grade potentiostat, only the OCP was compared. The sensor correctly measured the potential provided by a DC voltage source. The sensors then were compared at their pH sensing ability. As each fabricated sensor has slightly different calibration equations, readings could not be

performed simultaneously, where two sensors are submerged and measured using each potentiostat type. However, the sensors were first submerged and measured using one potentiostat device and then resubmerged and compared with the new potentiostat device. This method inevitably introduced hysteresis and steady state errors due to the low sampling rate (for low power consumption). Despite this, the readings were highly agreeable for the open-circuit potential measurements. The portable sensors were able to pick up changes in pH as they were submerged from one pH buffer solution to the other and broadcast the measurements to the mobile device.

While the proof-of concept provided promising results, this result was expected as there are a wide range of DIY potentiostats in literature and their fabrication techniques are widely accessible [122], [127]. The real issues with the proof-of-concept device lie with the power consumption, which has yet to be measured, and its powering technique. The communication method, while valid for non-implantable devices, is likely not suitable for GORD diagnosis due to the usage of the 2.4 GHz band (a frequency that is readily absorbed by water and tissue). For reference, the Bravo® Capsule uses a 433 MHz frequency which would likely not have the same issue [112]. This is however a frequency that is more specialised and does not have the benefits of the BLE's robustness, cheap components, and widely available usage.

Author Contribution Statement

In Chapter 2, Jianhui Zhang aided with SEM imaging. Lulu Xu helped with initial printing.

In Chapter 3. COF/GO cell culturing, seeding, and assessment was carried out by Ashley Lam from the WEISS Centre. Jianhui Zhang carried out AFM measurements and aided with SEM imaging.

In Chapter 4, Noora Al Marri and Jiaxing Zhang aided with NFC coil design.

In Chapter 5, Jianhui Zhang aided with flow testing.